

Ab Initio Calculations of the Magnetic Properties of Bimetallic Alloys

by

Cecilia Johanna Aas

Thesis
submitted to the University of York
for the degree of

Doctor of Philosophy

Department of Physics
May 2013

Abstract

Magnetic recording technology is ubiquitous in the modern world and constitutes a corner stone of current research and development. Recent inventions such as heat-assisted magnetic recording and exchange-coupled media has focused magnetic recording research towards alloys exhibiting strong magnetocrystalline anisotropies. In this thesis, we investigate, from first principles using the screened Korringa-Kohn-Rostoker method, the effect of a range of compositional and microstructural defects and features upon the magnetocrystalline anisotropy energy (MAE) of FePt and CoPt alloys. We show that localised Pt alloying affects the MAE of bulk Co primarily through the Pt-induced effects on the Co sites. We demonstrate that stacking faults often reduce the Co MAE and that the effect of composite stacking faults upon the MAE is not necessarily additive, but synergistic. By varying the unit cell geometry and the compositional parameters of FePt, we show that the formation of complete Fe layers is, generally, the dominant factor in maintaining a large MAE. We investigate the magnetic properties (spin moments, magnetocrystalline anisotropy and magnetic exchange) across an Fe/FePt/Fe multilayer and show that the effective exchange exhibits a strong reduction at the Fe/FePt interfaces and that the MAE of the whole multilayer system is very slightly reduced by the presence of the Fe/FePt interfaces. Across all systems, we observe that localised features such as stacking faults, interfaces and localised alloying incur relatively long-ranged spatial oscillations in the MAE, which may, in turn, cause significant finite-size effects on the nano-scale.

Contents

Abstract	2
Contents	3
List of Figures	6
List of Tables	10
List of Symbols	11
List of Abbreviations	18
Acknowledgements	19
Declarations	21
Publications	22
1 Introduction	23
1.1 The History of Magnetic Recording	23
1.2 The Magnetic Recording Trilemma	25
1.3 Advanced Magnetic Materials	26
2 Theoretical Principles	29
2.1 Basic Concepts of Magnetism	29
2.1.1 Magnetic Exchange Interactions	30
2.1.2 Magnetocrystalline Anisotropy Energy	31

2.1.3	On-site and Inter-site Anisotropy	32
2.1.4	Magnetostatic Energy	32
2.1.5	Magnetic Behaviour	33
2.2	Density Functional Theory	34
2.2.1	Hohenberg-Kohn Theorem	34
2.2.2	Kohn-Sham Equations	35
2.2.3	Magnetism in DFT	37
2.2.4	The Local Spin Density Approximation	38
2.3	The Korringa-Kohn-Rostoker Method	38
2.3.1	The Green's Function	38
2.3.2	Multiple Scattering Theory	40
2.3.3	Screening	44
2.3.4	Evaluation of Magnetic Properties	46
2.3.5	Treatment of Chemically Disordered Systems	48
2.3.6	Summary of the KKR Method	49
3	Microstructural Defects and Localised Alloying in Cobalt	51
3.1	Computational Details	53
3.2	Localised Platinum Alloying in Cobalt	56
3.2.1	The System	56
3.2.2	Layer-Resolved Contributions to the MAE	57
3.2.3	Aggregate Variation in the MAE	63
3.2.4	Finite-Size and Short-Range Order Effects	67
3.3	Stacking Faults in hcp Cobalt	71
3.3.1	Types of Stacking Fault	71
3.3.2	The System	72
3.3.3	Stacking Fault Formation Energies	73
3.3.4	Layer-Resolved Contributions to the MAE	77
3.3.5	Aggregate Variation in the MAE	77
3.3.6	Composite Stacking Faults	80
3.4	Summary and Conclusions	83

4	Structural and Compositional Effects in FePt	85
4.1	Computational Details	88
4.2	Effect of Tetragonality on the MAE	90
4.3	Effects of Chemical Disorder and Composition on the MAE	93
4.4	Comparison of Calculations to Experiment	96
4.4.1	Ding <i>et al.</i> , J. Appl. Phys. 97 (2005) 10H303	99
4.4.2	Barmak <i>et al.</i> , J. Appl. Phys. 98 (2005) 033904	104
4.5	Effects of Vacuum Interfaces on the MAE	107
4.6	Summary and Conclusions	111
5	Interface Effects in Fe/FePt Multilayers	113
5.1	Computational Details	114
5.2	The Systems	115
5.3	Local Spin Moments	120
5.4	Effective Exchange	120
5.5	Magnetocrystalline Anisotropy Energy	124
5.5.1	Layer-Resolved MAE Contributions	124
5.5.2	On-site and Inter-site Anisotropies	126
5.5.3	Aggregate Change in the MAE of the FePt Phase	128
5.6	Summary and Conclusions	132
6	Summary and Outlook	134
	Appendix	139
A	Relations and Concepts within Multiple Scattering Theory	139
	References	146

List of Figures

1.1	The evolution of magnetic recording densities between 1956 and 2012.	24
1.2	The magnetic recording trilemma.	26
1.3	The effect of grain size on the signal-to-noise ratio for a magnetic recording medium in the grain size limit.	27
2.1	The contour \curvearrowright of the integral in Eq. (2.26).	40
3.1	The hexagonal close-packed lattice structure.	53
3.2	Convergence of the Co total energy and the Co magnetic moment with the angular momentum cut-off.	56
3.3	Sketch of the system used to study localised Pt alloying in Co.	58
3.4	The layer-resolved Co contributions, $D_i^{(Co)}$, to the MAE of the system shown in Fig. 3.3.	59
3.5	The valence charges and the shifts of the Madelung potentials for layers $ i \leq 13$ with Pt concentration $\nu = 0.02$	61
3.6	The species-resolved MAE contributions for layers $0 \leq i \leq 4$	62
3.7	The valence charges and the shifts of the Madelung potentials for atomic layer $i = 1$, as functions of the Pt concentration, ν	64
3.8	The change in the MAE of a system of 81 atomic layers, ΔK , as a function of the Pt concentration, ν	65
3.9	The change in the MAE per Pt atom as a function of the Pt concentration, ν	66
3.10	Approximate layer-resolved derivatives of the cobalt contributions to the MAE with respect to the Pt concentration, ν , evaluated at $\nu = 0.02$	68

3.11	The total change in the MAE per Pt atom, \bar{K}_{Pt} , as a function of the number of layers N included in the sum in Eq. (3.9) for different Pt concentrations v	69
3.12	Illustration of the cluster used in the real-space calculations of the MAE contributions in the vicinity of a Pt impurity in Co. . .	70
3.13	The \cdots ABAB \cdots and \cdots ABCABC \cdots stacking sequences of hexagonal layers.	71
3.14	The layer-resolved total energy contributions across four different types of stacking fault in hcp Co.	75
3.15	The aggregate variation in the total energy of hcp Co due to the presence of a stacking fault of type I_1 , I_2 , E or T_2	76
3.16	The layer-resolved MAE contributions across stacking faults I_1 , I_2 , E and T_2	78
3.17	The total change in the MAE due to the presence of stacking faults I_1 , I_2 , E and T_2 as a function of the number of layers N included in the sum in Eq. (3.12).	79
3.18	Comparison of $\Delta D_i^{(I_1 I_1)}$ and $\Delta D_i^{(I_1+I_1)}$ as per Eq. (3.13) and Eq. (3.14).	81
3.19	Comparison of the aggregate change in the MAE due to the presence of the composite stacking fault and the aggregate change in the MAE due to the presence of one isolated type I_1 stacking fault.	82
4.1	Illustration of variations in the tetragonality, the chemical order and the composition of FePt.	86
4.2	The phase diagram of FePt.	87
4.3	The variation of the fractional concentrations r_{Fe} and r_{Pt} with the chemical order parameter, s , for different compositions x of Fe_xPt_{1-x}	91
4.4	Using the coherent potential approximation, disordered Fe_xPt_{1-x} was modelled as a stack of alternating layers of $Fe_{r_{Fe}}Pt_{1-r_{Fe}}$ alloy and $Fe_{1-r_{Pt}}Pt_{r_{Pt}}$ alloy along the [001] axis.	92
4.5	The MAE per formula unit of perfectly ordered $Fe_{0.5}Pt_{0.5}$ as a function of the ratio of lattice parameters, c/a	92
4.6	The MAE per formula unit of Fe_xPt_{1-x} as a function of the chemical order parameter, s , for different compositions $0.4 \leq x \leq 0.6$	94

4.7	The species-resolved MAE contributions as functions of the degree of chemical order, s , for different compositions $0.4 \leq x \leq 0.6$.	95
4.8	The MAE per formula unit of $\text{Fe}_x\text{Pt}_{1-x}$ as a function of the Fe concentration in the nominal Fe layers, r_{Fe} , for different compositions $0.4 \leq x \leq 0.6$.	97
4.9	Comparison of SKKR calculations to experiment with regards to the MAE per formula unit of perfectly ordered $\text{Fe}_{0.5}\text{Pt}_{0.5}$ as a function of the ratio of lattice parameters, c/a .	98
4.10	The scaling of the MAE of perfectly ordered $\text{Fe}_{0.5}\text{Pt}_{0.5}$ with temperature, according to the Langevin dynamics simulation study of Mryasov <i>et al.</i> , Europhys. Lett. 69 (2005) 805.	99
4.11	Comparison to experiment for the calculated (SKKR) MAE per formula unit of perfectly ordered $\text{Fe}_{0.5}\text{Pt}_{0.5}$ using the experimental lattice parameters of Ding <i>et al.</i> , J. Appl. Phys. 97 (2005) 10H303, listed in Table 4.1.	101
4.12	Comparison to experiment for the calculated (SKKR-CPA) MAE per formula unit of partially disordered $\text{Fe}_{0.5}\text{Pt}_{0.5}$ using the lattice parameters and degrees of chemical order obtained by Ding <i>et al.</i> , J. Appl. Phys. 97 (2005) 10H303, listed in Table 4.1.	102
4.13	The MAE as a function of the chemical order parameter, s , for the five different sets of lattice parameters from Ding <i>et al.</i> , J. Appl. Phys. 97 (2005) 10H303, listed in Table 4.1.	103
4.14	Comparison of the theoretically predicted degrees of chemical order and the experimentally determined chemical order parameters from Ding <i>et al.</i> , J. Appl. Phys. 97 (2005) 10H303, listed in Table 4.1.	104
4.15	Comparison of the theoretical MAE values calculated using SKKR-CPA and the experimental MAE values of the $\text{Fe}_x\text{Pt}_{1-x}$ samples studied by Barmak <i>et al.</i> , J. Appl. Phys. 98 (2005) 033904, listed in Table 4.2.	106
4.16	The relaxed atomic layer spacings along the [001] axis in an FePt slab.	108
4.17	The change in the MAE of FePt due to the presence of Fe- and Pt-terminated (001) surfaces.	110
5.1	The layout of the Fe/FePt/Fe multilayer systems.	116

5.2	The relaxed atomic layer spacings, Δz_i , and the corresponding radii of atomic spheres, S_i , of a relaxed Fe/FePt/Fe system. . . .	119
5.3	The spin moments across Fe/FePt/Fe systems A , B and C	121
5.4	The layer-resolved effective isotropic exchange constant for Fe/FePt/Fe systems A , B and C	122
5.5	The layer-resolved MAE contributions across Fe/FePt/Fe systems A , B and C	125
5.6	The <i>d</i> -like spin- and orbital-projected local partial densities of states (LPDOS) for the interfacial Fe layers in an Fe/FePt/Fe system.	127
5.7	The layer-resolved on-site and inter-site anisotropies across Fe/FePt/Fe systems A , B and C	129
5.8	The layer-resolved MAE contributions across Fe/FePt/Fe system A and FePt/Fe/FePt/Fe/FePt system D	131
5.9	The abrupt break in a domain wall at an Fe/FePt interface due to the weak interlayer coupling in the interfacial Fe layer. . . .	133

List of Tables

2.1	The relations between the angular derivatives of the free energy as described by the anisotropic Heisenberg Hamiltonian, \hat{H}_{aHeis} , and the various elements of the exchange tensor \underline{J}_{ij} for the system being polarised along each of the three axes of the global frame of reference.	48
3.1	The type of stacking of each atomic layer with respect to its two neighbouring atomic layers.	72
4.1	Summary of experimental results from Ding <i>et al.</i> , J. Appl. Phys. 97 (2005) 10H303.	100
4.2	Summary of experimental results from Barmak <i>et al.</i> , J. Appl. Phys. 98 (2005) 033904.	105
5.1	The atomic layer layout of an Fe/FePt/Fe structure enclosed by bulk Fe.	116
5.2	The atomic layer layout of an FePt/Fe/FePt/Fe/FePt structure enclosed by bulk FePt.	116

List of Symbols

0_2	the 2x2 zero matrix
A	generic property of a quantum-mechanical system
\hat{A}	the operator associated with property A
a	lattice parameter
a_{2D}	in-plane lattice parameter in an Fe/FePt/Fe multilayer
$\mathbf{B}_{\text{eff}}(\mathbf{r})$	effective magnetic field
$\mathbf{B}_{\text{ext}}(\mathbf{r})$	external magnetic field
$\mathfrak{B}(z)$	effective perturbation potential in a chemically disordered system
c	speed of light, $3.0 \times 10^8 \text{ m}\cdot\text{s}^{-1}$ or lattice parameter
$D_i^{(\alpha)}$	contribution to the magnetocrystalline anisotropy from an atom of species α in atomic layer i (occasionally the species index is dropped)
$\Delta D_i^{(\alpha)}$	difference between $D_i^{(\alpha)}$ and the bulk MAE
$D_i^{(\alpha, \hat{\mathbf{n}})}$	contribution to $\frac{dE}{d\theta} _{\hat{\mathbf{n}}}$ from an atom of species α in atomic layer i
d_i	on-site anisotropy contribution of site i
$d_{\text{interface}}$	atomic layer separation at an Fe/FePt (001) interface
E	the total energy
E_{band}	band energy
E_{ext}	energy due to external potential
E_{form}	formation energy
E_H	Hartree energy
E_{Mad}	Madelung energy
E_{mag}	magnetostatic energy

E_{xc}	exchange-correlation energy
e	the electronic charge, 1.602×10^{-19} C
\mathbf{e}	unit vector along the easy axis in a uniaxial system
\mathcal{F}	the free energy
$f_{FD}(\varepsilon)$	the Fermi-Dirac distribution
$\hat{G}(z)$	the resolvent, or Green's function
$\hat{G}_0(z)$	resolvent of reference system
$G(z; \mathbf{r}, \mathbf{r}')$	the configuration space representation of the resolvent $\hat{G}(z)$
$\hat{G}^\pm(\varepsilon)$	the positive/negative side limits of the Green's function
$G(z)$	site- and angular momentum matrix representation of the Green's function
$\mathfrak{G}(z)$	the effective Green's function of a chemically disordered system
\hat{H}	Hamiltonian operator
\hat{H}_0	Hamiltonian operator of reference system
\hat{H}_{aHeis}	the anisotropic Heisenberg Hamiltonian
\hat{H}_{Heis}	first-order magnetic exchange (Heisenberg) Hamiltonian
\hat{H}_{KSD}	Kohn-Sham-Dirac Hamiltonian
$H_Q(z; \mathbf{r})$	Hankel-like solution of free-space Dirac equation
$\mathbf{H}_{\text{demag}}(\mathbf{r})$	local demagnetising field
$\hat{\mathcal{H}}$	the effective Hamiltonian of a chemically disordered system
\hbar	Planck's constant, 1.05×10^{-34} J·s
\hat{I}	the identity operator
I	current
I_2	the 2x2 identity matrix
I_4	the 4x4 identity matrix
i	index, or the imaginary number $\sqrt{-1}$
$\underline{\underline{J}}_{ij}$	3x3 magnetic exchange tensor for sites i and j
J_{ij}	the exchange interaction constant; $J_{ij} = \frac{1}{3} \text{Tr} \underline{\underline{J}}_{ij}$
J_{ij}^{RKKY}	the exchange interaction constant for RKKY exchange
J_i	the effective exchange interaction constant; $J_i = \frac{1}{3} \sum_j \text{Tr} \left\{ \underline{\underline{J}}_{ij} \right\}$
$J_i^Q(z; \mathbf{r})$	irregular scattering solution of single-site Dirac equation
$J_Q(z; \mathbf{r})$	Bessel-like solution of the free-space Dirac equation

K	uniaxial magnetocrystalline anisotropy energy (constant)
K_{Co}	MAE per bulk Co atom
K_{FePt}	MAE per bulk FePt formula unit
$K_{Fe}^{(FePt)}$	Fe contribution to K_{FePt}
$K_{Pt}^{(FePt)}$	Pt contribution to K_{FePt}
K_i	site- or layer-resolved contributions to the MAE
K_{Pt}	change in MAE of Co per Pt added
\bar{K}_{Pt}	average change in MAE of Co per Pt atom in the system
K_u	uniaxial magnetocrystalline anisotropy energy per volume
ΔK	change in total MAE
ΔK_i	difference between K_i and the bulk MAE per atom
$\Delta K_{FePt-slab}$	change in MAE of FePt phase due to Fe/FePt interfaces
$\Delta K_{surface}$	change in MAE due to the presence of a surface
ΔK_X	change in Co MAE due to the presence of stacking fault X
k_B	Boltzmann constant; $k_B = 1.38 \times 10^{-23} \text{ kg}\cdot\text{m}^2\cdot\text{s}^{-2}\cdot\text{K}^{-1}$
\mathbf{k}	wave vector
\mathbf{k}_F	the Fermi wave vector; $k_F = \sqrt{2m_e\varepsilon_F}/\hbar$
L	angular momentum quantum number
l	orbital angular momentum quantum number
l_{max}	angular momentum cut-off in spherical harmonics expansion
M_{sat}	saturation magnetisation
\mathbf{m}	classical magnetic moment
\mathbf{m}_i	localised magnetic moment on site i
m_i	magnitude of the localised magnetic moment on site i
$\mathbf{m}(\mathbf{r})$	local magnetisation density of the system in $\text{A}\cdot\text{m}^{-1}$
m_e	mass of electron, $9.11 \times 10^{-31} \text{ kg}$
m_l	orbital angular momentum quantum number
m_s	spin angular momentum quantum number
$N(\varepsilon)$	integrated density of states
N_e	total number of electrons
N_L	half the number of atomic Co layers in the interlayer
$n(\mathbf{r})$	electron density
$n_{\uparrow}(\mathbf{r}), n_{\downarrow}(\mathbf{r})$	majority and minority spin density

$n_0(\mathbf{r})$	ground state electron density
$n_{\text{in}}(\mathbf{r})$	input electron density for the Kohn-Sham scheme
$n_{\text{out}}(\mathbf{r})$	output electron density for the Kohn-Sham scheme
n_e	number of energy points
n_k	number of k -points
$n(\varepsilon)$	density of states
p	linear momentum
Q	relativistic composite angular momentum quantum number $Q = (\kappa, \mu)$
\mathbf{R}	nuclear coordinates
\mathbf{R}_i	real-space position at which the i^{th} scatterer is centred
\mathbf{R}_{ij}	interatomic separation vector of sites i and j
\mathbf{r}	real-space position in the global frame of reference <i>or</i> electronic coordinates
\mathbf{r}_i	real-space position in frame reference relative to the centre of the i^{th} scatterer
r_A	fraction of α -sites occupied by A-atoms
r_B	fraction of β -sites occupied by B-atoms
r_{Fe}	the fractional concentration of Fe in the nominal Fe layers of L1 ₀ FePt
r_{Pt}	the fractional concentration of Pt in the nominal Pt layers of L1 ₀ FePt
\mathbb{R}	the set of real numbers
\mathbf{S}	normalised magnetic moment
\mathbf{S}_i	normalised magnetic moment associated with site i
S_i	atomic sphere radius at site i
s	the chemical order parameter
$\hat{T}(z)$	the t-operator of a collection of scatterers
T	temperature
$T(\theta)$	magnetic torque
T_C	Curie temperature
\hat{T}_s	kinetic energy operator of non-interacting particles
T_s	kinetic energy of non-interacting particles

$\hat{t}_i(z)$	the t-operator of the i^{th} scatterer
$t_i^{Q'Q}(z)$	angular momentum representation of $\hat{t}_i(z)$
$t(z)$	site- and angular momentum matrix representation of $\hat{t}_i(z)$
t_{PL}	number of atomic layers in each principal layer
$u(\mathbf{r}, t)$	generic time- and space-dependent wavefunction
V	grain volume
\hat{V}	perturbation potential operator
$V_{\text{CPA}}(\mathbf{r})$	coherent potential of the coherent potential approximation
\hat{V}_{eff}	effective potential operator
$V_{\text{eff}}(\mathbf{r})$	effective potential
$V_{\text{ext}}(\mathbf{r})$	external potential
$V_i(\mathbf{r}_i)$	spherical potential centred on the i^{th} scatterer
$V_H(\mathbf{r})$	Hartree potential
V_{Mad}	Madelung potential
$V_t(\mathbf{r})$	lattice potential for a bulk system of species t
$V_{\text{VCA}}(\mathbf{r})$	effective potential of the virtual crystal approximation
$V_{\text{xc}}(\mathbf{r})$	exchange-correlation potential
v	Pt concentration in isolated atomic layer of $\text{Co}_{1-v}\text{Pt}_v$
v_i^α	concentration of species α on site i
x	spatial coordinate <i>or</i> Fe content of $\text{Fe}_x\text{Pt}_{1-x}$
x_t	concentration of species t
y	spatial coordinate
y_α	fraction of lattice sites occupied by A-atoms at perfect chemical order
y_β	fraction of lattice sites occupied by B-atoms at perfect chemical order
y_{Fe}	fraction of lattice sites occupied by Fe atoms in perfectly ordered $\text{Fe}_{0.5}\text{Pt}_{0.5}$
y_{Pt}	fraction of lattice sites occupied by Pt atoms in perfectly ordered $\text{Fe}_{0.5}\text{Pt}_{0.5}$
$Z_i^Q(z; \mathbf{r})$	regular scattering solution of single-site Dirac equation
z	spatial coordinate <i>or</i> complex energy (cf. ϵ)
∇	the gradient operator

α	species index, or the vector of 4x4 Dirac matrices	$\begin{pmatrix} \alpha_1 \\ \alpha_2 \\ \alpha_3 \end{pmatrix}$
α_j	the 4x4 Dirac matrix	$\begin{pmatrix} 0_2 & \sigma_j \\ \sigma_j & 0_2 \end{pmatrix}$
β	the 4x4 Dirac matrix	$\begin{pmatrix} I_2 & 0_2 \\ 0_2 & -I_2 \end{pmatrix}$
Γ_i	occupation parameter of site i ; $\Gamma_i = 1$ if site i is occupied by species A and $\Gamma_i = 0$ if site i is occupied by species B	
δ	infinitesimal real number	
δ_{ij}	the Kronecker delta	
$\delta(r)$	the delta function for any variable $r \in \mathbb{C}$	
ε	real energy	
ε_F	the Fermi energy	
ε_i	i^{th} eigenenergy	
η	the ratio $\frac{4K_u}{\mu_0 M_{\text{sat}}}$	
θ	polar angle from the \hat{z} -axis in the zx plane	
$\Theta(r)$	the Heaviside step function	
κ	see Q	
μ	see Q	
μ_0	the permeability of vacuum, $4\pi \cdot 10^{-7} \text{ N}\cdot\text{A}^{-2}$	
μ_B	Bohr magneton, $9.274 \times 10^{-24} \text{ J}\cdot\text{T}^{-1}$	
ξ_i	the i^{th} one-particle eigenfunction of the Kohn-Sham Hamiltonian	
Σ_1	the 4x4 matrix	$\begin{pmatrix} \sigma_1 & 0_2 \\ 0_2 & \sigma_1 \end{pmatrix}$
Σ_2	the 4x4 matrix	$\begin{pmatrix} \underline{\underline{\sigma_2}} & 0_2 \\ 0_2 & \underline{\underline{\sigma_2}} \end{pmatrix}$
Σ_3	the 4x4 matrix	$\begin{pmatrix} \underline{\underline{\sigma_3}} & 0_2 \\ 0_2 & \underline{\underline{\sigma_3}} \end{pmatrix}$
Σ	the vector of matrices	$\begin{pmatrix} \underline{\underline{\Sigma_1}} \\ \underline{\underline{\Sigma_2}} \\ \underline{\underline{\Sigma_3}} \end{pmatrix}$

$\underline{\underline{\sigma_1}}$	the Pauli spin matrix $\begin{pmatrix} 0 & 1 \\ 1 & 0 \end{pmatrix}$
$\underline{\underline{\sigma_2}}$	the Pauli spin matrix $\begin{pmatrix} 0 & -i \\ i & 0 \end{pmatrix}$
$\underline{\underline{\sigma_3}}$	the Pauli spin matrix $\begin{pmatrix} 1 & 0 \\ 0 & -1 \end{pmatrix}$
σ	the vector of Pauli spin matrices $(\underline{\underline{\sigma_1}}, \underline{\underline{\sigma_2}}, \underline{\underline{\sigma_3}})$
$\hat{\tau}_{ij}(z)$	the scattering path operator between sites i and j
$\tau_{ij}^{QQ'}(z)$	angular momentum space representation of $\hat{\tau}_{ij}(z)$
$\tau(z)$	site- and angular momentum matrix representation of $\hat{\tau}_{ij}(z)$
ϕ	polar angle from the \hat{x} -axis in the xy plane
Φ_i	i^{th} eigenspinor of Kohn-Sham-Dirac equation
ψ_n	n^{th} eigenstate
$\psi^{(0)}$	unperturbed state
$\psi^{(p)}$	perturbed state
Ψ_n	n^{th} eigenstate
$\Psi_{\text{electronic}}$	electronic wavefunction
Ψ_{nuclear}	nuclear wavefunction
Ψ_{total}	total wavefunction of an interacting electronic-nuclear system
Ω	the entire three-dimensional space
Ω_i	the real-space region covered by the i^{th} scatterer

List of Abbreviations

2D-BZ	two-dimensional Brillouin zone
AFM	antiferromagnet (-ic, -ism)
ASA	atomic sphere approximation
bcc	body-centred cubic (lattice)
CPA	coherent potential approximation
DFT	density functional theory
DOS	density of states
ECC	exchange-coupled composite (magnetic recording media)
fcc	face-centred cubic (lattice)
FM	ferromagnet (-ic, -ism)
HAMR	heat-assisted magnetic recording
hcp	hexagonal close-packed (lattice)
KKR	the Korringa-Kohn-Rostoker method
KSD	Kohn-Sham-Dirac
LKKR	the layered Korringa-Kohn-Rostoker method
LMTO	linear muffin-tin orbital
LSDA	local spin density approximation
LPDOS	local partial density of states
MAE	magnetocrystalline anisotropy energy
MST	multiple scattering theory
RKKY	Ruderman-Kittel-Kasuya-Yosida (exchange interaction)
SKKR	the screened Korringa-Kohn-Rostoker method
SPO	scattering path operator

Acknowledgements

Tanken gjev uro, tanken gjev sut; endå må du tenkja dine tankar ut.

Arne Garborg

It goes without saying that the completion of a thesis requires the advice and support of people much wiser, much greater and, in this particular case, much more patient than the author. I would like to take this opportunity to thank the many such people who have contributed to my life and research over the past four years.

First and foremost, I would like to acknowledge the support and advice of Professor Roy Chantrell, Professor László Szunyogh and Dr Phil Hasnip. I am forever indebted to them for their encouragement and counsel, without which this thesis would not be in existence. I would like to thank Roy for taking me on as his PhD student and for his supervision, enthusiasm and support. Roy's enormous generosity with regards to computational resources, collaborations, conferences and research visits has been crucial to the completion of this thesis and to my development towards becoming a scientist. I am humbled by László's kindness, enthusiasm and, most of all, superhuman patience and good humour in teaching me nearly everything I know about the Korringa-Kohn-Rostoker method and in letting me use his implementation of this method. Over the past few years, László has offered invaluable assistance and advice on everything from designing suitable systems through interpreting results to writing publications, for which I am deeply grateful. I am greatly indebted to Phil for providing constant encouragement and advice throughout the writing process and for many hours of fruitful and interesting discussions.

On a more general level, I have benefited greatly from discussions with Dr Thomas Ostler, Dr Richard Evans, Dr Ramón Cuadrado del Burgo, Professor Rex Godby, Professor Sarah Thompson, Professor Kevin O'Grady and many

other members of the Condensed Matter Physics Group at the University of York. Furthermore, I am grateful to Professor Katayun Barmak of Columbia University and Professor Jingsheng Chen of the National University of Singapore for thoroughly explaining and detailing their experimental work on FePt to me. Mr András Deák, Professor László Udvardi and Dr Krisztián Palotás, all of the Budapest University of Technology and Economics, have contributed to my understanding of the Korringa-Kohn-Rostoker method. I would also like to acknowledge the very useful comments on the published parts of this work by a number of anonymous referees. I acknowledge funding from EPSRC, Seagate Technology and the EU.

Anna Mäkinen, Rebecca Ronke, Dave Hunt, Phanwadee Chureemart and Elizabeth Edwards have, through their friendship and support, been crucial to the completion of this thesis. In particular, I would like to thank Rebecca and Dave for their careful reading of this manuscript at various points throughout the writing process. Moreover I would like to acknowledge the kindness and generosity of Mrs Liz Phillips, Mr William Joyce and the late Mrs Laura Fry in their helping me to remain active in my sport on a student budget.

Most of all, I would like to thank my parents, Morten and Helén, and my brother, Erik, for their love and constant support. In addition, I would like to thank my Dad for his persistence and patience in teaching me nearly every basic technicality of life and science that I know, from cooking, reading, driving and writing, through printer trouble-shooting and the finer details of sheep shearing, to integration by parts and Pythagoras' theorem. These skills have all come to good use during the course of this work.

Finally, if anyone was ever-present throughout the many ups and downs of my education and research so far, it was Pelle. I will always remember him remaining loyally awake by my side through many a late night of essay writing, coding, trouble-shooting, de-bugging, revising and reading and I will always remember his way of clinging desperately to my suitcase every time I left for the airport to travel to England.

Declarations

I declare that the work presented in this thesis, except where otherwise stated, is based on my own research under the supervision of Professor R W Chantrell and in close collaboration with Professor L Szunyogh. Furthermore, I declare that the work presented in this thesis has not been previously submitted for a degree in this or any other university.

Cecilia Aas

Publications

Parts of the work reported in this thesis have been, or may be, published in:

C. J. Aas, L. Szunyogh, J. S. Chen and R. W. Chantrell, *Magnetic anisotropy of FePt: Effect of lattice distortion and chemical disorder*, Applied Physics Letters **99** (2011) 132501

C. J. Aas, K. Palotás, L. Szunyogh and R. W. Chantrell, *The effect of a Pt impurity layer on the magnetocrystalline anisotropy of hexagonal close-packed Co: a first-principles study*, Journal of Physics: Condensed Matter **24** (2012) 406001

C. J. Aas, L. Szunyogh and R. W. Chantrell, *Effects of composition and chemical disorder on the magnetocrystalline anisotropy of Fe_xPt_{1-x} alloys*, Europhysics Letters **102** (2013) 57004

C. J. Aas, L. Szunyogh, R. F. L. Evans and R. W. Chantrell, *Effect of stacking faults on the magnetocrystalline anisotropy of hcp Co: a first-principles study*, Journal of Physics: Condensed Matter **25** (2013) 296006

C. J. Aas, P. J. Hasnip, R. Cuadrado, E. M. Plotnikova, L. Szunyogh, L. Udvardi and R. W. Chantrell, *Exchange coupling and magnetic anisotropy at Fe/FePt interfaces*, Submitted to Physical Review B.

Introduction

1.1 The History of Magnetic Recording

The phenomenon of magnetism has been known to mankind for centuries. The etymology of the very word “magnet” can be traced all the way back to the sixth century BC and the discovery of lodestone (i.e., magnetic iron ore) near the ancient city of Magnesia in Greece [1,2]. Today, research in magnetism has become central to technological development; electrical motors, magnetic recording and magnetic resonance imaging constitute but a small subset of the huge number of inventions that have sprung out of the study of magnetism and magnetic materials [3]. Magnetic recording, in particular, forms the very basis of modern information technology (see, e.g., [3,4]).

The idea of encoding and storing information within a magnetic material was first studied in 1888 by Oberlin Smith [4–6]. A decade later, in 1898, Valdemar Poulsen invented the first magnetic recording device, the *Telegraphone* [4–6]. The first magnetic tape recorder was constructed in 1931 by Fritz Pfleumer [4]. Today, one of the most common magnetic recording devices is the hard drive, the fundamental design of which comprises a write head, a read head and a recording medium [7]. The write head is a magnetic structure through which flows an electric current, representing the information that is to be recorded [7, 8]. This electric current induces a magnetic field which changes the local magnetisation in the recording medium [7, 8]. The recording medium consists of *bits*, i.e., closely spaced regions of uniform magnetisation, and the information is recorded as a binary sequence of ones and zeroes, represented by the presence or absence of a change in magnetisation between two bits, respectively. As it flies over the recording medium, the read head recovers the information in terms of the output voltage generated by these changes in magneti-

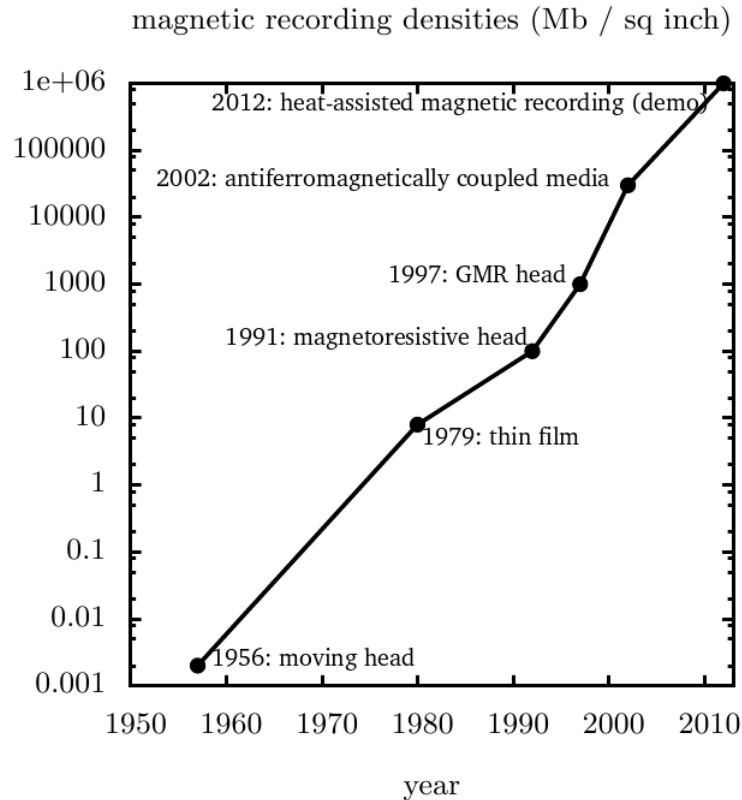


Figure 1.1: The evolution of magnetic recording densities between 1956 and 2012, from the first moving head hard drive marketed by IBM in 1956 to the Seagate demonstration of 1 Tb per square inch in 2012. The most recent progress stems from the development of exchange-coupled composite (ECC) media and heat-assisted magnetic recording (HAMR) technology. The data in the graph is taken from Ref. [10].

sation [7,8]. The first hard drive was marketed by IBM in 1956; it could hold 5 MB of data and weighed about a tonne [9]. As shown in Fig. 1.1, magnetic recording densities have since increased exponentially to reach today's palm-sized hard drives holding hundreds of gigabytes [4, 10, 11]. In 2012, Seagate demonstrated the first 1 Tb per square inch hard drive [12]. This development is the result of half a century of research into the behaviour of magnetic materials at progressively smaller length- and timescales.

Today's research is concerned with pico- to femtosecond processes on atomic length scales (see, e.g., [13–21]). Even within these confines, there is a multitude of levels of simulation, ranging from *ab initio* calculations, where atomic properties are calculated directly from quantum mechanics (see, e.g., [22–27]), through nanometre-scale localised-spin models, where the atomic magnetic moments are treated as semi-classical entities described by model Hamiltoni-

ans (see, e.g., [21, 28, 29]) to micrometre-scale micromagnetic models, in which the magnetisation of discrete, nano-sized elements is described as a fixed-length vector [30]. Each type of simulation has its own advantages and drawbacks and it is of great importance to the field of magnetism to start finding *multiscale approaches* that can link these different techniques (see, e.g., [27, 30–32]). The work in this thesis concerns the *ab initio* end of the scale, although we will also present some discussion of the mapping of our results onto localised-spin models.

1.2 The Magnetic Recording Trilemma

In designing materials for application as magnetic recording media, we are faced with the well-known *magnetic recording trilemma* [33]. As illustrated in Fig. 1.2, a good magnetic recording medium should exhibit thermal stability, high writability and a good signal-to-noise ratio. However, as we shall explain in this Section, we cannot maximise all three of these aspects simultaneously and instead a suitable compromise has to be found.

First, we shall note that the signal-to-noise ratio is inversely related to the grain size of the recording medium [11, 34, 35]. As illustrated in Fig. 1.3, the transitions between bits have to follow the grain boundaries of the recording medium. In the optimal case, which is commonly referred to as the *grain size limit*, the transition follows the grain boundaries closest to the desired spatial position of the transition [36]. The smaller the bits, the more accurate the transitions between bits and therefore the more accurate the reading of the information can be.

The thermal stability of a given magnetic recording medium can, generally, be quantified by the ratio $\frac{K_u V}{k_B T}$ where V is the grain volume, k_B is the Boltzmann constant, T is the operating temperature and K_u is the uniaxial *magnetocrystalline anisotropy energy (constant)* of the material (i.e., the energy required to rotate the direction of magnetisation from an “easy” crystallographic direction into a “hard” crystallographic direction; these concepts will be explained in further detail in Section 2.1.2) [37]. In order to avoid thermal instability, typically, the ratio $\frac{K_u V}{k_B T}$ needs to equal at least 50-70 [37]. Larger grain sizes and larger K_u thus improve the thermal stability. However, large K_u reduce the writability and large grain sizes reduce the signal-to-noise ratio; this is the essence of the magnetic recording trilemma [33].

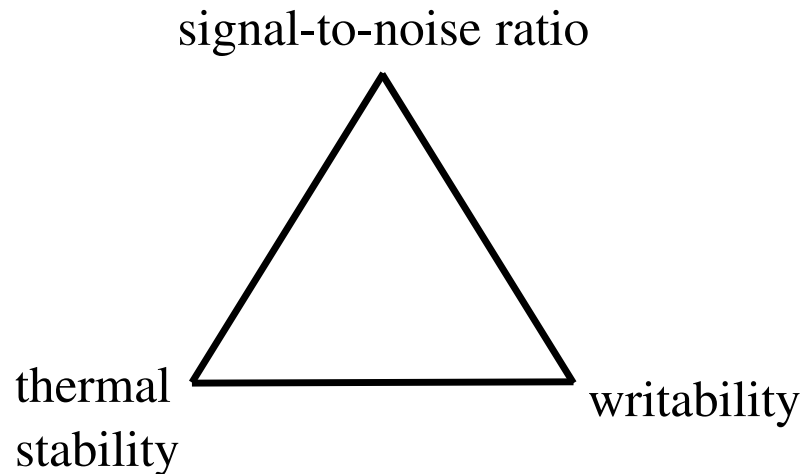


Figure 1.2: The magnetic recording trilemma.

In current developments within the magnetic recording industry, the focus is on using magnetic recording media with very large K_u , enabling smaller grain sizes (thus enhancing the signal-to-noise ratio and enabling larger magnetic recording densities) without reducing the thermal stability [38]. (The limit in which the grain size becomes too small for reliable thermal stability at a given K_u is generally referred to as the *superparamagnetic limit* [34].) In other words, the trilemma is addressed by trading reductions in the writability against improvements in the thermal stability [38]. As we shall see in the next Section, writability is then improved upon “artificially” by using external techniques to reduce the effective write field at a given K_u .

1.3 Advanced Magnetic Materials

As indicated in Fig. 1.1, new technologies like heat-assisted magnetic recording (HAMR) and exchange-coupled composite (ECC) media have contributed greatly to the development of magnetic recording densities in recent years. In HAMR (see, e.g., [39,40]), the magnetic recording medium is locally laser-heated. Information is written to the heated part of the medium while it is hot and therefore easy to write to. The medium is then rapidly cooled, stabilising the written information. In ECC, each grain contains a *soft* and a *hard* phase [41–44]. A (magnetically) soft material refers to a material which is easy to magnetise but which loses its magnetisation upon removal of the magnetising field [45]. A (magnetically) hard material, on the other hand, refers to per-

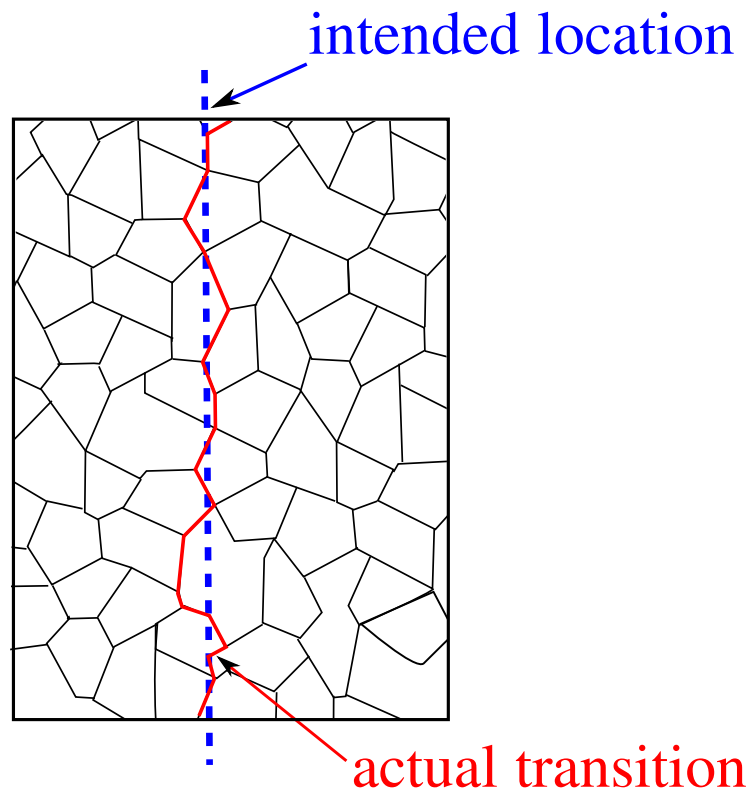


Figure 1.3: The effect of grain size on the signal-to-noise ratio for a magnetic recording medium originates in the fact that the transition between any two bits in a recording medium has to follow the grain boundaries. This sketch depicts the most optimistic case, the *grain size limit*, where the transition follows the grain boundaries closest to its desired spatial position. Figure based on Ref. [36].

manent magnets, i.e., materials that retain their magnetisation without the continuous application of an external field [45]. In ECC media, the soft phase acts, through its exchange coupling with the hard phase, as a “lever” in writing information to the hard phase, thereby reducing the effective write field [41–44]. Thermal stability is already ensured by the hardness of the hard phase. In short, HAMR and ECC address the magnetic recording trilemma (Fig. 1.2) by reducing the effective write field for a given K_u , thus allowing the use of magnetic recording media with larger K_u without further impact on the trilemma. As a consequence, the development of ECC and HAMR technologies has focused the development of magnetic recording media towards high- K_u alloys and nano-composites [38, 40, 45]. FePt and CoPt alloys are of particular interest, with K_u values in the range $10^6 - 10^7$ erg·cm⁻³ [46–50]. CoPt alloys are already used in current magnetic recording media and FePt is a strong candidate for application in HAMR. Moreover, Fe/FePt nano-composites are of particular interest for ECC applications [51, 52].

Consequently, unravelling in greater detail the underlying magnetic mechanisms and physical origins of the magnetic properties of FePt and CoPt remains crucial to the development of new devices. Therefore, a large part of current magnetic recording research is concerned with maximising K_u and elucidating the effects of chemical and microstructural changes on the magnetic properties of FePt and CoPt (see, e.g., [51, 53–60]). In this thesis, we address the effects of a range of chemical and microstructural aspects within an *ab initio* framework. In Chapter 3, we consider the effects of stacking faults and localised Pt alloying on the K_u of bulk cobalt. In Chapter 4 we investigate the effects of unit cell tetragonality, chemical disorder and composition on the K_u of FePt. In Chapter 5 we consider the layer-resolved magnetic properties of Fe/FePt soft-hard nano-composites and, in particular, the effect of the Fe/FePt interface on the K_u of the FePt phase. Due to its previous success in describing chemical disorder in alloys and its efficiency in describing systems of two-dimensional translational invariance, our *ab initio* method of choice is the screened Korringa-Kohn-Rostoker (SKKR) method. The SKKR method and the basic physics of magnetism are introduced in Chapter 2.

Theoretical Principles

2.1 Basic Concepts of Magnetism

Classically, a magnetic moment $\mathbf{m} = I\delta S$ is the result of a current-carrying loop (such as the orbital of an unpaired electron), where δS is the area of the loop and I is the current travelling around this loop [61]. Quantum-mechanically, electrons (and other fermions) possess not only orbital magnetic moments, but also intrinsic magnetic moments, commonly referred to as spin moments [62]. In materials, magnetism is an emergent phenomenon in the sense that what we sometimes consider localised, atomic magnetic moments are the result of cooperative electronic behaviour. The *adiabatic approximation* describes a situation where the dynamics of the emergent magnetic moments refers to a much longer time scale than that of the electronic motion [63–66]. In this picture, the magnetic moments can be considered in terms of a model Hamiltonian of localised, atomic, semi-classical magnetic moments.

Within the adiabatic approximation, magnetic behaviour can, furthermore, be dominated by transverse magnetic excitations (i.e., the motion of fixed-size magnetic moments) or by longitudinal excitations (i.e., changes in the magnitude of the magnetic moments). In the latter picture, which is by Stoner [67] and Bloch [68], magnetic properties are delocalised throughout the system, whereas in the former picture, which is by Heisenberg [69], magnetic properties can be thought of as the result of variations in the orientations of fixed-size atomic magnetic moments. Most materials exhibit properties on a sliding scale between these two extremes. Transition metal alloys, in particular, can often be considered within the transverse excitation limit [70–74]. Within the transverse excitation limit, we can consider the atomic moments in terms of normalised magnetic moments, \mathbf{S} . The long-range magnetic order, i.e., the long-range ori-

entation patterns of such fixed magnetic moments, is then the net result of an interplay of the *magnetostatic energy*, the *magnetocrystalline anisotropy*, *exchange interactions* and *thermal effects* [61]. These concepts are thus central to our understanding of magnetism in transition metal alloys. Before discussing these concepts in detail, it should be noted that although cgs units are in common usage within the magnetism community, within this thesis SI units will be used throughout.

2.1.1 Magnetic Exchange Interactions

Exchange interactions are interactions that arise from the exchange of fermions (e.g., electrons) between particles. *Magnetic* exchange interactions, in particular, refer to interactions by which a collection of magnetic moments mutually influence their relative orientations [62], and arise from the exchange of electrons between magnetic ions [62]. The exchange between two magnetic moments, \mathbf{S}_i and \mathbf{S}_j , located on sites i and j , is often quantified in terms of a 3x3 exchange tensor, $\underline{\underline{J}}_{ij}$. The exchange energy is then considered in terms of the Heisenberg Hamiltonian [69],

$$\hat{H}_{\text{Heis}} = -\frac{1}{2} \sum_{i \neq j} \mathbf{S}_i \underline{\underline{J}}_{ij} \mathbf{S}_j. \quad (2.1)$$

Exchange interactions are often characterised in terms of the corresponding isotropic exchange constant, $J_{ij} = \frac{1}{3} \text{Tr} \left\{ \underline{\underline{J}}_{ij} \right\}$. In fact, it should be noted that the original formulation of the Heisenberg model was constructed in terms of the exchange constants J_{ij} . We will therefore refer to Eq. (2.1) as the *extended* Heisenberg model. An exchange interaction with $J_{ij} > 0$ is generally referred to as a ferromagnetic (FM) interaction as it favours alignment of the two magnetic moments. An exchange interaction with $J_{ij} < 0$ is generally referred to as an antiferromagnetic (AFM) interaction as it favours anti-alignment of the two moments [62]. For the alloys considered in this thesis, the dominant type of magnetic exchange is the Ruderman-Kittel-Kasuya-Yosida (RKKY) exchange interaction, which arises from electron exchange through the valence electron sea surrounding the metal ions [75–77]. Due to screening effects, the strength of the isotropic RKKY exchange constant is oscillatory and slowly decaying with respect to the interatomic distance, R_{ij} ,

$$J_{ij}^{\text{RKKY}} \sim \frac{\cos(2\mathbf{k}_F \cdot \mathbf{R}_{ij})}{R_{ij}^3}, \quad (2.2)$$

where \mathbf{k}_F is the Fermi wave vector [78].

2.1.2 Magnetocrystalline Anisotropy Energy

Magnetic anisotropy is the difference in magnetic properties of a material when measured along different real-space directions [61]. The magnetocrystalline anisotropy energy, in particular, is the difference in the total energy of a system caused by aligning its magnetic moments along different crystallographic axes. An *easy axis* is a crystallographic direction along which the aligning of the magnetisation results in the lowest possible energy of the system. Similarly, a *hard axis* is a crystallographic direction along which the aligning of the magnetisation results in the largest possible energy. A uniaxial system is one in which there is only one easy axis [61]. For a uniaxial system, the variation in the total energy per volume due to the magnetocrystalline anisotropy can be expressed as

$$E(\theta) = K_u \sin^2 \theta \Rightarrow \begin{cases} \frac{dE}{d\theta} \big|_{\theta=\pi/4} = K_u \\ E \big|_{\theta=\pi/2} - E \big|_{\theta=0} = K_u \end{cases}, \quad (2.3)$$

where θ is the magnetisation direction with respect to the easy axis and K_u is the magnetocrystalline anisotropy energy per volume. In the following, we refer to the total magnetocrystalline anisotropy energy per atom (or, occasionally, per formula unit) simply as the magnetocrystalline anisotropy energy (MAE), K .

It should, furthermore, be noted that cubic systems may exhibit cubic magnetocrystalline anisotropy, which is of the form [62]

$$E(\mathbf{S}) = K_1 (S_x^2 S_y^2 + S_y^2 S_z^2 + S_z^2 S_x^2) + K_2 S_x^2 S_y^2 S_z^2 + \mathcal{O}\{S_{x,y,z}^8\}, \quad (2.4)$$

where $\mathbf{S} = (S_x, S_y, S_z)$ is the normalised magnetic moment and K_1 and K_2 are the lowest-order cubic magnetocrystalline anisotropy energy constants.

The existence of magnetocrystalline anisotropy implies that the spin moment associated with each particular atom must be somehow aware of the crystal structure. This “awareness” generally arises from the *spin-orbit interaction*, i.e., the interaction between the intrinsic angular momentum (i.e., the magnetic moment) and the orbital angular momentum (i.e., the orbital moment) of the electrons [79–81]. In a crystal, due to the coupling between the electric field

of the ions and the orbital motion of the electrons, the orbital moment resulting from the electronic motion will preferentially be oriented along particular crystallographic axes. Due to the spin-orbit interaction, the spin moments of the particles will, in turn, tend to align along the orbital moments. As a consequence, these materials exhibit magnetocrystalline anisotropy, i.e., there is one or several crystallographic axes along which it is easier to magnetise the system [61].

2.1.3 On-site and Inter-site Anisotropy

Adding a uniaxial magnetocrystalline anisotropy energy term to the extended Heisenberg Hamiltonian in Eq. (2.1), we obtain the anisotropic extended Heisenberg Hamiltonian for a uniaxial system,

$$\hat{H}_{\text{aHeis}} = -\frac{1}{2} \sum_{i \neq j} \mathbf{S}_i \underline{\underline{J}}_{ij} \mathbf{S}_j - \sum_i d_i (\mathbf{S}_i \cdot \mathbf{e})^2. \quad (2.5)$$

Here, d_i is the on-site anisotropy, \mathbf{S}_i is the normalised magnetic moment on site i , \mathbf{e} is the easy axis of the system and $\underline{\underline{J}}_{ij}$ is the exchange tensor as defined in Section 2.1.1, with elements

$$\underline{\underline{J}}_{ij} = \begin{pmatrix} J_{ij}^{xx} & J_{ij}^{xy} & J_{ij}^{xz} \\ J_{ij}^{yx} & J_{ij}^{yy} & J_{ij}^{yz} \\ J_{ij}^{zx} & J_{ij}^{zy} & J_{ij}^{zz} \end{pmatrix}. \quad (2.6)$$

By comparison with Eq. (2.3), we can see that, according to the anisotropic extended Heisenberg model, the magnetocrystalline anisotropy energy, K , is

$$K = E|_{\theta=\pi/2} - E|_{\theta=0} = \sum_i d_i + \frac{1}{2} \sum_{i \neq j} (J_{ij}^{zz} - J_{ij}^{xx}). \quad (2.7)$$

There are thus two contributions to the magnetocrystalline anisotropy energy: an on-site term and a term arising from the inter-site interactions.

2.1.4 Magnetostatic Energy

The *magnetostatic energy* of a magnetic system originates in the dipole-dipole interaction of the magnetic moments, i.e., in the interaction between each magnetic moment and the magnetic field of all the other magnetic moments around it. The larger the magnetisation of the system, the larger the magnetostatic en-

ergy, E_{mag} , of the system, as

$$E_{\text{mag}} = \frac{1}{2} \int_{\Omega} \mathbf{m}(\mathbf{r}) \cdot \mathbf{H}_{\text{demag}}(\mathbf{r}) d^3 \mathbf{r}, \quad (2.8)$$

where $\mathbf{m}(\mathbf{r})$ is the local magnetisation and $\mathbf{H}_{\text{demag}}(\mathbf{r})$ is the local demagnetising field, i.e., the field arising from the magnetisation of the material. The demagnetising field is generally opposed to the net magnetisation of the material; hence the name *demagnetising* field [3, 62]. The magnetostatic energy will thus be higher the more perfectly polarised the system is. It should be mentioned here that, although the work presented herein is not concerned with such effects, dipole-dipole interactions also give rise to magnetic *shape anisotropy*, i.e., depending on the shape of a magnetic object, it will be harder or easier to magnetise the object along certain directions relative to features of its shape (for details, see, e.g., Ref. [82]).

2.1.5 Magnetic Behaviour

As mentioned above, the magnetic behaviour of transition metals can often be considered in terms of an interplay of the magnetostatic energy, the magnetic exchange, the magnetocrystalline anisotropy and thermal effects. The magnetocrystalline anisotropy will favour magnetic moments in alignment with certain crystallographic axes and exchange interactions will favour parallel (or anti-parallel) alignment of the magnetic moments with each other [83]. The larger the magnetisation of the material, however, the larger the magnetostatic energy [83]. As a result, magnetic materials will tend to form domains, i.e., regions of uniform magnetisation [83]. The magnetocrystalline anisotropy will favour thin domain walls, so that the magnetic moments are as well-aligned as possible with the crystallographic axes, whereas exchange interactions will favour wide domain walls, so that the magnetic moments are as well-aligned with each other as possible [83]. The long-range magnetic order of a system is therefore the result of a balance between the magnetostatic energy, the magnetocrystalline anisotropy and the exchange interactions. A system which is dominated by the magnetostatic energy is often referred to as a (magnetically) *soft* material as it will not hold its magnetisation unless exposed to an external field [45]. A (magnetically) *hard* system, on the other hand, will be dominated by the magnetocrystalline anisotropy energy and will therefore be able to maintain its magnetisation without the continuous application of an external field [45]. The softer the magnetic material, the easier it is to change the magnetisation of the material [45].

Thermal energy can help overcoming energy barriers between different magnetic states. However, thermal effects could also cause a complete break-down of magnetic long-range order. Ferromagnetic materials are often characterised in terms of their Curie temperature, which is the temperature at which the orientations of the atomic magnetic moments are so randomised (transverse excitation limit) or the magnitude of the magnetic moments so small (longitudinal excitation limit) that there is no net magnetisation [62]. For antiferromagnetic materials, the corresponding measure is the Néel temperature [62]. In terms of the thermal stability of information written to a magnetic recording medium, thermal effects will tend to corrupt the information by, e.g., causing accidental magnetic reversals. Whereas the exchange interaction is generally an isotropic interaction, the magnetocrystalline anisotropy, on the other hand, will enhance the thermal stability by favouring the alignment of the magnetic moments with certain crystallographic axes. In other words, the larger the magnetocrystalline anisotropy, the larger the activation barrier for the reversal of a bit [37]. This is why thermal stability is generally quantified in terms of the ratio of the total magnetocrystalline anisotropy, $K_u V$, to the thermal energy, $k_B T$ (cf. Section 1.2). Next, we will consider how to calculate the magnetocrystalline anisotropy and the magnetic exchange of a given material from first principles.

2.2 Density Functional Theory

Density functional theory (DFT) is a method of calculating the ground-state properties of solid state systems. The main *raison d'être* of DFT is the fact that solving the Schrödinger equation for a many-electron system is practically impossible due to the high dimensionality of the problem [84]. As we shall see, DFT circumvents the related difficulties by mapping the system of interacting electrons onto a one-particle Hamiltonian and focusing on obtaining the electron density (instead of the wavefunction) of the ground state. DFT is one of the most widely used methods in chemistry, material science and condensed matter physics and a huge number of auxiliary methods and approximations exist. Here we only present the basics of DFT and the particular techniques relevant to the work in this thesis. For further detail, see, e.g., Ref. [84].

2.2.1 Hohenberg-Kohn Theorem

Within the Born-Oppenheimer approximation, the coupled electronic and nuclear wavefunction, $\Psi_{\text{total}}(\mathbf{r}, \mathbf{R}) = \Psi_{\text{nuclear}}(\mathbf{R}) \times \Psi_{\text{electronic}}(\mathbf{r})$, can be decoupled as $\Psi_{\text{total}}^{\text{BO}}(\mathbf{r}, \mathbf{R}) = \Psi_{\text{electronic}}(\mathbf{r}, \{\mathbf{R}\})$, wherein the nuclear coordinates, $\{\mathbf{R}\}$, pa-

parameterise the electronic wavefunction [85]. This decoupling of the total wavefunction pictures a situation in which the electrons adjust instantaneously to a change in the nuclear configuration [85]. Within the Born-Oppenheimer approximation, therefore, we can consider the electrons moving in an external, static Coulomb potential $V_{\text{ext}}(\mathbf{r})$ created by the ions, which are considered as point charges. The *Hohenberg-Kohn theorem* is the basis of density functional theory and consists of two main statements, as follows [86].

- There is a one-to-one mapping between the external potential describing the system, $V_{\text{ext}}(\mathbf{r})$, and its ground-state electron density, $n_0(\mathbf{r})$. Consequently, the ground state total energy of the system is a unique functional of the ground state electron density, $n_0(\mathbf{r})$.
- The ground state electron density can be found variationally. The electronic density that minimises the total energy is the ground state electronic density and the corresponding value of the total energy is the ground state energy.

There also exists a number of generalisations of the Hohenberg-Kohn theorem, e.g., extensions to degenerate ground states and fully relativistic formulations [84, 87–90]. However, its original formulation (the above) suffices for our present goal of illustrating the underlying physics of DFT. In essence, the Hohenberg-Kohn theorem allows us to map a system of interacting electrons onto a one-particle Hamiltonian (i.e., a system of non-interacting electrons). Although the *wavefunction* obtained from the one-particle Hamiltonian will not reflect the physics of the interacting system, we can still perform the mapping such that the ground state electron *density* will be the same for the two systems.

2.2.2 Kohn-Sham Equations

According to the Hohenberg-Kohn theorem, finding the ground state energy of a many-body system is reduced to a direct minimisation of the total energy functional, $E[n(\mathbf{r})]$, with respect to the electron density, $n(\mathbf{r})$. The *Kohn-Sham scheme* [91] is a method of performing this minimisation in order to obtain the electron density corresponding to the ground state of the system, $n_0(\mathbf{r})$. It is based on replacing the real system of interacting electrons with an equivalent system of non-interacting electrons, exhibiting the same ground state electron density $n_0(\mathbf{r})$ as the interacting system. Kohn and Sham [91] split the total energy functional into a sum containing the non-interacting kinetic energy, $T_s[n(\mathbf{r})]$, the energy due to the external potential, $E_{\text{ext}}[n(\mathbf{r})]$, the Hartree energy,

$E_H[n(\mathbf{r})]$ and the exchange-correlation energy, $E_{xc}[n(\mathbf{r})]$,

$$E[n(\mathbf{r})] = T_s[n(\mathbf{r})] + E_{\text{ext}}[n(\mathbf{r})] + E_H[n(\mathbf{r})] + E_{xc}[n(\mathbf{r})]. \quad (2.9)$$

In the Kohn-Sham scheme, the one-particle Hamiltonian is

$$(\hat{T}_s + \hat{V}_{\text{eff}}) |\xi_i\rangle = \varepsilon_i |\xi_i\rangle, \quad (2.10)$$

where $|\xi_i\rangle$ is the i^{th} one-particle eigenstate, ε_i is the energy of the i^{th} one-particle eigenstate, \hat{T}_s is the non-interacting kinetic energy operator and $V_{\text{eff}}(\mathbf{r})$ is the effective potential

$$V_{\text{eff}}(\mathbf{r}) = \frac{\delta E_{\text{ext}}[n(\mathbf{r})]}{\delta n(\mathbf{r})} + \frac{\delta E_H[n(\mathbf{r})]}{\delta n(\mathbf{r})} + \frac{\delta E_{xc}[n(\mathbf{r})]}{\delta n(\mathbf{r})} = V_{\text{ext}}(\mathbf{r}) + V_H(\mathbf{r}) + V_{xc}(\mathbf{r}), \quad (2.11)$$

where V_{ext} is the external potential due to the atomic nuclei and the core electrons, V_H is the Hartree potential due to electron-electron interactions and V_{xc} is “any remaining contributions”, primarily due to exchange and correlations. The electron density $n(\mathbf{r})$, in turn, is calculated from

$$n(\mathbf{r}) = \sum_i^N |\xi_i(\mathbf{r})|^2. \quad (2.12)$$

The solution of the Kohn-Sham equations is the density, which is at the same time a parameter of Eq. (2.10) and Eq. (2.11). Thus an iterative approach is required,

1. a guess is made for an initial input density, $n_{\text{in}}(\mathbf{r})$
2. $V_{\text{eff}}(\mathbf{r})$ is calculated from $n_{\text{in}}(\mathbf{r})$ through Eq. (2.11)
3. the one-particle Schrödinger equation, Eq. (2.10), is solved, yielding the one-particle eigenstates, $\{\xi_i(\mathbf{r})\}$
4. the output density $n_{\text{out}}(\mathbf{r})$ is calculated from Eq. (2.12)
5. a new input density $n_{\text{in}}(\mathbf{r})$ is constructed from $n_{\text{out}}(\mathbf{r})$
6. the process is repeated from the second step until the input density $n_{\text{in}}(\mathbf{r})$ equals the output density $n_{\text{out}}(\mathbf{r})$ to within some pre-set convergence limit

It should be noted that the above argument refers to non-spin-polarised DFT. In this work, we are actually using spin-DFT, in which the electron density $n(\mathbf{r})$ is spin-resolved into two components, $n_{\uparrow}(\mathbf{r})$ and $n_{\downarrow}(\mathbf{r})$, and in which the

energy functional $E[n(\mathbf{r}), \mathbf{m}(\mathbf{r})]$ will in fact depend on both the electron density $n(\mathbf{r})$ and the magnetisation density $\mathbf{m}(\mathbf{r})$. However, the above algorithm applies very similarly for spin-DFT [84]. Implementations of DFT where the Kohn-Sham equations are solved using plane-wave expansions include, e.g., CASTEP [92–94] and VASP [95–98].

2.2.3 Magnetism in DFT

As mentioned in Section 2.1.2, the magnetocrystalline anisotropy of a system is generally a direct effect of the spin-orbit coupling within the system. In order to incorporate spin-orbit coupling in a non-perturbative way, in this work we use a relativistic version of the Kohn-Sham Eq. (2.10) [99], derived directly from the Dirac equation as

$$(-i\hbar c \boldsymbol{\alpha} \cdot \nabla + \beta m_e c^2 + V_{\text{eff}}(\mathbf{r}) I_4 + \beta \boldsymbol{\Sigma} \cdot \mathbf{B}_{\text{eff}}(\mathbf{r})) \Phi_i(\mathbf{r}) = \varepsilon_i \Phi_i(\mathbf{r}), \quad (2.13)$$

where $V_{\text{eff}}(\mathbf{r})$ is still defined as in Eq. (2.11) and, for an applied external field $\mathbf{B}_{\text{ext}}(\mathbf{r})$,

$$\mathbf{B}_{\text{eff}}(\mathbf{r}) = \mathbf{B}_{\text{ext}}(\mathbf{r}) + \frac{e\hbar}{2m_e c} \frac{\delta E_{xc}[n(\mathbf{r}), \mathbf{m}(\mathbf{r})]}{\delta \mathbf{m}(\mathbf{r})}. \quad (2.14)$$

Note that ∇ denotes the gradient operator, m_e the electron mass, e the electronic charge, \hbar Planck's constant and c the speed of light, while the following objects are defined,

$$\alpha_j = \begin{pmatrix} 0_2 & \sigma_j \\ \sigma_j & 0_2 \end{pmatrix} \quad \Sigma_j = \begin{pmatrix} \sigma_j & 0_2 \\ 0_2 & \sigma_j \end{pmatrix} \quad \beta = \begin{pmatrix} I_2 & 0_2 \\ 0_2 & -I_2 \end{pmatrix} \quad (2.15)$$

$$\sigma_1 = \begin{pmatrix} 0 & 1 \\ 1 & 0 \end{pmatrix} \quad \sigma_2 = \begin{pmatrix} 0 & -i \\ i & 0 \end{pmatrix} \quad \sigma_3 = \begin{pmatrix} 1 & 0 \\ 0 & -1 \end{pmatrix} \quad (2.16)$$

$$\boldsymbol{\alpha} = (\alpha_1, \alpha_2, \alpha_3) \quad \boldsymbol{\Sigma} = (\Sigma_1, \Sigma_2, \Sigma_3) \quad \boldsymbol{\sigma} = (\sigma_1, \sigma_2, \sigma_3). \quad (2.17)$$

Here, $\{\sigma_i\}$ are the Pauli spin matrices, 0_2 is the 2x2 zero matrix and I_2 is the 2x2 identity matrix. Eq. (2.13) is typically referred to as the Kohn-Sham-Dirac (KSD) equation and its eigenfunctions, $\{\Phi_i(\mathbf{r})\}$, are bi-spinors. The general idea of the iterative algorithm at the end of Section 2.2.2 still applies, although it is reformulated in a fully relativistic form in terms of spin-resolved electron densities and bi-spinors. In the following, we will refer to the Kohn-Sham-Dirac Hamiltonian,

$$\hat{H}_{KSD} = -i\hbar c \boldsymbol{\alpha} \cdot \nabla + \beta m_e c^2 + V_{\text{eff}}(\mathbf{r}) I_4 + \beta \boldsymbol{\Sigma} \cdot \mathbf{B}_{\text{eff}}(\mathbf{r}). \quad (2.18)$$

2.2.4 The Local Spin Density Approximation

The exact form of the exchange-correlation functional $E_{xc}[n(\mathbf{r}), \mathbf{m}(\mathbf{r})]$ is not known. In practice, therefore, an approximation of this functional has to be used. There exists a number of such approximations, e.g., the local spin density approximation (LSDA) and the generalised gradient approximation (GGA) [84]. In this work, we use the LSDA [100]. Within the LSDA, we model the (inhomogeneous) system of electrons in terms of an electron density which locally behaves as that of a homogeneous electron gas [100]. Within the LSDA, the exchange-correlation functional $E_{xc}[n(\mathbf{r}), \mathbf{m}(\mathbf{r})]$ has the form

$$E_{xc}[n(\mathbf{r}), \mathbf{m}(\mathbf{r})] = E_{xc}[n_{\uparrow}(\mathbf{r}), n_{\downarrow}(\mathbf{r})] = \int (n_{\uparrow}(\mathbf{r}) + n_{\downarrow}(\mathbf{r})) \varepsilon_{xc}^{hom}(n_{\uparrow}(\mathbf{r}), n_{\downarrow}(\mathbf{r})) d^3\mathbf{r}, \quad (2.19)$$

where the majority and minority spin densities, $n_{\uparrow}(\mathbf{r})$ and $n_{\downarrow}(\mathbf{r})$, are defined with respect to the local magnetisation direction, $\mathbf{m}(\mathbf{r})$, and where $\varepsilon_{xc}^{hom}(n_{\uparrow}(\mathbf{r}), n_{\downarrow}(\mathbf{r}))$ is the exchange-correlation energy per electron in the homogeneous electron gas, which can be accurately calculated using quantum Monte Carlo methods. In this work, we use the quantum Monte Carlo data of Ceperley and Alder [101] as parameterised by Vosko *et al.* [102].

2.3 The Korrington-Kohn-Rostoker Method

The Korrington-Kohn-Rostoker (KKR) method is a method of obtaining the solutions of the Kohn-Sham or the Kohn-Sham-Dirac equations [103,104]. Within KKR, these equations are solved in terms of the corresponding one-particle Green's function, rather than the one-particle wavefunction. As the theory of KKR is well documented in the literature (see, e.g., Refs. [105,106]), here we present only the main concepts and results relevant to this particular work.

2.3.1 The Green's Function

The resolvent $\hat{G}(z)$ of a Hamiltonian \hat{H} is defined as

$$\hat{G}(z) = (z\hat{I} - \hat{H})^{-1}, \quad (2.20)$$

where z is the (complex) energy and \hat{I} is the identity operator [107]. We normally refer to any representation of the resolvent $\hat{G}(z)$ as the Green's function

of \hat{H} [108]. The spectral representation of the resolvent $\hat{G}(z)$ is

$$\hat{G}(z) = \sum_n \frac{|\Psi_n\rangle\langle\Psi_n|}{z - \varepsilon_n}, \quad (2.21)$$

with side limits defined as

$$\lim_{|\delta|\rightarrow 0} \hat{G}(\varepsilon + i\delta) = \begin{cases} \hat{G}^+(\varepsilon) & \text{for } \delta > 0 \text{ (retarded)} \\ \hat{G}^-(\varepsilon) & \text{for } \delta < 0 \text{ (advanced)} \end{cases}, \quad (2.22)$$

where the complex energy z has been written as the sum of a real energy ε and an infinitesimal imaginary energy $i\delta$, i.e., $z = \varepsilon + i\delta$ (where δ can be positive or negative). The configuration space representation of $\hat{G}(z)$ is, meanwhile,

$$G(z; \mathbf{r}, \mathbf{r}') = \langle \mathbf{r} | \hat{G}(z) | \mathbf{r}' \rangle = \sum_n \frac{\Psi_n(\mathbf{r})\Psi_n^*(\mathbf{r}')}{z - \varepsilon_n}. \quad (2.23)$$

Physically, $G(z; \mathbf{r}, \mathbf{r}')$ can be interpreted as a *propagator* in energy space, i.e., the probability amplitude of propagation between \mathbf{r} and \mathbf{r}' for a particle of given energy z .

The physical observables of a system can be evaluated from its Green's function as follows. The statistical average $\langle A \rangle$ of a physical observable A can be evaluated as [109]

$$\langle A \rangle = \sum_j f_{FD}(\varepsilon_j) \langle \Psi_j | \hat{A} | \Psi_j \rangle, \quad (2.24)$$

where \hat{A} is the Hermitian operator associated with A , $f_{FD}(\varepsilon)$ is the Fermi-Dirac distribution and ε_j and $|\Psi_j\rangle$ refer to the eigenenergy and eigenfunction of the j^{th} eigenstate of the system. Using the spectral representation of $\hat{G}(z)$,

$$\hat{G}(z) = \sum_j \frac{|\Psi_j\rangle\langle\Psi_j|}{z - \varepsilon_j} \Rightarrow f_{FD}(z) \text{Tr} \{ \hat{A} \hat{G}(z) \} = \sum_j \frac{f_{FD}(z) \langle \Psi_j | \hat{A} | \Psi_j \rangle}{z - \varepsilon_j}, \quad (2.25)$$

it can be shown that, for a temperature of zero Kelvin (see, e.g., Ref. [105]),

$$\langle A \rangle = -\frac{1}{\pi} \text{Im} \left\{ \int_{\curvearrowright} f_{FD}(z) \text{Tr} \{ \hat{A} \hat{G}(z) \} dz \right\} \quad (2.26)$$

$$= \mp \frac{1}{\pi} \text{Im} \left\{ \int_{-\infty}^{\infty} f_{FD}(\varepsilon) \text{Tr} \{ \hat{A} \hat{G}^{\pm}(\varepsilon) \} d\varepsilon \right\}, \quad (2.27)$$

where \curvearrowright denotes a semicircular contour in the upper complex semi-plane as illustrated in Fig. 2.1.

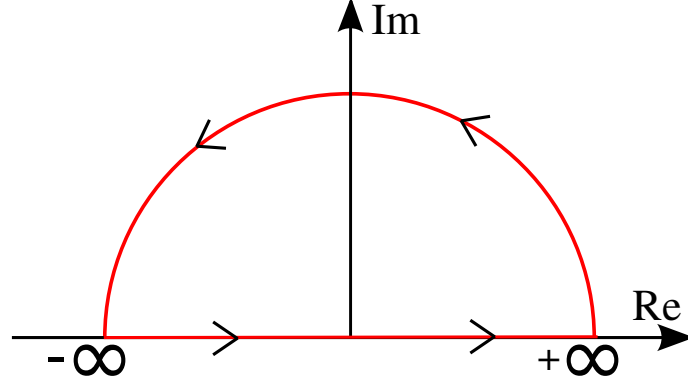


Figure 2.1: The contour \curvearrowright of the integral in Eq. (2.26).

In particular, the number of electrons, N_e , can be evaluated by setting $\hat{A} = \hat{I}$, giving

$$N_e = \mp \frac{1}{\pi} \text{Im} \left\{ \int_{-\infty}^{\infty} f_{FD}(\varepsilon) \text{Tr} \{ \hat{G}^{\pm}(\varepsilon) \} d\varepsilon \right\} = \int_{-\infty}^{\infty} f_{FD}(\varepsilon) n(\varepsilon) d\varepsilon, \quad (2.28)$$

where the density of states, $n(\varepsilon)$,

$$n(\varepsilon) = \mp \frac{1}{\pi} \text{Im} \{ \text{Tr} \{ \hat{G}^{\pm}(\varepsilon) \} \}. \quad (2.29)$$

Eq. (2.29) derives from the fact that, in the limit towards real energies, the imaginary part of the trace of the Green's function approaches a sum of delta functions centred on the eigenenergies of the system. Using the density of states we can, e.g., evaluate the band energy of the system,

$$E_{\text{band}} = \int_{-\infty}^{\varepsilon_F} \varepsilon n(\varepsilon) d\varepsilon. \quad (2.30)$$

Thus, the Green's function is a very powerful tool in describing electronic structure. In the next Section, we summarise the procedure of obtaining the Green's function within the KKR method.

2.3.2 Multiple Scattering Theory

In the KKR method, the Green's function is evaluated within the framework of multiple scattering theory (MST). Within this framework, the system \hat{H} is considered as a perturbation to some reference system, \hat{H}_0 , i.e.,

$$\hat{H} = \hat{H}_0 + \hat{V}, \quad (2.31)$$

where \hat{V} is the perturbation. Traditionally in MST, the reference system \hat{H}_0 is free space, meaning \hat{V} is the one-particle effective potential of the system. According to the *Dyson equation* (see Ref. [105] and Appendix A.2 for details) the resolvent of \hat{H} , $\hat{G}(z)$, can be expanded in terms of the resolvent of the reference system, $\hat{G}_0(z)$, as an infinite Born series,

$$\begin{aligned}\hat{G}(z) &= \hat{G}_0(z) + \hat{G}_0(z)\hat{V}\hat{G}_0(z) + \hat{G}_0(z)\hat{V}\hat{G}_0(z)\hat{V}\hat{G}_0(z) + \dots \\ &= \hat{G}_0(z) + \hat{G}_0(z)\hat{T}(z)\hat{G}_0(z),\end{aligned}\quad (2.32)$$

where we have defined the transition operator, or t-operator, $\hat{T}(z)$,¹ as

$$\begin{aligned}\hat{T}(z) &= \hat{V} + \hat{V}\hat{G}_0(z)\hat{V} + \hat{V}\hat{G}_0(z)\hat{V}\hat{G}_0(z)\hat{V} + \dots \\ &= \hat{V} + \hat{V}\hat{G}_0(z)\hat{T}(z) \\ &= (\hat{I} - \hat{V}\hat{G}_0(z))^{-1}\hat{V}.\end{aligned}\quad (2.33)$$

Within the KKR method, the solid is considered as a collection of independent scatterers. In other words, we divide the space Ω into a set of disjoint cells, $\{\Omega_i\}$, each of which is centred on a different spatial position \mathbf{R}_i [105]. Mathematically this is equivalent to considering the overall potential $V(\mathbf{r})$ as a superposition of potentials $\{V_i(\mathbf{r}_i)\}$ (each such potential corresponding to one scatterer),

$$V(\mathbf{r}) = \sum_i V_i(\mathbf{r}_i), \quad (2.34)$$

where the potentials $\{V_i(\mathbf{r}_i)\}$ are spatially bounded and, commonly, spherically symmetric, i.e.,

$$V_i(\mathbf{r}_i) = \begin{cases} V_i(r_i) & \text{if } r_i < S_i \\ 0 & \text{elsewhere} \end{cases}. \quad (2.35)$$

Here, S_i is the radius of the scatterer and $\mathbf{r}_i = \mathbf{r} - \mathbf{R}_i$ is the spatial position relative to the centre of the scatterer. In the present work, the space Ω is divided into cells as per the atomic sphere approximation (ASA) [110–112] and the potentials are obtained from the electron density, $n(\mathbf{r})$, through the local spin density approximation (LSDA). Within the ASA, the total volume of the (spherical) scatterers is defined to be equal to the total lattice volume. As a consequence, within the ASA, the scatterers will not be strictly disjoint. However, for the case of cubic and hexagonal close-packed materials, their overlap will be relatively small [113, 114]. It should be noted here that KKR can be applied also to arbitrarily shaped potentials (see, e.g., Refs. [115, 116]), although no such

¹The transition operator, $\hat{T}(z)$, is not to be confused with the non-interacting kinetic energy operator, \hat{T}_s .

calculations were performed in this work.

For a collection of disjoint scatterers as described in Eq. (2.35), any scattering process can be decomposed into sequences of scattering events at specific sites. Therefore, the overall t-operator, $\hat{T}(z)$, can be expressed in terms of the single-site t-operators, $\hat{t}_i(z) = (\hat{I} - \hat{V}_i \hat{G}_0(z))^{-1} \hat{V}_i$ (cf. Eq. (2.33)), as

$$\begin{aligned} \hat{T}(z) &= \sum_i \hat{t}_i(z) + \sum_{i,j} \hat{t}_i(z) \hat{G}_0(z) (1 - \delta_{ij}) \hat{t}_j(z) \\ &\quad + \sum_{i,j,k} \hat{t}_i(z) \hat{G}_0(z) (1 - \delta_{ij}) \hat{t}_j(z) \hat{G}_0(z) (1 - \delta_{jk}) \hat{t}_k(z) + \dots \end{aligned} \quad (2.36)$$

$$= \sum_{i,j} \hat{\tau}_{ij}(z), \quad (2.37)$$

where $\hat{\tau}_{ij}(z)$ is the scattering path operator (SPO) [117], which is defined to transfer an incoming electronic wave at site j to an outgoing electronic wave at site i via all possible scattering paths,

$$\begin{aligned} \hat{\tau}_{ij}(z) &= \hat{t}_i(z) \delta_{ij} + \hat{t}_i(z) \hat{G}_0(z) (1 - \delta_{ij}) \hat{t}_j(z) \\ &\quad + \sum_k \hat{t}_i(z) \hat{G}_0(z) (1 - \delta_{ik}) \hat{t}_k(z) \hat{G}_0(z) (1 - \delta_{kj}) \hat{t}_j(z) + \dots \end{aligned} \quad (2.38)$$

The SPO can, in turn, be expressed in terms of the structural resolvent operator, $\hat{G}_{ij}(z)$, which describes every possible propagation route between the two sites i and j ,

$$\hat{G}_{ij}(z) = \hat{G}_0(z) (1 - \delta_{ij}) + \sum_{k,l} \hat{G}_0(z) (1 - \delta_{ik}) \hat{\tau}_{kl}(z) \hat{G}_0(z) (1 - \delta_{lj}), \quad (2.39)$$

as

$$\hat{\tau}_{ij}(z) = \hat{t}_i(z) \delta_{ij} + \hat{t}_i(z) \hat{G}_{ij}(z) \hat{t}_j(z). \quad (2.40)$$

For practical application, we require the configuration space representations of the above operators. In order to obtain $G_0(z; \mathbf{r}, \mathbf{r}')$ and $t_i(z; \mathbf{r}, \mathbf{r}')$ within fully relativistic KKR, the Kohn-Sham-Dirac equation (Eq. (2.13)) has to be solved for the free particle and for the single-site potential (see Eq. (2.34)), respectively. For this purpose, we have to distinguish the right and left solutions, $|\Phi\rangle$ and $\langle\tilde{\Phi}|$, of the Dirac equation (see Eq. (2.18)) as

$$\begin{aligned} (z - \hat{H}_{KSD}) |\Phi\rangle &= 0 \\ \langle\tilde{\Phi}| (z - \hat{H}_{KSD}) &= 0. \end{aligned} \quad (2.41)$$

The relativistic free-particle Green's function, $G_0(z; \mathbf{r} + \mathbf{R}_i, \mathbf{r} + \mathbf{R}_j)$, can be expressed as [118]

$$\begin{aligned}
G_0(z; \mathbf{r} + \mathbf{R}_i, \mathbf{r}' + \mathbf{R}_j) &= \frac{z + m_e c^2}{2m_e c^2} \sum_{Q, Q'} J_Q(z; \mathbf{r}) G_{0,ij}^{QQ'}(z) \tilde{J}_{Q'}^\dagger(z; \mathbf{r}') \\
&\quad - \delta_{ij} \left(ip \frac{z + m_e c^2}{2m_e c^2} \right) \sum_Q \left[J_Q(z; \mathbf{r}) \tilde{H}_Q^\dagger(z; \mathbf{r}') \Theta(r' - r) \right. \\
&\quad \left. + H_Q(z; \mathbf{r}) \tilde{J}_Q^\dagger(z; \mathbf{r}') \Theta(r - r') \right], \tag{2.42}
\end{aligned}$$

where Q is the relativistic composite angular momentum index, $Q = (\kappa, \mu)$, J_Q (\tilde{J}_Q^\dagger) and H_Q (\tilde{H}_Q^\dagger) are the Bessel- and Hankel-like bi-spinor right (left) solutions of the free-particle Dirac equation, respectively, and $\Theta(r)$ is the Heaviside step function. The indexing in terms of the relativistic composite angular momentum arises from the fact that, when spin-orbit coupling becomes significant, the non-relativistic angular momentum numbers l and s are no longer good quantum numbers. Instead one considers the *total* angular momentum quantum number, j . The relativistic angular momentum numbers can be related to the non-relativistic quantum numbers as [118]

$$\kappa = \begin{cases} l & \text{for } j = l + \frac{1}{2} \\ -l - 1 & \text{for } j = l - \frac{1}{2} \end{cases} \tag{2.43}$$

$$\mu = \{-j, -j + 1, \dots, j - 1, j\} \tag{2.44}$$

Furthermore, in Eq. (2.42), the free-particle relativistic *structure constants*, $G_{0,ij}^{QQ'}$, can be obtained directly from the geometry of the lattice, independently of the atomic properties of each site. Similarly, solving the single-site Kohn-Sham-Dirac equation entails evaluating the angular momentum representation of the single-site t-operator,

$$t_i^{QQ'}(z) = \frac{z + m_e c^2}{2m_e c^2} \int_{|\mathbf{r}| \leq S_i} \int_{|\mathbf{r}'| \leq S_i} \tilde{J}_Q^\dagger(z; \mathbf{r}) t_i(z; \mathbf{r} + \mathbf{R}_i, \mathbf{r}' + \mathbf{R}_i) J_{Q'}(z; \mathbf{r}') d^3 \mathbf{r}' d^3 \mathbf{r}. \tag{2.45}$$

The matrix elements $t_i^{QQ'}$ are obtained by matching the single-site scattering solutions with the free-particle solutions at $r = S_i$.

The site- and angular momentum matrix representation of the scattering path operator, $\tau(z)$, can be related to the site- and angular momentum matrix representations of the single-site t-operator, $t(z)$, and the free-particle Green's func-

tion, $G_0(z)$, as

$$\tau(z) = (t(z) - G_0(z))^{-1} = (M(z))^{-1}. \quad (2.46)$$

Eq. (2.46) is a matrix equation (in site- and angular momentum space) and can be regarded as the main equation of KKR. Here, the separation of the geometrical properties of the system (encased in $G_0(z)$) and the atomic-level properties of the individual scatterers (encased in $t(z)$) is clearly demonstrated. The matrix $M(z)$ is often referred to as the *KKR matrix* [105].

Having obtained $\tau_{ij}^{QQ'}$ from Eq. (2.46), the final result is the configuration space representation of the one-particle Green's function, which, within fully relativistic KKR, can be expressed as [106]

$$\begin{aligned} G(z; \mathbf{r} + \mathbf{R}_i, \mathbf{r}' + \mathbf{R}_j) = & \frac{z + m_e c^2}{2m_e c^2} \sum_{Q, Q'} Z_i^Q(z; \mathbf{r}) \tau_{ij}^{QQ'} \tilde{Z}_j^{Q'\dagger}(z; \mathbf{r}') \\ & - \delta_{ij} \frac{z + m_e c^2}{2m_e c^2} \sum_Q \left[Z_i^Q(z; \mathbf{r}) \tilde{J}_i^{Q\dagger}(z; \mathbf{r}') \Theta(r - r') \right. \\ & \left. + J_i^Q(z; \mathbf{r}) \tilde{Z}_i^{Q\dagger}(z; \mathbf{r}') \Theta(r' - r) \right], \end{aligned} \quad (2.47)$$

where $Z_i^Q(z; \mathbf{r})$ and $J_i^Q(z; \mathbf{r})$ are the regular and irregular scattering solutions of the single-site Dirac equation, respectively, with the tilde representing again solutions of the Dirac equation from the left as defined in Eq. (2.41). In practice, the expansion in Eq. (2.47) is performed up to some cut-off angular momentum value, l_{max} . In other words, the KKR method is a minimal basis set method. The convergence of physical properties with l_{max} can be slow and that the computational effort scales as $(l_{max} + 1)^6$ [119, 120].

2.3.3 Screening

Within traditional KKR, the reference system in Eq. (2.31) is free space, for which the Green's function,

$$G_{\text{free}}(z; \mathbf{r}, \mathbf{r}') = -\frac{\exp\left(-i\sqrt{\frac{2m_e z}{\hbar^2}} |\mathbf{r} - \mathbf{r}'|\right)}{4\pi |\mathbf{r} - \mathbf{r}'|}, \quad (2.48)$$

only falls off $\frac{1}{\text{distance}}$, meaning the free-particle structure constants (see Eq. (2.42) and Eq. (2.46)) are long-ranged. This leads to a relatively dense KKR matrix (see Eq. (2.46)) and cubic scaling of the computational effort with the size of the system.

Screening refers to the localising of the structure constants through a scaling transformation [121, 122], i.e., through a change of reference system [105]. By choosing, e.g., a reference system of repulsive potentials outlining the geometry of the system, the screened structure constants will exhibit an exponential decay with distance [122]. As a result, the KKR matrix becomes a sparse matrix, thus simplifying the calculation of its inverse and reducing the scaling of the computational effort with system size. The new reference system (obviously) does not represent the real, physical matrix in which the atoms are embedded, but rather an intermediate reference system. However, the Green's function of the reference system relative to free space only needs to be calculated once, whereas the Green's function of the system of interest relative to the reference system has to be performed once in every Kohn-Sham iteration [122].

Screening is particularly useful for *layered* systems, i.e., for systems exhibiting two-dimensional translational invariance but not necessarily three-dimensional translational invariance. In particular, in the following, we consider systems consisting of two semi-infinite crystals, separated by an *interlayer* (the region of interest). The interlayer is divided into one or more *principal layers*, which, in turn, comprise a given number of (consecutive) atomic layers, t_{PL} . Using screened structure constants as above, the principal layers can be constructed such that the couplings can be truncated beyond nearest-neighbour principal layers.² It can be shown that, within this formalism, the KKR matrix is block-tridiagonal [121, 122], each block corresponding to the angular momentum and site dimensions of one principal layer, $(l_{max} + 1)t_{PL} \times (l_{max} + 1)t_{PL}$. Since such block-tridiagonal matrices can be inverted by order- N algorithms, the computational effort now scales linearly with the size of the system, as opposed to the cubic scaling with system size of the traditional KKR method [122].

Finally, we should point out that, in a layered system as described above, the structure constants within each atomic monolayer can be obtained by Fourier transform and integration over the two-dimensional Brillouin zone. Such a procedure, in essence, maps the three-dimensional problem onto a one-dimensional problem of a stack of atomic monolayers [123]. Therefore, in the following, *layer-resolved* contributions will refer to contributions towards a particular observable from each atomic layer. Such contributions are generally quoted *per atom*, meaning per representative atom of a given species in a given atomic layer.

²The number of atomic layers, t_{PL} , is generally decided upon by evaluating the convergence of the quantities of interest with respect to t_{PL} .

2.3.4 Evaluation of Magnetic Properties

Having obtained the Green's function of the system (Eq. (2.47)) and having established that the band energy can be evaluated from the Green's function (Eqs. (2.29–2.30)), we are now in a position to evaluate the magnetocrystalline anisotropy energy (MAE) of the system. Within the *force theorem* (for details, see, e.g., Refs. [124–128]), the MAE can be evaluated as the difference in the fully-relativistic band energies caused by the polarisation of the magnetisation along the hard and easy axes, provided the calculations of the fully-relativistic band energies for each of the two magnetisation energies are performed using the same self-consistent scalar-relativistic potential [129, 130].³ That is, the MAE of a uniaxial system, K , can, within the force theorem, be evaluated as

$$K = E_{\text{band}}^{(\text{hard})} - E_{\text{band}}^{(\text{easy})}, \quad (2.49)$$

where $E_{\text{band}}^{(\text{hard})}$ ($E_{\text{band}}^{(\text{easy})}$) is the band energy for a system polarised along the hard (easy) axis of the lattice and where both band energies are evaluated using the same scalar-relativistic self-consistent potential.

One issue with the evaluation of K in Eq. (2.49) is the numerical stability of evaluating a small difference between two relatively large numbers [131]. The smaller the MAE of the system, the more significant this issue becomes. The *torque method*, which is an alternative approach of evaluating the MAE, can often provide improved numerical stability [131, 132]. The method is based upon evaluating the MAE from the magnetic torque, $T(\theta)$, i.e., the angular derivative of the energy. In particular, for a uniaxial system (ignoring higher-order terms, cf. Eq. (2.3)),

$$T(\theta) = \frac{dE(\theta)}{d\theta} = 2K \sin \theta \cos \theta \Rightarrow T\left(\theta = \frac{\pi}{4}\right) = K. \quad (2.50)$$

Within the MST framework, for a given direction of magnetisation polarisation $\hat{\mathbf{n}}$, the site-and-species-resolved contributions, $D_i^{(\alpha, \hat{\mathbf{n}})}$, to the angular derivative in the total energy, $\left. \frac{\partial E}{\partial \theta} \right|_{\hat{\mathbf{n}}}$, can be evaluated as [132]

$$D_i^{(\alpha, \hat{\mathbf{n}})} = -\frac{1}{\pi} \text{Im} \int_{-\infty}^{\varepsilon_F^{(\hat{\mathbf{n}})}} \text{Tr} \left\{ \frac{\partial t_i^{-1}(\varepsilon; \alpha, \hat{\mathbf{n}})}{\partial \theta} \tau_{ii}^{-1}(\varepsilon; \alpha, \hat{\mathbf{n}}) \right\} d\varepsilon, \quad (2.51)$$

where ε_F is the Fermi energy and, in case species α occupies site i , $t_i(\varepsilon) =$

³Note that *scalar-relativistic* here refers to neglecting the spin-orbit term in the Kohn-Sham-Dirac Hamiltonian.

$\{t_i^{QQ'}(\varepsilon)\}$ and $\tau_{ii}(\varepsilon) = \{\tau_{ii}^{QQ'}(\varepsilon)\}$ denote the angular momentum matrix representations of the single-site t-operator and the site-diagonal scattering path operator, respectively. All these quantities are evaluated at the direction of the magnetisation $\hat{\mathbf{n}}$ [132]. Referring back to Eq. (2.50), $\theta = \pi/4$ corresponds to $\hat{\mathbf{n}} = (1/\sqrt{2}, 0, 1/\sqrt{2})$.

Furthermore, within the magnetic force theorem, the variation in the free energy, \mathcal{F} , with the site-resolved magnetisation polarisation directions $\{\phi_i, \theta_i\}$ can be evaluated from the relevant single-site t-matrices and scattering path operators as follows [133],

$$\frac{\partial^2 \mathcal{F}}{\partial \phi_i \partial \phi_j} = -\frac{1}{\pi} \int_{-\infty}^{\varepsilon_F} \text{Tr} \left\{ \tau_{ji}(\varepsilon) \frac{\partial t_i^{-1}(\varepsilon)}{\partial \phi_i} \tau_{ij}(\varepsilon) \frac{\partial t_i^{-1}(\varepsilon)}{\partial \phi_j} \right\} d\varepsilon \quad (2.52)$$

$$\frac{\partial^2 \mathcal{F}}{\partial \phi_i \partial \theta_j} = -\frac{1}{\pi} \int_{-\infty}^{\varepsilon_F} \text{Tr} \left\{ \tau_{ji}(\varepsilon) \frac{\partial t_i^{-1}(\varepsilon)}{\partial \phi_i} \tau_{ij}(\varepsilon) \frac{\partial t_i^{-1}(\varepsilon)}{\partial \theta_j} \right\} d\varepsilon \quad (2.53)$$

$$\frac{\partial^2 \mathcal{F}}{\partial \theta_i \partial \theta_j} = -\frac{1}{\pi} \int_{-\infty}^{\varepsilon_F} \text{Tr} \left\{ \tau_{ji}(\varepsilon) \frac{\partial t_i^{-1}(\varepsilon)}{\partial \theta_i} \tau_{ij}(\varepsilon) \frac{\partial t_i^{-1}(\varepsilon)}{\partial \theta_j} \right\} d\varepsilon. \quad (2.54)$$

One can show that the second derivatives of the free energy as described by the anisotropic Heisenberg Hamiltonian (cf. Eq. (2.5)),

$$\hat{H}_{\text{aHeis}} = -\frac{1}{2} \sum_{ij} \mathbf{S}_i \underline{\underline{J}}_{ij} \mathbf{S}_j - \sum_i d_i (\mathbf{S}_i \cdot \mathbf{e})^2, \quad (2.55)$$

can be related directly to the elements of the magnetic exchange tensor, $\underline{\underline{J}}_{ij}$, by polarising the magnetisation of the system as summarised in Table 2.1. The relations in Table 2.1 are straightforwardly derived by considering the direction cosines of the normalised magnetic moment $\mathbf{S}_i = (\sin \theta_i \cos \phi_i, \sin \theta_i \sin \phi_i, \cos \theta_i)$; the details of this derivation can be found in Ref. [133]. As the elements of the exchange tensor can thus be evaluated from the derivatives in Eqs. (2.52–2.54), these equations form the basis of the evaluation of magnetic exchange tensors in this work. In practice, these derivatives are evaluated by calculating the effect on the total energy from small perturbations in the directions, $\{\phi_i, \theta_i\}$, of the localised magnetic moments.

In addition to the exchange tensors listed in Table 2.1, the on-site anisotropy (see Eq. (2.7)) can be evaluated from the site-diagonal part of the angular second-order derivatives obtained when the system is polarised along the $\hat{\mathbf{x}}$ -axis (i.e.,

polarisation direction	$\frac{\partial^2 \mathcal{F}}{\partial \phi_i \partial \phi_j} =$	$\frac{\partial^2 \mathcal{F}}{\partial \theta_i \partial \theta_j} =$	$\frac{\partial^2 \mathcal{F}}{\partial \phi_i \partial \theta_j} =$	$\frac{\partial^2 \mathcal{F}}{\partial \theta_i \partial \phi_j} =$
$\hat{\mathbf{x}}$ -axis ($\theta = \pi/2, \phi = 0$)	J_{ij}^{yy}	J_{ij}^{zz}	$-J_{ij}^{yz}$	$-J_{ij}^{zy}$
$\hat{\mathbf{y}}$ -axis ($\theta = \pi/2, \phi = \pi/2$)	J_{ij}^{xx}	J_{ij}^{zz}	$-J_{ij}^{xz}$	$-J_{ij}^{zx}$
$\hat{\mathbf{z}}$ -axis ($\theta = 0$)	J_{ij}^{yy}	J_{ij}^{xx}	J_{ij}^{yx}	J_{ij}^{xy}

Table 2.1: The relations between the angular derivatives of the free energy as described by the anisotropic Heisenberg Hamiltonian, \hat{H}_{aHeis} , and the various elements of the exchange tensor \underline{J}_{ij} for the system being polarised along each of the three axes of the global frame of reference.

$$\theta_i = \pi/2, \phi_i = 0 \quad \forall i,$$

$$d_i = \frac{1}{2} \left(\left. \frac{\partial^2 \mathcal{F}}{\partial \theta_i \partial \theta_i} \right|_{\hat{\mathbf{x}}} - \left. \frac{\partial^2 \mathcal{F}}{\partial \phi_i \partial \phi_i} \right|_{\hat{\mathbf{x}}} \right). \quad (2.56)$$

Finally, the inter-site anisotropy in Eq. (2.7) can be evaluated from the off-diagonal angular second-order derivatives,

$$J_{ij}^{zz} - J_{ij}^{xx} = \frac{1}{2} \left(\left. \frac{\partial^2 \mathcal{F}}{\partial \theta_i \partial \theta_j} \right|_{\hat{\mathbf{y}}} + \left. \frac{\partial^2 \mathcal{F}}{\partial \theta_i \partial \theta_j} \right|_{\hat{\mathbf{x}}} - \left. \frac{\partial^2 \mathcal{F}}{\partial \phi_i \partial \phi_j} \right|_{\hat{\mathbf{y}}} - \left. \frac{\partial^2 \mathcal{F}}{\partial \theta_i \partial \theta_j} \right|_{\hat{\mathbf{z}}} \right), \quad (2.57)$$

where $\hat{\mathbf{x}}$, $\hat{\mathbf{y}}$ and $\hat{\mathbf{z}}$ correspond to the magnetisation polarisation directions as in Table 2.1.

2.3.5 Treatment of Chemically Disordered Systems

A number of results in this thesis concerns chemically disordered alloys. Chemical disorder poses a problem to first principles calculations primarily due to the breaking of translational symmetry. Within DFT, therefore, chemical disorder is often modelled in a mean-field manner, using, e.g., the Virtual Crystal Approximation (VCA) [134–136] or the Coherent Potential Approximation (CPA) [137–140].

Within the VCA, chemical disorder in a system is modelled as an effective background potential; at each point the potential is simply replaced by a concentration-averaged potential, i.e.,

$$V_{\text{VCA}}(\mathbf{r}) = x_0 V_0(\mathbf{r}) + x_1 V_1(\mathbf{r}) + \cdots + x_N V_N(\mathbf{r}), \quad (2.58)$$

where x_t is the concentration of species t and $V_t(\mathbf{r})$ is the potential of the pure

species t .

The CPA is similar to the VCA in that it entails using an effective potential to describe chemical disorder [141]. In contrast to the VCA, however, the effective potential within the CPA is derived directly from the scattering properties of the disordered system. At the heart of the CPA is the idea that, for any given level of chemical disorder, one may consider the average of the Green's function over the entire set of realisations of this particular level of disorder, $\langle \hat{G}(z) \rangle$, as an effective Green's function, $\hat{\mathfrak{G}}(z)$, i.e.,

$$\langle \hat{G}(z) \rangle = \left\langle \frac{1}{z - \hat{H}} \right\rangle = \hat{\mathfrak{G}}(z) = \frac{1}{z - \hat{\mathfrak{H}}}. \quad (2.59)$$

Here, $\hat{\mathfrak{H}}$ is the Hamiltonian of the effective medium, defining the *coherent potential*, \hat{V}_{CPA} . For each electron, the local potential experienced by that electron is replaced by the coherent potential. Through the Dyson equation (for details, see, e.g., Ref. [105] and Appendix A.5), this leads to the relation

$$\langle \hat{G}(z) \rangle = \hat{\mathfrak{G}}(z) + \hat{\mathfrak{G}}(z) \langle \hat{T}(z) \rangle \hat{\mathfrak{G}}(z). \quad (2.60)$$

Thus, the CPA requirement $\langle \hat{G}(z) \rangle = \hat{\mathfrak{G}}(z)$ is fulfilled if and only if

$$\langle \hat{T}(z) \rangle = 0. \quad (2.61)$$

The physical significance of Eq. (2.61) is that there should be zero additional scattering of the effective medium with respect to that of the configuration-averaged medium [141]. As the CPA is expressed as a condition on $\hat{T}(z)$, it fits neatly into the SKKR formalism [140]. In practice, the single-site CPA condition, i.e., $\langle \hat{t}_i(z) \rangle = 0$, is solved. This approximation of the CPA condition in Eq. (2.61) is exact up to third order in $\hat{t}_i(z)$ [138]. The CPA is generally considered a more consistent and, overall, better approach than the VCA as the CPA does not resort to the ansatz approach of the VCA [142].

2.3.6 Summary of the KKR Method

The main strengths of the KKR method are its separation of atomic and geometric properties [105] and the ease with which its formalism allows the CPA to be incorporated in calculations [140]. The *Screened* KKR (SKKR) method [121, 122] is particularly efficient for layered systems; for such systems, the SKKR method exhibits linear scaling of the computational effort with respect to the size of the system [105]. The main convergence parameters of the KKR

method are the angular momentum cut-off, l_{max} , the size of the principal layers, t_{PL} , the number of energy points sampled for the energy integrals (Fig. 2.1), n_e , and the number of k -points sampled at each energy point, n_k . In this work, most results have been obtained using the fully relativistic spin-polarised SKKR method within the LSDA+ASA. We have used an implementation of the SKKR method developed by Professor László Szunyogh of the Budapest University of Technology and Economics. Within this thesis we treat this implementation of SKKR much like a black box. Consequently, in the following, we present not only our results and interpretations, but also a number of checks of our calculations against experiments and calculations in literature.

Microstructural Defects and Localised Alloying in Cobalt

In today's hard drives, the magnetic recording medium is typically comprised of two or more layers of hexagonal close-packed (hcp) CoPt-based alloy [56, 143, 144]. However, in the current state of the development towards higher recording densities and smaller grain sizes, such CoPt alloys have almost reached their superparamagnetic limit [38, 59, 60]. Consequently, an understanding of how to maximise the magnetocrystalline anisotropy energy (MAE) in CoPt-based systems is an important practical problem for further development of the related devices. In particular, since the magnetic properties of these alloys are highly sensitive to the amount and the spatial distribution of the Pt content, understanding the effects of localised alloying and microstructural defects on the MAE of CoPt-based systems are issues of significant interest within the development of magnetic recording devices.

The magnetic properties of CoPt as functions of the Pt content and distribution have been studied extensively (see, e.g., Refs. [58, 145–149]). Moreover, in recent experimental work [150–153] it was demonstrated that the MAE of Co can be tuned by irradiating a Pt/Co/Pt system with Ga^+ ions. This tuning effect is thought to be a combined effect of lattice distortions [152] and localised Co-Pt alloying at the Co/Pt interfaces [150]. Generally it is agreed that the addition of Pt to a magnetic material, such as Fe or Co, influences the magnetic properties (in particular, the MAE) of the material primarily through the strong spin-orbit coupling of Pt [154, 155]. It is often found, however, that the maximum MAE as a function of Pt concentration is limited by, e.g., the formation of new phases [156] or the presence of stacking faults [56, 157, 158].

Stacking faults constitute one of the most common types of microstructural defects in close-packed metals. In fact, the large degrees of ductility and malleability observed in many such metals are a direct effect of the relative ease with which stacking faults form in such metals [159]. Measurements of the effects of stacking faults are generally performed in terms of the stacking fault density, which can be determined from X-ray diffraction spectra (see, e.g., Refs. [56,144,157,160,161]). For a magnetic recording medium, the presence of stacking faults is generally considered detrimental [162–164]. As disturbances in the microstructure, the presence of stacking faults will generally worsen the signal-to-noise ratio of the medium [56]. Stacking faults may also break the local lattice symmetry and, as a consequence, impact drastically on the MAE [162].

In the literature, there is a large number of experimental studies into stacking fault formation energies and the effects of stacking faults on the MAE of various magnetic recording alloys [144,162]. However, in experiment, the real effect of a stacking fault might be obscured by other, correlated phenomena. Amongst other issues, stacking faults may affect, or be affected by, the presence and distribution of an alloying component [145]. For CoPt, in particular, the Pt concentration and the stacking fault density are often correlated in experiment [165]. It has in fact been suggested that, due to the existence of such correlations, stacking fault formation energies obtained from *ab initio* calculations may actually be fundamentally more accurate than those obtained from experiment [159]. With the dramatic increase in computational power over the past two decades, a number of theoretical methods have been developed for predicting the properties and effects of stacking faults (see, e.g., Ref. [166]). In particular, there is a large number of *ab initio* studies of the formation energies of given types of stacking faults in particular metals (see, e.g., Refs. [159,167–169]). The effect on magnetic properties, such as the effect on the MAE of a particular stacking fault, is however less commonly explored.

In short, therefore, the isolated and combined effects of localised Pt alloying and stacking faults upon the MAE of hcp Co and hcp CoPt are of significant interest to the magnetic recording industry. The SKKR method appears an ideal method for combining studies of alloying and stacking faults; the inherent symmetries of a stacking fault fit elegantly into the SKKR formalism (see Section 2.3.3 and Section 3.3.2) and the coherent potential approximation (CPA) can be effectively used within the KKR formalism to model chemical disorder [170]. In fact, SKKR-CPA has previously reproduced a number of experimen-

tal results for disordered magnetic alloys (see, e.g., Refs. [140, 149, 171–174]) and layered KKR (LKRR) has in the past generated good agreement with experimental stacking fault formation energies in face-centred cubic (fcc) metals [167]. With this in mind, we set out to investigate (i) the effect of an $\text{Co}_{1-y}\text{Pt}_y$ atomic layer upon the MAE of bulk hcp Co and (ii) the effect of isolated and composite stacking faults on the MAE of bulk hcp Co. This work was performed with a view to investigate synergistic effects. In other words, it was hoped that if the effects on the MAE of stacking faults and Pt impurities could both be successfully described using SKKR, then we could treat composite systems with stacking faults and Pt impurities to investigate any synergistic effects that may arise. Due to computational and time constraints, so far only the two separate studies are finished and presented in this Chapter, which is based on Refs. [175, 176].

3.1 Computational Details

The ground state of pure cobalt is a hexagonal close-packed structure, as illustrated in Fig. 3.1. Throughout the work presented in this Chapter, we used the experimentally observed lattice parameters for hexagonal close-packed cobalt, $a = 2.51 \text{ \AA}$ and $c = 4.07 \text{ \AA}$ [177].

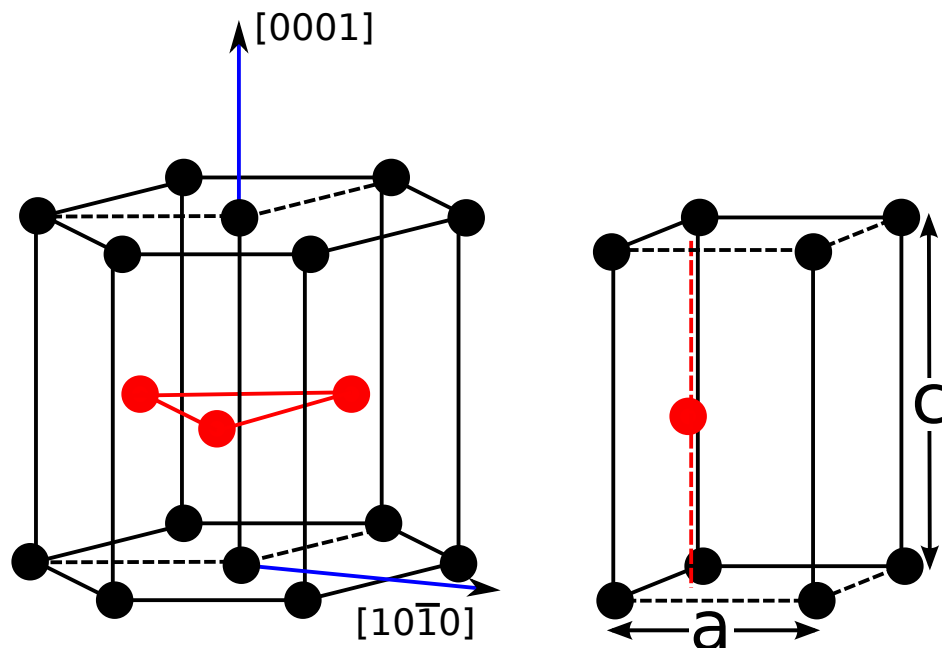


Figure 3.1: The hexagonal close-packed lattice structure.

As described in Section 2.3, we employed the SKKR method and performed

our calculations within the local spin density approximation (LSDA) of density functional theory (DFT) as parameterised by Vosko *et al.* [102]. The effective potentials and fields were treated in the framework of the atomic sphere approximation (ASA). It should be noted that the LSDA+ASA fails in describing the orbital moment of bulk Co accurately (see, e.g., Ref. [129]). Although full-potential and LSDA+U approaches may provide a more accurate description of hcp Co [178, 179], to the best of our knowledge there exists no such implementations of SKKR that can treat the sizes of system that we require in the following. Instead, therefore, we have employed a somewhat simplistic extension of the relativistic electron theory known as the orbital polarisation (OP) correction [180–184], which was implemented within the KKR method by Ebert and Battocletti [185]. Throughout our calculations, the corresponding Kohn-Sham-Dirac equations were solved using a spherical wave expansion up to an angular momentum number of $l_{max} = 3$, although the OP correction was applied only for the $l = 2$ terms.

As detailed in Section 2.3.4, the MAE was evaluated within the magnetic force theorem [99, 129], whereby the total energy of the system can be replaced by the single-particle (band) energy. In particular, for hcp Co, we calculated the MAE, K , as

$$K = \left. \frac{dE_{\text{band}}}{d\theta} \right|_{\theta=\pi/4}, \quad (3.1)$$

where θ denotes the angle of the spin-polarisation with respect to the [0001] axis. In particular, the angle θ is in the plane of the [0001] and the [10 $\bar{1}$ 0] axis, corresponding to the easy and hard axes of cobalt, respectively (see Fig. 3.1) [37]. Within the KKR formalism, K can be decomposed into site- and species-resolved contributions,

$$K = \sum_{i,\alpha} v_i^\alpha D_i^{(\alpha)}, \quad (3.2)$$

where v_i^α denotes the concentration of species α at site i and $D_i^{(\alpha)}$ denotes the corresponding derivative of the band energy. These site- and species-resolved contributions to the MAE, $D_i^{(\alpha)}$, are calculated using the torque method as described in Ref. [131] and summarised in Section 2.3.4, i.e.,

$$D_i^{(\alpha)}(\hat{\mathbf{n}}) = -\frac{1}{\pi} \text{Im} \int_{-\infty}^{\varepsilon_F(\hat{\mathbf{n}})} \text{Tr} \left\{ \frac{\partial t_i^{-1}(\varepsilon; \alpha, \hat{\mathbf{n}})}{\partial \theta} \tau_{ii}(\varepsilon; \alpha, \hat{\mathbf{n}}) \right\} d\varepsilon, \quad (3.3)$$

where $\varepsilon_F(\hat{\mathbf{n}})$ is the Fermi energy and, in the case that species α occupies site i , $t_i(\varepsilon)$ and $\tau_{ii}(\varepsilon)$ stand for the angular momentum matrices of the single-site t -operator and the site-diagonal scattering path operator, respectively. All these

quantities are evaluated keeping the direction of the magnetisation $\hat{\mathbf{n}} = (1/\sqrt{2}, 0, 1/\sqrt{2})$, corresponding to $\theta = \pi/4$ in Eq. (3.1). Note that $\hat{\mathbf{n}}$ refers to the polarisation of the spin moments; the orbital moments are assumed to be approximately parallel to these. Since the deviation of the Co orbital moment is within 1 degree of the corresponding spin moment and the Pt orbital moment is within 0.3 degrees of the corresponding spin moment, this is probably a valid assumption. In line with the SKKR formalism (cf. Section (2.3.3)), the MAE contributions are related to a 2D unit cell and therefore, in the following, the index i in Eq. (3.3) is used to label atomic layers rather than sites.

We obtained the self-consistent potentials and fields for the MAE calculation from fully relativistic LSDA+OP calculations.¹ The size of each principal layer was kept to two atomic layers, providing convergence of within 5 % for the MAE. In calculating the MAE, we sampled 20 energy points for the energy integral in Eq. (3.3). We employed a dense mesh in the two-dimensional Brillouin zone (2D-BZ), which, at the energy point closest to the Fermi energy, comprised 5764 k -points in the irreducible wedge of the 2D-BZ (corresponding to more than 34 000 k -points in the full 2D-BZ). This leaves the MAE well converged (to within 5 %) with respect to the number of energy points and the number of k -points. However, while the aforementioned angular momentum cut-off, $l_{max} = 3$, yields a reasonable convergence of the total energies and magnetic moments (see Fig. 3.2), it represents (at best) an MAE convergence to within 15 % of the accepted value. Still, in view of $l_{max} = 3$ being a very commonly used angular momentum cut-off for transition alloys [119, 120] and in view of the $(l_{max} + 1)^6$ scaling of computational effort, this appeared an acceptable trade-off with respect to the computational resources available [119, 120].

To test our computational method (in particular, the OP correction) we first calculated the MAE of bulk hcp cobalt. Excluding the OP correction we obtained an easy-plane magnetisation perpendicular to the [0001] axis and a MAE of 6.7 $\mu\text{eV}/\text{atom}$, while including the OP correction resulted in an easy axis parallel to the [0001] axis and a MAE of 84.4 $\mu\text{eV}/\text{atom}$. The latter result is in much better agreement with the experimental value of 65.5 $\mu\text{eV}/\text{atom}$ [188] and with the experimental easy axis being along the [0001] axis. Our result also compares well with that of Trygg *et al.* [186], who calculated $K = 110 \mu\text{eV}/\text{atom}$ for hcp cobalt using a full-potential LMTO method including the OP correction.

¹Note that the force theorem remains applicable; see, e.g., Refs. [129, 186, 187].

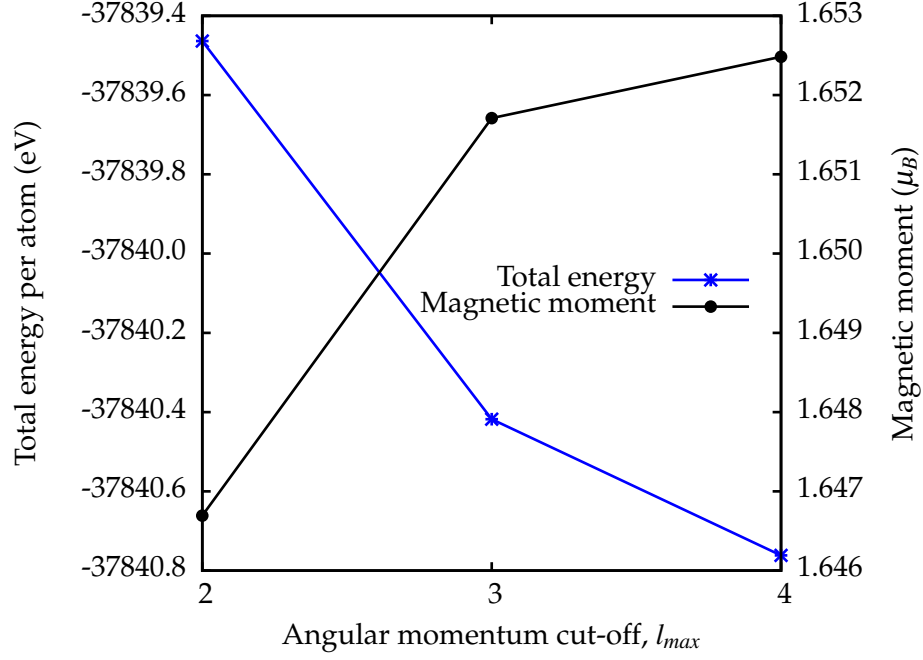


Figure 3.2: Convergence of the total energy per Co atom and the Co magnetic moment with the angular momentum cut-off, l_{max} . These self-consistent relativistic LSDA-OP calculations were performed using two atomic layers per principal layer and 20 energy points, each with 91 k -points.

3.2 Localised Platinum Alloying in Cobalt

3.2.1 The System

As discussed in Section 2.3.3, the formalism of the SKKR method requires the system to be layered, i.e., the system has to be infinite and periodic in the x - and y -directions. Moreover, the region of interest (the *interlayer*) for which the MAE is calculated, has to be positioned in between two semi-infinite bulk systems along the z -axis. Adhering to these requirements, we considered a system as illustrated in Fig. 3.3, wherein the z -direction is defined to be parallel to the [0001] axis of the hcp lattice. Two bulk hcp Co systems, semi-infinite along the z -direction and infinite and periodic in the x - and y -directions, enclose the interlayer. The interlayer, in turn, consists of $2N_L$ hcp Co atomic layers (corresponding to N_L unit cells along the [0001] axis) that are periodic and infinite along the x - and y -directions. In one of the central atomic layers, a fraction v of the Co atoms are replaced by Pt atoms by means of the CPA. In other words, the system studied comprises one atomic layer of substitutional $\text{Co}_{1-v}\text{Pt}_v$ alloy, enclosed by hcp Co in the $\pm z$ -directions. Due to the two-dimensional translational symmetry of the system, we considered layer-resolved rather than site-resolved contributions to the MAE. Consequently, in the following, the index

i in Eq. (3.2) is used to label atomic layers. The $\text{Co}_{1-\nu}\text{Pt}_\nu$ layer is indexed $i = 0$ and will be referred to as the *impurity layer*.

The layer-resolved MAE contributions are calculated only for the interlayer. Thus, in order to ensure that we include all significant contributions to the total MAE caused by the presence of the impurity layer, we increased the number of atomic layers in the interlayer until the MAE contributions of the atomic layers $\{N_L - 3, \dots, N_L\}$ and $\{-N_L + 1 \dots -N_L + 4\}$ remained within 1 % of the bulk Co MAE for $\nu = 1$. We found that this condition requires $N_L = 40$, i.e., a total of 80 layers in the interlayer.

Due to the need to include the OP correction as discussed in Section 3.1, the self-consistent calculations are computationally intensive. Therefore, self-consistent potentials were obtained only for layers $-13 \leq i \leq 14$. We then appended the bulk hcp Co potential to the outer layers $-39 \leq i \leq -14$ and $15 \leq i \leq 40$, i.e., we neglected any self-consistency effects for these layers. In order to safeguard the viability of this approach, we made use of the fact that the layer-resolved MAE contributions would be expected to exhibit reflection symmetry about the impurity layer, i.e., the MAE contributions from layers i and $-i$ should be identical to within the accuracy of the calculation. In order to check the viability of neglecting self-consistency for layers $-39 \leq i \leq -14$ and $15 \leq i \leq 40$, we can thus compare the MAE contributions from layers 14 (with relaxed self-consistent potential) and -14 (with unrelaxed bulk Co potential); reassuringly, these agree to within 0.02 %.

3.2.2 Layer-Resolved Contributions to the MAE

First, we considered the layer-resolved contributions to the MAE from the $2N_L$ ($= 80$) atomic layers depicted in Fig. 3.3. In Fig. 3.4 we show the results of performing the calculations described in Section 3.1 on the system in Fig. 3.3 with $\nu = 0.01$ and $\nu = 0.02$. Even for such small Pt concentrations, the presence of the impurity layer induces significant oscillations in the MAE contributions. In fact, these oscillations reach 10 % of the bulk Co MAE. In particular, for $\nu = 0.02$, the Co MAE contributions from layers $i = \pm 1$ are enhanced to nearly $94 \mu\text{eV}$, while those from layers $i = \pm 2$ are reduced to nearly $76 \mu\text{eV}$. For layers further away from the impurity layer ($|i| \geq 5$), oscillations in $D_i^{(\text{Co})}$ with rapidly decreasing amplitude can be seen. As required, the layer-resolved Co MAE contributions approach the bulk Co MAE, $84.4 \mu\text{eV}$, towards the outer edges of the interlayer ($i \rightarrow N_L = 40$ and $i \rightarrow -(N_L - 1) = -39$). Moreover, the

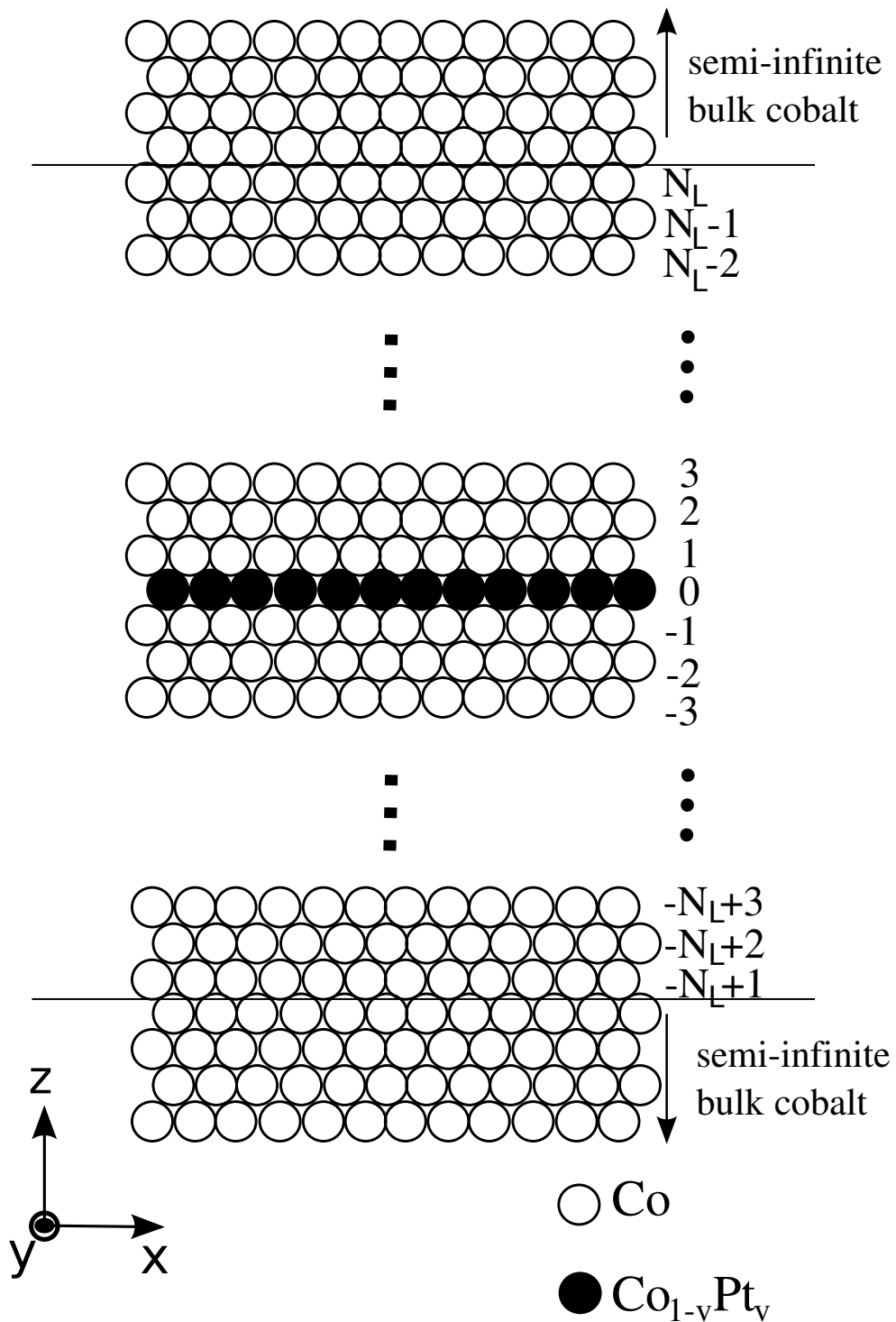


Figure 3.3: Sketch of the system used to study localised Pt alloying in Co. The system contained N_L hcp unit cells, i.e., $2N_L$ atomic layers, positioned in between two semi-infinite systems of bulk Co. In the zero-indexed layer, indicated by black circles, a random substitutional alloy with Pt, $\text{Co}_{1-v}\text{Pt}_v$, was considered. Note that the \hat{z} -axis was defined to be parallel to the $[0001]$ axis of the hcp crystal.

mirror symmetry about the impurity layer, $D_i^{(Co)} = D_{-i}^{(Co)}$, is fulfilled with a high accuracy.

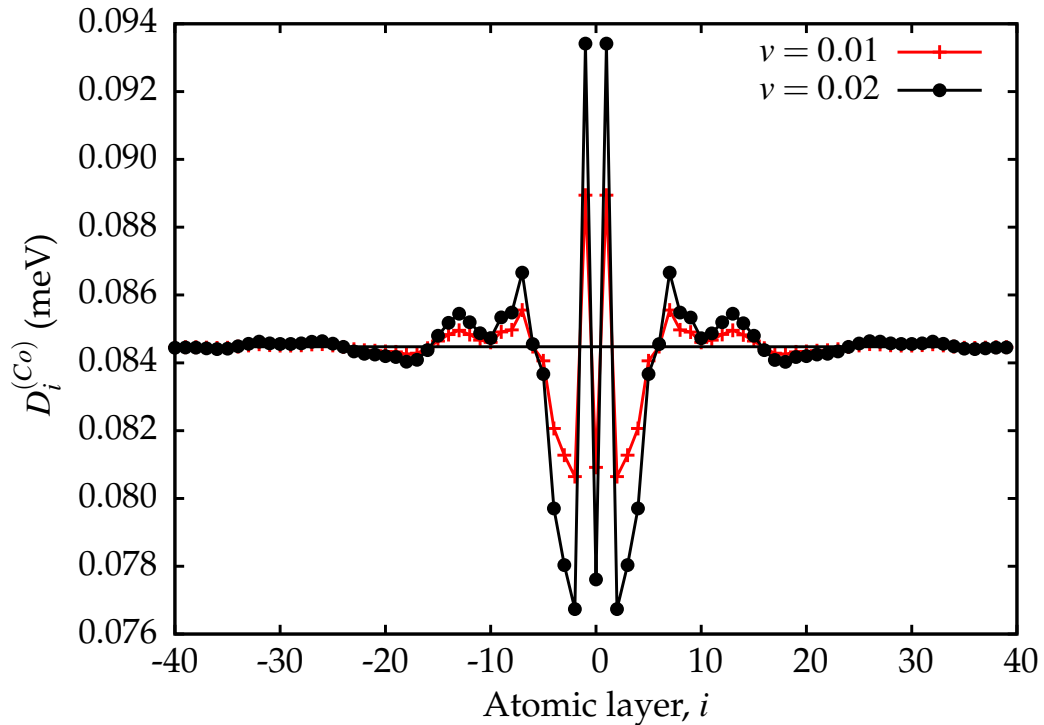


Figure 3.4: The calculated layer-resolved Co contributions to the MAE, $D_i^{(Co)}$ (see Eq. (3.3)), across the system shown in Fig. 3.3 for $v = 0.01$ (red +) and $v = 0.02$ (black •). The MAE of bulk Co is indicated by the solid black horizontal line. Solid lines connecting the symbols serve as guides for the eye.

Earlier studies of the MAE of impurities have shown that the MAE is extremely sensitive to the presence of Friedel oscillations² in the charge density [191,192]. We therefore investigated whether it is possible to relate the results in Fig. 3.4 to the change in the valence charge on the cobalt atoms as a function of the distance from the impurity layer, which is shown in Fig. 3.5 (a). Here we can see that the Co atoms in the impurity layer and, in particular, the Co atoms in layers adjacent to the impurity layer, gain extra charge. For layers further away from the impurity layer, the valence charge rapidly approaches the bulk valence charge, $9.00 e$. The energy shift of the layer-resolved cobalt valence band position is well described by the layer-resolved change in the Madelung potential.³ As is evident from Fig. 3.5 (b), an enhanced (reduced) charge at

²Friedel oscillations [189] are oscillations in the charge density resulting from the presence of a localised defect in a Fermi gas or Fermi liquid. For details, see, e.g., Ref. [190]. In essence, the finite size of the electron waveform leads to a situation where the screening of a localised defect will cause ripples of over- and under-compensation in the charge density.

³The Madelung potential is the shift in the orbital energy that happens as a result of inserting

the cobalt sites is accompanied with a downward (upward) shift of the valence states. If we compare this to Fig. 3.4, the shift of the valence states is strongly correlated with the MAE contributions from the cobalt layers adjacent the impurity layer. However, the changes in the MAE contributions from more distant cobalt layers are also subject to the fine changes in the valence states caused by the presence of the impurity layer.

Next, we considered the effect of the Pt concentration in the impurity layer, ν , on the species-resolved MAE contribution from each atomic layer. This is shown in Fig. 3.6 for layers $0 \leq |i| \leq 4$ (note that, to within numerical accuracy, $D_{-i} = D_i$ due to the reflection symmetry about the impurity layer). In the impurity layer $i = 0$, (Fig. 3.6 (a)), the Co contribution $D_0^{(Co)}$ is reduced by the addition of Pt for concentrations up to about $\nu = 0.15$ and then enhanced for concentrations $0.15 < \nu < 0.50$. For concentrations $\nu > 0.50$, $D_0^{(Co)}$ is again reduced with increasing ν and at $\nu \approx 0.9$, $D_0^{(Co)}$ vanishes. Note that $D_0^{(Co)}$ for $\nu \rightarrow 1$ (not calculated here) would correspond to the contribution of a single Co atom in a pure Pt layer which, in general, would differ from zero. The direct Pt contribution, $D_0^{(Pt)}$, approaches the very small value of 0.01 meV as $\nu \rightarrow 0$, rapidly increases up to 0.30 meV at $\nu \approx 0.5$ and then peaks at $D_0^{(Pt)} \approx 0.35$ meV at $\nu \approx 0.85$. As can be inferred from Fig. 3.6, the most significant impact of the Pt alloying on the MAE occurs in the cobalt layers adjacent to the impurity layer. $D_1^{(Co)}$ increases almost linearly from the bulk Co MAE at $\nu = 0$ to about 0.7 meV at $\nu = 1$. As already seen in Fig. 3.4, the cobalt contributions $D_i^{(Co)}$ from layers further out ($2 \leq i \leq 4$) decrease with increasing ν and even become negative at $\nu \approx 0.25$ for $i = 2$ and 3. For $\nu > 0.5$ these contributions exhibit a modest increase, although $D_2^{(Co)}$ still remains negative.

In order to pinpoint the physical origin of the large enhancement of the MAE contribution from layer 1 with increasing ν shown in Fig. 3.6 (a), we investigated the change in the valence states projected onto the cobalt atoms in this layer. As can be seen in Fig. 3.7 (a), the valence charge on these cobalt atoms increases approximately linearly with the platinum concentration, from $Q = 9.00 e$ at $\nu = 0$ to $Q = 9.16 e$ at $\nu = 1$. This enhancement of the valence charge has to be accompanied by a downshift in the corresponding valence states, which can be characterised by the amount of change in the Madelung potential. Such a downshift in the Madelung was indeed confirmed, as shown in Fig. 3.7 (b). Here we can see that the change in the Madelung potential is also linear in ν

the atom into the solid state system, i.e., the Madelung potential describes the potential well within which a particular charged particle resides. If the charge on this particle increases, there has to be a corresponding downshift in the Madelung potential.

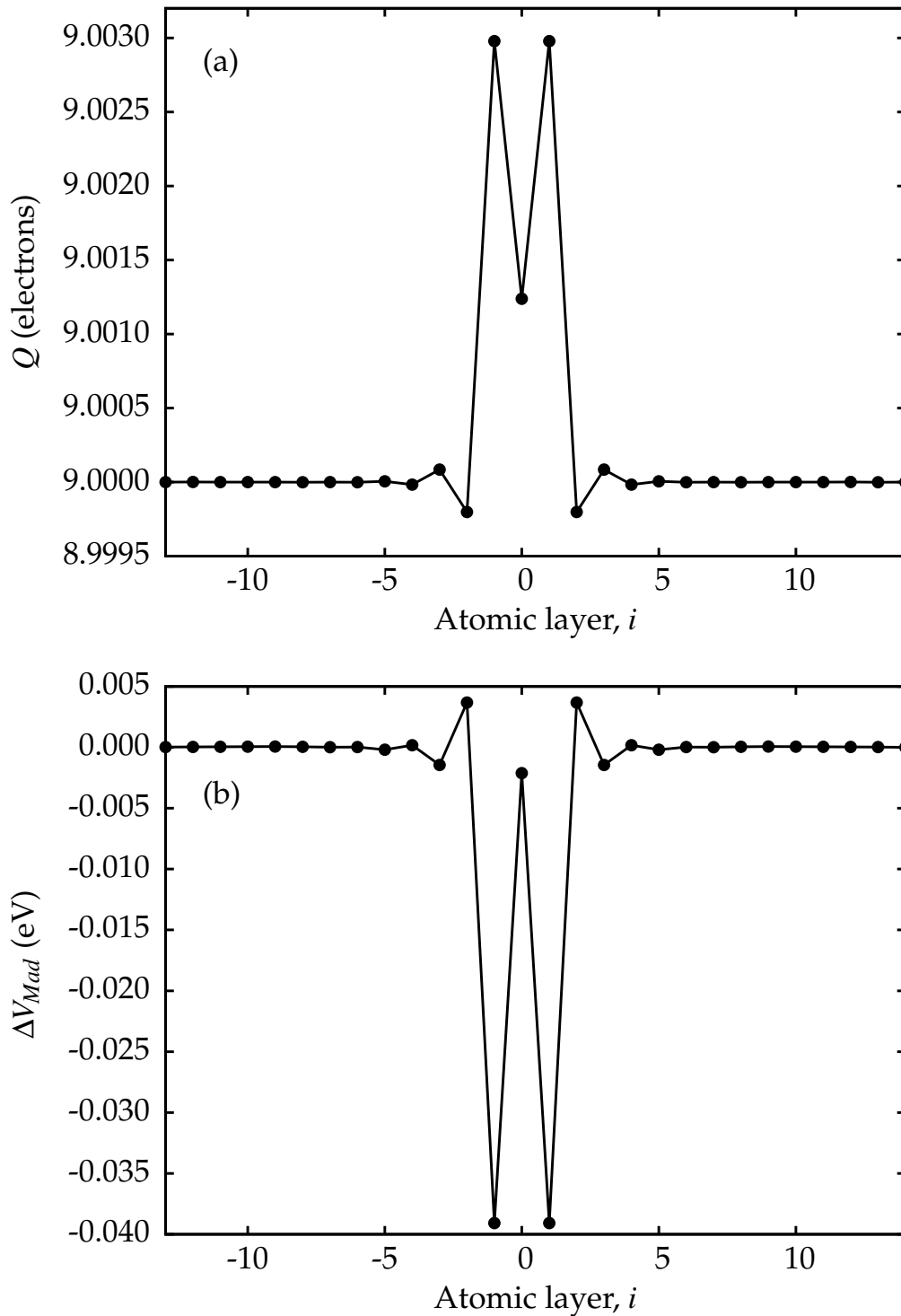


Figure 3.5: The calculated (a) valence charge on the cobalt atoms, Q , and (b) relative shift of the Madelung potentials with respect to the bulk case, ΔV_{Mad} , for layers $-13 \leq i \leq 13$ and for a Pt concentration of $\nu = 0.02$. Solid lines connecting the symbols serve as guides for the eye.

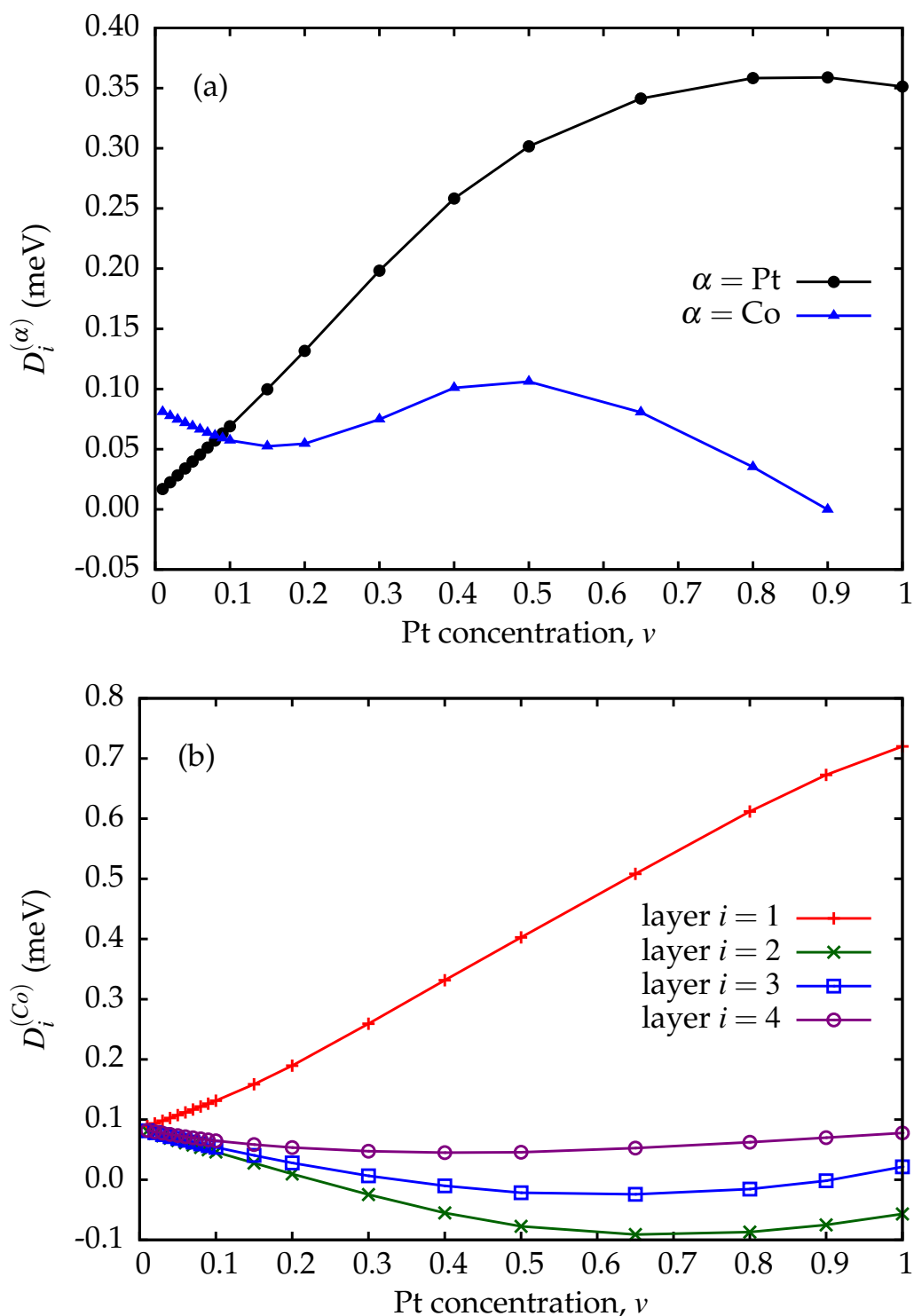


Figure 3.6: The calculated species-resolved MAE contributions for (a) the impurity layer: $D_0^{(\text{Pt})}$ (black \bullet) and $D_0^{(\text{Co})}$ (blue \blacktriangle) and (b) the Co layers: $D_1^{(\text{Co})}$ (red $+$), $D_2^{(\text{Co})}$ (green \times), $D_3^{(\text{Co})}$ (blue \square) and $D_4^{(\text{Co})}$ (purple \circ). Solid lines connecting the symbols serve as guides for the eye.

(but instead reduced with increasing ν). Thus, the large enhancement of the MAE contribution from layer 1 with increasing ν can be related directly to the monotonic shift in the valence states.

The dependence of the MAE of hcp Co on the band-filling was investigated in Ref. [129] and, in the range of $9 \leq Q \lesssim 9.2$, a change in the MAE of about 0.03 meV per atom was reported [129]. This is obviously a much weaker dependence than what we obtain for $D_1^{(Co)}$ in Fig. 3.6 (b). The main difference between our study and that of Ref. [129] is that in our case the change in the band-filling is accompanied by the breaking of the bulk symmetry upon the addition of Pt atoms, giving rise to an enhanced uniaxial magnetic anisotropy when a complete Pt layer is being formed. Furthermore, it should be pointed out that because our calculations rely on a non-perturbative treatment of the spin-orbit coupling (unlike, e.g., Ref. [193]), there is no obvious way of relating the spatial and species-resolved decompositions of the MAE to a simple microscopic mechanism. According to Ref. [192] we can, however, suppose that the valence electrons at the Co sites experience strong spin-orbit coupling upon hybridising with mobile conduction electrons that scatter on Pt sites. This picture is consistent with the large enhancement of $D_1^{(Co)}$ with increasing Pt concentration (Fig. 3.6 (b)).

3.2.3 Aggregate Variation in the MAE

While the layer-resolved MAE contributions are certainly interesting from a theoretical point of view, from an experimental and engineering point of view, the aggregate change in the MAE of the system is the more interesting quantity. We considered two different ways of visualising the aggregate change in the MAE: the net change in the MAE, ΔK , and the net change in the MAE per Pt atom added to the impurity layer, K_{Pt} .

The net change in the MAE, ΔK , can be calculated as a weighted sum of the layer-resolved deviations from the bulk cobalt MAE, i.e.,

$$\Delta K(\nu) = \nu D_0^{(Pt)} + (1 - \nu) D_0^{(Co)} + 2 \sum_{i=1}^{40} D_i^{(Co)} - 81 K_{Co}, \quad (3.4)$$

where K_{Co} is the calculated bulk hcp Co MAE, 84.4 $\mu\text{eV}/\text{atom}$. Note that we have taken into account the off-centre positioning of the impurity layer by doubling the Co contributions $D_i^{(Co)}$ for $i \in [1, 40]$. Thus, in total, a system of 81

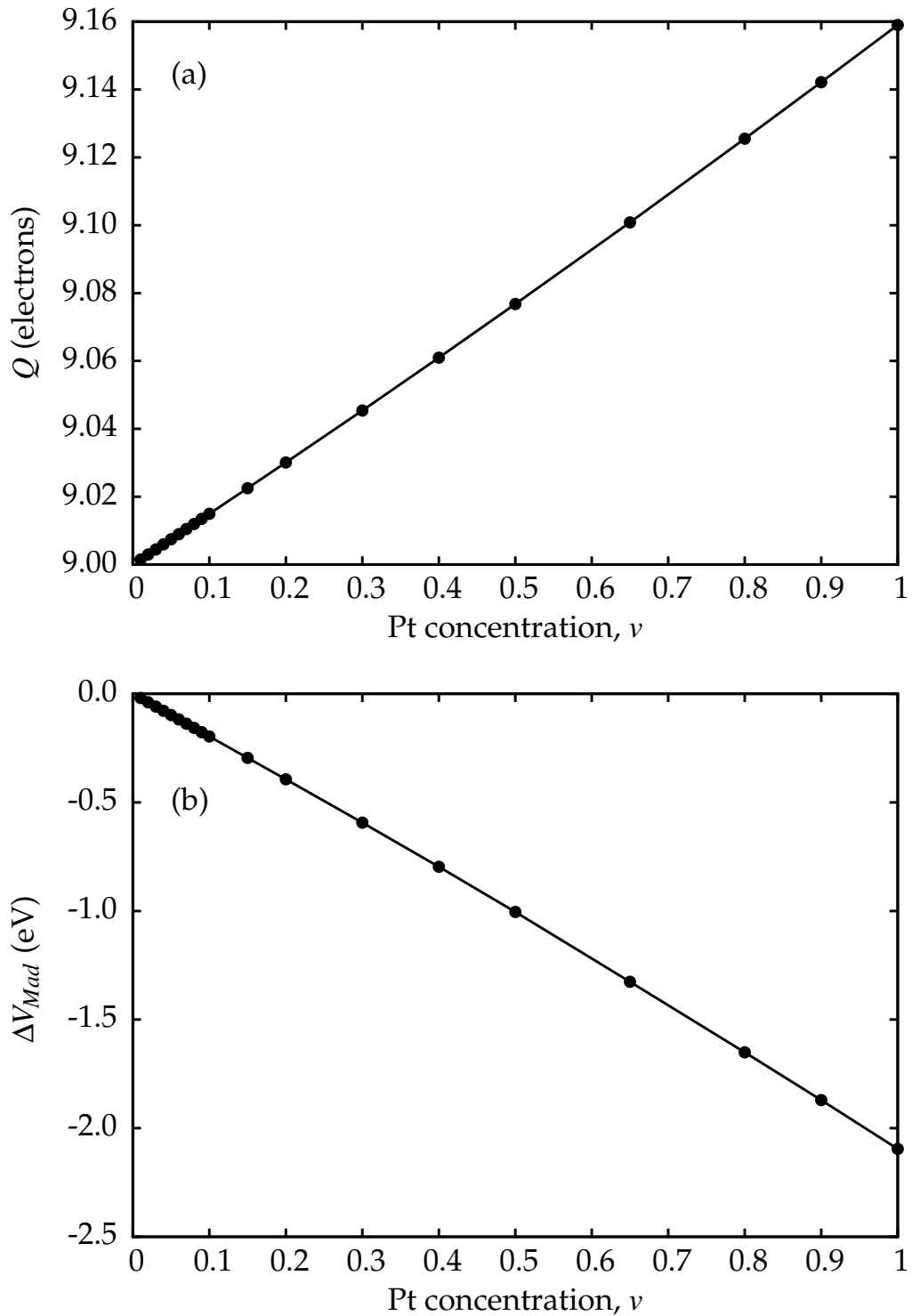


Figure 3.7: The calculated (a) valence charge on the Co atom, Q , and (b) relative shift of the Madelung potential with respect to the bulk case, ΔV_{Mad} , for layer $i = 1$ as a function of the Pt concentration, ν . Solid lines connecting the symbols serve as guides for the eye.

layers is considered. ΔK is shown as a function of ν in Fig. 3.8, demonstrating that for small Pt concentrations ($\nu < 0.24$) the addition of Pt to bulk Co actually reduces the total MAE of the system by up to about $80 \mu\text{eV}$. This is in contrast to the direct contribution of Pt, $D_0^{(Pt)}$, which, as seen in Fig. 3.6 (a), is positive for all values of ν . The MAE reduction for small ν in Fig. 3.8 stems, primarily, from the reduction in the Co contributions, $D_i^{(Co)}$, in layers $i = 0, 2, 3$ and 4 (see Fig. 3.6). ΔK becomes positive for $\nu > 0.24$ as the increasing direct Pt contribution, $D_0^{(Pt)}$, gains larger weight (note the ν -weighting of $D_0^{(Pt)}$ in Eq. (3.4)) and due to the large enhancement of $D_1^{(Co)}$ with increasing ν . At $\nu = 1$, $\Delta K = 1.4$ meV, which is approximately four times the direct Pt contribution, $D_0^{(Pt)} \approx 0.35$ meV for $\nu = 1$.

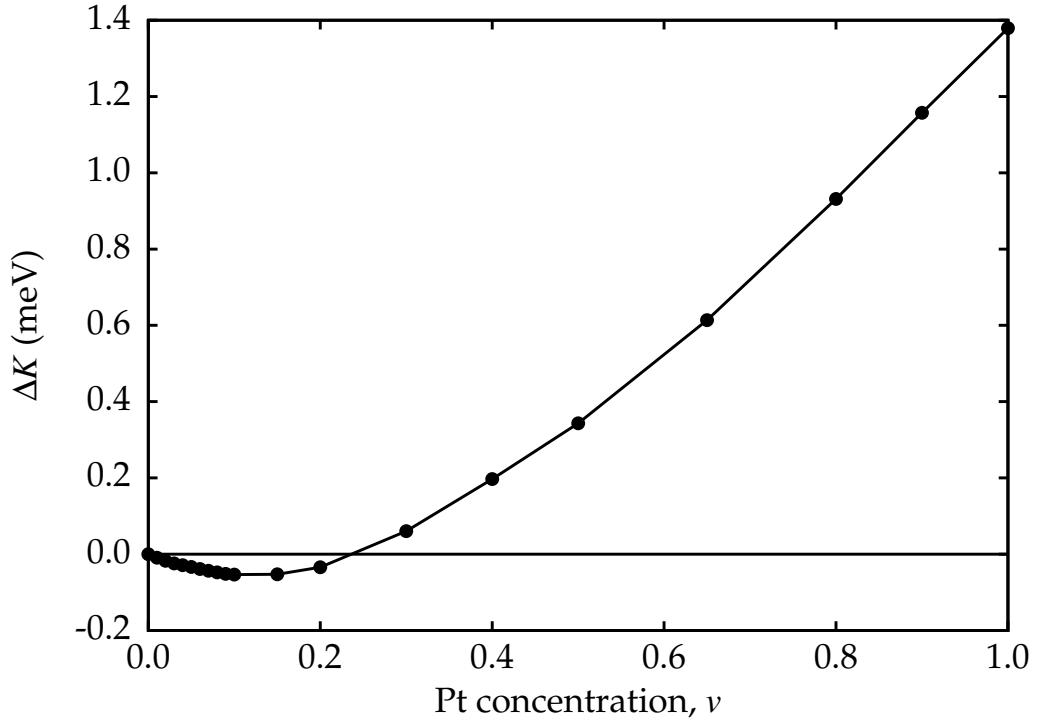


Figure 3.8: The calculated change in the MAE, ΔK , of a system of 81 atomic layers (see Eq. (3.4)), as a function of the Pt concentration, ν . The solid line connecting the symbols serves as a guide for the eye.

For nano-sized systems, it might be of interest to consider *the change in the MAE per Pt atom in the system*, \bar{K}_{Pt} , defined by

$$\bar{K}_{Pt}(\nu) = \frac{\Delta K(\nu)}{\nu}, \quad (3.5)$$

and also, the change in the MAE per Pt atom added to the system, K_{Pt} , given by

$$K_{Pt}(v) = \frac{d(\Delta K(v))}{dv}. \quad (3.6)$$

We obtained $K_{Pt}(v)$ by fitting a fourth-order polynomial to the function $\Delta K(v)$ in Fig. 3.8 and finding the derivative of this polynomial analytically. As is apparent from Fig. 3.9, both \bar{K}_{Pt} and K_{Pt} are monotonically increasing with increasing v , starting with the same value of about -1 meV at $v = 0$. \bar{K}_{Pt} crosses zero at $v \approx 0.24$, while K_{Pt} crosses zero at $v \approx 0.11$ (i.e., where the function $\Delta K(v)$ reaches its minimum). For a complete Pt layer immersed in bulk cobalt, i.e., for $v = 1$, $\bar{K}_{Pt} = \Delta K \approx 1.4$ meV. A comparison with Fig. 3.6 reveals that about 25 % of this value arises from the direct Pt contribution, $D_0^{(Pt)}$, and the rest from induced cobalt contributions. Interestingly, the change in the MAE by addition of a Pt atom to the system, $K_{Pt}(v)$, exhibits a relatively large value of about 2.5 meV at $v = 1$. From Fig. 3.6 (a) it can be inferred that the direct Pt contribution, $D_0^{(Pt)}$, has nearly zero slope in this region of v and thus this large value of K_{Pt} stems mainly from an increase in $D_i^{(Co)}$ for $1 \leq |i| \leq 4$ near $v = 1$.

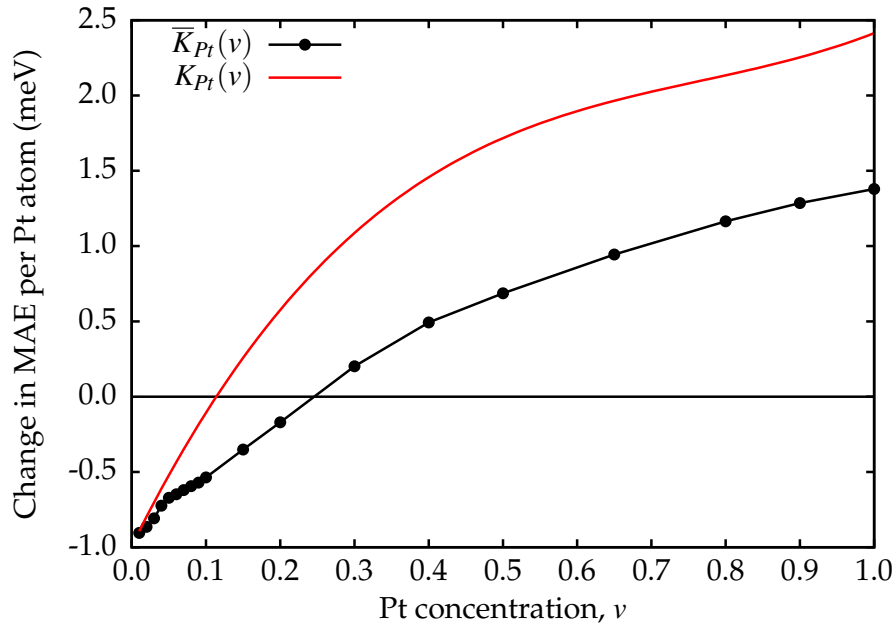


Figure 3.9: The calculated change in the MAE per Pt atom as a function of the Pt concentration, v . Black \bullet : average change in the MAE per Pt atom in the system, $\bar{K}_{Pt}(v)$ (see Eq. (3.5)). The black solid line connecting the symbols serves as a guide for the eye. Red solid line: the change in the MAE per Pt atom added, $K_{Pt}(v)$ (see Eq. (3.6)), as calculated from a polynomial fit of $\Delta K(v)$ in Fig. 3.8.

In the limit $v \rightarrow 0$, the value of $K_{Pt}(v)$ corresponds to the case of a single Pt atom

being added to bulk cobalt. In this limit, \bar{K}_{Pt} and K_{Pt} should be identical and this is fairly well confirmed by our calculations as both \bar{K}_{Pt} and K_{Pt} approach -1 meV as $\nu \rightarrow 0$. $K_{Pt}(0)$ can be expressed as

$$K_{Pt}(0) = D_0^{(Pt)}(0) - K_{Co} + \sum_{i=-40}^{40} \left. \frac{dD_i^{(Co)}(\nu)}{d\nu} \right|_{\nu=0}. \quad (3.7)$$

The physical meaning of the above equation is that adding a Pt atom to bulk cobalt has two effects on the MAE of the system: the first two terms, $D_0^{(Pt)}(0) - K_{Co}$, represent the direct contribution of a cobalt atom being replaced by a Pt atom, whereas the last term of Eq. (3.7) quantifies the induced change of the Pt on the MAE contributions from the cobalt atoms that are not being replaced by Pt. Since the direct Pt contribution is about -0.07 meV (see also Fig. 3.6 (a)), the value of $K_{Pt}(0) = -1$ meV can again only be explained by the induced cobalt contributions.

In order to investigate the origin and robustness of the large value of $K_{Pt} \approx -1$ meV in the limit $\nu \rightarrow 0$, we investigated the layer-resolved derivatives of the Co MAE contributions with respect to the Pt concentration, ν , calculated as

$$\left. \frac{dD_i^{(Co)}(\nu)}{d\nu} \right|_{\nu_j} = \frac{D_i^{(Co)}(\nu_{j+1}) - D_i^{(Co)}(\nu_{j-1})}{\nu_{j+1} - \nu_{j-1}} \quad (3.8)$$

for a small Pt concentration ν_j where j indexes a discrete set of Pt concentrations in ascending order. Fig. 3.10 shows $\left. \frac{dD_i^{(Co)}(\nu)}{d\nu} \right|_{\nu_j}$ as a function of atomic layer index i for $\nu_j = 0.02$. This figure is obviously closely related to Fig. 3.6; for small ν , the Co MAE contributions $\{D_i^{(Co)}\}$ show an increasing tendency with increasing ν for $|i| = 1$ and $|i| \geq 6$, while they exhibit a decreasing trend for $2 \leq |i| \leq 5$. The latter effect overcomes the former one, leading to the relatively large value of $K_{Pt}(0) = -1$ meV.

3.2.4 Finite-Size and Short-Range Order Effects

Finally, we considered possible finite-size effects of the long-ranged spatial oscillations in the MAE shown in Fig. 3.4, i.e., effects of truncating the system to a thickness less than the $2N_L$ atomic layers considered up to this point. This was achieved by truncating the sum in Eq. (3.4) to yield the truncated version

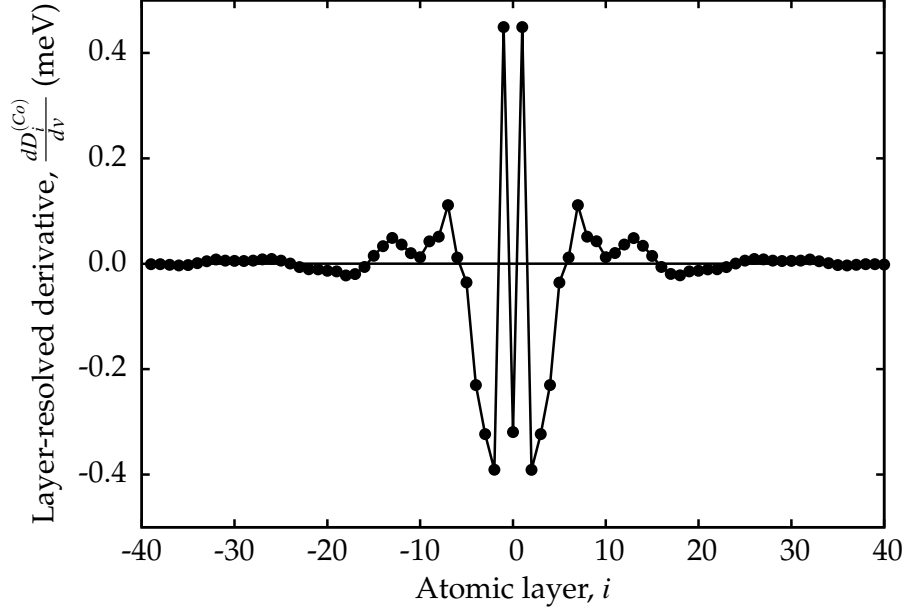


Figure 3.10: The calculated approximate layer-resolved derivatives of the Co MAE contributions, $D_i^{(Co)}$, with respect to the Pt concentration, v (see Eq. (3.8)), evaluated at $v = 0.02$. The solid line connecting the symbols serves as a guide for the eye.

of Eq. (3.5), i.e.,

$$\bar{K}_{Pt}(v, N) = \frac{1}{v} \left(vD_0^{(Pt)} + (1-v)D_0^{(Co)} + 2 \sum_{i=1}^N D_i^{(Co)} - (2N+1)K_{Co} \right) \quad (3.9)$$

for $1 \leq N \leq 40$. Fig. 3.11 shows $\bar{K}_{Pt}(N)$ for $v = 0.01, 0.05, 0.10$ and 0.20 . In all these cases, there is a maximum in $\bar{K}_{Pt}(N)$ at $2N+1 = 3$ layers, corresponding to including only one cobalt layer on each side of the impurity layer in the sum. This is because the induced effect on $D_1^{(Co)}$ by the addition of Pt is strongly positive for all v (see Fig. 3.4 and Fig. 3.6 (b)). There is a significant minimum in the calculated $\bar{K}_{Pt}(N)$ at $2N+1 \approx 11$ layers. We can see from Fig. 3.4 and Fig. 3.6 (b) that this minimum is due to the reduction in $D_i^{(Co)}$ for $3 \leq |i| \leq 5$ caused by the addition of Pt. $\bar{K}_{Pt}(N)$ then exhibits a local maximum at $2N+1 \approx 31$, mostly due to the cobalt contributions in layers $8 \leq |i| \leq 15$ counterbalancing the cobalt contributions of opposite sign in layers $3 \leq |i| \leq 5$ (cf. Fig. 3.4). Concerning the overall accuracy of the calculated MAE, the aggregate effect of the oscillations in the MAE remain significant for approximately $2N+1 < 70$ layers, i.e., for approximately 35 layers on either side of the impurity layer. In general, the variation in \bar{K}_{Pt} with N spans more than 1.5 meV for all values of v . The aggregate change in the MAE due to localised Pt alloying in a Co sample would thus be expected to be extremely sensitive to the system thickness for thicknesses

up to about $2N + 1 < 40$ layers (~ 8 nm). This could of course have significant implications for measuring the MAE in thin film samples. Note that this finite-size effect would be superimposed upon and, in all likelihood, amplified by, quantum interferences arising from the boundaries of the finite film sample [194].

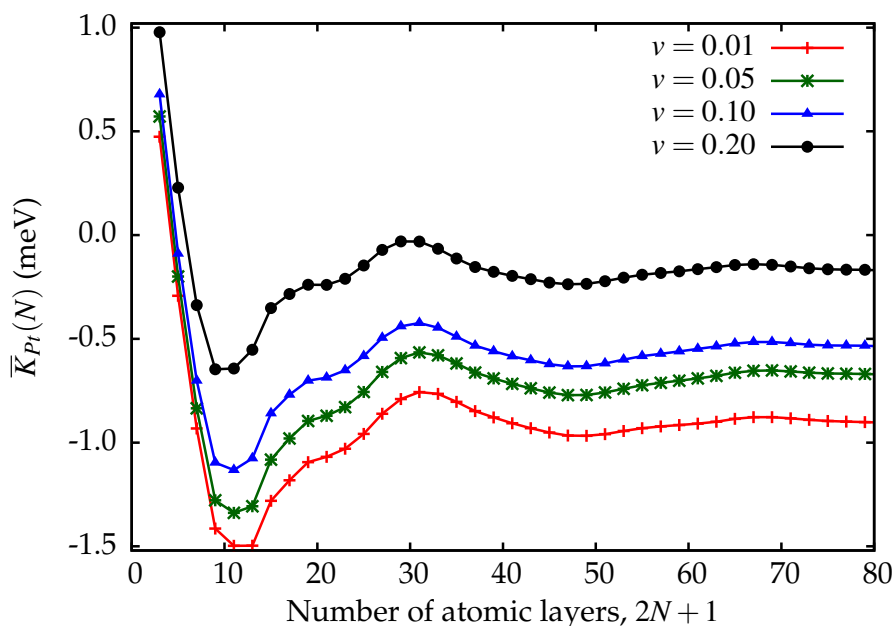


Figure 3.11: The calculated total change in the MAE per Pt atom, \bar{K}_{Pt} , as a function of the number of layers N included in the sum in Eq. (3.9) for $\nu = 0.01$ (red +), $\nu = 0.05$ (green \times), $\nu = 0.10$ (blue \blacktriangle) and $\nu = 0.20$ (black \bullet).

It should be noted that, being a mean-field approach, the CPA neglects both structural and electronic short-range order effects. Such short-range order effects are likely to be most strongly pronounced for small Pt concentrations ν . Therefore, our results in the low- ν limit should be tested against another method. An attempt at such a test of short-range electronic relaxation effects was performed by employing a fully relativistic real-space embedded cluster Green's function technique as combined with the SKKR method (for details, see Ref. [195]).⁴ Using a bulk hcp Co host, this method was applied to a cluster comprising a central Pt atom surrounded by Co atoms in a hcp arrangement. Using a total of 158 Co atoms around the central Pt atom in the cluster, the Co atoms were arranged geometrically as 36 , 2×30 , 2×19 and 2×12 Co atoms in layers 0 , ± 1 , ± 2 and ± 3 , respectively. This results in a sphere-like cluster, containing all the Co neighbours of the central Pt atom up to the third-nearest-

⁴These calculations were performed by Prof. L. Szunyogh and Dr. K. Palotás of the Budapest University of Technology and Economics, Hungary.

neighbour shell in the hcp structure (see Fig. 3.12). The site-resolved MAE contributions were calculated for the entire cluster.⁵ For comparison with Fig. 3.11, the aggregate MAE was calculated from these site-resolved MAE contributions including one, two and three neighbour shells (see Fig. 3.12), which, in turn, corresponds to including 12, 56 and 158 cobalt atoms, respectively. The corresponding values of \bar{K}_{Pt} for these three cases were calculated as 0.67 meV, -0.31 meV and -0.38 meV, respectively.³ A comparison with the values in Fig. 3.11 related to $2N + 1 = 3, 5$ and 7 for $\nu = 0.01$ (which is the closest approximation to the case of an impurity), reveals that both the trend and the magnitude of \bar{K}_{Pt} in Fig. 3.11 are in satisfactory agreement with the cluster calculations. This is despite the fact that the values of \bar{K}_{Pt} calculated for the cluster incorporate only an incomplete summation over sites in each atomic layer.

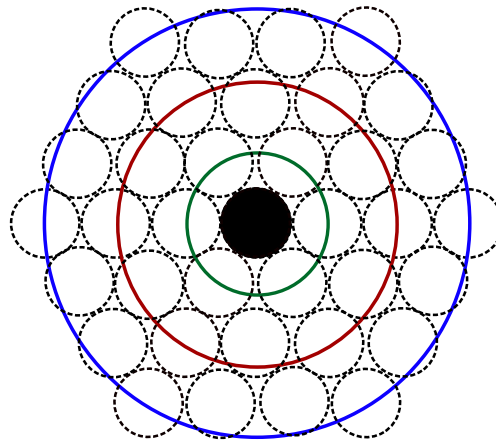


Figure 3.12: Illustration of the cluster used in the real-space calculations of the MAE contributions in the vicinity of a Pt impurity in Co. The black, filled circle corresponds to a Pt atom and the empty, dashed-line circles correspond to Co atoms. The green circle refers to interatomic distances of a_{NN} , the red circle refers to interatomic distances of $2a_{NN}$ and the blue circle refers to interatomic distances of $3a_{NN}$, where a_{NN} corresponds to the nearest-neighbour interatomic separation.

⁵These calculations were performed by Prof. L. Szunyogh and Dr. K. Palotás of the Budapest University of Technology and Economics, Hungary.

3.3 Stacking Faults in hcp Cobalt

3.3.1 Types of Stacking Fault

As is illustrated in Fig. 3.13, hexagonally close-packed atomic layers can be stacked either in an $\dots ABAB\dots$ sequence, yielding a hcp lattice structure or in an $\dots ABCABC\dots$ sequence, yielding a face-centred cubic (fcc) lattice structure [196]. In the hcp lattice structure, the stacking direction corresponds to the $[0001]$ axis of the lattice, whereas for the fcc lattice structure, the stacking direction corresponds to the $[111]$ axis of the lattice.

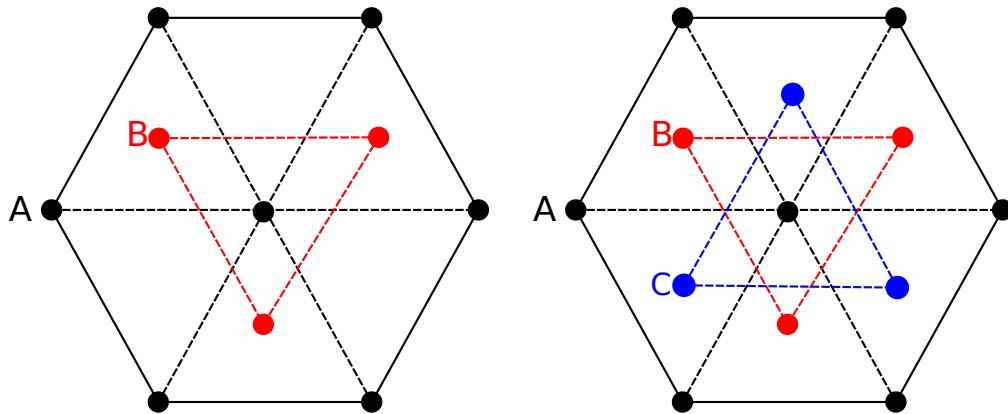


Figure 3.13: The $\dots ABAB\dots$ (left) and $\dots ABCABC\dots$ (right) stacking sequences of hexagonal layers, yielding the hcp structure and the fcc structure, respectively. In the hcp lattice structure, the stacking direction corresponds to the $[0001]$ axis of the lattice, whereas in the fcc lattice structure, the stacking direction corresponds to the $[111]$ axis of the lattice.

In a hcp lattice, a *stacking fault* is defined as an interruption in the $\dots ABAB\dots$ stacking sequence. One can of course visualise any number of such interruptions, however, some stacking faults will form more readily than others due to differences in the associated formation energies and formation mechanisms [167]. In line with previous studies of stacking faults in hcp metals [159, 197], in this study we considered the following four types of stacking fault, denoted in standard notation as I_1 , I_2 , E and T_2 [198, 199].

- I_1 (intrinsic): $\dots B A B A \text{ } \text{ } \text{ } C B C B \dots$
- I_2 (intrinsic): $\dots A B A B | C A C A \dots$
- E (extrinsic): $\dots A B A B \text{ } \text{ } \text{ } C A B A B \dots$

- T_2 (twin-like): $\dots A B A B \zeta B A B A \dots$

Here, the vertical line denotes the *fault plane*, i.e., the plane of reflection symmetry of the stacking fault [196]. In an *intrinsic* stacking fault (I_1 and I_2), one half of the crystal has shifted with respect to the other half [196]. The fault plane is correctly stacked with respect to the stacking sequence of either half, i.e., with respect to the stacking sequences on either side of the fault [196]. The stacking fault I_1 is a growth fault while the stacking fault I_2 is a deformation fault [159]. In the *extrinsic* stacking fault (E), one atomic layer has shifted so that it is incorrectly stacked with respect to the atomic layers on either side of it [196,200]. In the *twin-like* fault (T_2), the stacking sequence is reflected in the fault plane [159]. The location of the fault plane can be more easily seen from considering the type of stacking of each atomic layer with respect to its two neighbouring atomic layers, as follows in Table 3.1.

I_1 :	$\dots \underbrace{B}_{\text{hcp}} \underbrace{A}_{\text{hcp}} \underbrace{B}_{\text{hcp}} \underbrace{A}_{\text{hcp}} \underbrace{B}_{\text{fcc}} \underbrace{C}_{\text{hcp}} \underbrace{B}_{\text{hcp}} \underbrace{C}_{\text{hcp}} \underbrace{B}_{\text{hcp}} \dots$
I_2 :	$\dots \underbrace{A}_{\text{hcp}} \underbrace{B}_{\text{hcp}} \underbrace{A}_{\text{hcp}} \underbrace{B}_{\text{fcc}} \underbrace{C}_{\text{fcc}} \underbrace{A}_{\text{hcp}} \underbrace{C}_{\text{hcp}} \underbrace{A}_{\text{hcp}} \dots$
E:	$\dots \underbrace{A}_{\text{hcp}} \underbrace{B}_{\text{hcp}} \underbrace{A}_{\text{hcp}} \underbrace{B}_{\text{fcc}} \underbrace{C}_{\text{fcc}} \underbrace{A}_{\text{fcc}} \underbrace{B}_{\text{hcp}} \underbrace{A}_{\text{hcp}} \underbrace{B}_{\text{hcp}} \dots$
T_2 :	$\dots \underbrace{A}_{\text{hcp}} \underbrace{B}_{\text{hcp}} \underbrace{A}_{\text{hcp}} \underbrace{B}_{\text{fcc}} \underbrace{C}_{\text{hcp}} \underbrace{B}_{\text{fcc}} \underbrace{A}_{\text{hcp}} \underbrace{B}_{\text{hcp}} \dots$

Table 3.1: The type of stacking of each atomic layer with respect to its two neighbouring atomic layers.

3.3.2 The System

As already discussed in Section 2.3.3 and Section 3.2.1, the formalism of the SKKR implementation requires the system to be layered, i.e., the system needs to be periodic and infinite in the x - and y -directions. Moreover, the region of interest (the *interlayer*) needs to be positioned in between two semi-infinite bulk systems. Stacking faults are phenomena that lend themselves well to this formalism as the geometry of each atomic layer is unaffected; the stacking fault is merely a change in the stacking sequence of the atomic layers. Moreover, the original bulk stacking is retained on either side of the stacking fault. In line with the SKKR formalism, thus, we considered again an interlayer of $2N_L$ atomic layers of Co, positioned in between two semi-infinite bulk cobalt systems (cf. Section 3.2). At the centre of the interlayer, we introduced each one

of the different types of stacking fault in turn and performed our calculations. In the following, we refer to the fault plane as the zeroth atomic layer, $i = 0$. The two atomic layers adjacent to the fault plane are then indexed $i = \pm 1$, and so on. Note that in the case of the type I_2 stacking fault, the fault plane lies in between two atomic layers. Therefore, in the following, for type I_2 the atomic layers are indexed $\pm \frac{1}{2}, \pm \frac{3}{2} \dots$ rather than $0, \pm 1, \pm 2 \dots$.

In line with previous first-principles studies of stacking faults in close-packed metals, we ignored any structural relaxation effects (see, e.g., Ref. [167]). The effects of such relaxations are often negligible because atoms in the faulted part of the system tend to retain their close-packed coordination numbers despite the presence of the fault [159,200–204]. Due to the long-ranged nature of the effects of a stacking fault on the MAE, we required relatively large interlayers of $2N_L \approx 80$ (cf. Section 3.2.1). As mentioned already in Section 3.2.1, the computational effort associated with performing fully relativistic self-consistent calculations is significant. Therefore, we obtained self-consistent potentials and fields only for the 20 centremost atomic layers of the interlayer, $-9 \leq i \leq 10$, and used the bulk hcp Co potential for the atomic layers further away from the stacking fault ($i \leq -10$ and $i \geq 11$).

3.3.3 Stacking Fault Formation Energies

Before exploring how the stacking faults influence the MAE of bulk Co, we would like to gain an idea of their formation energy. Not only would this serve to verify our model against previous work, but it would also provide an estimate of the likelihood of formation of each stacking fault. The formation energy of a stacking fault is the difference in total energy between an unfaulted bulk system and a bulk system containing (only) the stacking fault. Within the SKKR-ASA scheme, the LSDA total energy can be cast into contributions related to individual atomic cells, E_i , comprising the kinetic energy, the intracell Hartree energy and the exchange-correlation energy, and into the two-cell Madelung (or intercell Hartree) energy, E_{Mad} [105]. It should be noted here that the presence of a stacking fault might cause a non-negligible shift in the Madelung energy due to charge redistributions. However, from our self-consistent calculations we found that ΔE_{Mad} is on the order of $\sim 0.5 \text{ mJ}\cdot\text{m}^{-2}$ for all four stacking faults. Since the typical stacking fault formation energies are approximately two orders of magnitude larger than this value, in the following we consider only the layer-resolved (cell-like) total energy contributions.

The layer-resolved total energy contributions across stacking faults I_1 , I_2 , E and T_2 are shown in Fig. 3.14 for $l_{max} = 2$.⁶ Reassuringly, the expected mirror symmetry about the fault plane ($i = 0$) is fulfilled to high accuracy and the bulk Co total energy is retained towards the edges of the interlayer ($i \rightarrow \pm 40$). In order to evaluate the formation energies, we considered the following cumulative sums of the layer-resolved offsets from the bulk Co total energy,

$$\begin{aligned}\Delta E_{I_1, E, T_2}(N) &= E_0 - E_{Co} + 2 \sum_{i=1}^N (E_i - E_{Co}) \\ \Delta E_{I_2}(N) &= 2 \sum_{i=\frac{1}{2}}^{N-\frac{1}{2}} (E_i - E_{Co}),\end{aligned}\quad (3.10)$$

where E_{Co} is the bulk Co total energy calculated within the SKKR method for the same set of parameters, -37839.45877 eV/atom. The formation energy of a given stacking fault X , $E_{\text{form}}^{(X)}$, is then defined as

$$E_{\text{form}}^{(X)} = \lim_{N \rightarrow \infty} \Delta E_X(N). \quad (3.11)$$

In reality, of course, N has to be some finite number at which $\Delta E_X(N)$ has converged to within error. The calculated values of $\Delta E_{I_1}(N)$, $\Delta E_{I_2}(N)$, $\Delta E_E(N)$ and $\Delta E_{T_2}(N)$ are shown in Fig. 3.15. It is evident from Fig. 3.15 that, in order to obtain $E_{\text{form}}^{(X)}$ to within error, we need to include nearly $N = 15$ atomic layers on either side of the given stacking fault. It should be noted that this long-ranged nature of the effect of the stacking fault on the total energy could have significant impact within nano-sized systems as the formation energy (and, consequently, the likelihood of formation) of a stacking fault could be slightly different depending on its location in relation to, e.g., other imperfections as well as surfaces and interfaces in the sample. From Fig. 3.15 we obtain the following formation energies, with a possible error of ~ 0.2 meV due to the Madelung energy not being included:

$$\begin{aligned}E_{\text{form}}^{(I_1)} &\approx 16 \text{ meV} \approx 40 \text{ mJ} \cdot \text{m}^{-2} \\ E_{\text{form}}^{(I_2)} &\approx 48 \text{ meV} \approx 122 \text{ mJ} \cdot \text{m}^{-2} \\ E_{\text{form}}^{(E)} &\approx 62 \text{ meV} \approx 160 \text{ mJ} \cdot \text{m}^{-2} \\ E_{\text{form}}^{(T_2)} &\approx 39 \text{ meV} \approx 100 \text{ mJ} \cdot \text{m}^{-2}\end{aligned}$$

⁶Unfortunately, for $l_{max} = 3$, a bug was discovered in the evaluation of the total energy. (Note that this has no impact on the evaluation of the MAE, which is evaluated from the band energies.) Due to time constraints, we therefore had to resort to $l_{max} = 2$ for the evaluation of stacking fault formation energies.

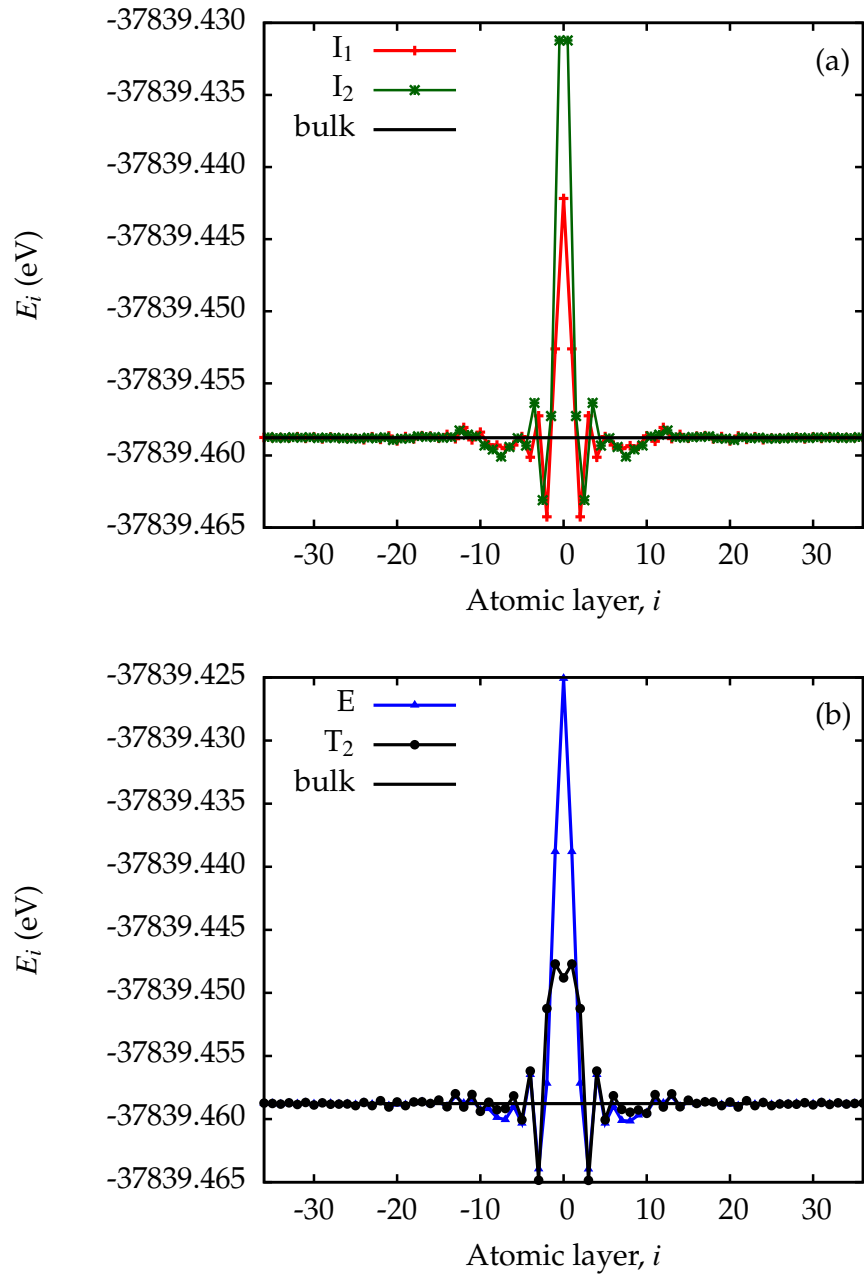


Figure 3.14: The calculated layer-resolved total energy contributions across stacking faults (a) I_1 (red +) and I_2 (green *) and (b) E (blue ▲) and T_2 (black ●). The black horizontal line corresponds to the total energy per atom of bulk hcp Co. The zeroth layer refers to the fault plane, i.e., the plane of reflection symmetry of the system. Solid lines connecting the symbols serve as guides for the eye.

for stacking faults I_1 , I_2 , E and T_2 , respectively. As expected, all stacking faults incur a positive change in the total energy, i.e., our calculations correctly identified the unfaulted crystal as energetically favourable to the faulted systems. In addition, the relative formation energies appear to reflect the number of fcc-like atomic layers present in each type of stacking fault (cf. Table 3.1). Accordingly, the intrinsic stacking fault type I_1 is the most likely to occur (in an equilibrated system) as it exhibits the lowest formation energy. Stacking faults of type E are the least likely to occur. Our overall results agree well with, e.g., Refs. [167, 168], wherein the formation energies of stacking faults in fcc metals are studied. In particular, Refs. [167, 168] report that the formation energies of extrinsic and intrinsic (deformation) stacking faults are generally significantly larger than the twin fault formation energy. Despite the difference in geometry, our calculated values for the hcp Co intrinsic stacking fault I_2 and the hcp Co extrinsic fault E are in reasonable agreement to those obtained in Refs. [167, 168] for fcc Ni (which is next to Co in the periodic table): $\sim 180 \text{ mJ}\cdot\text{m}^{-2}$ for the intrinsic (deformation) stacking fault and $\sim 150\text{-}180 \text{ mJ}\cdot\text{m}^{-2}$ for the extrinsic fault.

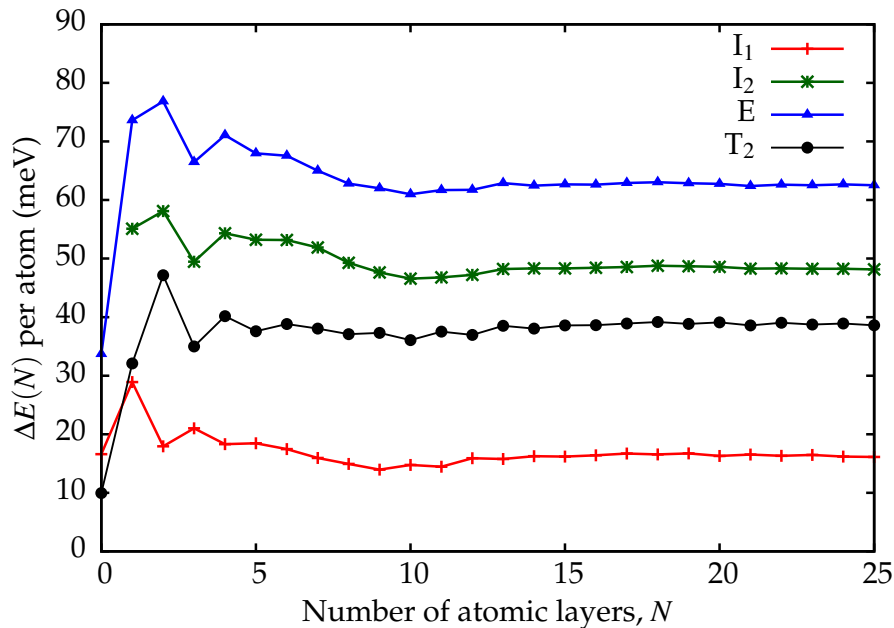


Figure 3.15: The calculated aggregate variation in the total energy of hcp Co for $l_{max} = 2$ due to the presence of a stacking fault of type I_1 (red +), I_2 (green *), E (blue ▲) or T_2 (black ●); see Eq. (3.10). Solid lines connecting the symbols serve as guides for the eye.

As an aside, it should be noted that, before performing the total energy calculations for the entire $N_L = 40$ interlayer presented in Fig. 3.14, we first performed calculations on a smaller interlayer in order to check for artefacts in the cal-

culated total energy caused by the use of the non-self-consistent, bulk Co potential for the outermost atomic layers of the $N_L = 40$ interlayer. In particular, we performed two calculations of the layer-resolved total energy contributions in an interlayer consisting of 32 atomic layers (i.e., $N_L = 16$), exhibiting a type I_1 stacking fault at its centre. In the first calculation, the potentials for all 32 atomic layers were obtained self-consistently, whereas in the second calculation, we obtained self-consistent potentials only for the 20 centremost layers, $-9 \leq i \leq 10$, and used the bulk Co potential for the remaining six atomic layers at either edge of the interlayer. We found that the use of the bulk potential for these layers only has a small effect (within 1 part in 10^6) on the total energy contributions of the layers $10 \leq |i| \leq 13$. The use of the bulk Co potential (rather than a self-consistent potential) for the outermost atomic layers thus appears not to have any significant effects on our evaluation of formation energies.

3.3.4 Layer-Resolved Contributions to the MAE

The layer-resolved MAE contributions across the four different stacking faults listed in Section 3.3.1 are shown in Fig. 3.16 for $l_{max} = 3$. We note that the reflection symmetry about the fault plane ($i = 0$) is well reproduced in the layer-resolved MAE contributions for all stacking faults. Furthermore, we note that all stacking faults induce long-ranged, jagged oscillations in the MAE contributions. Still, reassuringly, the MAE approaches the bulk Co MAE, $84.4 \mu\text{eV}$, towards the edges of the interlayer ($|i| \rightarrow 40$). For stacking faults I_1 , I_2 and T_2 , the MAE contributions become negative at the centre of the fault, favouring thus an in-plane easy axis in these layers. For the type E stacking fault, the layer-resolved MAE contributions near the centre are also reduced, although they do retain very small positive values.

3.3.5 Aggregate Variation in the MAE

We considered next the *total* effect of each stacking fault on the MAE. For this purpose, it is convenient to construct the following cumulative sums

$$\begin{aligned} \Delta K_{I_1, E, T_2}(N) &= D_0 - K_{Co} + 2 \sum_{i=1}^N (D_i - K_{Co}) \\ \Delta K_{I_2}(N) &= 2 \sum_{i=\frac{1}{2}}^{N-\frac{1}{2}} (D_i - K_{Co}), \end{aligned} \quad (3.12)$$

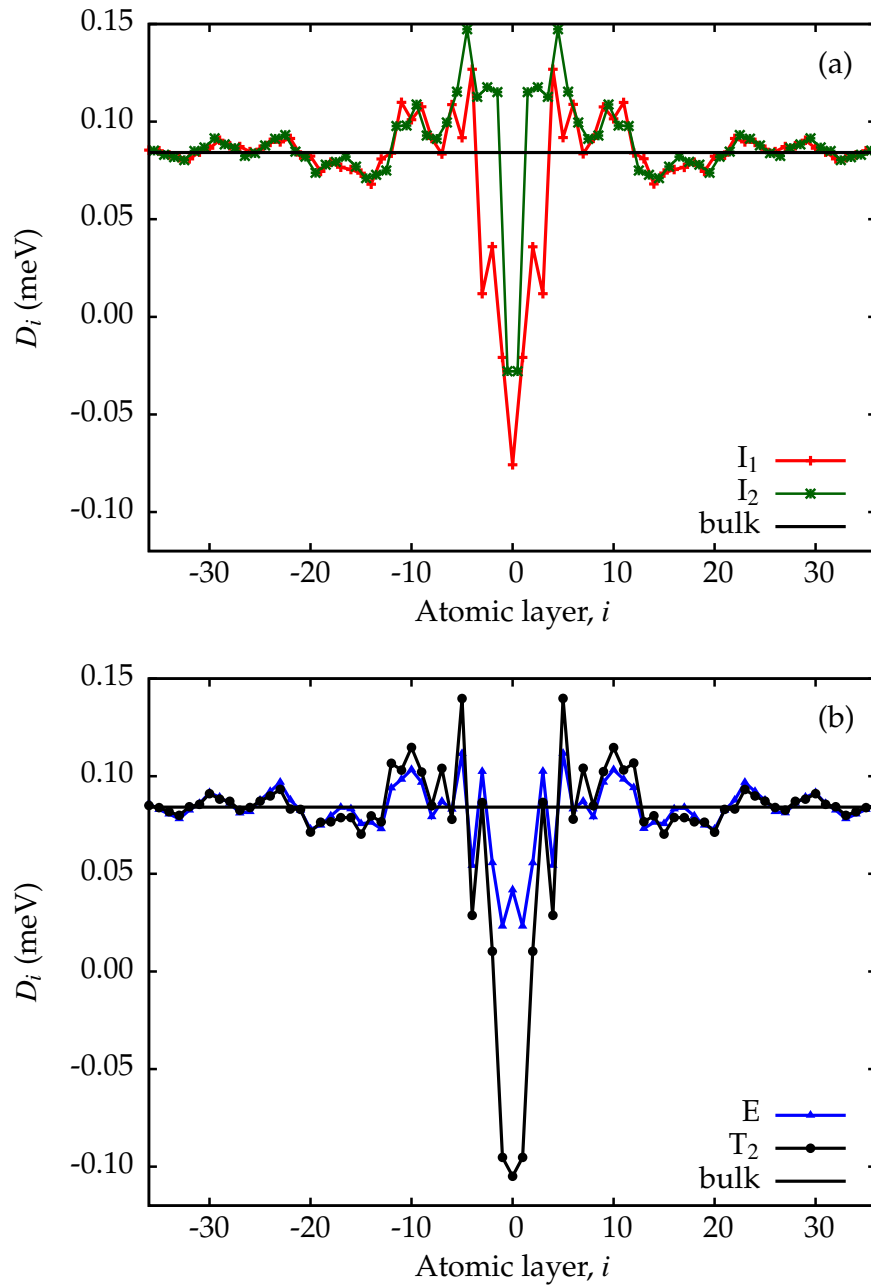


Figure 3.16: The calculated layer-resolved contributions to the MAE for stacking faults (a) I_1 (red +) and I_2 (green *) and (b) E (blue ▲) and T_2 (black ●). The zeroth layer refers to the centre of reflection symmetry of the system. The black horizontal line is the corresponding bulk MAE per atom, $84.4 \mu\text{eV}$ per atom. Solid lines connecting the symbols serve as guides for the eye.

where i is the atomic layer index, K_{Co} is the bulk Co MAE, $84.4 \mu\text{eV}$, and D_i are the layer-resolved MAE contributions from Fig. 3.16. The total effect of any given stacking fault X on the MAE is then $\Delta K_X = \lim_{N \rightarrow \infty} \Delta K_X(N)$. Fig. 3.17 shows $K_X(N)$ for the four different stacking faults as functions of N . For stacking faults I_1 , E and T_2 , the total number of layers included is $2N + 1$ whereas for stacking fault I_2 (where the plane of reflection symmetry lies in between two atomic layers), the total number of layers included is $2N$. $N = 0$ refers to the case where the sum has not been included at all, i.e., the value shown is simply the zeroth contribution, $D_0 - K_{Co}$.

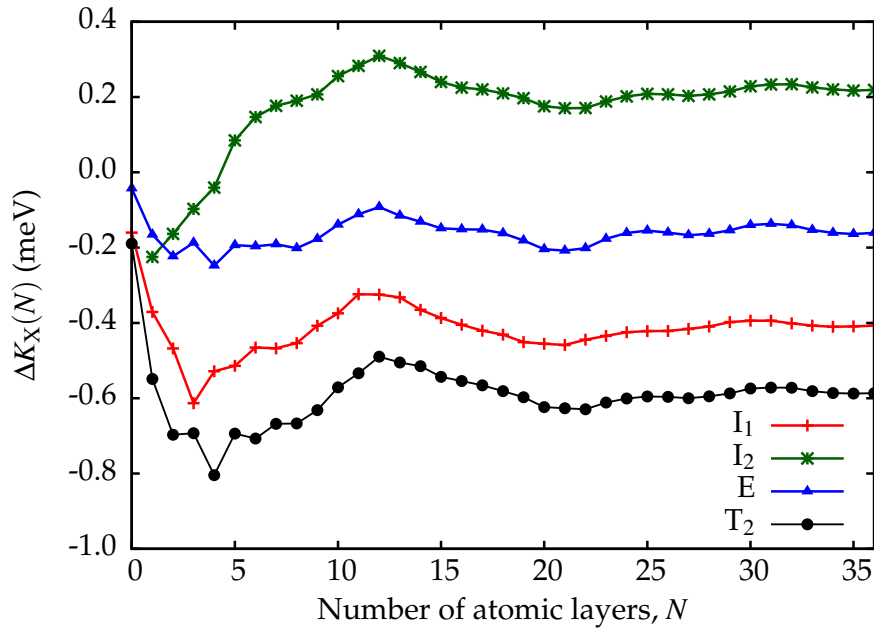


Figure 3.17: The calculated total change in the MAE as a function of the number of atomic layers N included in the sum in Eq. (3.12), for stacking faults of type I_1 (red +), I_2 (green *), E (blue ▲) and T_2 (black ●). Solid lines connecting the symbols serve as guides for the eye.

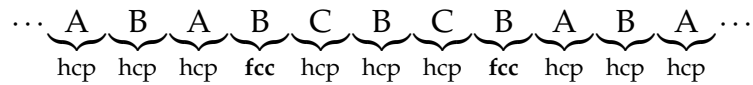
Surprisingly, for $N \geq 5$, the type I_2 stacking fault appears to enhance the MAE, i.e., it appears to strengthen the $[0001]$ easy axis. As seen from Fig. 3.16 (a), this is due to the positive MAE contributions induced by the I_2 stacking fault on its neighbouring atomic layers $|i| \geq 2$. These apparently outweigh the strongly negative MAE contributions induced in the centre of the I_2 stacking fault. This is an unexpected result as stacking faults are typically reported to lower the MAE [56]. It should however be noted that, of the stacking faults studied here, I_2 has the next highest formation energy and may, therefore, be less commonly observed in experiment. For the stacking faults I_1 , E and T_2 , the aggregate change in the MAE is negative. This is well in line with experimental observations, e.g., those of Ref. [56].

It is quite a remarkable feature that, as seen from Fig. 3.17, the total change in the MAE does not settle until at $N \approx 35$ atomic layers. This long-ranged behaviour could give rise to significant finite-size effects in nano-sized samples (cf. Section 3.2.4). Moreover, it might have consequences for the comparison of theoretical stacking fault studies to experiment, since expressing the calculated properties of one isolated stacking fault in terms of the stacking fault density now appears non-trivial.

3.3.6 Composite Stacking Faults

Experimentally, the presence of stacking faults is normally quantified in terms of the stacking fault density, which is partly a measure of how close together the stacking faults are located. As the simplest assumption, the change in the MAE due to the presence of a number stacking faults in a sample is approximated by the sum of the changes in the MAE due to each individual stacking fault. However, the long-ranged oscillations in the MAE caused by the presence of a stacking fault as observed in Section 3.3.4 indicates that the situation is far more complex.

As a first step towards investigating this, we considered the effect of introducing two stacking faults in the same system. In particular, we considered two stacking faults of type I_1 , separated by three atomic layers. In other words, we considered the composite stacking fault



In the following, we denote this composite stacking fault I_1I_1 . The separation of three atomic layers was chosen because three is often kept as the number of nearest-neighbour shells included in computational models of stacking faults (see, e.g., Ref. [56]). A double type I_1 stacking fault was chosen for a composite stacking fault primarily because, of the four types of stacking fault considered in this work, the type I_1 stacking fault exhibits the lowest formation energy (see Fig. 3.15) and is, therefore, more likely to be observed in experiment.

In Fig. 3.18, we show the layer-resolved deviations from the bulk Co MAE

across a system exhibiting the composite stacking fault I_1I_1 ,

$$\Delta D_i^{(I_1I_1)} = D_i^{(I_1I_1)} - K_{Co}, \quad (3.13)$$

as well as the layer-resolved deviations from the bulk Co MAE of two isolated type I_1 stacking faults centred on atomic layers $i = \pm 2$,

$$\Delta D_i^{(I_1+I_1)} = \Delta D_{i+2}^{(I_1)} + \Delta D_{i-2}^{(I_1)} = D_{i+2}^{(I_1)} + D_{i-2}^{(I_1)} - 2K_{Co}. \quad (3.14)$$

If $\Delta D_i^{(I_1I_1)}$ and $\Delta D_i^{(I_1+I_1)}$ were exactly equal for all atomic layers i , then the aggregate effect of the composite stacking fault would be additive, i.e., exactly twice that of an isolated type I_1 stacking fault. However, as is shown in Fig. 3.18, $\Delta D_i^{(I_1I_1)}$ and $\Delta D_i^{(I_1+I_1)}$ deviate significantly, particularly in the layers $|i| < 2$, i.e., in the layers separating the two stacking faults.

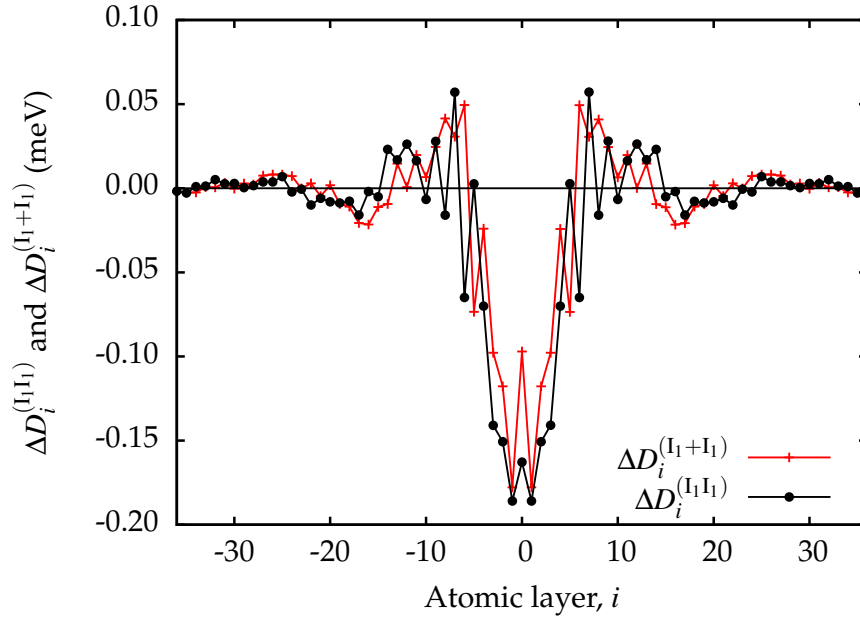


Figure 3.18: The calculated layer-resolved MAE deviations $\Delta D_i^{(I_1I_1)}$ and $\Delta D_i^{(I_1+I_1)}$ as defined in Eq. (3.13) and Eq. (3.14). Black \bullet represent the layer-resolved deviations $\Delta D_i^{(I_1I_1)}$ from the bulk Co MAE across the composite stacking fault. Red $+$ represent the layer-resolved deviations $\Delta D_i^{(I_1+I_1)}$ from the bulk Co MAE of two superposed Type I_1 stacking faults, centred on atomic layers $i = \pm 2$. Solid lines connecting the symbols serve as guides for the eye.

As is shown in Fig. 3.19, the aggregate change in the Co MAE due to the composite stacking fault I_1I_1 ,

$$\Delta K_{I_1I_1}(N) = D_0^{(I_1I_1)} - K_{Co} + 2 \sum_{i=1}^N \left(D_i^{(I_1I_1)} - K_{Co} \right), \quad (3.15)$$

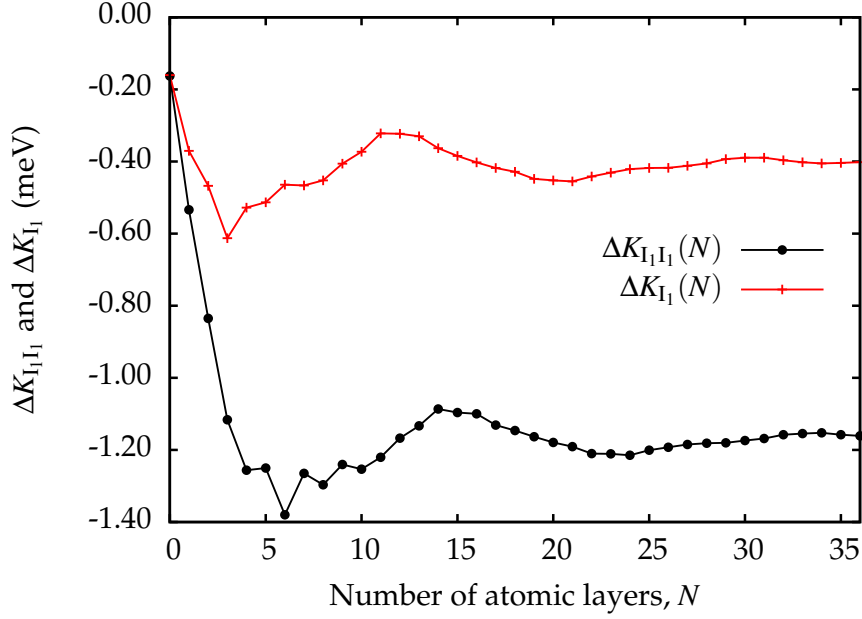


Figure 3.19: Comparison of the aggregate change in the MAE due to the presence of the composite stacking fault and the aggregate change in the MAE due to the presence of one isolated type I_1 stacking fault. Black \bullet represent the aggregate change in the MAE, $\Delta K_{I_1 I_1}$, of the composite stacking fault (see Eq. (3.15)) as a function of N . Red $+$ represent the aggregate change in the MAE, ΔK_{I_1} , of a single type I_1 stacking fault (see Eq. (3.12)) as a function of N . Solid lines connecting the symbols serve as guides for the eye.

appears to be approaching ~ -1.18 meV per atom as $N \rightarrow \infty$. This is almost three times the aggregate change in the Co MAE due to a single type I_1 stacking fault, which approaches ~ -0.40 meV per atom as $N \rightarrow \infty$ (Fig. 3.17 and Fig. 3.19). In other words, the two stacking faults interact to yield a stronger effect on the total MAE than what two isolated stacking faults of the same type would. This appears to be mainly due to the MAE contributions of the atomic layers located in between the two stacking faults. This could have significant consequences for predicting the resulting MAE in dynamical models used to explain experimental data. To draw any further conclusions, a systematic study of the stacking fault types and separations would be required. We expect that this study would be computationally intensive as interlayers (or supercells) of up to approximately 160 atomic layers would probably be required in order to enclose the MAE contributions from two stacking faults that are far enough apart not to interact.

3.4 Summary and Conclusions

In this Chapter, we have presented the results of our first-principles SKKR calculations of the local MAE contributions across two different bulk Co systems. The first system contained one atomic layer of $\text{Co}_{1-\nu}\text{Pt}_\nu$ of varying Pt concentration, ν , and the second system contained a stacking fault of varying type. Our work was inspired by previous experimental work (e.g., Refs. [56,151]) on the possible effects of localised Pt alloying and stacking faults on the MAE of Co-rich hcp CoPt alloy. Separating the direct effects on the MAE from any correlated or synergistic phenomena by means of theoretical models is of paramount importance to the interpretation of the experimental data.

We found that localised Pt alloying in bulk Co influences the total MAE of the system primarily through the induced changes in the MAE contributions on the Co sites. As a result, although the direct Pt contribution to the MAE was found to be positive for all Pt concentrations $0 \leq \nu \leq 1$, in the limit of $\nu \rightarrow 0$, adding a Pt atom to the system actually reduced the total MAE by approximately -1 meV, corresponding to approximately -3 mJ·m⁻². For large Pt concentrations $\nu \rightarrow 1$, on the other hand, the change in the MAE per Pt atom added was found to approach $+1.4$ meV. The cross-over from negative to positive aggregate changes in the MAE due to the addition of Pt was found to occur at $\nu \approx 0.1$. In relation to these calculations, we also demonstrated that the CPA, which is a mean-field approach, yielded results in reasonable agreement with real-space SKKR studies of an isolated Pt impurity in Co.

In terms of stacking faults, we considered two intrinsic faults (one growth fault and one deformation fault), an extrinsic fault, a twin-like fault and a composite fault consisting of two intrinsic growth faults. In good agreement with experiment, the intrinsic growth fault, the extrinsic fault and the twin-like fault were shown to reduce the MAE. While the intrinsic deformation fault actually enhanced the MAE, we found that this fault exhibits a relatively large formation energy; the intrinsic deformation fault may, therefore, be less commonly observed in experiment. The effect on the MAE by the composite stacking fault was shown to be synergistic, amounting to nearly three times the effect on the MAE of an isolated intrinsic growth fault. This result could have significant impact on the modelling of stacking faults as well as on the interpretation of experimental results.

Finally, our calculations showed that stacking faults and localised Pt alloying

both induce significant, long-ranged spatial oscillations in the Co MAE. These oscillations exhibit a typical length scale of ~ 10 nm (corresponding to ~ 30 atomic layers) and could, therefore, cause significant finite-size effects in determining the MAE of nano-sized systems.

With regards to future research, we propose a systematic study of the MAE as a function of the stacking fault separation. Since experimental results are normally quoted in terms of the stacking fault density and since closely spaced stacking faults appear to have synergistic effects on the MAE, the proposed study would be of significant importance for the verification of our results against experiment. Moreover, as the Pt concentration and the stacking fault density are often correlated in experiment, it would be of strong interest to investigate the combined effects of Pt alloying and stacking faults on the MAE of hcp Co, i.e., to combine the systems of Section 3.2 and Section 3.3. Finally, it should be noted that, throughout our work, we have neglected possible structural relaxation effects. The comparison of our results to real-space SKKR calculations suggests that structural relaxation effects around a Pt impurity are negligible and previous work suggests that structural relaxation effects due to the presence of a stacking fault are only very minor. Nevertheless, it would be prudent to at least check the robustness of our results against, e.g., variations in the atomic layer separations near the stacking fault or $\text{Co}_{1-s}\text{Pt}_s$ layer.

Structural and Compositional Effects in FePt

Recent developments in the field of magnetic recording technology have, as discussed in Chapter 1, enabled reductions in the effective write field. This allows for the use of (magnetically) harder recording media without loss of writability. As a consequence, a large fraction of current magnetic recording research is concerned with maximising the magnetocrystalline anisotropy energy (MAE) of the magnetic recording medium [38]. As illustrated in Fig. 4.1 (a), $L1_0$ FePt is a face-centred tetragonal (fct) structure, consisting of alternating Fe and Pt layers along the [001] direction. $L1_0$ FePt exhibits an extraordinarily large MAE, $\sim 5 \times 10^7 \text{ erg}\cdot\text{cm}^{-3}$ and it is therefore a material of great interest to the magnetic recording industry [38]. In particular, FePt is a strong candidate for use as a magnetic recording medium in devices based on heat-assisted magnetic recording (HAMR) technology [205]. In early 2012, Seagate Technology demonstrated the first prototype of a HAMR device and there is a strong drive to commercialise such a product [12].

One of the main obstacles for commercialisation is the fragility of the large MAE of FePt in real situations. This fragility is believed to stem partly from the fact that the antiferromagnetic (AFM) and ferromagnetic (FM) phases of FePt are very close in energy; even slight variations in the FePt unit cell shape, composition or chemical ordering (see Fig. 4.1) may impact drastically on the balance between these two phases [206, 207]. This imposes a fine balance between stabilising the FM state of FePt and maximising its MAE [206]. Moreover, while its large MAE is associated with its $L1_0$ phase, FePt also exhibits stable FePt_3 and Fe_3Pt phases as well as a chemically disordered, cubic phase (see Fig. 4.2) [208, 209]. Accordingly, FePt exhibits phase transitions with re-

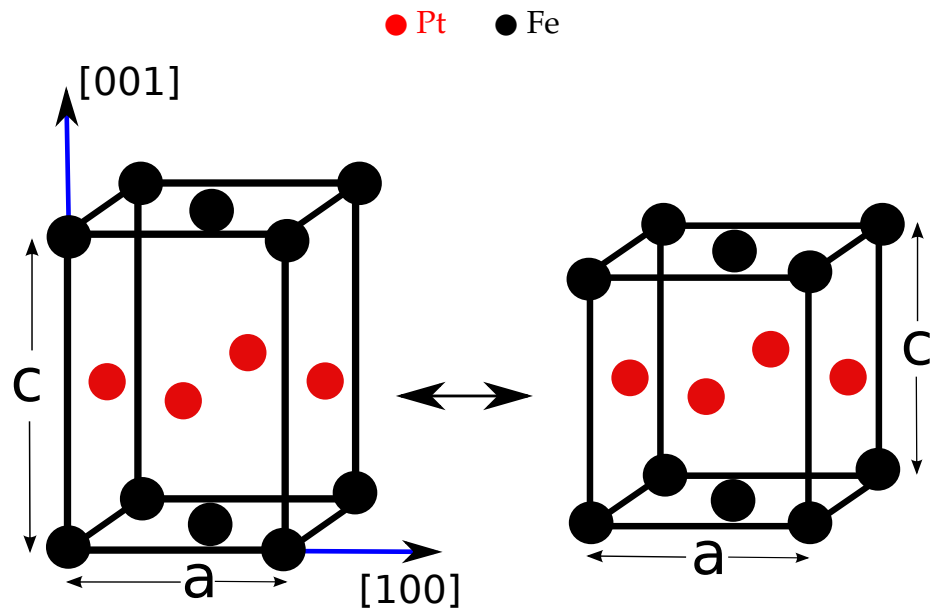
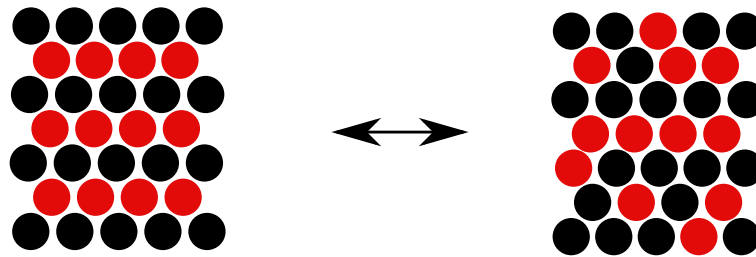
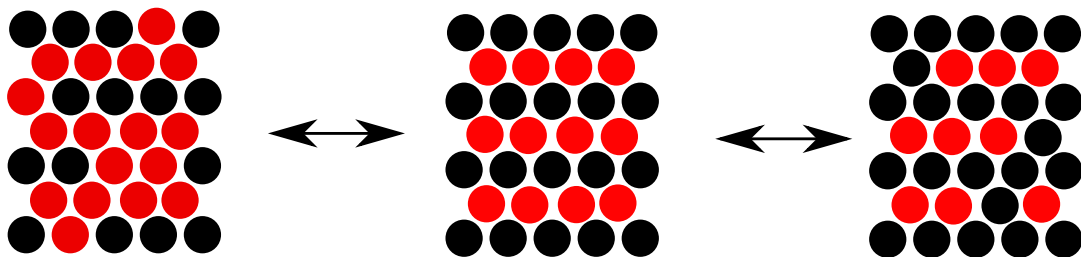
(a) Variation in unit cell tetragonality, c/a (b) Variation in chemical order, s (c) Variation in composition, x

Figure 4.1: Illustration of variations in (a) the unit cell tetragonality, quantified by the ratio of lattice parameters, c/a , (b) the level of chemical order, quantified by the chemical order parameter, s , and (c) the composition x of $\text{Fe}_x\text{Pt}_{1-x}$. Note that it is only for $x = 0.50$ that perfect layering (corresponding to the chemical order parameter $s = 1$) can be obtained.

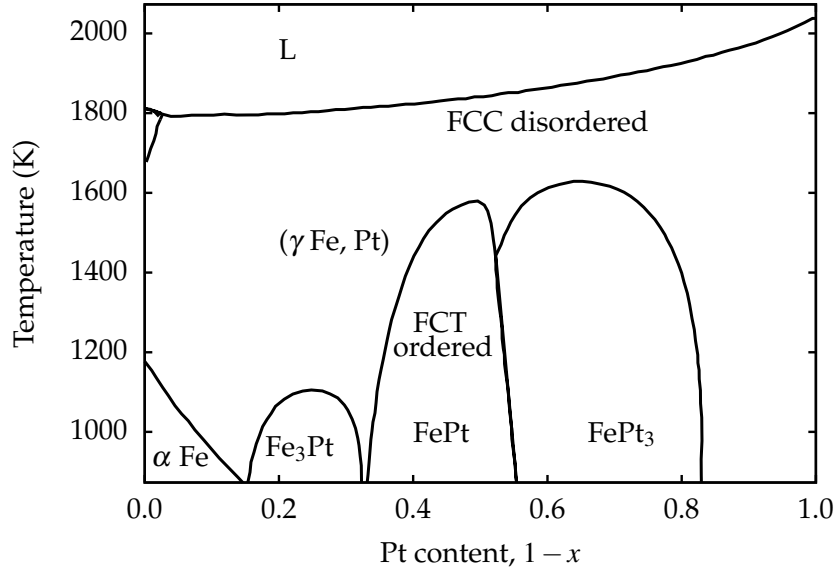


Figure 4.2: The phase diagram of FePt. Data from Refs. [208,209].

spect to composition, chemical order and unit cell tetragonality. Therefore, in order to commercialise FePt-based magnetic recording devices, it is of crucial importance to elucidate the effects of chemical disorder, composition and unit cell tetragonality on the FePt MAE. Consequently this is a very active field of research. For example, the large and negative effect of chemical disorder on the MAE of $\text{Fe}_{0.5}\text{Pt}_{0.5}$ has been confirmed both experimentally [210] and theoretically [55,171]. The effects of lattice strain have also been investigated theoretically [55,206,211–213] and experimentally [57,214]. However, in experiment, the degree of chemical order, s , the composition, x , and the tetragonality of the unit cell, c/a , are correlated through the choice of substrate upon which to grow the sample. Therefore, in reality, it may be impossible to explore the entire phase diagram of FePt in a commercially viable way. In order to maximise the FePt MAE in hard drive production it is, therefore, crucial to determine to which relative degree each of the factors in Fig. 4.1 influence the MAE of FePt and how these factors combine to yield a particular MAE.

In this Chapter, which is based on Refs. [55,213], we consider the isolated, combined and relative effects of tetragonality, chemical disorder and composition on the FePt MAE. In particular, we perform SKKR calculations of the FePt MAE in relation to two experimental publications, Refs. [57,58]. These two experimental studies investigate the effects of the substrate properties on the MAE of $\text{Fe}_x\text{Pt}_{1-x}$. In Ref. [57], variations in the tetragonality and the degree of chemical order are instigated by means of varying the sample-substrate lattice

mismatch across five $\text{Fe}_{0.5}\text{Pt}_{0.5}$ samples. In Ref. [58], variations in the tetragonality, the degree of chemical order and the composition are instigated by means of varying the substrate deposition temperature across three $\text{Fe}_x\text{Pt}_{1-x}$ samples. Our calculations were performed in order to (i) determine theoretically the effects on the MAE of each of the aspects in Fig. 4.1 in isolation, (ii) verify our calculations against the experiments in Refs. [57, 58], (iii) separate the contributions of the variations in tetragonality, chemical disorder and composition towards the experimental variation in the MAE in Refs. [57, 58] and (iv) investigate any effects of the substrate-induced correlation between the tetragonality, the chemical disorder and the composition. To that end, we first performed systematic SKKR-CPA calculations considering only one of the aspects in Fig. 4.1 at a time and then performed direct comparisons of our SKKR-CPA calculations to the experiments in Refs. [57, 58]. Finally, we considered the effects of surfaces on the FePt MAE in order to estimate the applicability of our conclusions to thinner FePt samples.

4.1 Computational Details

As described in detail in Chapter 2, we used Density Functional Theory (DFT) within the Local Spin Density Approximation (LSDA) as parameterised by Vosko *et al.* [102]. The effective potentials and fields were treated within the atomic sphere approximation (ASA). The MAE was evaluated using the magnetic force theorem [99] as discussed in Section 2.3.4. In particular, the MAE, K , was evaluated as the difference in band energies,

$$K = E_{\text{band}}^{[100]} - E_{\text{band}}^{[001]} \quad (4.1)$$

where $E_{\text{band}}^{[100]}$ ($E_{\text{band}}^{[001]}$) is the band energy of the FePt system when its magnetisation is polarised along the hard (easy) [100] ([001]) axis of the FePt lattice (see Fig. 4.1 (a)). In line with the force theorem, we evaluated the band energies for the two polarisation directions using the same underlying self-consistent potential. For FePt (and many other transition metal alloys), the self-consistent potentials and fields used in the evaluation of the MAE can be safely taken from self-consistent scalar-relativistic calculations [105, 215]. Accordingly, in the following, self-consistent potentials and fields were obtained using the scalar-relativistic approximation [216] and solving the Kohn-Sham-Dirac equation using a spherical wave expansion up to an angular momentum cut-off of $l_{\text{max}} = 3$. The size of the principal layers was set to four atomic layers. The energy integrations associated with Eq. (4.1) were performed by sampling 20

energy points along a semi-circular contour in the upper complex semi-plane (Fig. 2.1). At the energy point closest to the real axis, the k -integration was performed using 5050 k -points in the irreducible segment of the two-dimensional Brillouin zone. With respect to the screening, the number of energy points used and the number of k -points used, this ensures an accuracy of within 5 % of the MAE. However, our choice of angular momentum cut-off, $l_{max} = 3$, yields, at best, only ~ 15 % convergence of the MAE. Nevertheless, $l_{max} = 3$ is very commonly used for evaluating the magnetic properties of transition alloys [119, 120] and the 15 % convergence appears a reasonable trade-off as the computational effort scales as $(l_{max} + 1)^6$ [120].

The degree of chemical order is quantified in terms of a chemical order parameter [217, 218]. For a binary alloy A_xB_{1-x} , the chemical order parameter, s , is defined in terms of the occupation of the α -sites, which in a perfectly ordered phase would house only A-atoms, and the β -sites, which in a perfectly ordered phase would house only B-atoms. The chemical order parameter is defined to be $s = 1$ when all α -sites house A-atoms and all β -sites house B-atoms. Complete chemical disorder is characterised by $s = 0$ and signifies a situation in which the A- and B-atoms are uniformly distributed across the α - and β -sites. That is, the α - and β -sites are equally likely to house an A-atom and equally likely to house a B-atom. The definition of s is therefore

$$s = r_A + r_B - 1 = \frac{r_A - x}{y_\beta} = \frac{r_B - (1 - x)}{y_\alpha} \quad (4.2)$$

where y_α (y_β) is the fraction of α -sites (β -sites) relative to the total number of sites in the lattice and r_A (r_B) is the fraction of α -sites (β -sites) occupied by A-atoms (B-atoms).

There is a number of important aspects to note about the chemical order parameter in the case of FePt. In its maximally ordered $L1_0$ state (see Fig. 4.1 (a)), FePt consists of alternating Fe- and Pt-layers along the [001] direction; thus, $y_{Fe} = y_{Pt} = 0.50$. In the following, we refer to these two alternating layers as the nominal Fe layers and the nominal Pt layers, respectively. As illustrated in Fig. 4.1, perfect chemical order, $s = 1$, can only be achieved in $Fe_{0.5}Pt_{0.5}$, i.e., only for $x = 0.50$. Whenever $x \neq 0.5$ there will be either too few Fe atoms ($x < 0.5$) or too few Pt atoms ($x > 0.5$) to fill every other layer to yield the perfectly layered $L1_0$ structure. In general, for a given composition x of Fe_xPt_{1-x} , the maximum achievable chemical order parameter is $s = 1 - 2|0.5 - x|$. The parameter r_{Fe} is the fraction of sites in each nominal Fe layer that are occupied

by Fe atoms. Similarly, r_{Pt} is the fraction of sites in each nominal Pt layer that are occupied by Pt atoms. Note that for different compositions x , the same degree of chemical order s refers to different $r_{Fe,Pt}$, as illustrated in Fig. 4.3. Using the coherent potential approximation (CPA) [137,170], in the following we modelled chemically disordered Fe_xPt_{1-x} as a stack of alternating layers of $Fe_{r_{Fe}}Pt_{1-r_{Fe}}$ alloy and $Fe_{1-r_{Pt}}Pt_{r_{Pt}}$ alloy, as illustrated in Fig. 4.4.

4.2 Effect of Tetragonality on the MAE

Using the methods detailed in Section 4.1, we first investigated the effect of variations in the unit cell tetragonality, c/a , on the MAE of perfectly ordered bulk $L1_0$ $Fe_{0.5}Pt_{0.5}$. The unit cell volume was kept constant at 55 \AA^3 , consistent with the experimentally observed $L1_0$ $Fe_{0.5}Pt_{0.5}$ lattice parameters $a = 3.85 \text{ \AA}$ and $c = 3.71 \text{ \AA}$ [219,220] (see Fig. 4.1 (a)). Our results are shown in Fig. 4.5, which reveals a strongly positive dependence of the MAE on c/a in the range $0.9a \leq c \leq a$; the MAE increases by about 70 % from approximately 2.15 meV per formula unit (f.u.) at $c = 0.9a$ to approximately 3.70 meV/f.u. at $c = a$. These results are in excellent agreement with previous work, e.g., Refs. [211,221]. At the experimentally observed $c/a \approx 0.964$, we obtain an MAE of around 3.37 meV/f.u, also in good agreement with previous work [193,211,215,222]. It should be noted, however, that the range of c/a ratios in Fig. 4.5 may well span regions where the FePt FM state becomes unstable with respect to the AFM state (see, e.g., Refs. [206,207]). Moreover, the overlap of the atomic spheres within the ASA will change slightly with the change in c/a and the possible effects of this variation in overlap on the MAE are difficult to trace explicitly. However, the fact that our results are in good agreement with, e.g., the full-potential calculations of Lyubina *et al.* [211], suggests that such effects of variations in the overlap is small.

Before moving on, it should be noted that approximately 95 % of the MAE observed in Fig. 4.5 originates on the Fe sites. It is generally accepted that the strong spin-orbit coupling of Pt is a major component of the large MAE of FePt [28,193,211,223] and in the perturbative KKR calculations of Solovyev *et al.* [193], the largest MAE contributions are indeed observed on the Pt sites. This may appear contradictory, however, in Ref. [215], it is suggested that, due to the strong 3d-5d hybridisation of Fe and Pt, the spin-orbit contribution of Pt is in fact observed on Fe sites for non-perturbative approaches like ours.

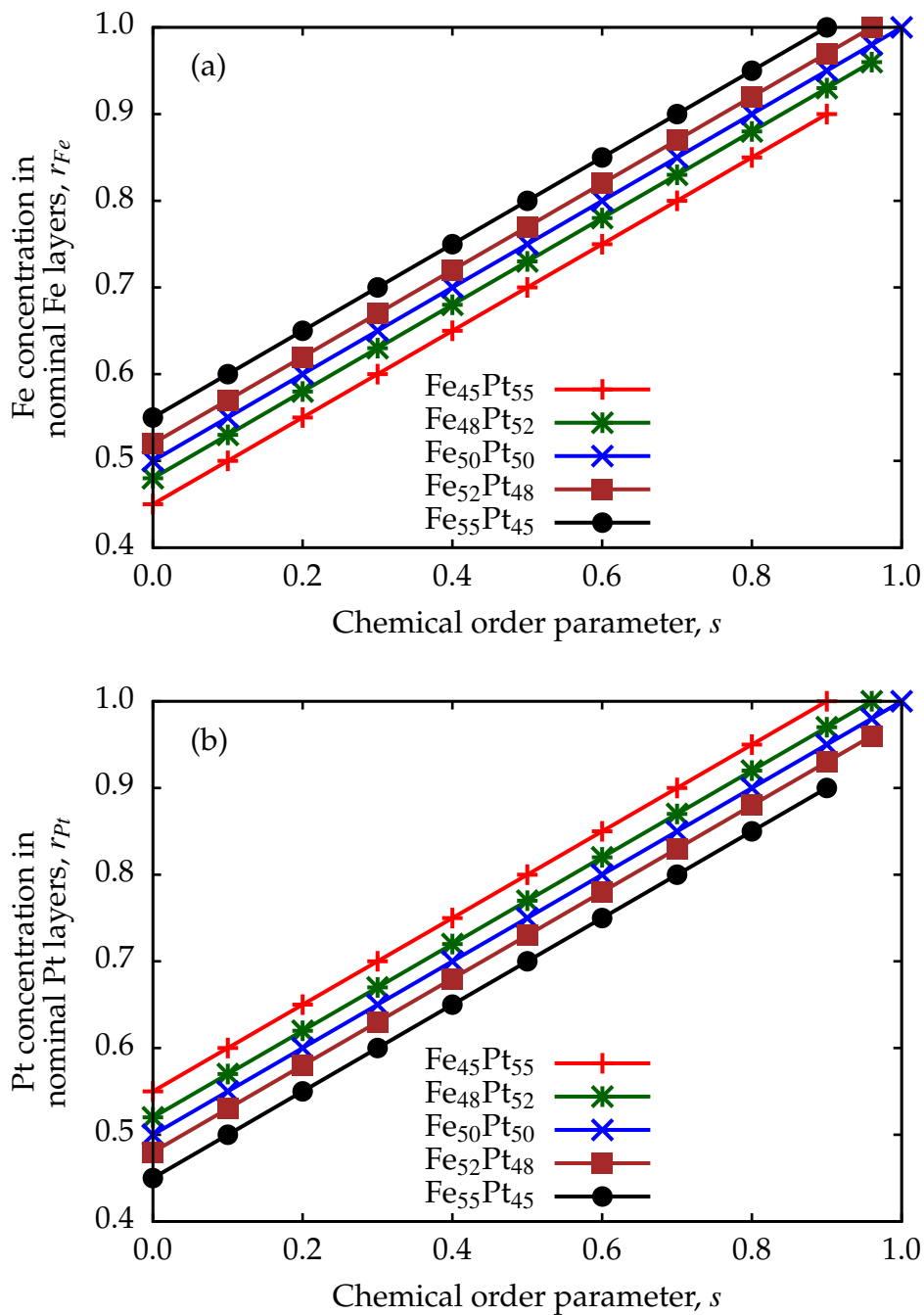


Figure 4.3: The variation of r_{Fe} and r_{Pt} with the chemical order parameter, s , for different compositions x of $\text{Fe}_x\text{Pt}_{1-x}$. Note that for compositions $x \neq 0.5$, the maximum achievable degree of chemical order is not $s = 1$, but $s = 1 - 2|0.5 - x|$.

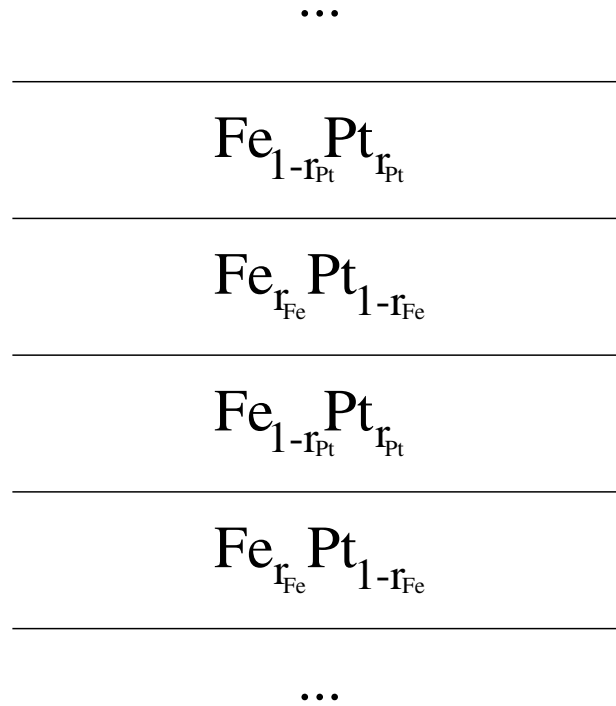


Figure 4.4: Using the coherent potential approximation, disordered $\text{Fe}_x\text{Pt}_{1-x}$ was modelled as a stack of alternating layers of $\text{Fe}_{r_{\text{Fe}}}\text{Pt}_{1-r_{\text{Fe}}}$ alloy and $\text{Fe}_{1-r_{\text{Pt}}}\text{Pt}_{r_{\text{Pt}}}$ alloy along the [001] axis.

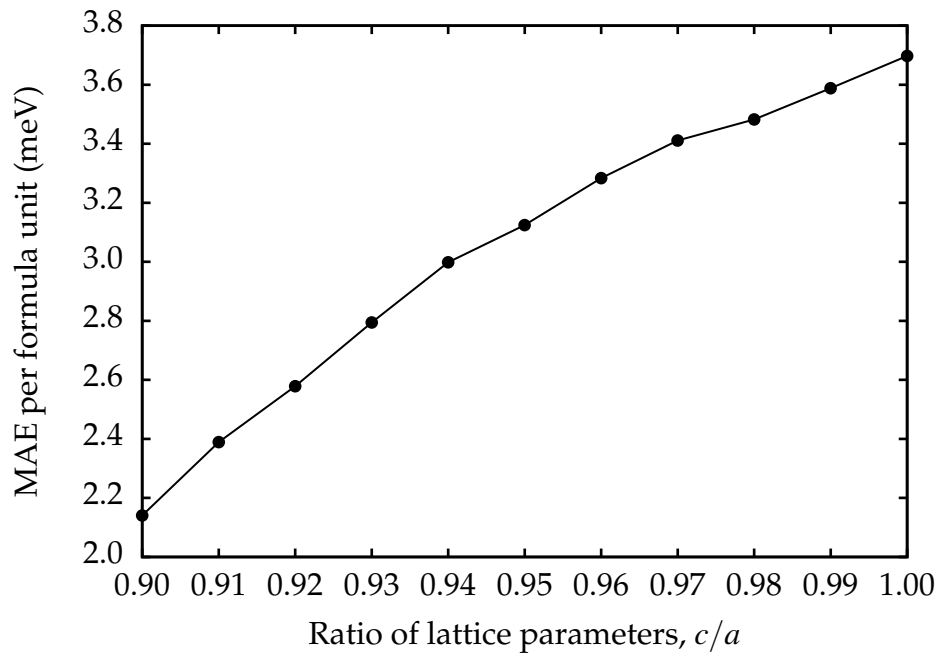


Figure 4.5: The calculated MAE per formula unit of perfectly ordered $\text{Fe}_{0.5}\text{Pt}_{0.5}$ as a function of the ratio of lattice parameters, c/a . The solid line connecting the symbols serves as a guide for the eye.

4.3 Effects of Chemical Disorder and Composition on the MAE

One of the main conclusions in the study by Barmak *et al.* [58] is that, with regards to achieving a large MAE, slightly Fe-rich $\text{Fe}_x\text{Pt}_{1-x}$ may be preferable to $\text{Fe}_{0.5}\text{Pt}_{0.5}$. In this Section we set out to explore the origin of this observation and to determine whether it is a pure effect of composition or whether it is also related to the chemical order of the sample as, in experiment, the two quantities will be correlated. To that end, we used the lattice parameters measured for one of the samples in Ref. [58], $a = 3.857 \text{ \AA}$ and $c = 3.706 \text{ \AA}$, and varied the chemical order parameter, s , and the composition, x , independently while keeping a and c constant. The results are shown in Fig. 4.6 for bulk $\text{Fe}_x\text{Pt}_{1-x}$ across the range of compositions $0.4 \leq x \leq 0.6$. Note that beyond this range of compositions, the L1_0 structure becomes unstable with respect to other phases [208, 209].

Our results in Fig. 4.6 are in good agreement with the conclusion of Ref. [58] inasmuch as for any given degree of chemical order, s , the MAE increases with increasing Fe content, x . However, even maximally ordered $\text{Fe}_x\text{Pt}_{1-x}$ with $x > 0.5$ cannot achieve the MAE of 3.31 meV/f.u. obtained for perfectly ordered $\text{Fe}_{0.5}\text{Pt}_{0.5}$. For a given composition x , we note a nearly quadratic dependence of the MAE on s . This strongly negative effect of chemical disorder on the MAE is in good accordance with previous work [53, 171]. At $s = 0$, the MAE becomes negative for $0.4 \leq x \leq 0.6$. This is in contrast to the zero MAE reported in Ref. [53] for completely disordered FePt. However, in Ref. [53], the unit cell is assumed to be cubic. Comparing our study with [53] thus suggests that the “residual” negative MAE which remains at complete chemical disorder is probably due to the lattice tetragonality, i.e., due to $a \neq c$. In experiment, where the lattice parameters cannot be frozen while varying the chemical order and composition, according to the FePt phase diagram (Fig. 4.2) we would expect the unit cell to become cubic as the chemical order deteriorates, thus removing this “residual” anisotropy.

In order to elucidate the origin of the variation in the MAE with the composition and the chemical disorder, we considered next the species-resolved contributions to the MAE. The MAE per formula unit can be decomposed into species-resolved MAE contributions D_γ^l as

$$K = r_{\text{Fe}}D_{\text{Fe}}^{\text{Fe}} + (1 - r_{\text{Fe}})D_{\text{Pt}}^{\text{Fe}} + (1 - r_{\text{Pt}})D_{\text{Fe}}^{\text{Pt}} + r_{\text{Pt}}D_{\text{Pt}}^{\text{Pt}} \quad (4.3)$$

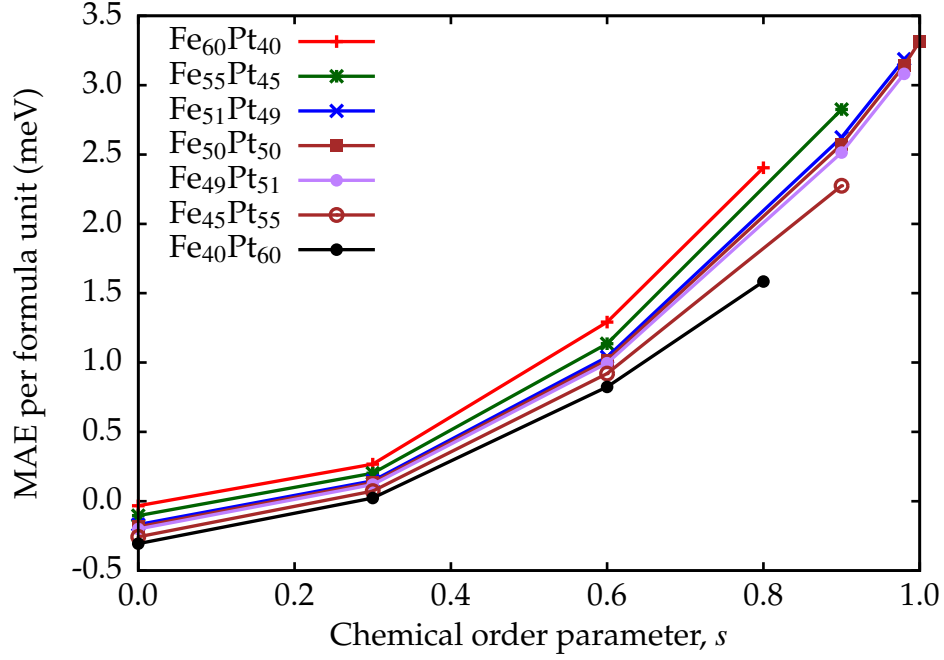


Figure 4.6: The calculated MAE per formula unit of $\text{Fe}_x\text{Pt}_{1-x}$ as a function of the chemical order parameter, s , for different compositions $0.4 \leq x \leq 0.6$. Solid lines connecting the symbols serve as guides for the eye.

where D_γ^l ($\gamma, l = \text{Fe or Pt}$) denotes the MAE contribution from an atom of species γ when positioned a layer which in a perfectly ordered $\text{Fe}_{0.5}\text{Pt}_{0.5}$ would have contained only atoms of species l . For the compositions $x = 0.4, 0.5$ and 0.6 , in Fig. 4.7 we show D_γ^l as a function of the chemical order parameter, s . In completely disordered FePt ($s = 0$), the nominal Fe layers and the nominal Pt layers are chemically identical. Therefore, at $s = 0$, the Fe contributions in both layers are equal and take on a small negative value for $s = 0$, which decreases in magnitude with increasing x and practically vanishes at $x = 0.6$. The Pt contributions, on the other hand, are nearly zero for all compositions x when $s = 0$. As the chemical order s increases, the Fe contribution in the nominal Fe layers at $s = 0.8$ increases rapidly with increasing x to about 1.8 meV, 2.0 meV and 2.2 meV for $x = 0.4, 0.5$ and 0.6 , respectively. For the fully ordered case, $x = 0.5$ and $s = 1$, $D_{\text{Fe}}^{\text{Fe}}$ even takes the value of about 3.15 meV, constituting 95 % of the total value of the MAE (3.31 meV/f.u.). In contrast, the Fe contribution in the nominal Pt layers decreases until $s \simeq 0.3$, then slightly increases and, for $x \geq 0.5$, reaches a small positive value (< 0.5 meV) at maximal chemical order. The magnitude of the Pt contributions remains almost negligible (< 0.15 meV) over the whole range of chemical order.

As indicated by the results in Fig. 4.7, the dominant contribution to the MAE in Eq. (4.3) is $r_{\text{Fe}} D_{\text{Fe}}^{\text{Fe}}$. It is, therefore, intuitive to replot Fig. 4.6 as a function

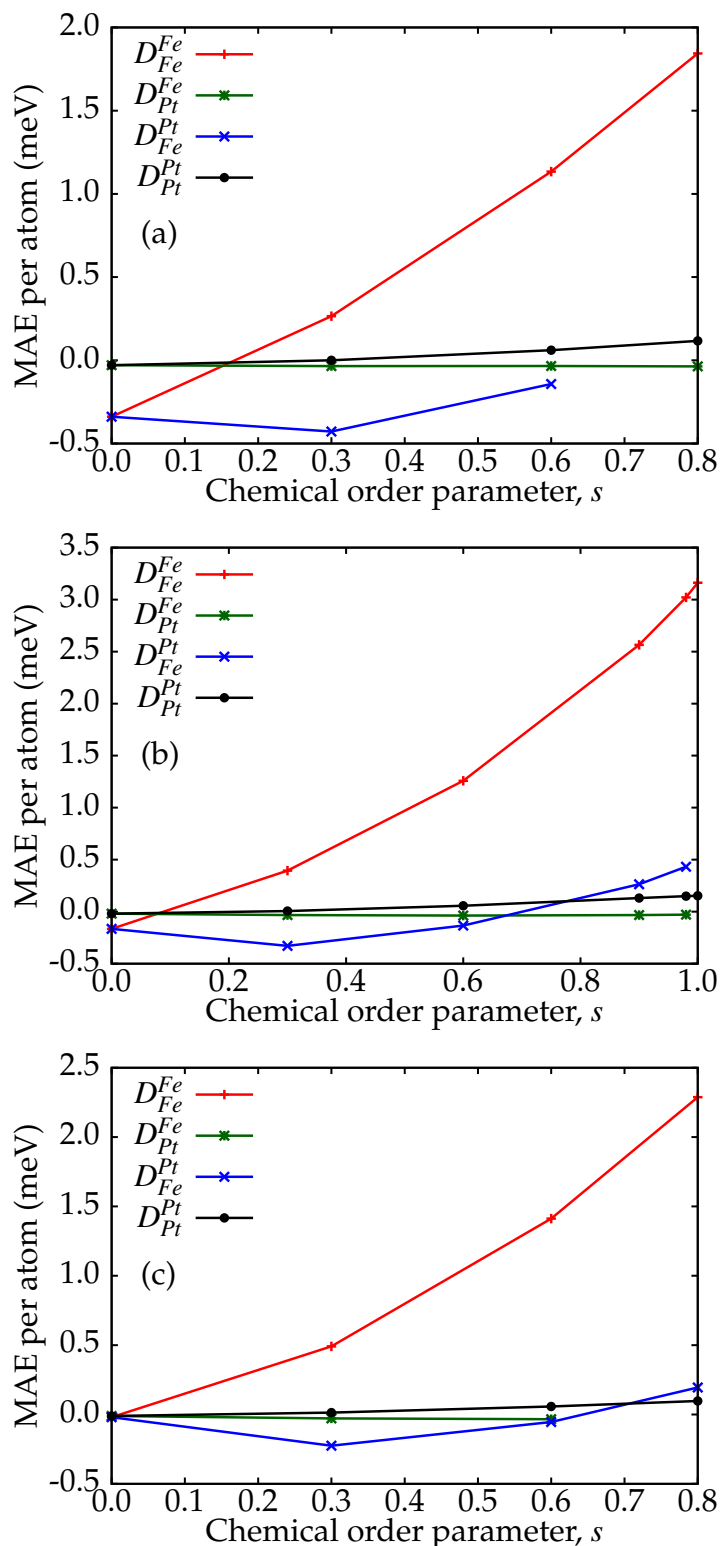


Figure 4.7: The calculated species-resolved MAE contributions as a function of the degree of chemical order s for compositions (a) $x = 0.40$, (b) $x = 0.50$ and (c) $x = 0.60$. Red + represent D_{Fe}^{Fe} , i.e., contributions from the Fe atoms in nominal Fe layers. Green * represent D_{Pt}^{Fe} , i.e., contributions from the Pt atoms in nominal Fe layers. Blue × represent D_{Fe}^{Pt} , i.e., contributions from the Fe atoms in nominal Pt layers. Black • represent D_{Pt}^{Pt} , i.e., contributions from the Pt atoms in nominal Pt layers. Solid lines connecting the symbols serve as guides for the eye.

of the Fe concentration in the nominal Fe layers, r_{Fe} . This interpretation of the MAE is shown in Fig. 4.8 for different compositions x . Here we see that the MAE per formula unit increases monotonically with r_{Fe} , as would be expected from the results of Fig. 4.7. Since $r_{Fe} = x + \frac{s}{2}$, the horizontal range of the curves in Fig. 4.6 is halved and, more importantly, the curves are shifted to the right by x . Therefore, for a fixed value of r_{Fe} , the order of the curves with respect to x is reversed as compared the order of curves for a fixed value of s in Fig. 4.6. The chemical order parameter, s , is related to r_{Fe} and the composition x as $s = 2(r_{Fe} - x)$ and a sample of composition x will thus reach $r_{Fe} = 1$ (i.e., a situation in which the nominal Fe-layers contain Fe only) at $s = 2(1 - x)$. Therefore, Fe-rich $\text{Fe}_x\text{Pt}_{1-x}$ will exhibit completely filled Fe layers, $r_{Fe} = 1$, at a smaller degree of chemical order, s , than $\text{Fe}_{0.5}\text{Pt}_{0.5}$, which requires $s = 1$ in order to exhibit completely filled Fe layers. This is why the Fe-rich $\text{Fe}_x\text{Pt}_{1-x}$ exhibits a larger MAE at a given degree of chemical order; systems with complete Fe layers will always exhibit a higher MAE than systems with $r_{Fe} < 1$. However, for maximally ordered, Fe-rich $\text{Fe}_x\text{Pt}_{1-x}$ the Pt layers are still only partially populated by Pt, i.e., $r_{Pt} < 1$. This partial population of the nominal Pt layers is also detrimental to the MAE although the effect on the MAE is weaker than that of r_{Fe} . This is why, at $r_{Fe} = 1$, the MAE increases as x decreases towards $x = 0.50$ (i.e., the minimum possible x for $r_{Fe} = 1$); r_{Pt} approaches a value of 1. Therefore, although the MAE increases with the Fe content, x , for a given degree of chemical disorder, perfectly ordered $\text{Fe}_{0.5}\text{Pt}_{0.5}$ still yields the largest possible MAE.

4.4 Comparison of Calculations to Experiment

So far, we have discussed the general effects of unit cell tetragonality, chemical disorder and composition on the MAE of FePt. In order to verify our calculations against experiment and in order to investigate any implications of the fact that the tetragonality, chemical disorder and composition are (typically) correlated in experiment, we consider next a direct comparison to the experiments in Refs. [57,58].

By way of introduction, one of the expected results of the experimental work in Ref. [57] was that the MAE would increase with the c/a ratio [224], which would be in line with our results in Fig. 4.5. However, as shown in Fig. 4.9, the experimental MAE values obtained in Ref. [57] fall off with increasing c/a ratio. Moreover, while the MAE magnitudes that we obtain in our SKKR calculations, ~ 3 meV/f.u., are in good agreement with previous theoretical

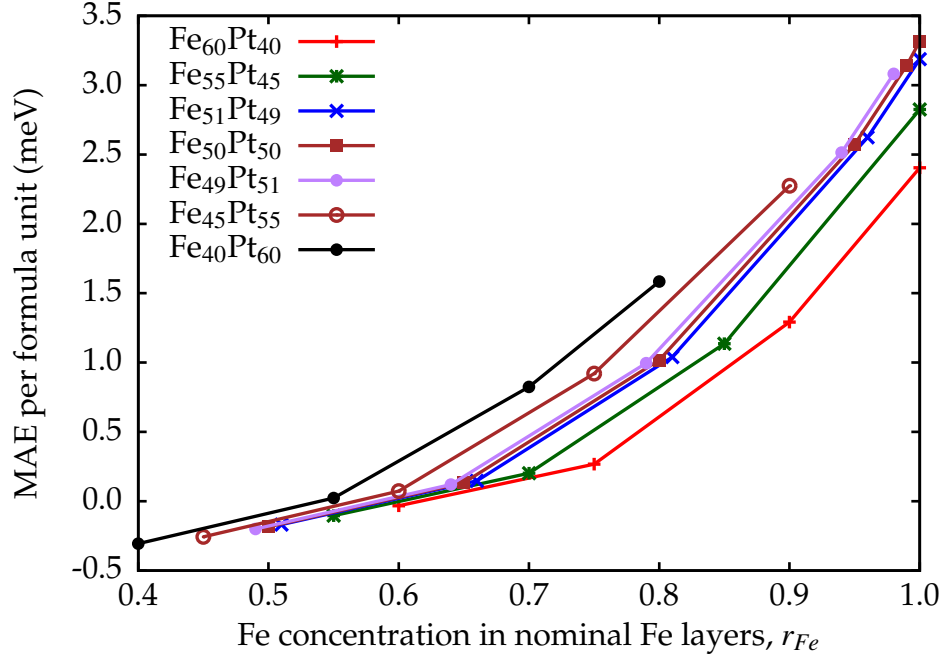


Figure 4.8: The calculated MAE per formula unit of $\text{Fe}_x\text{Pt}_{1-x}$ as a function of the Fe concentration in the nominal Fe layers, r_{Fe} , for different compositions $0.4 \leq x \leq 0.6$. Solid lines connecting the symbols serve as guides for the eye.

work [211,222] and low-temperature experiments [53], these MAE values are several times larger than the experimental MAE values in Ref. [57,58].

One of the most obvious sources of discrepancy between the SKKR calculations and experiment is the difference in temperature. Our calculations refer to a situation at 0 K, whereas the measurements of the FePt MAE in Refs. [57,58] were performed at room temperature. As the MAE should vanish at the Curie temperature, it is a rapidly decreasing function of temperature. Whilst the temperature dependence of the MAE of perfectly ordered $\text{Fe}_{0.5}\text{Pt}_{0.5}$ has been previously calculated in terms of different theoretical methods [28,125], here we did not attempt to carry out a similar process, since the required site-resolved information is not currently available for chemically disordered systems. Instead, for an approximate comparison with experiments at room temperature, we used the temperature scaling for perfectly ordered $L1_0$ $\text{Fe}_{0.5}\text{Pt}_{0.5}$ reported in the Langevin dynamics study of Mryasov *et al.* [28]. Fig. 4.10 is produced from the data of Ref. [28] and shows that the MAE, K , scales with temperature as $K_{T=293K} \sim 0.6K_{T=0K}$. However, as shown in Fig. 4.9, even after such an adjustment for temperature effects, the corresponding MAE-values obtained from SKKR are still much larger than those measured in experiment. In previous first-principles studies of FePt [211], difficulties in determining the order parameter experimentally has been suggested as one potential reason for this

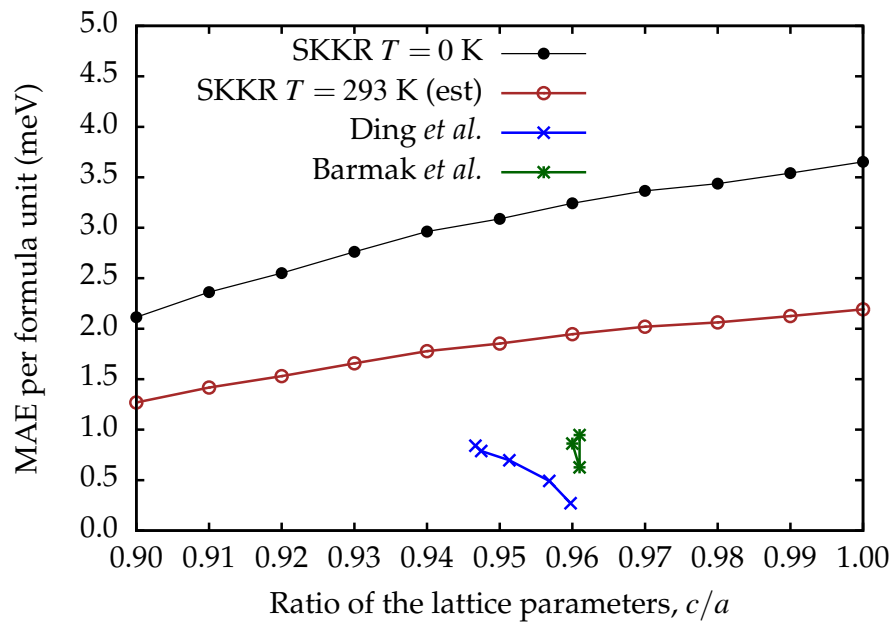


Figure 4.9: Comparison of SKKR calculations to experiment with regards to the MAE of perfectly ordered $\text{Fe}_{0.5}\text{Pt}_{0.5}$ as a function of the lattice parameter ratio, c/a . Black \bullet represent the SKKR MAE values from Fig. 4.5. Brown \circ represent the SKKR MAE values from Fig. 4.5 scaled down by a factor of 0.6 to account for temperature effects in accordance with Fig. 4.10. Blue \times represent the experimental data obtained by Ding *et al.* [57]. Green $*$ represent the experimental data obtained by Barmak *et al.* [58].

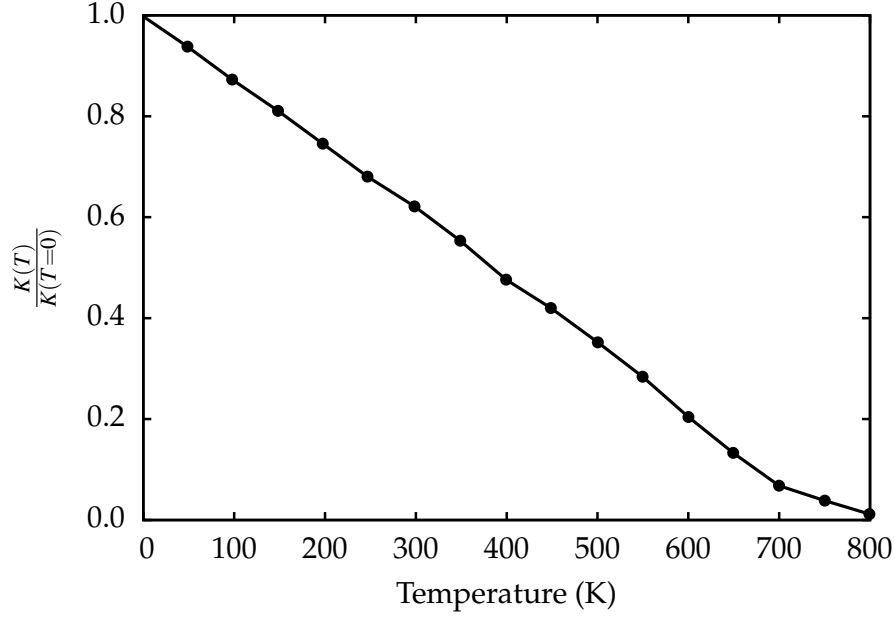


Figure 4.10: The scaling of the MAE of perfectly ordered $\text{Fe}_{0.5}\text{Pt}_{0.5}$ with temperature, according to the Langevin dynamics simulation study of Mryasov *et al.* [28]. Data from Ref. [28]

magnitude discrepancy. Moreover, as already mentioned, the change in the c/a ratio in Refs. [57,58] is correlated with changes in the unit cell volume, the degree of chemical order and the composition. In the following, we consider the effects of these factors for each of the two experiments in turn.

4.4.1 Comparison to Ding *et al.* [57]

Let us concentrate first on the study published by Ding *et al.* [57]. In this study, experiments were performed on five thin film $\text{Fe}_{0.5}\text{Pt}_{0.5}$ samples, each deposited on a different substrate [57]. A strong variation in the MAE with the degree of sample-substrate lattice mismatch was identified [57]. The substrate-sample lattice mismatch naturally imposes a variation in the lattice parameters across the samples, but also causes a variation in the degree of chemical order across the samples. In Ref. [57], the chemical order parameters were derived from the integrated X-ray diffraction intensities $I(001)$ and $I(002)$ ((xyz) denoting the plane of diffraction), through the relationship $s \sim \sqrt{I(001)/I(002)}$ (see, e.g., Refs. [210,214]) and normalising s to unity for the most highly ordered sample, i.e., sample no. 3. Unfortunately, due to an incomplete rocking curve¹ being obtained for the samples in Ref. [57], the normalisation process carries uncertain errors [224]. The experimental data of Ref. [57] are summarised in

¹A rocking curve plots the variation in X-ray intensity with diffraction angle.

Table 4.1. It should be noted that these samples are approximately 20 nm (60 formula units) thick, meaning surface effects are, in all likelihood, negligible [57,224].

Sample	a (Å)	c (Å)	s	$r_{Fe} = r_{Pt}$	K (meV/f.u.)	$I(001)/I(002)$
1	3.86673	3.69977	0.709	0.8545	0.493	1.000
2	3.88279	3.69387	0.978	0.9890	0.696	1.900
3	3.89752	3.68964	1.000	1.0000	0.841	1.985
4	3.89646	3.69175	0.965	0.9825	0.788	1.850
5	3.86954	3.71378	0.615	0.8075	0.271	0.7536

Table 4.1: Summary of experimental results from Ding *et al.* [57]; lattice parameters, a and c , chemical order parameter, s , magnetocrystalline anisotropy energy per formula unit, K , and diffraction intensity ratio, $I(001)/I(002)$. The Fe concentration in the nominal Fe layers, r_{Fe} , has been evaluated from Eq. (4.2) using that, for FePt, $y_{Fe} = y_{Pt} = 0.5$. Note that because $x = 0.5$ across all samples, $r_{Fe} = r_{Pt}$ across all samples.

Using the methods described in Section 4.1, we performed systematic calculations of the MAE of each of the FePt samples in Table 4.1. In order to separate the effects of the lattice distortion and the chemical disorder, we split our study into three stages. In our first set of calculations, the FePt samples were modelled as perfectly ordered $\text{Fe}_{0.5}\text{Pt}_{0.5}$ with lattice parameters according to Table 4.1. As can be inferred from Fig. 4.11, after scaling our calculated MAE values down by a factor of 0.6 in order to account for temperature effects, these values spread around 1.9 meV/f.u., showing only a very minor dependence on the variation of the lattice parameters. Moreover, this small variation between the samples is contrary to the experimentally observed trend. It appears, thus, that the lattice distortion alone cannot explain the trend of the MAE obtained in the experiment.

Subsequently, the degree of chemical order in each sample (as given in Table 4.1) was taken into account. The corresponding results are shown in Fig. 4.12. In accordance with earlier work [171] and our results in Section 4.3, chemical disorder drastically reduced the MAE; for sample no. 1 ($s = 0.709$) we obtained a value of 1.4 meV/f.u. and for sample no. 5 ($s = 0.615$) we obtained a MAE of 1.0 meV/f.u. In contrast, for samples no. 2 and 4, which exhibit a high degree of chemical order, the MAE was reduced by less than 10 %, and for sample no. 3 ($s = 1$) the MAE remained unchanged with respect to our previous calculations. Taking into account again a reduction by a factor of 0.6 due to temperature effects, it is obvious that the inclusion of chemical disorder has sig-

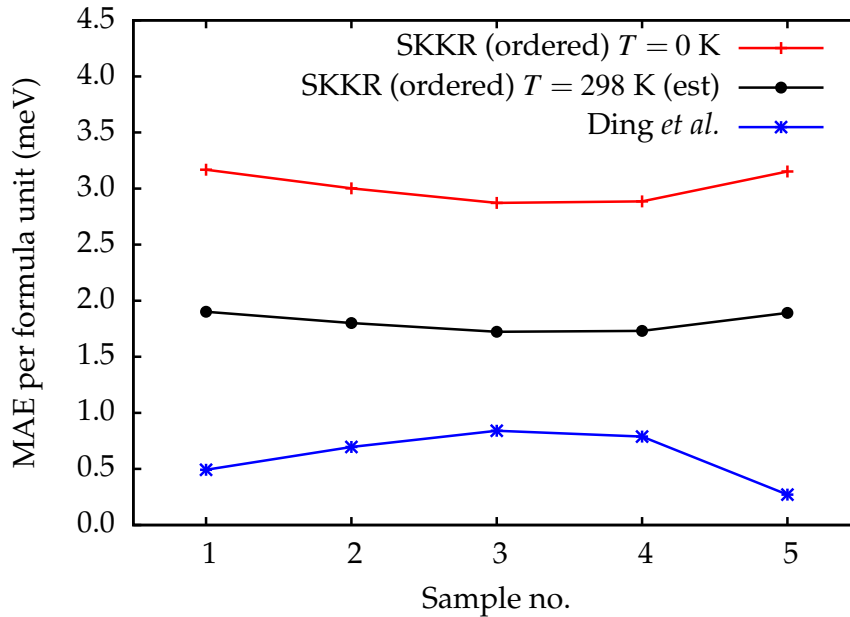


Figure 4.11: Comparison to the experiment in Ref. [57] for the calculated (SKKR) MAE per formula unit of perfectly ordered $\text{Fe}_{0.5}\text{Pt}_{0.5}$ using the experimental lattice parameters listed in Table 4.1. Red + represent the calculated MAE per formula unit for each of the FePt samples in Table 4.1 modelled as perfectly ordered $\text{Fe}_{0.5}\text{Pt}_{0.5}$. Black • represent the same values scaled down by a factor of 0.6 in order to account for temperature induced effects. Blue * represent the experimental values from Ref. [57]. Solid lines connecting the symbols serve as guides for the eye.

nificantly improved the agreement between experiment and theory: the trend of the MAE between the different samples is now correct and the magnitudes of the MAE are closer to the range reported by the experiment. In conclusion thus, the experimental MAE variation observed in Ref. [57] is, to a great extent, an effect of the variation in chemical disorder, s , across the samples.

As already mentioned, the chemical order parameters in Table 4.1 were derived from measured integrated diffraction intensity ratios [210, 214]. However, due to an incomplete rocking curve, the measured diffraction intensities, and thereby the experimentally obtained chemical disorder parameters, can only be considered approximate values. Furthermore, we note the assumption that the sample with highest MAE, sample no. 3, refers to perfect chemical order, $s = 1$. This appears a reasonable working hypothesis, but one worth investigating theoretically since it is central to the interpretation. This motivated us to perform a third set of calculations, in which the theoretical MAE was fitted to the experimental MAE using the degree of chemical order parameter, s , as a fitting parameter. In Fig. 4.13 (a), for each of the samples in Ref. [57]

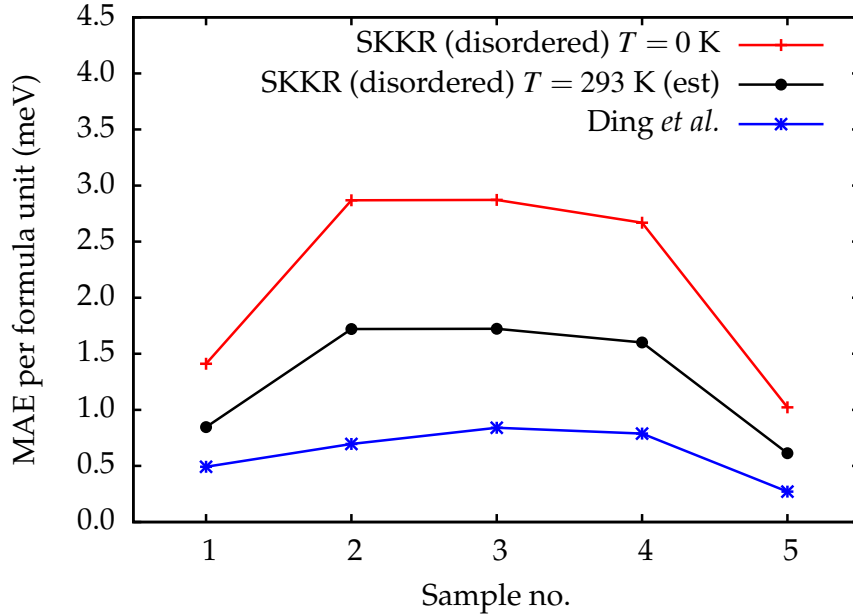


Figure 4.12: Comparison of the calculated MAE per formula unit of partially disordered $\text{Fe}_{0.5}\text{Pt}_{0.5}$ using the lattice parameters and the degrees of chemical order as obtained for each sample in Ref. [57], listed in Table 4.1. Red + represent the calculated MAE per formula unit for each of the FePt samples in Table 4.1 modelled as partially disordered alloys with the degree of disorder given by the experiment. Black • represent the same values scaled down by a factor of 0.6 in order to account for temperature induced effects. Blue * represent the experimental values. Solid lines connecting the symbols serve as guides for the eye.

we present the calculated MAE for an appropriate set of chemical order parameters. In Fig. 4.13 (a), the empty circles represent the intersection of our SKKR-CPA calculations with the experimental MAE values for each sample as indicated. This determines the best-fit order parameter that corresponds to the experimental MAE value. In accordance with the results of Section 4.3, for a given sample, i.e., for fixed lattice parameters, the theoretical MAE shows a non-linear dependence on s . Despite this non-linear dependence of the MAE on s , interestingly, there is a nearly perfect linear correlation between the experimental MAE and the best-fit chemical order parameters as indicated by the linear fit in Fig. 4.13 (b). Obviously, this remarkable linear behavior is the result of a subtle interplay of the dependence of the MAE on the lattice distortion and the chemical disorder. This may, however, be specific to the FePt samples in Ref. [57] rather than being a general property.

Finally, in Fig. 4.14 we summarise the experimental and theoretically predicted values of the chemical disorder parameter s . Across all samples, a smaller de-

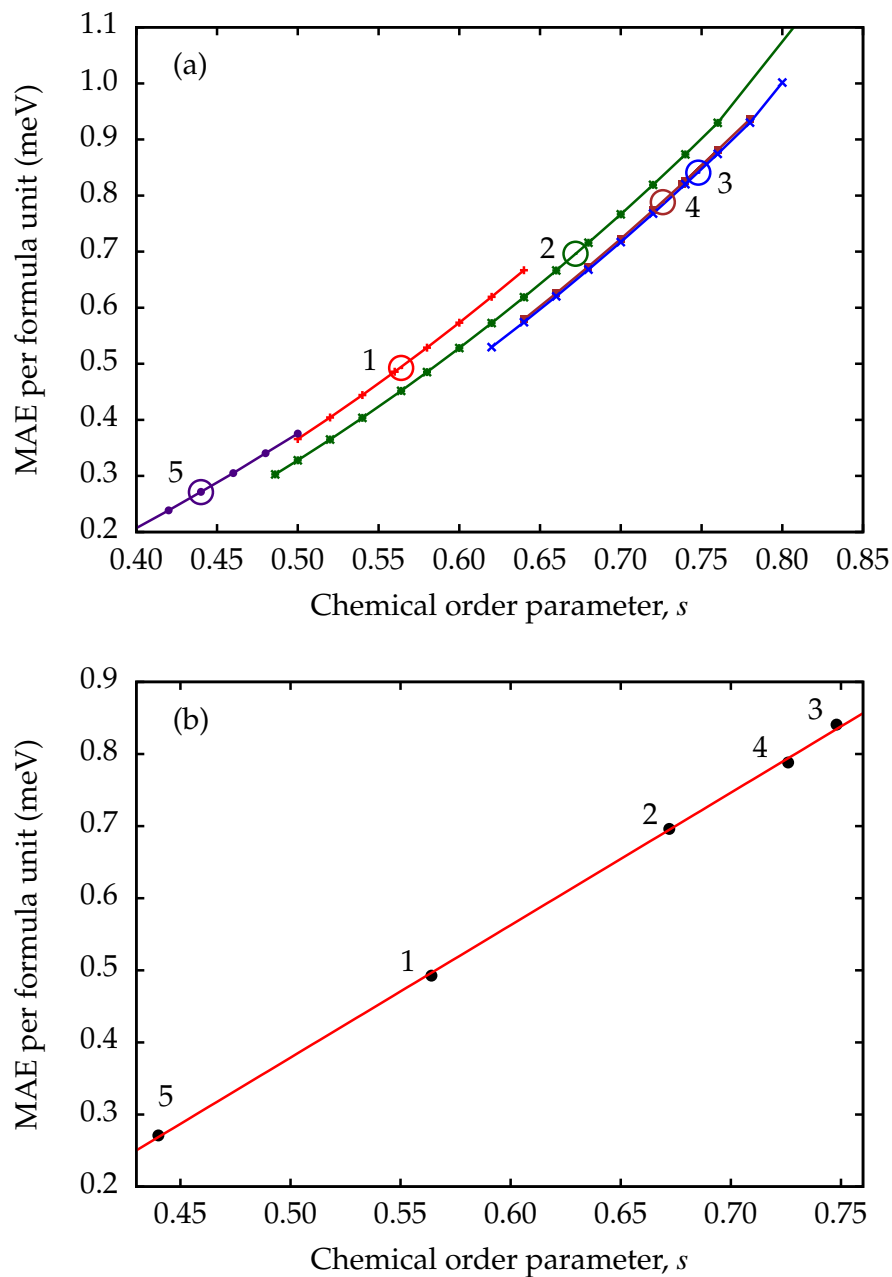


Figure 4.13: Top panel, (a): the MAE as a function of the chemical order parameter, s , for the five different sets of lattice parameters in Table 4.1, i.e., for samples 1 (red +), 2 (green *), 3 (blue x), 4 (brown ■) and 5 (purple ●). The large, empty circles show the intersection of these curves with the experimental MAE in corresponding colours for each sample. Bottom panel, (b): Black ● represent the intersections with the experimental MAE as indicated by the large circles in the top panel. The red line is a linear fit and the number labels refer to the sample numbers as given in Table 4.1.

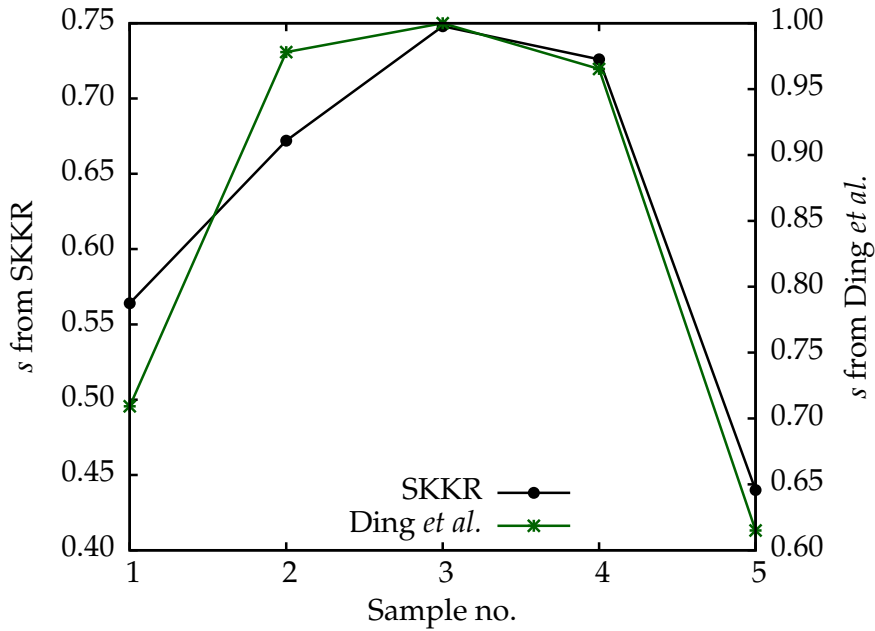


Figure 4.14: Comparison of the theoretically predicted degrees of chemical order (black ●) and the experimentally determined chemical order parameters from Ref. [57] (green *). Solid lines connecting the symbols serve as guides for the eye.

degree of chemical order was fitted than predicted by experiment. For samples 1, 2, 3, 4 and 5, the fitted $s \simeq 0.564$, 0.672, 0.748, 0.726 and 0.440, respectively. The fitted theoretical values of s follow a very similar trend to that of the experimental values, which is consistent with the normalisation of the chemical order parameter in the experiment being uncertain. The magnitude difference between the experimental data and the theoretical predictions could thus be an effect of the normalisation of the chemical order parameters. This is explored further in the next Section as in the experiment by Barmak *et al.* [58], the chemical order parameters were determined absolutely rather than relying on a normalisation assumption.

4.4.2 Comparison to Barmak *et al.* [58]

The experimental study of the MAE of $\text{Fe}_x\text{Pt}_{1-x}$ published by Barmak *et al.* [58] is similar to that of Ding *et al.* [57] inasmuch as the properties of the samples are controlled by, and correlated through, the properties of the substrate. However, in Ref. [58], the samples are distinguished from each other not only in terms of their lattice parameters, a and c , and their degrees of chemical order, s , but also in terms of their composition, x . Moreover, unlike Ding *et al.*, Barmak *et al.* do not rely on the normalisation assumption that the most highly ordered

sample is perfectly ordered. Instead, Barmak *et al.* obtain the absolute chemical order parameters from the integrated X-ray diffraction intensities by employing a number of corrections and obtaining the atomic form factors [225–228]. Comparing our SKKR-CPA calculations to the experimental results of Barmak *et al.* would thus hopefully shed light on whether the magnitude discrepancy observed in Fig. 4.12 could be attributed to the chemical order normalisation procedure employed in Ref. [57]. The experimental measurements of the FePt MAE performed by Barmak *et al.* [58] are summarised in Table 4.2.

Sample	x	a (Å)	c (Å)	c/a	s	r_{Fe}	r_{Pt}	K (meV/f.u.)
1	0.462	3.870	3.721	0.961	0.89	0.907	0.983	0.453
2	0.511	3.863	3.710	0.960	0.93	0.976	0.954	0.709
3	0.520	3.857	3.706	0.961	0.89	0.965	0.925	0.775

Table 4.2: Summary of experimental results from Barmak *et al.* [58]; lattice parameters, a and c , chemical order parameter, s , magnetocrystalline anisotropy energy per formula unit, K and composition, x . The Fe concentration in the nominal Fe layers, r_{Fe} , and the Pt concentration in the nominal Pt layers, r_{Pt} , have been evaluated from Eq. (4.2) using that $y_{Fe} = y_{Pt} = 0.5$.

Since the samples studied in Ref. [58] are approximately 50 nm thick, surface effects are probably negligible and we thus modelled the samples as bulk lattices. As shown in Fig. 4.15, we performed three sets of SKKR-CPA calculations. The first set only took into account changes in the lattice geometry across the samples in Table 4.2 (i.e., the variation in the lattice parameters), while assuming equiatomic composition, $x = 0.5$, and perfect long-range chemical order, $s = 1$. In this set of calculations, the SKKR-CPA trend in the MAE across the samples exhibits only minor variations ($< 3\%$) and is quite different to the experimental trend. This is in accordance with our comparisons to Ref. [57] in Section 4.4.1; the lattice strain itself has very little effect on the experimental trend in the MAE across the samples. (Note, though, that the spread in c/a across the samples is smaller in Ref. [58] than in Ref. [57].)

In the second set of calculations, we introduced the composition x as given in experiment, while keeping the degree of chemical order constant at $s = 0.89$. As seen in Fig. 4.15, this greatly improves the trend and magnitude of the MAE with respect to the experimental values, however, the relative change of the MAE from sample no. 1 to sample no. 2 is still underestimated ($< 15\%$) in comparison to the experiment ($\sim 50\%$). Finally, we included also the variation of chemical order as given in the experiment. Within this set of calculations, the relative change between samples no. 1 and sample no. 2 is improved ($\sim 30\%$),

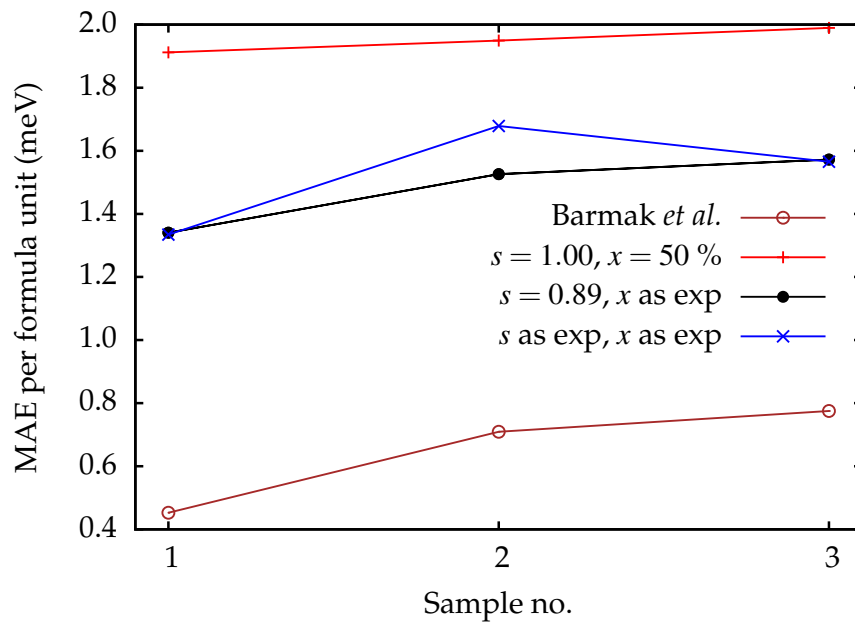


Figure 4.15: Comparison of the experimental MAE values of the $\text{Fe}_x\text{Pt}_{1-x}$ samples studied by Barmak *et al.* [58] and the calculated SKKR-CPA MAE values. Brown \circ represent the experimental values. Red $+$ represent SKKR MAE values using the experimental lattice parameters, but assuming $x = 0.5$ and $s = 1$. Black \bullet represent SKKR-CPA MAE values using the experimental lattice parameters and the experimental compositions x , but keeping $s = 0.89$. Blue \times represent SKKR-CPA MAE values using the experimental lattice parameters and the experimental values of x and s . Solid lines connecting the symbols serve as guides for the eye.

but, in contrast to the experiment, a slightly decreasing trend between sample no. 2 and sample no. 3 is predicted. Note, however, that these latter changes are within the range of both theoretical and experimental error. Thus we conclude that, in good agreement with our comparison to [57], also in Ref. [58] compositional effects dominate the experimental trend in the MAE.

Looking at the magnitude of the calculated values of the MAE versus the experimental values of the MAE in Fig. 4.15, even in the third set of calculations and despite employing the “temperature scaling” described in Fig. 4.10, the SKKR-CPA MAE values are about 2-2.5 times larger than the measured MAE values. In fact, the magnitude discrepancy in Fig. 4.15 is very similar to the magnitude difference observed in Fig 4.12. Unlike in the experiment by Ding *et al.* [57], here we are considering absolute experimental chemical order parameter values, albeit with large error bars. The similarity between our two comparisons thus suggests that the chemical order parameter normalisation procedure in Ref. [57] is a relatively minor contribution to the overall magnitude difference in Fig 4.12.

4.5 Effects of Vacuum Interfaces on the MAE

In this Chapter so far, we have discussed the effects of chemical disorder, unit cell shape and composition on the MAE of bulk FePt. As an aside, it would be interesting to investigate how well our conclusions would hold for smaller FePt samples by, e.g., evaluating the possible effects on the FePt MAE by the presence of a (001) surface. To this end, we constructed two semi-infinite FePt systems with a (001) vacuum interface: one system was terminated by an Fe layer and the other system by a Pt layer. We then performed SKKR calculations for these two systems using exactly the same techniques and parameters as detailed in Section 4.1, but resolving the total MAE, K , (cf. Eq. (4.1)) into the MAE contributions from each atomic layer,

$$K_i = E_{\text{band},i}^{[100]} - E_{\text{band},i}^{[001]} \quad (4.4)$$

Here, K_i is the MAE contribution per atom of atomic layer i and $E_{\text{band},i}^{[100]}$ ($E_{\text{band},i}^{[001]}$) is the band energy contribution per atom of atomic layer i for a system polarised along the [100] ([001]) axis of the FePt lattice.

As an approximation of the optimal geometry of the two semi-infinite systems, we used the optimised geometry of an FePt slab as obtained in CASTEP

[92–94, 229].² The geometry optimisation of this slab, which contained 12 atomic layers, was performed within the LSDA. The in-plane lattice parameters were kept fixed at $a = b = 3.760 \text{ \AA}$ (corresponding to the LSDA bulk FePt lattice parameters), while the distances between the atomic layers along the [001] axis were optimised to yield a minimum total energy [229]. The resulting atomic layer spacings, Δz , of the geometrically optimised FePt slab are shown in Fig. 4.16.

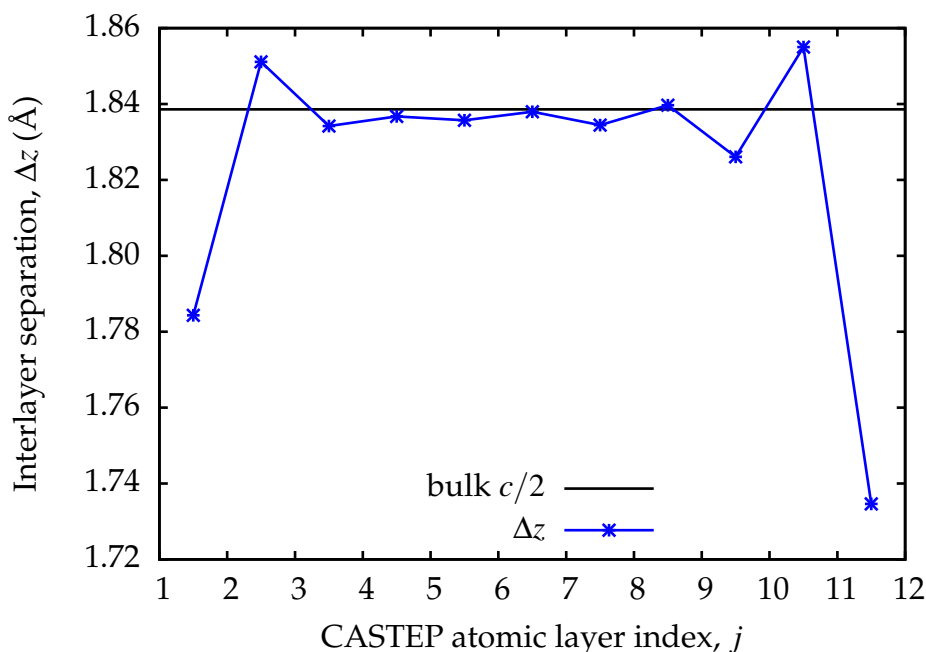


Figure 4.16: The relaxed atomic layer spacings along the [001] axis in an FePt slab as obtained in CASTEP by Hasnip [229]. Note that the FePt unit cell spans two atomic layers. Therefore, the atomic layer spacing corresponds to $c/2$.

In order to perform a direct comparison with the results of the previous Sections in this Chapter, the optimised geometry of Fig. 4.16 was scaled up isotropically to the experimental FePt lattice constant $a = b = 3.85 \text{ \AA}$. This appears to be the best compromise in being able to perform the comparison. While there exists other forms of the exchange-correlation functional which would probably yield lattice parameters closer to the experimental lattice parameters, such as the generalised gradient approximation (GGA) [230], for consistency we remained with the LSDA. As the FePt slab is Fe-terminated at one end and Pt-terminated at the other end, we considered each half of the optimised slab geometry in turn in order to construct the Fe-terminated ($1 \leq j \leq 6$ in Fig. 4.16) and Pt-terminated ($7 \leq j \leq 12$ in Fig. 4.16) semi-infinite systems. Beyond the

²The CASTEP geometry optimisation of the FePt slab was performed by Dr. P. J. Hasnip of the University of York, United Kingdom.

first six atomic layers of the semi-infinite FePt systems, the atomic layer spacings were kept constant and equal to the spacing of the two central atomic layers in Fig. 4.16.

In order to evaluate the surface MAE contribution in the Fe- and Pt-terminated systems, we considered the aggregate change in the MAE due to the presence of the surface, $\Delta K_{\text{surface}}$, as a cumulative sum of the layer-resolved offsets from the bulk MAE contributions, ΔK_i ,

$$\Delta K_{\text{surface}}(N) = \sum_{i=0}^{N-1} \Delta K_i \Rightarrow \Delta K_{\text{surface}} = \lim_{N \rightarrow \infty} \sum_{i=0}^{N-1} \Delta K_i \quad (4.5)$$

with

$$\Delta K_i = \begin{cases} K_i - K_{\text{Pt}}^{(\text{FePt})} & \text{for Pt sites } i \\ K_i - K_{\text{Fe}}^{(\text{FePt})} & \text{for Fe sites } i \end{cases} \quad (4.6)$$

where K_i is the layer-resolved MAE contribution, $K_{\text{Pt}}^{(\text{FePt})}$ ($K_{\text{Fe}}^{(\text{FePt})}$) is the Pt (Fe) MAE contribution per atom in bulk FePt and i is the atomic layer index, with $i = 0$ indicating the surface atomic layer and increasing i corresponding to atomic layers further away from the surface.

The layer-resolved offsets from the bulk MAE, ΔK_i , and the cumulative change in the MAE, $\Delta K_{\text{surface}}(N)$, are shown in Fig. 4.17. First we note that the surfaces induce long-ranged spatial oscillations in the MAE, spanning ~ 15 atomic layers. In terms of the contributions towards the value of $\Delta K_{\text{surface}}$ for the Fe- and Pt-terminated systems, we note that the Fe MAE offsets are dominant in both systems. In the Pt-terminated case, the Fe contributions are positive for the first two Fe layers, whereas in the Fe-terminated case, they are negative. In the Pt-terminated case, there is also a significant positive contribution from the surface Pt layer. As a consequence, the aggregate change in the MAE due to the Pt surface is positive, $\Delta K_{\text{surface}} \approx 1.6 \text{ meV} \approx 3.5 \text{ mJ}\cdot\text{m}^{-2}$. For the Fe-terminated system, on the other hand, $\Delta K_{\text{surface}}$ is negative and appears to settle at approximately $-2.75 \text{ meV} \approx -5.9 \text{ mJ}\cdot\text{m}^{-2}$. Pt-termination is known to be the more stable configuration [231], i.e., Pt tends to migrate towards the surface of a finite-size FePt system. Therefore, neglecting any chemical disorder effects associated with Pt migration processes, the results in Fig. 4.17 suggest that the presence of a surface in FePt will enhance the MAE. Relating these results back to our comparisons with the experiments of Refs. [57, 58] in Section 4.4.1 and Section 4.4.2, the surface enhancement of the total MAE would amount to no more than 0.05 meV per atom, well within experimental and theoretical error.

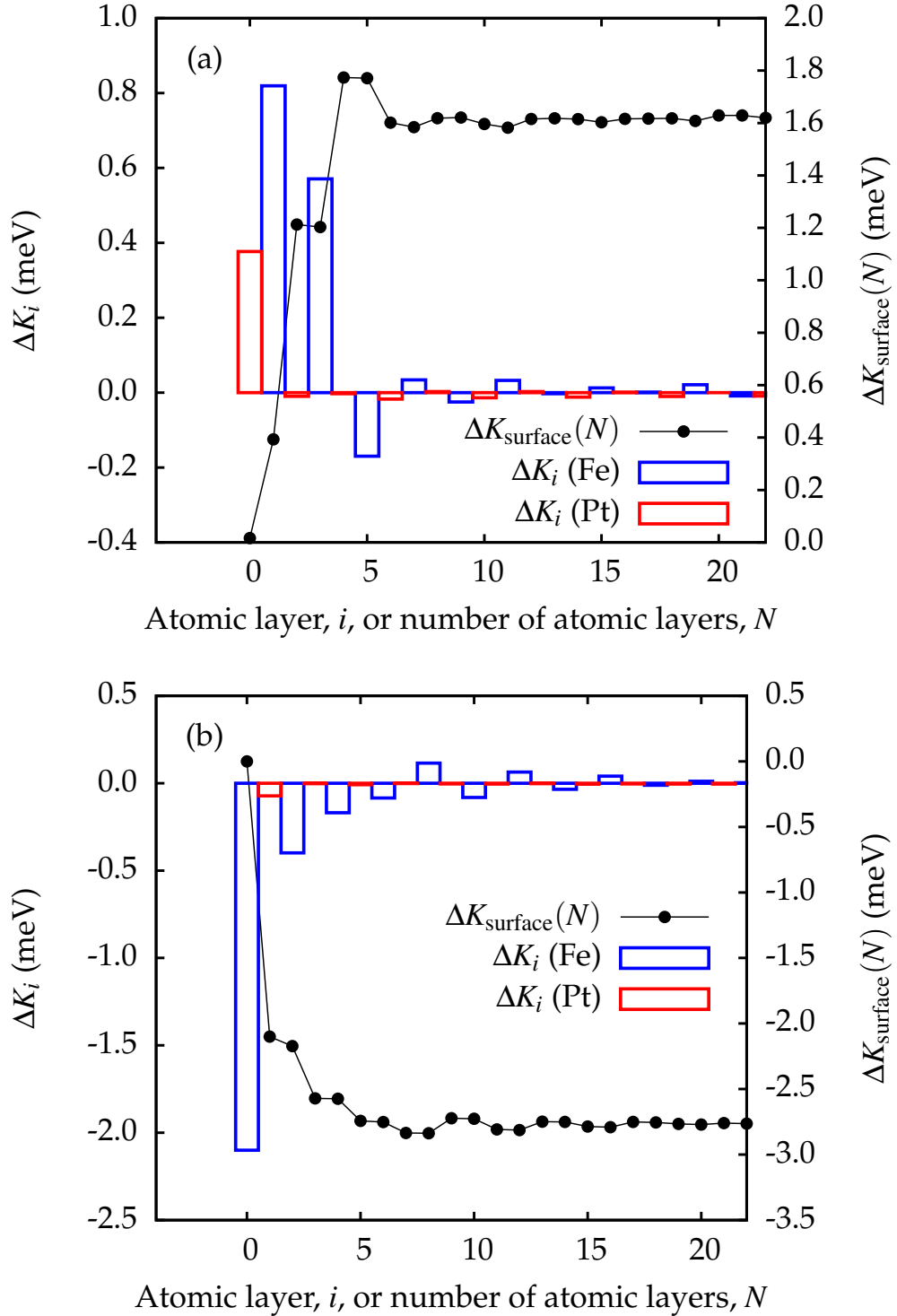


Figure 4.17: The change in the MAE of FePt due to the presence of the (001) surface in (a) a Pt-terminated semi-infinite FePt system and (b) an Fe-terminated semi-infinite FePt system. Blue boxes represent the deviation in the layer-resolved Fe MAE contributions from the bulk, $K_i - K_{\text{Fe}}^{(\text{FePt})}$. Red boxes represent the deviation in the layer-resolved Pt MAE contributions from the bulk, $K_i - K_{\text{Pt}}^{(\text{FePt})}$. The black \bullet represent the cumulative change in the MAE, $\Delta K_{\text{surface}}(N)$, as a function of the number N of atomic layers beneath the surface included in the sum. Solid lines connecting the symbols serve as guides for the eye.

4.6 Summary and Conclusions

The effects of any substrate-controlled properties of FePt, such as unit cell tetragonality, composition and degree of chemical order, on the magnetocrystalline anisotropy energy (MAE) of FePt are of significant interest to the magnetic recording industry. This is primarily because the production of FePt magnetic recording media entails striking a balance between maximising the FePt MAE and stabilising the ferromagnetic (FM) state of FePt in a commercially viable way. In this Chapter we have investigated the direct effects of the unit cell tetragonality, the composition and the degree of chemical order on the MAE of L1₀-like Fe_xPt_{1-x}, as well as the possible effects of substrate-induced correlations between these three factors. We have demonstrated good agreement of our calculations with the experimental trends of Refs. [57,58], although with a magnitude offset between our calculations and the experimental MAE values.

The main conclusion of this Chapter is that the MAE of FePt depends primarily on the concentration of Fe in the nominal Fe layers of the L1₀ structure, r_{Fe} . The more completely filled the nominal Fe layers are with Fe, the larger the MAE. In practice, this means that, at a given degree of chemical order, the MAE will increase with increasing Fe content. This is an important result as the Fe content is believed to stabilise the FM state of FePt [206]. Similarly, at a given composition, the MAE will increase with increasing degrees of chemical order. As a result of exhibiting complete Fe layers *and* complete Pt layers, perfectly ordered Fe_{0.5}Pt_{0.5} yields the largest possible FePt MAE. While we did find that the MAE increases with increasing c/a ratio, our comparisons to the experiments in Refs. [57,58] revealed that, due to the substrate-induced correlations between the experimental c/a ratio, composition and chemical order, the effect of r_{Fe} on the MAE often overrides completely any c/a -induced variation in the MAE. As an aside, we evaluated the effect on the FePt MAE by the presence of a (001) surface, obtaining $-5.9 \text{ mJ}\cdot\text{m}^{-2}$ and $+3.5 \text{ mJ}\cdot\text{m}^{-2}$ for Fe- and Pt-terminated systems, respectively. Surface effects in the MAE were observed in up to approximately 15 atomic layers beneath the surface.

With regards to improving our model, it would be of particular interest to address the magnitude difference between our results and room-temperature experiments such as those in Refs. [57,58]. (Note that KKR is already known to agree with low-temperature MAE measurements of highly ordered FePt [171].) Throughout our calculations, we have used the temperature scaling of the MAE for perfectly ordered Fe_{0.5}Pt_{0.5} as obtained by Mryasov *et al.* [28]. How-

ever, it is possible that variations in chemical disorder and composition may impact upon this scaling. It has been shown, experimentally [210] and theoretically [132], that the scaling of the MAE with temperature is steeper for disordered FePt, although not to the extent that it could explain the entire aforementioned magnitude difference. However, in addition, the experimental determination of the chemical order parameter is known to be difficult and often carries large error bars; given the strongly negative effect of chemical disorder upon the MAE, this could also contribute to the magnitude discrepancy. Finally, part of the magnitude discrepancy could potentially be attributed to limitations of our very method, such as, in particular, our choice of angular momentum cut-off, $l_{max} = 3$ (see, e.g., Ref. [119]). A natural next step for this work would be to investigate each one of the above issues in turn.

With regards to future research, it would be of significant interest to relate our results to the magnetic phase diagram of FePt. In particular, by mapping our results onto the loci in the FePt phase diagram that describe the combination of FePt properties resulting from lowest-cost production methods, we believe that our work could be a significant contribution in optimising the production of FePt magnetic recording media. Another important aspect is the mapping of our results onto effective spin Hamiltonians (see, e.g., Ref. [28]) for the construction of multiscale FePt models. This mapping is, however, non-trivial as, due to the strong 3d-5d Fe-Pt hybridisation, our non-perturbative SKKR calculations relate the main part of the MAE to the Fe sites, despite the fact that the main contribution to the MAE comes from the spin-orbit coupling of Pt [215]. Moreover, mapping SKKR-CPA results onto an effective Hamiltonian presents further difficulties as it constitutes mapping mean-field results onto a model of localised spin moments. Nevertheless, we hope to see these issues addressed and resolved, perhaps by reformulating the effective Hamiltonian proposed by Mryasov *et al.* [28] and by considering configurational averages within this reformulated model.

Interface Effects in Fe/FePt Multilayers

As touched upon in Section 2.1.5, the ratio of the magnetocrystalline anisotropy energy (MAE), K_u , of a magnetic material to its saturation magnetisation, M_{sat} , $\eta = \frac{4K_u}{\mu_0 M_{\text{sat}}^2}$, is a measure of the magnetic hardness of the material [232,233]. The larger the fraction η , the harder the magnet, i.e., the harder it is to change its magnetisation state. An *exchange spring* is a composite structure consisting of a soft ($\eta \ll 1$) and a hard ($\eta \gg 1$) magnetic phase [233]. Near the soft/hard interface, the magnetisation of the soft phase is pinned to that of the hard phase. Further away from the interface, the application of an external magnetic field can rotate the magnetisation direction of the soft phase to be different from the magnetisation direction of the hard phase. Because even the “best” hard magnetic materials exhibit saturation magnetisations below that of many soft magnetic materials [232], exchange springs were first suggested as an alternative to permanent magnets, which are often chemically reactive and generally relatively expensive [233]. A wealth of different soft/hard nano-composites have been investigated in the literature (see, e.g., Refs. [234–241]). Experimentally, the Fe/FePt system is a highly suitable system for studying the fundamental properties of nano-composite magnetic systems as the properties are relatively easy to control [242].

Within the magnetic recording industry, exchange-coupled soft/hard nano-composites are of significant interest for their potential application in exchange-coupled composite (ECC) magnetic recording media. In particular, due to the high saturation magnetisation of body-centred cubic (bcc) α -Fe and the large MAE of $L1_0$ FePt, Fe/FePt nano-composites are of significant interest for such applications. The α -Fe phase of such a nano-composite would, through its

exchange coupling with FePt, deliver the desired “levering” effect of reducing the effective write field, while the hardness (i.e., the large MAE) of the FePt phase would safeguard the thermal stability of the written information [243]. Consequently, there exists a large number of experimental studies on the subject of realising Fe/FePt heterostructures and investigating their magnetic properties, see, e.g., Refs. [51, 237, 240, 241, 243]. Moreover, Sabiryanov and Jaswal [52] have studied the isotropic exchange and the spin moments in an Fe/FePt/Fe heterostructure from first principles. In particular, it is of significant interest to determine the effect of the Fe/FePt interface itself upon the aggregate magnetic properties of the nano-composite.

The aim of this Chapter is to investigate in detail the effect of the Fe/FePt interface on the magnetic exchange tensors and the MAE of an Fe/FePt/Fe heterostructure by means of first-principles calculations. Not only is this important from the above point of view of understanding the properties of this nano-composite, but such site-resolved information is also central to the development and parameterisation of computational localised-spin models. In particular, the work presented in this Chapter has recently been mapped to a linear-chain model of domain wall dynamics [244].

5.1 Computational Details

As described in Section 2.3 and using exactly the same parameters as in Chapter 4 (see Section 4.1), we employed the fully relativistic SKKR method [105] to evaluate the magnetic properties of four (slightly) different Fe/FePt/Fe systems; these systems are listed in Section 5.2. Following Section 2.3.4, the layer-resolved contributions to the MAE, K_i , were evaluated using the torque method, i.e.,

$$K_i = \left. \frac{dE_i}{d\theta} \right|_{\theta=\pi/4}. \quad (5.1)$$

Meanwhile, the exchange tensors,

$$\underline{\underline{J}}_{ij} = \begin{pmatrix} J_{ij}^{xx} & J_{ij}^{xy} & J_{ij}^{xz} \\ J_{ij}^{yx} & J_{ij}^{yy} & J_{ij}^{yz} \\ J_{ij}^{zx} & J_{ij}^{zy} & J_{ij}^{zz} \end{pmatrix}, \quad (5.2)$$

were evaluated through Eqs. (2.52 – 2.54) as described in Ref. [133] and summarised in Section 2.3.4.

Furthermore, in terms of the anisotropic extended Heisenberg Hamiltonian of Eq. (2.5),

$$\hat{H}_{\text{aHeis}} = -\frac{1}{2} \sum_{i \neq j} \mathbf{S}_i \underline{J}_{ij} \mathbf{S}_j - \sum_i d_i (\mathbf{S}_i \cdot \mathbf{e})^2, \quad (5.3)$$

the MAE, K , can be cast into on-site and inter-site contributions as per Eq. (2.7). If we define the layer-resolved inter-site anisotropy,

$$K_{i,\text{inter-site}} = \frac{1}{2} \sum_{j, j \neq i} (J_{ij}^{zz} - J_{ij}^{xx}), \quad (5.4)$$

the layer-resolved MAE contributions in Eq. (5.1) can be compared within the Heisenberg model to

$$K_i = d_i + K_{i,\text{inter-site}}. \quad (5.5)$$

In the following, we evaluated d_i and $K_{i,\text{inter-site}}$ as per Eq. (2.56) and Eq. (2.57), respectively. It should be noted that the sum in Eq. (5.4) over j can be cast into sums over atomic layers and over sites within atomic layers. The latter sum, in particular, suffers from convergence problems because the (RKKY) exchange decays, at best, as $1/R_{ij}^3$, where R_{ij} denotes the distance between atoms i and j [78,245,246]. For this reason the corresponding sum was transformed into an integral in k -space using Eqs. (2.52 – 2.54); for further detail, see Ref. [133].

5.2 The Systems

As discussed in Section 2.3.3, the formalism of the SKKR method requires the Fe/FePt/Fe multilayer structure to be considered in terms of an *interlayer* (i.e., the region of interest for which the magnetic properties are to be calculated), stacked in between two semi-infinite bulk systems. As shown in Fig. 5.1, the stacking of the interlayer and the semi-infinite bulk systems was arranged along the [001] axis (of the FePt lattice) due to the convenience of constructing (001) Fe/FePt interfaces in such a setup. The interlayer was, furthermore, constructed such that the [100] axis of the L1₀ FePt lattice was rotated 45° relative to the [100] axis of the bcc Fe lattice. This construction was used in order to provide a good fit between the experimental in-plane lattice parameters of Fe and FePt, 2.87 Å and $3.85/\sqrt{2} \approx 2.72$ Å, respectively [219,220,247]. Within SKKR, the magnetic properties of the interlayer are evaluated at the Fermi level of the semi-infinite bulk systems enclosing the interlayer. For comparison, therefore, we considered two different layouts of the interlayer, as follows.

- (i) 8 Fe layers + 17 Pt/Fe/⋯/Fe/Pt layers + 7 Fe layers
(positioned in between two semi-infinite bulk Fe systems, indexed as

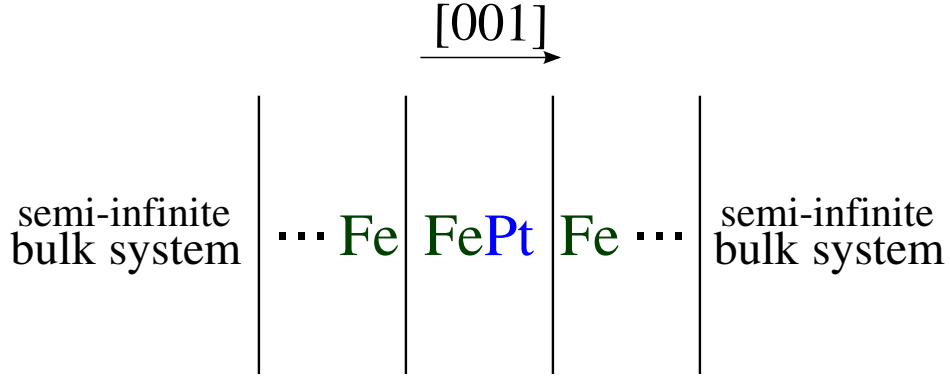


Figure 5.1: The layout of the Fe/FePt/Fe multilayer systems, adhering to the requirements of the SKKR formalism. The interlayer is stacked in between two semi-infinite bulk systems along the [001] axis of the FePt lattice. Note that the Fe/FePt interfaces are (001) interfaces, i.e., perpendicular to the stacking direction.

shown in Table 5.1)

- (ii) 2 Fe/Pt layers + 8 Fe layers + 17 Pt/Fe/.../Fe/Pt layers + 8 Fe layers + 3 Pt/Fe/Pt atomic layers
(positioned in between two semi-infinite bulk FePt systems, indexed as shown in Table 5.2)

AL index, $i =$...	<i>-10</i>	<i>-9</i>	-8	-7	<i>-6</i>	...	-1	0	1	...	6	7	8	9	10	...
species	...	<i>Fe</i>	<i>Fe</i>	Pt	Fe	Pt	...	Fe	Pt	Fe	...	Pt	Fe	Pt	<i>Fe</i>	<i>Fe</i>	...

Table 5.1: The atomic layer (AL) layout for an Fe/FePt/Fe structure enclosed by bulk Fe. Italicised chemical symbols refer to the Fe phase and bold face chemical symbols refer to the FePt phase.

AL index, $i =$...	-19	-18	-17	...	-9	-8	-7	...	7	8	9	...	17	18	19	...
species	...	Fe	Pt	<i>Fe</i>	...	<i>Fe</i>	Pt	Fe	...	Fe	Pt	<i>Fe</i>	...	<i>Fe</i>	Pt	Fe	...

Table 5.2: The atomic layer (AL) layout of an FePt/Fe/FePt/Fe/FePt structure enclosed by bulk FePt. Italicised chemical symbols refer to the Fe phase and bold face chemical symbols refer to the FePt phase.

We considered four different Fe/FePt/Fe systems, labelled **A**, **B**, **C** and **D**.

A System **A** is a geometrically unrelaxed system based on layout (i), with an overall two-dimensional lattice parameter $a_{2D} = a_{\text{FePt}}^{(\text{exp})} / \sqrt{2} \approx 2.723 \text{ \AA}$, where $a_{\text{FePt}}^{(\text{exp})} = 3.852 \text{ \AA}$ is the experimental in-plane lattice parameter of the L1₀ lattice of FePt [219, 220]. Note that 2.723 Å is within 5 % of the

experimental lattice parameter of bcc Fe, $a_{\text{Fe}}^{(\text{exp})} = 2.87 \text{ \AA}$ [247]. For the FePt part of the system we used the experimentally measured FePt c/a ratio of $c_{\text{FePt}}/a_{2\text{D}} = 0.964$, while for the bcc Fe part, $c_{\text{Fe}} = a_{2\text{D}}$. At the Fe/FePt interfaces (see Table 5.1), we set the distance between the atomic layers $i = -9$ and $i = -10$, as well as between the atomic layers $i = 9$ and $i = 10$, to

$$d_{\text{interface}} = \frac{c_{\text{Fe}} + c_{\text{FePt}}}{4}. \quad (5.6)$$

B System **B** is also based on layout (i). However, here the atomic layer spacings were obtained from a geometry optimisation in CASTEP,¹ keeping $a_{2\text{D}} = a_{\text{Fe}}^{(\text{LSDA})}$, where $a_{\text{Fe}}^{(\text{LSDA})}$ is the bulk Fe lattice parameter obtained within the LSDA in CASTEP, 2.659 \AA [229]. The resulting optimised structure was then scaled up isotropically to the experimental FePt lattice parameter, $a_{2\text{D}} = 2.723 \text{ \AA}$, in order to enable a direct comparison of the results for system **B** with those for system **A**. It should be noted here that the CASTEP geometry optimisation yields a FePt c/a ratio of 0.978 and an Fe region which is slightly tetragonal (rather than cubic), with the ratio $c_{\text{Fe}}/a_{\text{Fe}} \approx 1.06$. As this tetragonalisation must be due to the presence of the FePt slab and as the CASTEP geometry optimisations are based on a supercell approach [229] (i.e., the whole Fe/FePt/Fe structure is repeated indefinitely along the [001] direction), the optimised geometry of system **B** probably corresponds more closely to a repeated multilayer structure than system **A**.

C System **C** is identical to system **B** except we maintained the LSDA lattice parameter even in the SKKR calculations. In other words, throughout system **C**, $a_{2\text{D}} = a_{\text{Fe}}^{(\text{LSDA})}$.

D System **D** is an unrelaxed system based layout (ii), i.e., it is enclosed in bulk FePt. Throughout, the in-plane lattice parameter, $a_{2\text{D}}$, was kept at the experimental FePt bulk lattice parameter $a_{\text{FePt}}^{(\text{exp})} = 2.723 \text{ \AA}$. At each of the four Fe/FePt interfaces (see Table 5.2) in this system, again the atomic layer spacing was set to $d_{\text{interface}}$ as in Eq. (5.6).

Systems **A**, **B** and **C** are immersed in bulk Fe and their magnetic properties are thus evaluated at the Fermi energy of bulk Fe. Similarly, the magnetic properties of system **D** are evaluated at the Fermi energy of bulk FePt. Throughout this study we concentrate on systems **A** and **B**. This is because, within the FePt phase, system **C** exhibits an atomic volume of merely 12.99 \AA^3 , whereas system **B** exhibits an atomic volume of 13.97 \AA^3 , which is much closer to the experi-

¹The CASTEP calculations were performed by Dr. P. J. Hasnip of the University of York, UK.

mental FePt atomic volume used in system **A**, 13.77 \AA^3 . We use system **C** to check for any direct effects of the scaling involved in constructing system **B**. Since the considered Fe and FePt phases are quite thick, as expected, the magnetic properties of system **D** turned out to be very similar to those of system **A**. Therefore, in this study, we used system **D** only for calibrating the change in the MAE of the FePt slab with respect to the bulk FePt MAE in Section 5.5.

For systems **B** and **C**, after having specified the vertical coordinate, z_i , of each atomic layer i from the CASTEP geometry optimisations, we needed to determine the corresponding atomic volumes, $\{\Omega_i\}$, of this optimised geometry. (Note that, due to the two-dimensional translational invariance of the system, the volume Ω_i corresponds to the volume of any atom in a given atomic layer i , i.e., i is still the atomic layer index.) The only strict requirement here is that the sum of the atomic volumes within the interlayer should be equal to the total lattice volume of the interlayer. The choice of the individual atomic volumes is, however, arbitrary. As a simple construction, the corresponding (Fe or FePt) bulk atomic volumes were retained in all atomic layers except for in the six atomic layers forming the Fe-Fe-Fe-Pt-Fe-Pt sequence at each Fe/FePt interface (i.e., in layers $7 \leq |i| \leq 12$). The remaining lattice volume, $\Delta\Omega$, was then distributed across the atomic layers $7 \leq |i| \leq 12$ in accordance with the corresponding atomic layer spacings, i.e.,

$$\begin{aligned} \Delta\Omega &= \sum_{i=7}^{i=12} \Omega_i \\ \Omega_7 : \Omega_8 : \dots : \Omega_{11} : \Omega_{12} &= l_7 : l_8 : \dots : l_{11} : l_{12}, \end{aligned} \quad (5.7)$$

where l_i refers to the atomic layer spacings, i.e.,

$$l_i = \frac{1}{2} |z_{i+1} - z_{i-1}|, \quad (5.8)$$

where z_i is the vertical position (along the [001] axis of the FePt lattice) of the i^{th} atomic layer. It should be mentioned here that $\Delta\Omega$ corresponds to the lattice volume of layers $7 \leq i \leq 12$ to within 0.2 %. Fig. 5.2 depicts the interlayer distances, $\Delta z_i = z_{i+1} - z_i$, and the radii of the atomic spheres, S_i (defined through $\Omega_i = \frac{4\pi}{3} S_i^3$), according to the construction of Eq. (5.7).

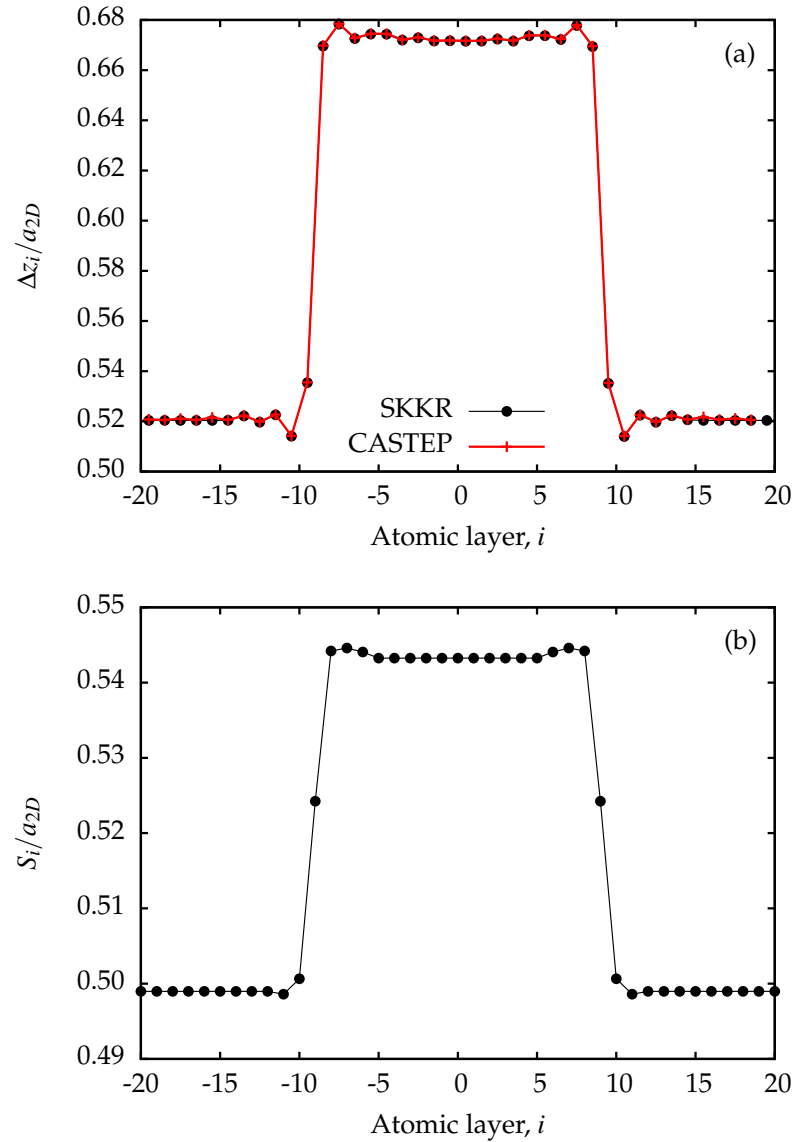


Figure 5.2: The relaxed atomic layer spacings, Δz_i (top), and the corresponding radii of atomic spheres, S_i (bottom), as used for systems **B** and **C**. In the top panel (a), red + represent the atomic layer spacings obtained from CASTEP in Ref. [229] and black • represent the atomic layer spacings separations used in the SKKR calculations. In the bottom panel (b), black • represent the radii of atomic spheres as used in the SKKR calculations. Note that for the SKKR calculations, S_i and l_i are constant for layers $|i| > 16$. Solid lines connecting the symbols serve as guides for the eye.

5.3 Local Spin Moments

The calculated atomic spin moments for the Fe/FePt/Fe systems are plotted in Fig. 5.3, displaying a fairly similar picture for systems **A** and **B**. In the interior of the FePt slab ($|i| \leq 6$) the moments are very close to their bulk values in FePt, $m_{\text{Fe}}^{(\text{FePt})} = 2.86 \mu_{\text{B}}$ and $m_{\text{Pt}}^{(\text{FePt})} = 0.32 \mu_{\text{B}}$. Moreover, the Fe moments approach their bulk Fe values at the edges of the interlayer ($|i| \rightarrow 15$). However, the bulk Fe spin moment is slightly enhanced in system **B**, $m_{\text{Fe}}^{(\text{Fe,B})} = 2.07 \mu_{\text{B}}$, as compared to system **A**, $m_{\text{Fe}}^{(\text{Fe,A})} = 1.97 \mu_{\text{B}}$. This difference is, in all likelihood, due to the slight tetragonality of the Fe unit cell along the [001] direction in system **B**. Another apparent difference between systems **A** and **B** occurs in the interfacial Fe layers $i = \pm 9$, where the moment is about 10 % larger in system **B** than in system **A**. Moreover, unlike in system **A**, in system **B** the spin moments in layers $i = \pm 10$, $m_{\pm 10}$, are enhanced with respect to the bulk Fe moments. For system **C**, which exhibits distinctly smaller atomic volumes than systems **A** and **B**, the spin moments are somewhat reduced in comparison to those of system **B** but the transition from bulk Fe moments to bulk FePt moments remains smooth. As expected, thus, the transition in the spin moment magnitudes from bulk Fe to bulk FePt is smoother in the optimised geometries.

5.4 Effective Exchange

In order to characterise the strength of the isotropic exchange interactions in a magnetic system, one often defines a site-resolved effective exchange parameter, J_i , defined for a given site i as

$$J_i = \sum_{j(\neq i)} J_{ij} = \frac{1}{3} \sum_{j(\neq i)} \text{Tr} \left\{ \underline{\underline{J_{ij}}} \right\}, \quad (5.9)$$

where $\underline{\underline{J_{ij}}}$ is the exchange tensor as defined in Section 2.1.1 and the sum is over all neighbouring sites j . For a system exhibiting two-dimensional translational invariance, J_i must of course be identical for every site in a given atomic layer. Therefore, in the following, i denotes the atomic layer index. For systems **A**, **B** and **C**, we calculated J_i by considering all neighbours within a distance of seven $a_{2\text{D}}$, which ensured a reliable convergence (within 3 %) of the sum in Eq. (5.9). The calculated layer-resolved effective exchange parameters are plotted in Fig. 5.4 for systems **A** and **B**.

Within the FePt slab, the effective exchange parameters of systems **A** and **B**

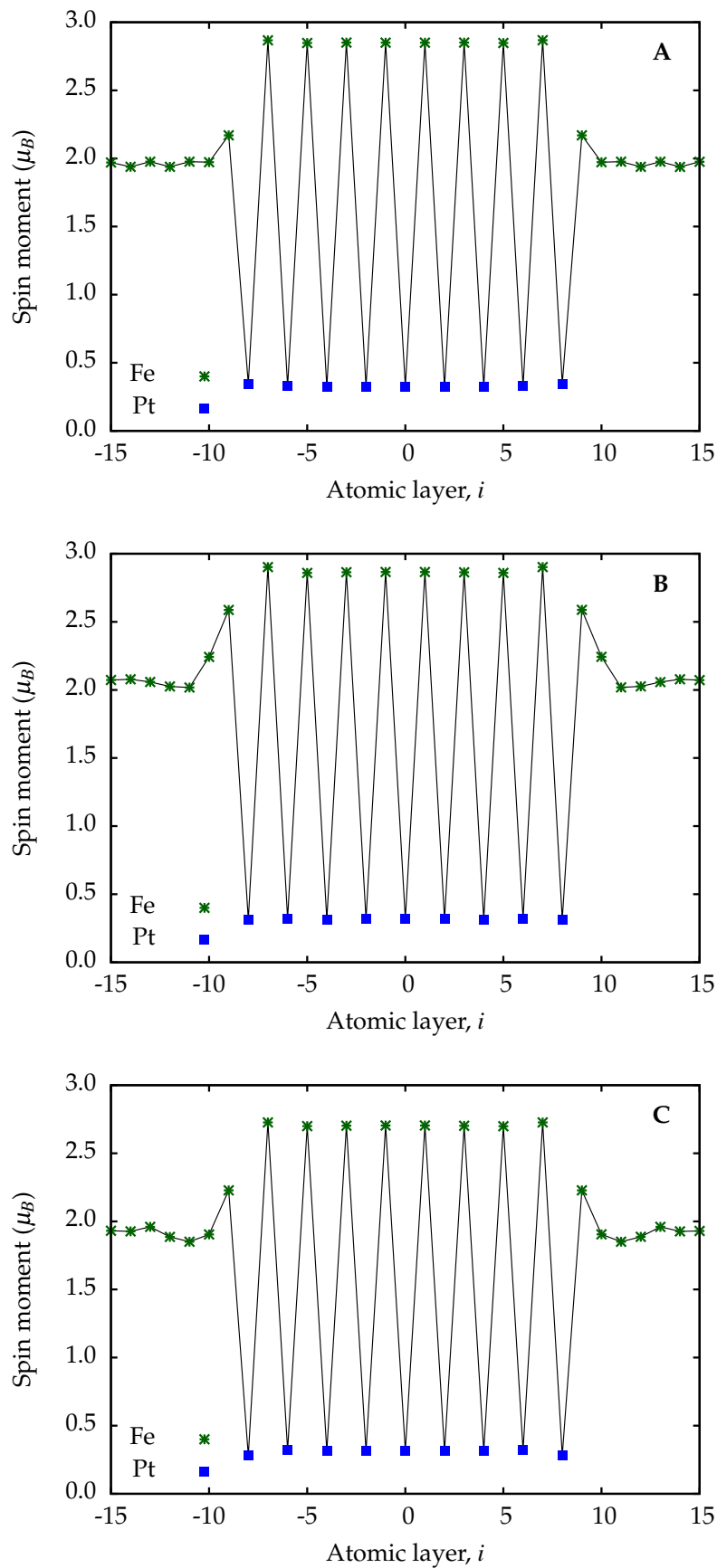


Figure 5.3: The calculated atomic spin moment in each atomic layer i across systems **A**, **B** and **C**. Green * represent Fe moments and blue ■ represent Pt moments. Solid lines connecting the symbols serve as guides for the eye.

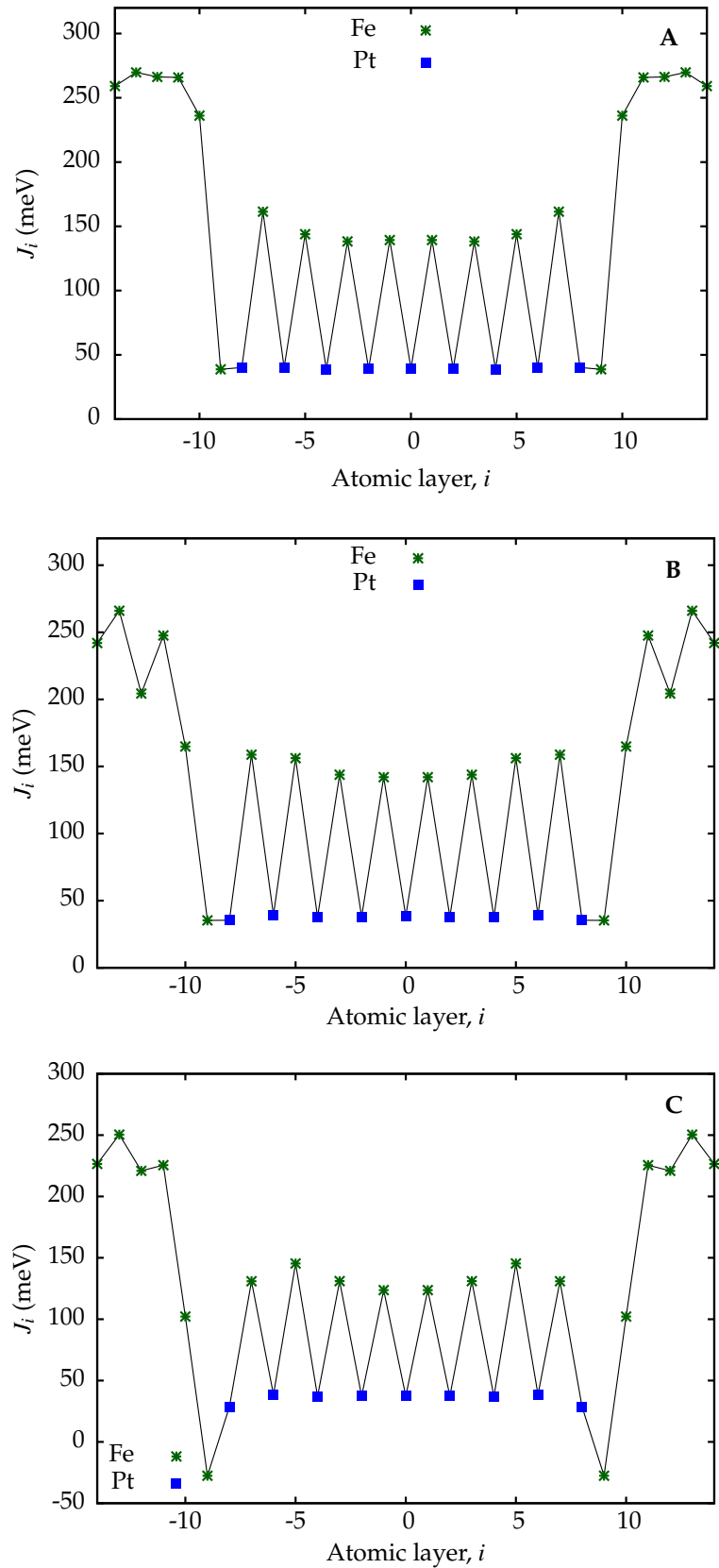


Figure 5.4: The layer-resolved effective isotropic exchange constant $J_i = \frac{1}{3} \sum_j \text{Tr} \left\{ \underline{\underline{J}}_{ij} \right\}$ for Fe/FePt/Fe systems **A**, **B** and **C**, where the sum is over the neighbours within seven lattice parameters. Solid lines connecting the symbols serve as guides for the eye.

exhibit very similar layer-resolved behaviours. The value of J_i for the Fe layers is about 150 meV in the centre of the FePt slab and slightly enhanced at the edges of the slab (i.e., towards layers $i = \pm 7$). This is mainly a consequence of an enhancement of the ferromagnetic, nearest-neighbour, intra-layer Fe-Fe interactions. We observe this enhancement also in system **C**, however, here the exchange in layers $i = \pm 7$ is somewhat reduced with respect to the exchange of layers $i = \pm 5$. This is because while the ferromagnetic, nearest-neighbour, intra-layer Fe-Fe interaction continues to strengthen towards the Fe/FePt interface (just as in systems **A** and **B**), there is a substantial reduction in the ferromagnetic next-nearest-neighbour intra-plane Fe-Fe interaction. Across all three systems **A**, **B** and **C**, the effective exchange parameter of about 40 meV observed in the Pt layers stems mainly from the strongly ferromagnetic nearest-neighbour Fe-Pt interactions.

The Fe phase of the Fe/FePt/Fe systems is characterised by much larger effective exchange parameters, $J_i \sim 260$ meV, than the FePt phase. The large effective exchange of the soft (Fe) phase is a crucial property in exchange-coupled magnetic recording media as it enables the “levering” effect in switching the magnetisation of the hard (FePt) phase. It should be noted that the effective exchange parameters calculated for the interior of the FePt slab and the Fe bulk part of the system correspond to mean-field Curie temperatures of $T_C^{\text{FePt}} \sim 700\text{K}$ and $T_C^{\text{Fe}} \sim 1000\text{K}$, in good agreement with the corresponding experimental values [248, 249].

At the Fe/FePt interface, the effective exchange of the Fe layers drops drastically. In systems **A** and **B**, the Fe layers $i = \pm 9$ exhibit an effective exchange of merely ~ 40 meV, almost identical to the effective exchange of the Pt layers. This reduction in J_i originates in a weakening of the ferromagnetic intra-layer Fe-Fe interactions in layers $i = \pm 9$ and the relatively weak exchange of the layers $i = \pm 9$ with the soft layers $|i| \geq 10$. What remains is essentially the ferromagnetic nearest-neighbour Fe-Pt interactions and the (slightly enhanced) Fe-Fe interactions with layers $i = \pm 7$, yielding $J_{\pm 9} \sim 40$ meV. For system **C**, the reduction of J_i in layers $i = \pm 9$ is even greater. This is because, on top of the overall weakening of the intra-layer Fe-Fe interactions for $i = \pm 9$, the next-nearest-neighbour intra-layer Fe-Fe interaction even becomes antiferromagnetic. Our results for the unrelaxed system **A** are in satisfactory agreement with the effective exchange reported for an unrelaxed Fe/FePt/Fe heterostructure in Ref. [52], although the magnitudes of J_i are significantly smaller in Ref. [52].

Interestingly, in system **A**, the effective exchange of the Fe layers $i = \pm 10$, $J_{\pm 10} \sim 230$ meV, i.e., it almost recovers the bulk Fe value. In contrast, in system **B**, $J_{\pm 10}$ remains remarkably small (~ 160 meV). Also, in system **B** the effective exchange exhibits relatively large fluctuations throughout the Fe layers $|i| \geq 10$. Although we observe oscillations across all the pair-wise interactions of these Fe layers, the strongest contribution to the oscillatory behaviour comes from the ferromagnetic, nearest-out-of-plane-neighbour Fe-Fe interactions. This is to be expected as the variation in the interlayer distance between these Fe atoms (due to the geometrical optimisation and the slightly tetragonal Fe unit cell in system **B**) will affect the shape of the hybridised orbitals. This picture is further supported by the differences between systems **B** and **C**, indicating that these fluctuations are highly sensitive to the scaling of the lattice parameters involved in constructing system **B**.

5.5 Magnetocrystalline Anisotropy Energy

5.5.1 Layer-Resolved MAE Contributions

Fig. 5.5 shows the layer-resolved MAE contributions, K_i , as calculated for systems **A**, **B** and **C** (see Eq. (5.1)). For systems **A** and **B**, the MAE contributions of the Fe layers in the FePt phase oscillate between about 2.5 meV and 3 meV. The frequency and the magnitude of these oscillations are different for the two systems. As these oscillations appear to arise from quantum interference effects between the two interfaces, this difference between systems **A** and **B** can probably be attributed to the different boundary conditions at the Fe/FePt interfaces. In particular, the oscillations appear damped in the optimised geometry of system **B**, settling more quickly in this system than in system **A**. In system **C**, the FePt MAE settles at a slightly larger value than in systems **A** and **B**, probably due to the difference in atomic volumes. In all three systems, the Pt MAE contributions are very small, ~ 0.2 meV, and the Fe MAE contributions rapidly approach zero in the Fe phase.

As a remarkable difference between systems **A** and **B**, in system **A** the Fe layers at the Fe/FePt interfaces (layers $i = \pm 9$) exhibit a contribution of about -0.25 meV to the MAE, while in system **B** this contribution is positive, ~ 1 meV. In system **C**, this positive MAE contribution remains, although the magnitude is significantly reduced. In order to gain an understanding of this difference,

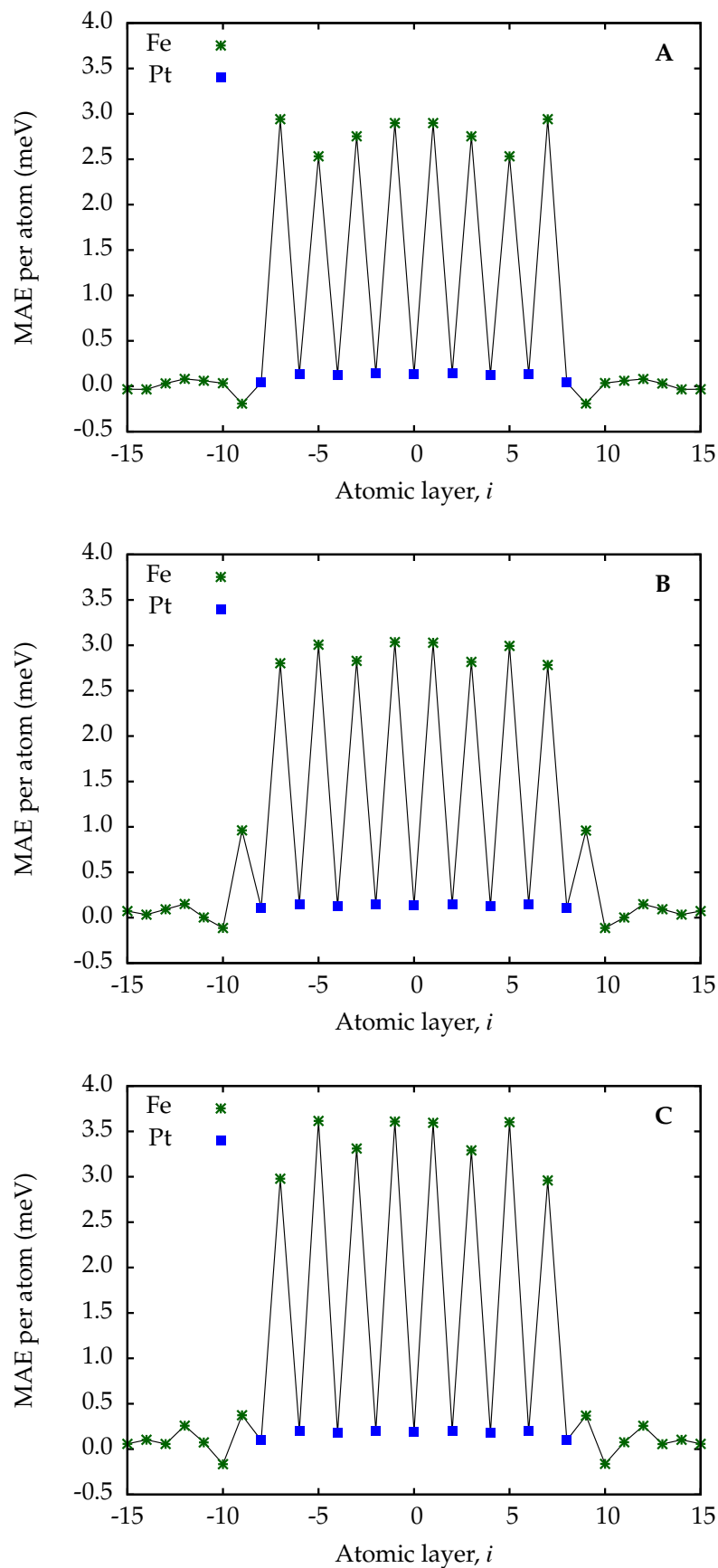


Figure 5.5: The calculated layer-resolved MAE contributions across systems **A**, **B** and **C**. The blue ■ represent the Pt contributions to the MAE and the green * represent the Fe contributions to the MAE. Solid lines connecting the symbols serve as guides for the eye.

we tried applying Bruno's arguments in terms of second order perturbation theory [80,250]. In short, the MAE can be highly sensitive to the density of states near the Fermi level because the spin-orbit interaction gives rise to couplings between occupied and unoccupied states [80]. The magnitude of the contribution of a given coupling to the MAE is inversely proportional to the energy difference between the two states involved [80]. Denoting the orbital angular momentum quantum number as m_l and the spin angular momentum quantum number as m_s , in-plane anisotropy is favoured by couplings where $\{\Delta m_l = 0, \Delta m_s = \pm 1/2\}$ and by couplings where $\{\Delta m_l = \pm 1, \Delta m_s = 0\}$ [251–253]. Meanwhile, perpendicular anisotropy is favoured by couplings where $\{\Delta m_l = 0, \Delta m_s = 0\}$ and by couplings where $\{\Delta m_l = \pm 1, \Delta m_s = \pm 1/2\}$ [251–253]. In order to analyse the origin of the MAE in layers $i = \pm 9$, we performed self-consistent scalar-relativistic calculations from which we obtained the local partial densities of states (LPDOS). Fig. 5.6 shows our calculated d -like spin- and orbital-resolved LPDOS at layers $i = \pm 9$ for systems **A** and **B**. The LPDOS clearly shows a strong spin-polarisation in this layer, which is a necessary condition to apply the above perturbation theory. Comparing systems **A** and **B**, the d_{z^2} -LPDOS is almost insensitive to the geometry optimisation, while the optimisation appears to shift a considerable weight of the $d_{xz,yz}$ -LPDOS (and, to some extent, also of the d_{xy,x^2-y^2} -LPDOS) towards the Fermi level in the occupied regime in both spin-channels. The unoccupied part of the minority spin-channel of these orbital-resolved states is also affected by the geometry optimisation. However, except for a reduction in the unoccupied minority-spin $d_{xz,yz}$ -LPDOS, the differences between the spin- and orbital-resolved LPDOS of systems **A** and **B** are very minor in the vicinity of the Fermi level. Furthermore, the small changes that do occur have opposing effects upon the MAE. The spin-orbit interaction gives rise to couplings between the d_{xz} and d_{yz} states, inducing a perpendicular MAE, as well as to couplings between the $d_{xz,yz}$ and d_{z^2} states, inducing an in-plane MAE [250]. Therefore, it is hardly possible to identify a distinct origin of the differences in $K_{\pm 9}$ for systems **A** and **B**.

5.5.2 On-site and Inter-site Anisotropies

The layer-resolved on-site and inter-site anisotropy contributions (see Eq. (5.4) and Eq. (5.5)) for systems **A**, **B** and **C** are shown in Fig. 5.7. For each system, the shape of $K_{i,\text{inter-site}}$ across the atomic layers i in Fig. 5.7 coincides reasonably well with that of K_i presented in Fig. 5.5. Remarkably, Eq. (5.5) is satisfied to high accuracy in the sense that the sums of the on-site and inter-site contributions in each atomic layer in Fig. 5.7 correspond closely to the layer-resolved

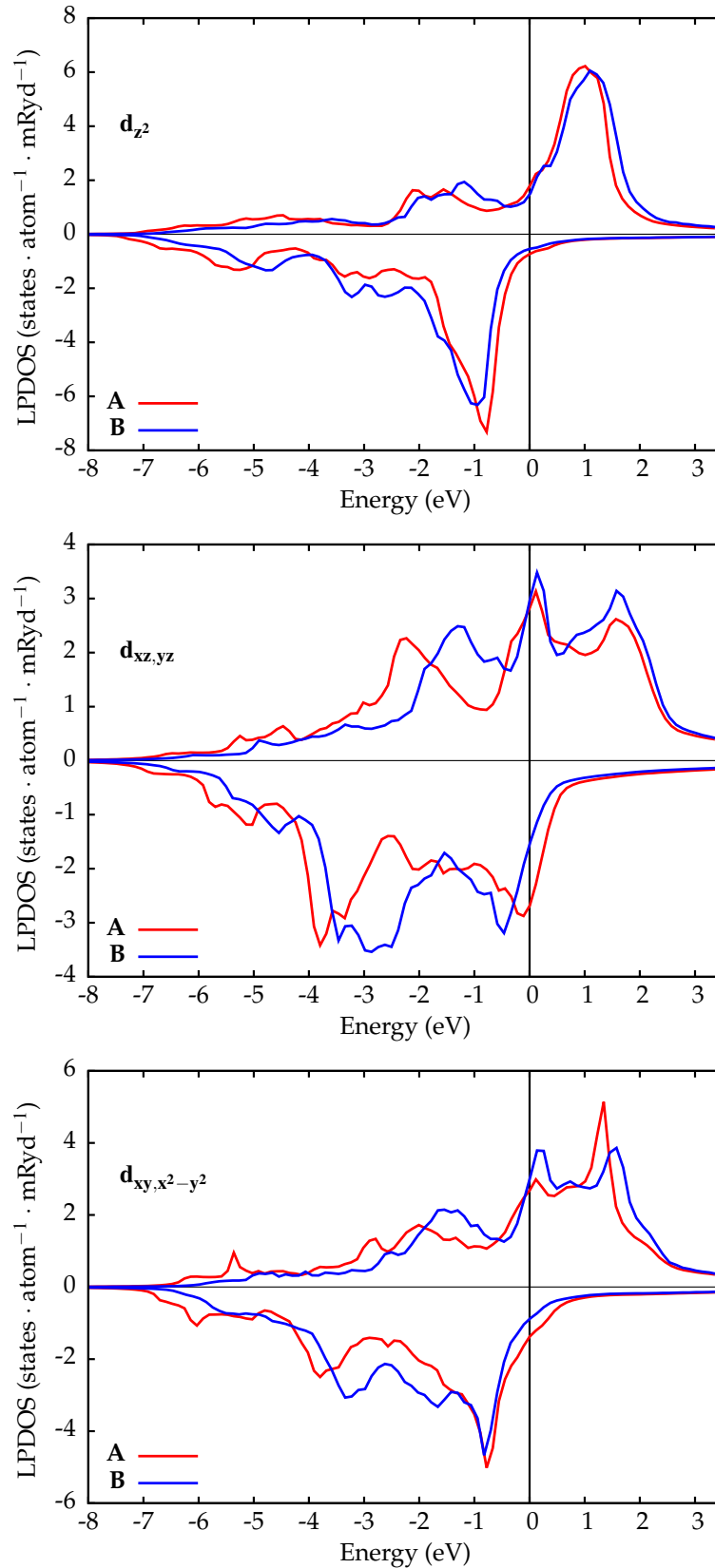


Figure 5.6: The calculated d -like spin- and orbital-projected local partial densities of states (LPDOS) for the interfacial Fe layers $i = \pm 9$ in systems **A** (in red) and **B** (in blue). Top panel: d_{z^2} ($m_\ell = 0$), centre panel: d_{xz} and d_{yz} ($m_\ell = \pm 1$), bottom panel: d_{xy} and $d_{x^2-y^2}$ ($m_\ell = \pm 2$). Positive and negative values represent minority and majority spin-channels, respectively. The origin along the energy axis has been shifted to the Fermi energy.

MAE contributions in Fig. 5.5. This lends substantial credit to the use of the tensorial exchange interactions in spin-dynamics simulations of Fe/FePt nanocomposites. Moreover, it is evident from Fig. 5.5 that approximately 90 % of the MAE of FePt is associated with anisotropic Fe-Fe inter-site interactions. This result is in good agreement with the results of Mryasov *et al.* [28], which strongly suggest that the MAE of the FePt systems arise mainly from effective Fe-Fe inter-site interactions, mediated by the spin-orbit coupling on the Pt atoms.

Furthermore, we note from Fig. 5.7 that the change in K_i at the Fe/FePt interface (i.e., in layers $i = \pm 9$) between systems **A** and **B** stems mostly from the inter-site anisotropy. Using the arguments of Mryasov *et al.* [28], this can be explained in terms of the strong (Pt) spin-orbit coupling experienced by the electrons scattering between these Fe atoms and the Pt atoms in the adjacent layer $i = \pm 8$. Interestingly, in system **A** this induced anisotropy effect is suppressed and the small negative contribution to the MAE in these layers is of on-site origin.

Across all three systems in Fig. 5.7, the on-site anisotropies are quite small (~ 0.5 meV/atom) and stable on the Fe sites within the FePt slab. Within the Fe phase, and on the Pt sites, the on-site anisotropies practically vanish. The only significant difference in the on-site contributions occurs in layers $i = \pm 9$, where system **B** exhibits almost zero on-site anisotropy as opposed to the negative on-site anisotropies $d_{\pm 9}$ of systems **A** and **C**. While the inter-site anisotropy magnitudes are much larger in system **C** than in systems **A** and **B**, the trend in the inter-site anisotropies across system **C** does follow a similar trend to that of the inter-site anisotropies in system **B**. Altogether, thus, as expected, the inter-site anisotropy is highly sensitive to the relative positions of the atomic layers, whereas the on-site anisotropy is not.

5.5.3 Aggregate Change in the MAE of the FePt Phase

Finally, we considered the difference between the MAE of the FePt phase in an Fe/FePt/Fe multilayer and the MAE of bulk FePt. This point is of strong technological interest since, in ECC applications, it would be desirable to maintain, or even increase, the MAE of the hard (FePt) phase in order to safeguard the thermal stability of the written information. The effect upon the FePt MAE by the formation of the multilayer structure is thus an important aspect. In order to make our estimate comparable to experiment, it should be noted that

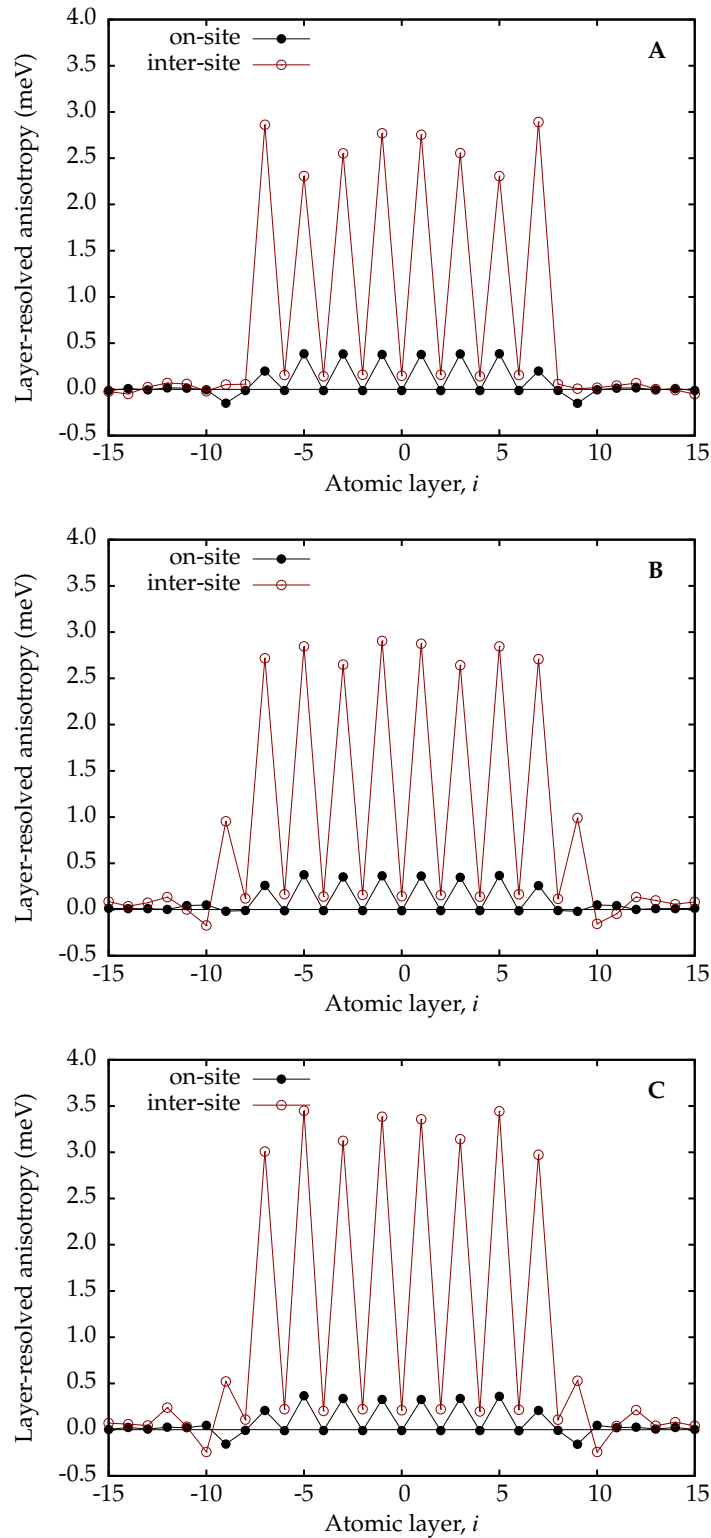


Figure 5.7: The layer-resolved on-site (black \bullet) and inter-site (brown \circ) anisotropies for systems **A**, **B** and **C** see Eq. (5.5). Solid lines connecting the symbols serve as guides for the eye.

the construction of systems **A**, **B** and **C** is equivalent to the following three scenarios.

- (i) an Fe/Pt/Fe/.../Fe/Pt/Fe system immersed in bulk Fe
- (ii) a Pt/Fe/Pt/.../Pt/Fe/Pt system immersed in bulk Fe
- (iii) a Pt/Fe/Pt/.../Pt/Fe system immersed in bulk Fe

Therefore, keeping in mind that systems **A**, **B** and **C** incorporate nine Pt layers, we have, on average, included eighteen atomic layers of FePt. It is apparent from Fig. 5.5 that, for the chosen thickness of the FePt phase, the effect of a single Fe/FePt interface can hardly be extracted due to the strong quantum interference effects between the two Fe/FePt interfaces. Thus we considered instead the change in the FePt MAE generated by the presence of the Fe phases,

$$\Delta K_{\text{FePt-slab}} = -9K_{\text{FePt}} + \sum_{i=-15}^{15} K_i, \quad (5.10)$$

where we have included also the Fe phase in the sum and where K_{FePt} is the bulk FePt MAE per formula unit. As already mentioned in Section 4.2, for bulk FePt, we calculated $K_{\text{FePt}} = 3.37$ meV/f.u. Note that the MAE of bulk Fe is neglected in Eq. (5.10) as bulk bcc Fe would be expected to exhibit zero uniaxial MAE.

In order to evaluate $\Delta K_{\text{FePt-slab}}$, we needed to take into consideration the fact that the evaluation of the MAE contributions across the systems **A**, **B** and **C** was performed using the bulk Fe Fermi energy, not the bulk FePt Fermi energy (see Section 5.2). Therefore, we cannot compare the MAE contributions of systems **A**, **B** and **C** directly to the MAE of bulk FePt. In order to calibrate K_{FePt} for systems **A** and **B**, we used system **D** (an FePt/Fe/FePt/Fe/FePt system immersed in bulk FePt, see Section 5.2). As shown in Fig. 5.8, we obtained a very similar shape of K_i across the atomic layers i for systems **A** and **D**. However, at the centre of the FePt phase of system **D**, K_i is very slightly larger so that the MAE of bulk FePt, $K_{\text{FePt}} \approx 3.37$ meV/f.u., is retained to within 1 %. Since, at the centre of the FePt phase, the corresponding MAE contributions in system **A** are consistently approximately 0.33 meV/f.u. smaller, we used a corrected value of $K_{\text{FePt}} = 3.04$ meV/f.u. in order to evaluate $\Delta K_{\text{FePt-slab}}$ (Eq. (5.10)) for systems **A** and **B**. Note that this calibration does not apply to system **C** due to the stark difference in lattice parameters and atomic volumes between systems **C** and **D** (see Section 5.2).

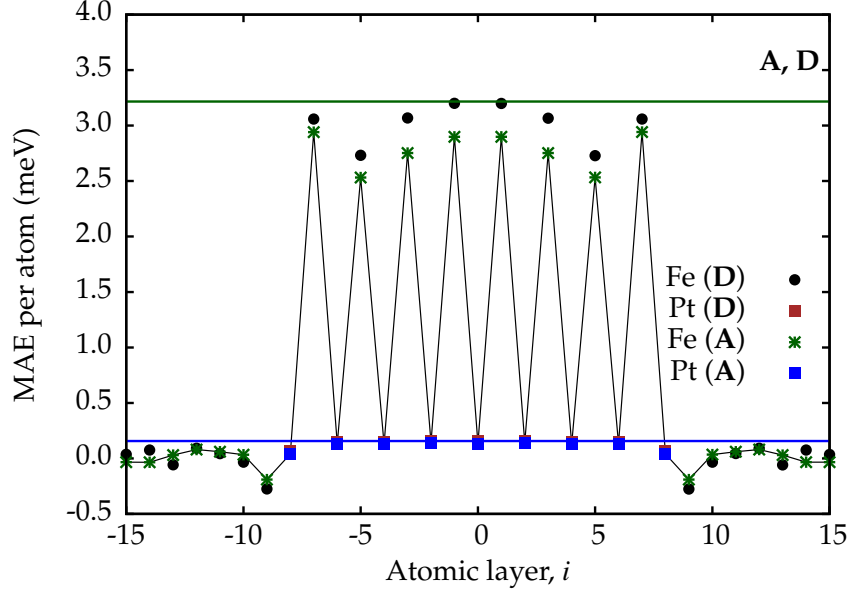


Figure 5.8: The layer-resolved MAE contributions across systems **A** and **D**. For system **A**, blue ■ represent the Pt MAE contributions and green * represent the Fe MAE contributions. For system **D**, black • represent the Fe contributions to the MAE and brown ■ represent the Pt contributions to the MAE. The green and blue horizontal lines correspond to the Fe and Pt MAE contributions in bulk FePt, respectively. Solid lines connecting the symbols serve as guides for the eye.

For system **A**, we obtained a reduction in the total MAE, $\Delta K_{\text{FePt-slab}}^{\text{A}} \approx -4.2 \text{ meV} \approx -9 \text{ mJ}\cdot\text{m}^{-2}$. This reduction stems primarily from the interfacial layers $i = \pm 9$, see Fig. 5.5. From this figure it is obvious that the contribution of the Fe layers $i = \pm 9$ to the MAE of the FePt slab is “missing” in the sense that, within system **A**, these Fe layers are more akin to bulk Fe. In system **B**, the interfacial Fe layers appear more FePt-like and exhibit enhanced contributions to the MAE. Moreover, as already mentioned, the MAE of the FePt phase settles more quickly in system **B** than in system **A**. Consequently, for system **B** the MAE of bulk FePt is almost entirely retained, $\Delta K_{\text{FePt-slab}}^{\text{B}} \approx -0.4 \text{ meV} \approx -0.9 \text{ mJ}\cdot\text{m}^{-2}$. We note that, in comparison to system **B**, the MAE contributions from layers $i = \pm 9$ in system **C** are smaller in relation to the bulk FePt MAE of system **C**. It is therefore reasonable to assume that, if we could perform the same calibration and calculation for system **C**, the value of $\Delta K_{\text{FePt-slab}}^{\text{C}}$ would be less negative than $\Delta K_{\text{FePt-slab}}^{\text{A}}$, but more negative than $\Delta K_{\text{FePt-slab}}^{\text{B}}$. Comparing the values of $\Delta K_{\text{FePt-slab}}$ for systems **A** and **B** to the total MAE of the FePt slab immersed in Fe, 26.9 meV, we conclude that the MAE of a realistic $(\text{Fe}_m/(\text{FePt})_k)_n$ ($m \gtrsim 10, k \gtrsim 9$) multilayer sequence is only very slightly reduced with respect to the MAE of $n \cdot k$ FePt bulk layers.

5.6 Summary and Conclusions

In this Chapter, we have presented first-principles calculations of the exchange interactions and the magnetocrystalline anisotropy energy (MAE) of three different Fe/FePt/Fe systems. One system was based on an unrelaxed geometry, exhibiting the experimental in-plane lattice parameter of FePt throughout, whereas the other two systems were based on an optimised Fe/FePt/Fe geometry obtained in CASTEP.² One of the two geometrically optimised systems was isotropically scaled up to the experimental FePt in-plane lattice parameter for direct comparison with the unrelaxed system.

In accordance with previous work on an unrelaxed Fe/FePt/Fe multilayer [52], we found a dramatic reduction in the effective exchange coupling at the Fe/FePt interface. Importantly, this reduction remains also in the geometrically optimised systems. The effective exchange of the (soft) Fe phase was found to be very sensitive to the geometry optimisation. This is an important find as the reduction of the effective write field in ECC media depends crucially on the (large) effective exchange of the soft phase. From the tensorial exchange interactions, evaluated by means of the relativistic torque method [133], we showed, furthermore, that the MAE of the FePt phase and the interface MAE are dominated by anisotropic inter-site exchange interactions. Our calculations also indicated that the formation of an Fe/FePt multilayer sequence reduces the perpendicular MAE with respect to the corresponding bulk FePt MAE, but only very slightly ($< 2\%$). This is also an important find as the thermal stability of Fe/FePt-based ECC media would be strongly dependent on the MAE of the FePt phase.

In terms of application to multiscale models, the results of this Chapter have already been mapped to a domain wall model, illustrating that the reduction of the effective exchange at the Fe/FePt interface leads to an abrupt change in the domain wall structure (see Fig. 5.9) [244].³ Moreover, the results in this Chapter strongly suggest that the magnetic anisotropy of the Fe/FePt nano-composite system can be properly accounted for within an anisotropic extended Heisenberg spin model containing tensorial exchange interactions. The fact that the MAE of the system could accurately be recovered from the spin model parameters, i.e., from the on-site and inter-site anisotropies, lends great support to the application of such parameters in localised-spin simula-

²The geometry optimisation was performed by Dr. P. J. Hasnip of the University of York, UK.

³The domain wall model and calculations were developed and performed by Prof. R. W. Chantrell of the University of York, UK.

tions. We can also conclude that the division of the total MAE into on-site and inter-site contributions yields consistent results with the work of Mryasov *et al.* [28].

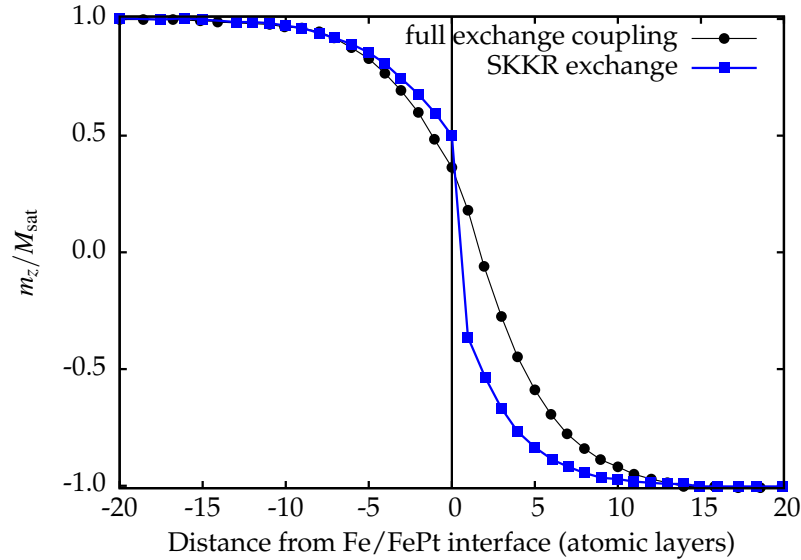


Figure 5.9: Blue ■: The abrupt break in a domain wall at an Fe/FePt interface due to weak interlayer coupling at the Fe/FePt interface. Black ●: the smooth domain wall of a fully exchange-coupled interface.

As for further work, it would be of significant interest to investigate the applicability of our results to models of FePt nanoparticles. For such finite-size systems, it would be of strong interest to investigate the effect of the aforementioned quantum interference effects between the two Fe/FePt interfaces by varying the thickness of the Fe and FePt phases. We expect, however, that a study diverse enough to draw any definite conclusions would be quite computationally intensive as, with our current setup, each one of the graphs in Fig. 5.5 corresponds to about 600 CPU hours.

Summary and Outlook

The overarching theme of the work presented in this thesis has been the optimisation of the magnetic properties of magnetic recording alloys. As the magnetic recording industry is moving towards technologies incorporating magnetic recording media of extremely high magnetocrystalline anisotropy energy (MAE), understanding the physical origins of any deviations in the MAE and other magnetic properties of high-MAE alloys constitutes an enormous field of research. In this thesis, we have explored a range of microstructural and compositional features that are believed to have an impact upon the magnetic properties of, in particular, CoPt and FePt. All our calculations have been performed within the same first-principles framework: the screened Korringa-Kohn-Rostoker (SKKR) method. Our aim has been two-fold. First there is the question of what, exactly, is the impact of these factors upon the magnetic properties of these alloys and how do these factors interact to yield a particular experimental outcome? Secondly, there is also the computational aspect – how can we combine these studies and how can we map our results onto larger-scale models?

First, we considered localised microstructural and compositional effects in hcp Co as Co-rich CoPt alloy is very commonly used as a magnetic recording medium in present devices (cf., e.g., [56]). We found that the presence of localised Pt alloying affects the MAE of hcp bulk Co primarily through the Pt-induced changes in the Co MAE contributions, rather than through the direct Pt MAE contributions. This leads to a situation where, although the direct Pt MAE contributions remain positive across all concentrations of Pt, the total change in the MAE is dominated by the Co contributions and, therefore, becomes negative at small Pt concentrations. In terms of the microstructure of Co alloys, we considered the effects of the presence of stacking faults on the

Co MAE. As expected from experiment, the presence of a stacking fault was generally found to reduce the MAE. Moreover, the effect of a composite stacking fault was found to be synergistic rather than additive, i.e., closely spaced stacking faults may have a greater impact upon the MAE than the sum of MAE deviations caused by each stacking fault in isolation.

Next, we considered the effects of chemical disorder, composition and unit cell shape on the MAE of L1₀-like Fe_xPt_{1-x} alloys. Such alloys are of significant interest to the magnetic recording industry for their potential application within exchange-coupled composite (ECC) media and within devices based on heat-assisted magnetic recording (HAMR) technology. In good agreement with previous work, we showed that the ratio of the FePt lattice parameters, c/a , is positively related to the FePt MAE, while the presence of chemical disorder drastically reduces the MAE. Moreover, we demonstrated good agreement between our calculations and the experimental trends of Refs. [57, 58], albeit with a magnitude offset. Furthermore, our calculations revealed that, as a consequence of the substrate-induced correlations between the lattice parameters, the chemical disorder and the composition within the experiments of Refs. [57, 58], the effects of chemical disorder and composition completely override any c/a -induced variations in the MAE. By evaluating independently the effects of chemical disorder and composition upon the MAE, we arrived at our main conclusion: the dominant factor in determining the MAE of FePt is, typically, the Fe concentration in the nominal Fe layers of the L1₀ structure. As a consequence, for any given degree of chemical order, the MAE will increase with increasing Fe content. As the Fe content in FePt is believed to stabilise the ferromagnetic state of FePt [206], this find is of significant importance.

Finally, we considered the impact of the Fe/FePt interface upon the magnetic properties of Fe/FePt nano-composites. Soft/hard nano-composites such as Fe/FePt are of strong technological interest for their potential application in ECC media. We showed that, for an Fe/FePt/Fe heterostructure, the total MAE of the system is only very slightly reduced with respect to the corresponding bulk FePt MAE. This suggests that an Fe/FePt ECC medium could exhibit a thermal stability close to that of bulk FePt. Moreover we showed that, although the soft (Fe) phase exhibits a strong coupling with the hard (FePt) phase, which is what enables the reduction of the effective write field within ECC media, this coupling is very sensitive to changes in the atomic layer separations. Furthermore, our calculations revealed a drastic reduction in the effective exchange at the Fe/FePt interface, which has a significant impact upon,

e.g., the domain wall dynamics at such an interface [244].

Across the systems studied, we noted some similarities in the behaviour of the MAE. First, reductions in the symmetry (caused by, e.g., chemical disorder or disruptions in the microstructure) often reduce the MAE, however, not always, as demonstrated by the stacking fault type I_2 in Chapter 3. Secondly, the presence of interfaces, surfaces, localised alloying and stacking faults all incur relatively long-ranged oscillations in the MAE. To some extent, these oscillations appear to be an effect of Friedel oscillations and other quantum interference effects. In some cases, the oscillatory behaviour is reminiscent of the effects of quantum well states (see, e.g., Refs. [254–256]). However, deriving a microscopic picture of the physical origins of these oscillations is probably non-trivial.

Looking back at our method, we note a number of strengths and weaknesses. We chose the screened Korringa-Kohn-Rostoker (SKKR) method primarily because its formalism allows for a computationally efficient description of systems and features exhibiting two-dimensional symmetry, such as, e.g., $L1_0$ lattices, stacking faults, surfaces and interfaces. The linear scaling of the computational effort with system size within the SKKR method allowed us to study relatively large systems and long-ranged variations in the magnetic properties. Moreover, SKKR-CPA, i.e., the combination of the SKKR method with the coherent potential approximation (CPA), is a method well suited to the description of substitutional alloys [170]. Although it exhibits the drawbacks of being a mean-field approach, the CPA does, in the relevant parts of our particular study, yield results in reasonable agreement with real-space calculations of localised substitutional disorder. Throughout our work, furthermore, we employed the local spin density approximation (LSDA). While the LSDA is a very commonly used exchange-correlation functional and while it appears to yield robust results in this work, it should be noted that it is relatively simplistic and only really applicable for systems in which the electron density varies relatively slowly. It should also be noted that our use of the atomic sphere approximation (ASA) could leave artefacts in the results originating in the overlap of the atomic spheres. Such artefacts are difficult to trace, however, the overlap within close-packed alloys is generally small [113]. Finally, a known weakness of the KKR method is the relatively slow convergence of the magnetic properties with the angular momentum cut-off, l_{max} , and the relatively costly scaling of computational effort with l_{max} . Our choice of $l_{max} = 3$ constituted a compromise between the available computational resources and

the accuracy provided by this cut-off. Despite these weaknesses of our approach, our results are consistent with previous calculations and experiments. We are therefore confident that the results presented in this thesis are at the very least qualitatively correct, hold some quantitative predictive power and are, in most cases, directly comparable to experiment. Nevertheless, it would be prudent to check the robustness of our results against non-ASA and non-LSDA approaches as well as, in particular, against calculations with larger angular momentum cut-offs.

With regards to the possible mapping of our results onto multiscale models of FePt, we note, in particular, three important facts. First, within our SKKR calculations, the main contribution to the FePt MAE is observed on the Fe sites, despite the fact that the large MAE of FePt is generally attributed to the strong spin-orbit coupling of Pt (see, e.g., Ref. [28]). This is an effect of the strong Fe 3d – Pt 5d hybridisation in FePt, causing the effect of the large spin-orbit coupling of Pt on the MAE to be observed on the Fe sites because the Fe sites exhibit stronger spin-polarisation [215]. For this reason, a direct mapping of our results onto the effective FePt Hamiltonian of Ref. [28] might not be possible. Secondly, we note that it is non-trivial to map our SKKR-CPA results for chemically disordered FePt onto an effective spin Hamiltonian because that would entail mapping mean-field results onto localised properties. However, we do note that, for ordered FePt, the division of the MAE into on-site and inter-site contributions as per the anisotropic Heisenberg Hamiltonian (which is the basis of the effective Hamiltonian in Ref. [28]) appears to be in good agreement with our results; our calculated MAE values could be accurately recovered from the sums of the on-site and inter-site anisotropies. Thus, although it might not be possible to map our results directly to already-existent localised-spin models of FePt, it might still be possible to construct an effective FePt Hamiltonian that can be parameterised by the results presented in this thesis.

In conclusion, we have, over the course of this thesis, shown that (a) localised compositional and microstructural disorder yields relatively long-ranged effects in the MAE, (b) the presence of localised or delocalised disorder generally reduces the total MAE (with a few exceptions) and (c) mapping our FePt results onto the effective FePt Hamiltonian of Mryasov *et al.* [28] might not be directly possible, however, the general idea of applying an SKKR-parameterised anisotropic Heisenberg-type Hamiltonian to FePt appears valid. In terms of taking the research further, it would be of strong interest to combine the results

of localised Pt alloying and stacking faults in Chapter 3 to predict possible effects of stacking faults on the Pt alloying process and the effect of having Pt impurities stuck at, or otherwise affected by, the presence of stacking faults. Moreover, for FePt it would be of strong interest to map our results to the commercial viability of different types of substrates and to the FePt phase diagram loci that these particular substrates allow. Finally, with regards to the aforementioned long-ranged oscillations in the MAE, we propose further systematic study of the related synergistic phenomena and finite-size effects.

Relations and Concepts within Multiple Scattering Theory

A.1 Propagators

The term *propagator* generally refers to an operator that propagates a state forwards in time [257]. Consider the time-dependent Schrödinger equation

$$\hat{H}\Psi_n(\mathbf{r},t) = i\hbar\frac{\partial}{\partial t}\Psi_n(\mathbf{r},t), \quad (\text{A.1})$$

and the time-independent Schrödinger equation

$$\hat{H}\psi_n(\mathbf{r}) = E_n\psi_n(\mathbf{r}). \quad (\text{A.2})$$

The stationary eigenstates of the time-dependent Schrödinger equation are

$$\Psi_n(\mathbf{r},t) = \psi_n(\mathbf{r})e^{-i\frac{E_n t}{\hbar}} \quad (\text{A.3})$$

for $n = 0, 1, \dots$, where the $\psi_n(\mathbf{r})$ are the eigenstates of the time-independent Schrödinger equation. These eigenstates $\{\psi_n(\mathbf{r})\}$ are orthonormal and form a complete set, i.e.

$$\int \psi_n(\mathbf{r})\psi_m(\mathbf{r})d\mathbf{r} = \delta_{nm} \quad \text{orthonormalisation}, \quad (\text{A.4})$$

$$\sum_n \psi_n(\mathbf{r})\psi_n^*(\mathbf{r}') = \delta(\mathbf{r} - \mathbf{r}') \quad \text{closure}. \quad (\text{A.5})$$

The completeness of the eigenfunctions $\{\psi_n(\mathbf{r})\}$ means that any wavefunction

$u(\mathbf{r}, t)$ may be expanded in the eigenfunctions $\{\psi_n(\mathbf{r})\}$ as

$$u(\mathbf{r}, t) = \sum_n c_n \psi_n(\mathbf{r}) e^{-i \frac{E_n t}{\hbar}}, \quad (\text{A.6})$$

where the expansion coefficients $\{c_n\}$ can be found from the overlap between $u(\mathbf{r}, t)$ and $\psi_n(\mathbf{r})$

$$c_n = \int \psi_n^*(\mathbf{r}) u(\mathbf{r}, 0) d\mathbf{r}, \quad (\text{A.7})$$

Thus, combining equations (A.6) and (A.7),

$$u(\mathbf{r}, t) = \sum_n \left[\int \psi_n^*(\mathbf{r}') u(\mathbf{r}', 0) d\mathbf{r}' \right] \psi_n(\mathbf{r}) e^{-i \frac{E_n t}{\hbar}} \quad (\text{A.8})$$

$$= \sum_n \left[\int \psi_n^*(\mathbf{r}') e^{-i \frac{E_n t}{\hbar}} \psi_n(\mathbf{r}) u(\mathbf{r}', 0) d\mathbf{r}' \right] \quad (\text{A.9})$$

$$= \int \left[\sum_n \psi_n^*(\mathbf{r}') e^{-i \frac{E_n t}{\hbar}} \psi_n(\mathbf{r}) u(\mathbf{r}', 0) \right] d\mathbf{r}' \quad (\text{A.10})$$

$$= \int \left[\sum_n \psi_n^*(\mathbf{r}') e^{-i \frac{E_n t}{\hbar}} \psi_n(\mathbf{r}) \right] u(\mathbf{r}', 0) d\mathbf{r}' \quad (\text{A.11})$$

$$= \int K(t; \mathbf{r}, \mathbf{r}') u(\mathbf{r}', 0) d\mathbf{r}', \quad (\text{A.12})$$

where the kernel is

$$K(t; \mathbf{r}, \mathbf{r}') = \sum_n \psi_n^*(\mathbf{r}') e^{-i \frac{E_n t}{\hbar}} \psi_n(\mathbf{r}) = \langle \mathbf{r}'' | \hat{K}(t) | \mathbf{r} \rangle. \quad (\text{A.13})$$

The operator $\hat{K}(t)$ is known as the *propagator* (or *quantum evolution operator*) since it propagates a state $u(\mathbf{r}, 0)$ to a later time, giving $u(\mathbf{r}, t)$. In other words, $K(t; \mathbf{r}, \mathbf{r}')$ is the probability amplitude of a particle propagating from position \mathbf{r} to position \mathbf{r}' in a given time t . The Laplace transform of $K(t; \mathbf{r}, \mathbf{r}')$ is the Green's function $G(z; \mathbf{r}, \mathbf{r}')$, meaning $\hat{G}(z)$ is also a propagator; it is the probability amplitude of propagation between \mathbf{r} and \mathbf{r}' for a particle of energy ε .

A.2 Dyson Equation

The Dyson equation relates the Green's function of a perturbed system, $\hat{G}_p(z)$, to the Green's function of an unperturbed system, $\hat{G}_0(z)$ [105, 258, 259]. Writing these two resolvents as

$$\hat{G}_0(z) = (z\hat{I} - \hat{H}_0)^{-1} \quad (\text{A.14})$$

$$\hat{G}_p(z) = (z\hat{I} - \hat{H})^{-1}, \quad (\text{A.15})$$

where $\hat{H} = \hat{H}_0 + \hat{V}$ and \hat{V} is the (Hermitian) perturbation, the relation

$$\hat{G}_p(z) = \hat{G}_0(z) + \hat{G}_p(z)\hat{V}\hat{G}_0(z) = \hat{G}_0(z) + \hat{G}_0(z)\hat{V}\hat{G}_p(z) \quad (\text{A.16})$$

is known as the *Dyson equation* [105, 258]. In terms of the configuration space representations, equation (A.16) can be written

$$G_p(z; \mathbf{r}, \mathbf{r}') = G_0(z; \mathbf{r}, \mathbf{r}') + \int G_0(z; \mathbf{r}, \mathbf{r}'')V(\mathbf{r}'')G_p(z; \mathbf{r}'', \mathbf{r}')d\mathbf{r}'' , \quad (\text{A.17})$$

where $G_p(z; \mathbf{r}', \mathbf{r}')$ again is the configuration space representation of the Green's function $\hat{G}_p(z)$.

The Dyson equation can be rewritten in an iterative fashion,

$$\hat{G}_p(z) = \hat{G}_0(z) + \hat{G}_0(z)\hat{V}\hat{G}_0(z) + \hat{G}_0(z)\hat{V}\hat{G}_0(z)\hat{V}\hat{G}_0(z) + \dots \quad (\text{A.18})$$

$$= \hat{G}_0(z) + \hat{G}_0(z) (\hat{V} + \hat{V}\hat{G}_0(z)\hat{V} + \dots) \hat{G}_0(z) . \quad (\text{A.19})$$

Defining the transition matrix, $\hat{T}(z)$,

$$\hat{T}(z) = \hat{V} + \hat{V}\hat{G}_0(z)\hat{V} + \hat{V}\hat{G}_0(z)\hat{V}\hat{G}_0(z)\hat{V} + \dots = \hat{V} + \hat{V}\hat{G}_p(z)\hat{V} , \quad (\text{A.20})$$

the Dyson equation can be written in closed form as

$$\hat{G}_p(z) = \hat{G}_0(z) + \hat{G}_0(z)\hat{T}(z)\hat{G}_0(z) . \quad (\text{A.21})$$

Note that the transition matrix is a geometric progression, i.e.

$$\hat{T}(z) = \hat{V} + \hat{V}\hat{G}_0(z)\hat{V} + \hat{V}\hat{G}_0(z)\hat{V}\hat{G}_0(z)\hat{V} + \dots = \hat{V} (\hat{I} - \hat{G}_0\hat{V})^{-1} . \quad (\text{A.22})$$

Note also that since

$$\hat{T}(z) = \hat{V} + \hat{V}\hat{G}_0(z)\hat{V} + \hat{V}\hat{G}_0(z)\hat{V}\hat{G}_0(z)\hat{V} + \dots = \hat{V} + \hat{V}\hat{G}_p(z)\hat{V} , \quad (\text{A.23})$$

and since

$$\hat{G}_p(z) = \hat{G}_0(z) + \hat{G}_0(z) (\hat{V} + \hat{V}\hat{G}_0(z)\hat{V} + \dots) \hat{G}_0(z) , \quad (\text{A.24})$$

it is true that

$$\hat{G}_p(z)\hat{V} = \hat{G}_0(z)\hat{T}(z) . \quad (\text{A.25})$$

A.3 Lippmann-Schwinger Equation

The *Lippmann-Schwinger equation* relates the eigenfunctions (i.e., the scattering solutions) of a perturbed system, $\{\psi_n^{(p)}\}$, to the eigenfunctions of an unperturbed system, $\{\psi_n^{(0)}\}$, as [260]

$$\psi^{(p)}(\mathbf{r}) = \psi^{(0)}(\mathbf{r}) + \int G_0(z; \mathbf{r}, \mathbf{r}') V(\mathbf{r}') \psi^{(p)}(\mathbf{r}') d\mathbf{r}', \quad (\text{A.26})$$

or, in operator notation,

$$|\psi^{(p)}\rangle = |\psi^{(0)}\rangle + \hat{G}_0(z) \hat{V} |\psi^{(p)}\rangle. \quad (\text{A.27})$$

The Lippmann-Schwinger equation may be derived as follows. Consider the two differential equations

$$(z\hat{I} - \hat{H}_0) |\psi^{(0)}\rangle = 0 \quad (\text{A.28})$$

$$\begin{aligned} (z\hat{I} - \hat{H}) |\psi^{(p)}\rangle &= (z\hat{I} - \hat{H}_0 - \hat{V}) |\psi^{(p)}\rangle = 0 \\ \Rightarrow (z\hat{I} - \hat{H}_0) |\psi^{(p)}\rangle &= \hat{V} |\psi^{(p)}\rangle. \end{aligned} \quad (\text{A.29})$$

The solution of equation (A.29) is the superposition of the general solution of the homogeneous equation (A.28) and the particular solution $|\psi_p^{(p)}\rangle$ of the inhomogeneous equation (A.29), i.e.,

$$|\psi^{(p)}\rangle = |\psi^{(0)}\rangle + |\psi_p^{(p)}\rangle. \quad (\text{A.30})$$

Substituting equation (A.30) into equation (A.29) yields

$$\begin{aligned} (z\hat{I} - \hat{H}_0) \left(|\psi^{(0)}\rangle + |\psi_p^{(p)}\rangle \right) &= \hat{V} |\psi^{(p)}\rangle \Rightarrow |\psi_p^{(p)}\rangle = (z\hat{I} - \hat{H}_0)^{-1} \hat{V} |\psi^{(p)}\rangle \\ &= \hat{G}_0(z) \hat{V} |\psi^{(p)}\rangle. \end{aligned} \quad (\text{A.31})$$

The final solution, i.e., the perturbed wavefunction, is thus

$$|\psi^{(p)}\rangle = |\psi^{(0)}\rangle + \hat{G}_0(z) \hat{V} |\psi^{(p)}\rangle. \quad (\text{A.32})$$

A.4 Lloyd's Formula

Lloyd's formula [261,262] relates the integrated density of states of a perturbed system \hat{H} in terms of the Green's function $\hat{G}_0(z)$ of the unperturbed system \hat{H}_0 and the perturbing potential \hat{V} (where $\hat{H} = \hat{H}_0 + \hat{V}$). The formula is ubiquitous

in multiple scattering theory and states that, for the integrated density of states $N(\varepsilon)$ of the perturbed system \hat{H} ,

$$N(\varepsilon) = N_0(\varepsilon) + \Delta N(\varepsilon), \quad (\text{A.33})$$

where

$$N_0(\varepsilon) = \int_{-\infty}^{\varepsilon} n_0(\varepsilon') d\varepsilon' = -\frac{1}{\pi} \int_{-\infty}^{\varepsilon} \text{Im} \left\{ \text{Tr} \left\{ \hat{G}_0^+(\varepsilon') \right\} \right\} d\varepsilon', \quad (\text{A.34})$$

and the quantity $\Delta N(\varepsilon)$ depends upon $\hat{G}_0(z)$ and \hat{V} as

$$\Delta N(\varepsilon) = -\frac{1}{\pi} \text{Im} \left\{ \text{Tr} \left\{ \ln \left\{ \hat{I} - \hat{G}_0^+(\varepsilon) \hat{V} \right\} \right\} \right\}. \quad (\text{A.35})$$

Lloyd's formula may be shown as follows (cf. e.g. [263]). First recall Dyson's equation (equation (A.16)), from which it can be seen that

$$\hat{G}_p(z) = \hat{G}_0(z) + \hat{G}_0(z) \hat{V} \hat{G}_p(z) = \hat{G}_0(z) (\hat{I} - \hat{V} \hat{G}_0(z))^{-1}. \quad (\text{A.36})$$

The (non-integrated) difference in the density of states between the perturbed and unperturbed states is

$$\Delta n(\varepsilon) = -\frac{1}{\pi} \text{Im} \left\{ \text{Tr} \left\{ \hat{G}_p(\varepsilon) - \hat{G}_0(\varepsilon) \right\} \right\} \quad (\text{A.37})$$

$$= -\frac{1}{\pi} \text{Im} \left\{ \text{Tr} \left\{ \hat{G}_0(\varepsilon) \hat{V} \hat{G}_p(\varepsilon) \right\} \right\} \quad (\text{A.38})$$

$$= -\frac{1}{\pi} \text{Im} \left\{ \text{Tr} \left\{ \hat{G}_0(\varepsilon) \hat{V} \hat{G}_0(\varepsilon) (\hat{I} - \hat{V} \hat{G}_0(\varepsilon))^{-1} \right\} \right\}. \quad (\text{A.39})$$

Using the identity [263]

$$\hat{G}_0(\varepsilon) \hat{G}_0(\varepsilon) = -\frac{d\hat{G}_0(\varepsilon)}{d\varepsilon}, \quad (\text{A.40})$$

it follows that

$$\Delta n(\varepsilon) = -\frac{1}{\pi} \text{Im} \left\{ \text{Tr} \left\{ \hat{G}_0(z) \hat{V} \hat{G}_0(z) (\hat{I} - \hat{V} \hat{G}_0(z))^{-1} \right\} \right\} \quad (\text{A.41})$$

$$= -\frac{1}{\pi} \text{Im} \left\{ \text{Tr} \left\{ \frac{d}{d\varepsilon} (\ln \{ \hat{I} - \hat{V} \hat{G}_0(z) \}) \right\} \right\}. \quad (\text{A.42})$$

The difference in the *integrated* density of states between the two systems, $\Delta N(\varepsilon)$ is thus

$$\Delta N(\varepsilon) = -\frac{1}{\pi} \text{Im} \left\{ \text{Tr} \left\{ \ln \left\{ \hat{I} - \hat{V} \hat{G}_0(\varepsilon) \right\} \right\} \right\}, \quad (\text{A.43})$$

which is Lloyd's formula. For a real potential \hat{V} , using equation (A.22), Lloyd's

formula can be written in terms of the transition matrix $\hat{T}(\varepsilon)$,

$$\Delta N(\varepsilon) = \frac{1}{\pi} \text{Im} \left\{ \text{Tr} \left\{ \ln \left\{ \hat{T}(\varepsilon) \right\} \right\} \right\} . \quad (\text{A.44})$$

A.5 The Coherent Potential Approximation

The coherent potential approximation (CPA) [137–140] is similar to the VCA in that it entails using an effective potential to describe chemical disorder in a binary alloy [141]. In contrast to the VCA, however, the effective potential within the CPA is derived directly from the scattering properties of the disordered system. At the heart of the CPA is the idea that, for any given level of chemical disorder s , one may consider the Green's function $\hat{G}(z)$ averaged over the entire set of realisations of this particular disorder s (i.e., all the different configurations of corresponding to this particular level of disorder s) as an effective Green's function $\hat{\mathfrak{G}}(z)$, i.e.,

$$\langle \hat{G}(z) \rangle = \left\langle \frac{1}{z - \hat{H}} \right\rangle = \hat{\mathfrak{G}}(z) = \frac{1}{z - \hat{\mathfrak{H}}} , \quad (\text{A.45})$$

where $\hat{\mathfrak{H}}$ is the Hamiltonian of an effective medium defining the *coherent potential* V_{CPA} . For each electron, the local potential experienced by that electron is replaced by the coherent potential.

Let us define \hat{V} as the superposition of local (real) site potentials

$$\hat{V} = \sum_j \hat{V}_j = \sum_j (\Gamma_j \hat{V}_A(\mathbf{r}_i) + (1 - \Gamma_j) \hat{V}_B(\mathbf{r}_i)) , \quad (\text{A.46})$$

where Γ_j is the occupation variable; $\Gamma_j = 1$ if site j is occupied by species A and $\Gamma_j = 0$ if site j is occupied by species B. Let us also define $\hat{\mathcal{W}}(z)$ as the superposition of (energy-dependent) translationally invariant site potentials

$$\hat{\mathcal{W}}(z) = \sum_j \hat{\mathcal{W}}_j(z) . \quad (\text{A.47})$$

Using definitions (A.46) and (A.47) the Hamiltonian \hat{H} can now be rewritten in terms of the effective Hamiltonian $\hat{\mathfrak{H}}$ as

$$\hat{H} = \hat{\mathfrak{H}} + \hat{V} - \hat{\mathcal{W}}(z) = \hat{\mathfrak{H}} + \hat{\mathfrak{B}}(z) , \quad (\text{A.48})$$

with

$$\hat{\mathfrak{B}}(z) = \sum_j \hat{\mathfrak{B}}_j(z). \quad (\text{A.49})$$

In terms of the effective medium,

$$\hat{G}(z) = \frac{1}{z - \hat{\mathfrak{H}} - \hat{\mathfrak{B}}(z)} \quad (\text{A.50})$$

$$\hat{\mathfrak{G}}(z) = \frac{1}{z - \hat{\mathfrak{H}}}. \quad (\text{A.51})$$

Treating $\hat{\mathfrak{B}}(z)$ as a perturbation potential, the following Dyson equations (cf. Eq.s (A.20) and (A.25)) may be written down

$$\hat{T}(z) = \hat{\mathfrak{B}}(z) + \hat{\mathfrak{B}}(z)\hat{\mathfrak{G}}(z)\hat{\mathfrak{B}}(z) \quad (\text{A.52})$$

$$\hat{G}(z) = \hat{\mathfrak{G}}(z) + \hat{\mathfrak{G}}(z)\hat{T}(z)\hat{\mathfrak{G}}(z). \quad (\text{A.53})$$

Since the effective Green's function $\hat{\mathfrak{G}}(z)$ has to be identical to its own configuration average (by definition of the effective medium), it can be seen that

$$\langle \hat{G}(z) \rangle = \hat{\mathfrak{G}}(z) + \hat{\mathfrak{G}}(z)\langle \hat{T}(z) \rangle \hat{\mathfrak{G}}(z). \quad (\text{A.54})$$

Thus, the CPA requirement $\langle \hat{G}(z) \rangle = \hat{\mathfrak{G}}(z)$ is fulfilled if and only if

$$\langle \hat{T}(z) \rangle = 0. \quad (\text{A.55})$$

Eq. (A.55) is known as the Coherent Potential Approximation [105] and has to be solved in an iterative fashion to self-consistency. From a physical point of view, it means that there should be zero additional scattering of the effective medium with respect to the configuration-averaged medium [141]. The CPA is generally considered a more consistent and, overall, better approach than the VCA as the effective potential of the VCA is derived from averaging the Hamiltonian at the outset, whereas the coherent potential is derived from averaging the scattering properties themselves [142]. As the CPA can be expressed as a condition on $\hat{T}(z)$, it fits very nicely into the SKKR formalism (see, e.g., [105, 140]).

References

- [1] K. J. Thurlow. *Chemical Nomenclature*. Berlin–Heidelberg–New York: Springer–Verlag, 1998.
- [2] N. Ida. *Engineering Electromagnetics*. Berlin–Heidelberg–New York: Springer–Verlag, 2004.
- [3] É. du Trémolet de Lacheisserie, D. Gignoux and M. Schlenker. *Magnetism: Fundamentals*. Berlin–Heidelberg–New York: Springer–Verlag, 2005.
- [4] E. D. Daniel, C. D. Mee and M. H. Clark. *Magnetic Recording: The First 100 Years*. New York: IEEE Press, 1999.
- [5] F. K. Engel. 1888-1988: A hundred years of magnetic sound recording. *Journal of the Audio Engineering Society*, 36:170, 1988.
- [6] M. Camras. *Magnetic Recording Handbook*. Berlin–Heidelberg–New York: Springer-Verlag, 1988.
- [7] A. A. Mamun, G. Guo, and C. Bi. *Hard Disk Drive: Mechatronics and Control*. Boca Raton: Taylor & Francis (CRC Press), 2006.
- [8] J. C. Mallinson. *The Foundations of Magnetic Recording 2E*. San Diego: Academic Press, 1993.
- [9] G. Hughes. *Hard Drive!: As the Disc Turns*. Charleston: BookSurge Publishing, 2007.
- [10] P. Kim and M. Suk. Ramp load/unload technology in hard disk drives. *Hitachi GST (White Paper)*, November 2007.
- [11] H.J. Richter. Density limits imposed by the microstructure of magnetic recording media. *Journal of Magnetism and Magnetic Materials*, 321:467, 2009.

- [12] Seagate Technology. Seagate reaches 1 terabit per square inch milestone in hard drive storage with new technology demonstration [press release]. March 2012.
- [13] H. Regensburger, R. Vollmer, and J. Kirschner. Time-resolved magnetization-induced second-harmonic generation from the Ni(110) surface. *Physical Review B*, 61:14716, 2000.
- [14] E. Beaurepaire, J.-C. Merle, A. Daunois, and J.-Y. Bigot. Ultrafast spin dynamics in ferromagnetic nickel. *Physical Review Letters*, 76:4250, 1996.
- [15] J. Hohlfeld, E. Matthias, R. Knorren, and K. H. Bennemann. Nonequilibrium magnetization dynamics of nickel. *Physical Review Letters*, 78:4861, 1997.
- [16] A. Scholl, L. Baumgarten, R. Jacquemin, and W. Eberhardt. Ultrafast spin dynamics of ferromagnetic thin films observed by fs spin-resolved two-photon photoemission. *Physical Review Letters*, 79:5146, 1997.
- [17] B. Koopmans, M. van Kampen, J. T. Kohlhepp, and W. J. M. de Jonge. Ultrafast magneto-optics in nickel: Magnetism or optics? *Physical Review Letters*, 85:844, 2000.
- [18] Th. Gerrits, H. A. M. van den Berg, J. Hohlfeld, L. Bär, and Th. Rasing. Ultrafast precessional magnetization reversal by picosecond magnetic field pulse shaping. *Nature*, 418:509, 2002.
- [19] A. V. Kimel, A. Kirilyuk, P. A. Usachev, R. V. Pisarev, A. M. Balbashov, and Th. Rasing. Ultrafast non-thermal control of magnetization by instantaneous photomagnetic pulses. *Nature*, 435:655, 2005.
- [20] B. Koopmans, J. J. M. Ruigrok, F. Dalla Longa, and W. J. M. de Jonge. Unifying ultrafast magnetization dynamics. *Physical Review Letters*, 95:267207, 2005.
- [21] T. A. Ostler, J. Barker, R. F. L. Evans, R. W. Chantrell, U. Atxitia, O. Chubykalo-Fesenko, S. El Moussaoui, L. Le Guyader, E. Mengotti, L. J. Heyderman, F. Nolting, A. Tsukamoto, A. Itoh, D. Afanasiev, B. A. Ivanov, A. M. Kalashnikova, K. Vahaplar, J. Mentink, A. Kirilyuk, Th. Rasing, and A. V. Kimel. Ultrafast heating as a sufficient stimulus for magnetization reversal in a ferrimagnet. *Nature Communications*, 3:666, 2012.

- [22] I. Turek, J. Kudrnovský, V. Drchal, and P. Bruno. Exchange interactions, spin waves, and transition temperatures in itinerant magnets. *Philosophical Magazine*, 86:1713, 2006.
- [23] J. Kübler. Ab initio estimates of the Curie temperature for magnetic compounds. *Journal of Physics: Condensed Matter*, 18:9795, 2006.
- [24] A. V. Andrianov, O. A. Saveléva, E. Bauer, and J. B. Staunton. Squeezing the crystalline lattice of the heavy rare-earth metals to change their magnetic order: Experiment and *ab initio* theory. *Physical Review B*, 84:132401, 2011.
- [25] S. Ouazi, S. Vlaic, S. Rusponi, G. Moulas, P. Bulushek, K. Halleux, S. Bornemann, S. Mankovsky, J. Minár, J.B. Staunton, H. Ebert, and H. Brune. Atomic-scale engineering of magnetic anisotropy of nanostructures through interfaces and interlines. *Nature Communications*, 3:1313, 2012.
- [26] J. B. Staunton. The electronic structure of magnetic transition metallic materials. *Reports on Progress in Physics*, 57:1289, 1994.
- [27] J. Thoene, S. Chadov, G. Fecher, C. Felser, and J. Kübler. Exchange energies, Curie temperatures and magnons in Heusler compounds. *Journal of Physics D: Applied Physics*, 42:084013, 2009.
- [28] O. N. Mryasov, U. Nowak, K. Y. Guslienko, and R. W. Chantrell. Temperature-dependent magnetic properties of FePt: Effective spin Hamiltonian model. *Europhysics Letters*, 69:805, 2005.
- [29] N. Kazantseva, D. Hinzke, U. Nowak, R. W. Chantrell, and O. Chubykalo-Fesenko. Atomistic models of ultrafast reversal. *Physica Status Solidi (b)*, 244:4389, 2007.
- [30] N. Kazantseva, D. Hinzke, U. Nowak, R. W. Chantrell, U. Atxitia, and O. Chubykalo-Fesenko. Towards multiscale modeling of magnetic materials: Simulations of FePt. *Physical Review B*, 77:184428, 2008.
- [31] L. Szunyogh, L. Udvardi, J. Jackson, U. Nowak, and R. W. Chantrell. Atomistic spin model based on a spin-cluster expansion technique: Application to the IrMn₃/Co interface. *Physical Review B*, 83:024401, 2011.
- [32] F. Garcia-Sanchez, O. Chubykalo-Fesenko, O. N. Mryasov, and R. W. Chantrell. Multiscale models of hard-soft composite media. *Journal of Magnetism and Magnetic Materials*, 303:282, 2006.

- [33] H. J. Richter and A. Yu. Dobin. Angle effects at high-density magnetic recording. *Journal of Magnetism and Magnetic Materials*, 287:41, 2005.
- [34] M. Martin, L. Plumer, J. van Elk, and D. Weller. *The Physics of Ultrahigh-Density Magnetic Recording*. Berlin–Heidelberg–New York: Springer–Verlag, 2001.
- [35] J. Mallinson. On extremely high density digital recording. *IEEE Transactions on Magnetics*, 10:368, 1974.
- [36] H. J. Richter and S. D. Harkness. Media for magnetic recording beyond 100 Gbit/in². *Materials Research Society Bulletin*, 31:384, 2006.
- [37] Y. Song. *High Density Data Storage: Principle, Technology, and Materials*. Singapore: World Scientific, 2009.
- [38] D. Weller, A. Moser, L. Folks, M. E. Best, W. Lee, M. F. Toney, M. Schwickert, J.-U. Thiele, and M. F. Doerner. High K_u materials approach to 100 Gbits/in². *IEEE Transactions on Magnetics*, 36:10, 2000.
- [39] R.E. Rottmayer, S. Batra, D. Buechel, W. A. Challener, J. Hohlfield, Y. Kubota, L. Li, B. Lu, C. Mihalcea, K. Mountfield, K. Pelhos, C. Peng, T. Rausch, M. A. Seigler, D. Weller, and X. Yang. Heat-assisted magnetic recording. *IEEE Transactions on Magnetics*, 42:2417, 2006.
- [40] S. N. Piramanayagam and T. C. Chong. *Developments in Data Storage: Materials Perspective*. Chichester: John Wiley & Sons Ltd., 2011.
- [41] D. Suess, T. Schrefl, S. Fahler, M. Kirschner, G. Hrkac, F. Dorfbauer, and J. Fidler. Exchange spring media for perpendicular recording. *Applied Physics Letters*, 87:012504, 2005.
- [42] D. Suess, T. Schrefl, R. Dittrich, M. Kirschner, F. Dorfbauer, G. Hrkac, and J. Fidler. Exchange spring recording media for areal densities up to 10 Tbit/in². *Journal of Magnetism and Magnetic Materials*, 290–291:551, 2005.
- [43] R. H. Victora and X. Shen. Composite media for perpendicular magnetic recording. *IEEE Transactions on Magnetics*, 41:537, 2005.
- [44] W. K. Shen, J. M. Bai, R. H. Victora, J. H. Judy, and J.-P. Wang. Composite perpendicular magnetic recording media using [Co/PdSi]_n as a hard layer and FeSiO as a soft layer. *Journal of Applied Physics*, 97:10N513, 2005.
- [45] J. M. D. Coey. *Magnetism and Magnetic Materials*. Cambridge: Cambridge University Press, 2010.

- [46] T. Klemmer, D. Hoydick, H. Okumura, B. Zhang, and W. A. Soffa. Magnetic hardening and coercivity mechanisms in $L1_0$ ordered FePd ferromagnets. *Scripta Metallurgica et Materialia*, 33:1793, 1995.
- [47] K. Ouchi. Recent advancements in perpendicular magnetic recording. *IEEE Transactions on Magnetics*, 37:1217, 2001.
- [48] S. Iwata, S. Yamashita, and S. Tsunashima. Perpendicular magnetic anisotropy and magneto-optical Kerr spectra of MBE-grown PtCo alloy films. *IEEE Transactions on Magnetics*, 33:3670, 1997.
- [49] S. Yamashita, S. Iwata, and S. Tsunashima. Magnetic anisotropy and magneto-optical effect of MBE-grown PtCo alloy films. *Journal of the Magnetics Society of Japan*, 21:433, 1997.
- [50] S. Sun, C. B. Murray, D. Weller, L. Folks, and A. Moser. Monodisperse FePt nanoparticles and ferromagnetic FePt nanocrystal superlattices. *Science*, 287:1989, 2000.
- [51] J. Zhou, R. Skomski, X. Li, W. Tang, G. C. Hadjipanayis, and D. J. Sellmyer. Permanent-magnet properties of thermally processed FePt and FePt-Fe multilayer films. *IEEE Transactions on Magnetics*, 38:2802, 2002.
- [52] R. F. Sabiryanov and S. S. Jaswal. Electronic structure and magnetic properties of hard/soft multilayers. *Journal of Magnetism and Magnetic Materials*, 177–181:989, 1998.
- [53] S. Ostanin, S. S. A. Razee, J. B. Staunton, B. Ginatempo, and E. Bruno. Magnetocrystalline anisotropy and compositional order in $Fe_{0.5}Pt_{0.5}$: Calculations from an *ab initio* electronic model. *Journal of Applied Physics*, 93:453, 2003.
- [54] Y. Kota and A. Sakuma. Magnetocrystalline anisotropy in FePt with $L1_0$ ordering and tetragonal distortion. *Journal of Applied Physics*, 111:07A310, 2012.
- [55] C. J. Aas, L. Szunyogh, J. S. Chen, and R. W. Chantrell. Magnetic anisotropy of FePt: Effect of lattice distortion and chemical disorder. *Applied Physics Letters*, 99:132501, 2011.
- [56] V. Sokalski, D. E. Laughlin, and J.-G. Zhu. Magnetic anisotropy and stacking faults in Co and $Co_{84}Pt_{16}$ epitaxially grown thin films. *Journal of Applied Physics*, 110:093919, 2011.

- [57] Y. F. Ding, J. S. Chen, E. Liu, C. J. Sun, and G. M. Chow. Effect of lattice mismatch on chemical ordering of epitaxial L1₀ FePt films. *Journal of Applied Physics*, 97:10H303, 2005.
- [58] K. Barmak, J. Kim, L. H. Lewis, K. R. Coffey, M. F. Toney, A. J. Kellock, and J.-U. Thiele. On the relationship of magnetocrystalline anisotropy and stoichiometry in epitaxial L1₀ CoPt (001) and FePt (001) thin films. *Journal of Applied Physics*, 98:033904, 2005.
- [59] D. N. Lambeth, E. M. T. Velu, G. H. Bellesis, L. L. Lee, and D. E. Laughlin. Media for 10 Gb/in.² hard disk storage: Issues and status (invited). *Journal of Applied Physics*, 79:4496, 1996.
- [60] M. Yu, M. F. Doerner, and D. J. Sellmyer. Thermal stability and nanostructure of CoCrPt longitudinal recording media. *IEEE Transactions on Magnetism*, 34:1534, 1998.
- [61] R. Skomski. *Simple Models of Magnetism*. Oxford: Oxford University Press, 2008.
- [62] S. Blundell. *Magnetism in Condensed Matter*. Oxford: Oxford University Press, 2001.
- [63] J. Kübler. *Theory of Itinerant Magnetism*. Oxford: Oxford University Press, 2000.
- [64] Q. Niu, X. Wang, L. Kleinman, W.-M. Liu, D. M. C. Nicholson, and G. M. Stocks. Adiabatic dynamics of local spin moments in itinerant magnets. *Physical Review Letters*, 83:207, 1999.
- [65] J. P. Liu, E. Fullerton, and O. Gutfleisch. *Nanoscale Magnetic Materials and Applications*. Berlin–Heidelberg–New York: Springer–Verlag, 2009.
- [66] T. Moriya. *Spin fluctuations in itinerant electron magnetism*. Berlin–Heidelberg–New York: Springer–Verlag, 1985.
- [67] E. C. Stoner. Collective electron ferromagnetism. *Proceedings of the Royal Society of London. Series A. Mathematical and Physical Sciences*, 165:372, 1938.
- [68] F. Bloch. Bemerkung zur elektronentheorie des ferromagnetismus und der elektrischen leitfähigkeit. *Zeitschrift für Physik*, 57:545, 1929.
- [69] W. Heisenberg. Zur theorie des ferromagnetismus. *Zeitschrift für Physik*, 49:619, 1928.

- [70] J. H. van Vleck. Models of exchange coupling in ferromagnetic media. *Reviews of Modern Physics*, 25:220, 1953.
- [71] J. Friedel, G. Leman, and S. Olszewski. On the nature of the magnetic couplings in transitional metals. *Journal of Applied Physics*, 32:S325, 1961.
- [72] J. Hubbard. The magnetism of iron. *Physical Review B*, 19:2626, 1979.
- [73] M. V. You and V. Heine. Magnetism in transition metals at finite temperatures. I. Computational model. *Journal of Physics F: Metal Physics*, 12:177.
- [74] A. J. Pindor, J. B. Staunton, G. M. Stocks, and H. Winter. Disordered local moment state of magnetic transition metals: a self-consistent KKR CPA calculation. *Journal of Physics F: Metal Physics*, 13:979.
- [75] M. A. Ruderman and C. Kittel. Indirect exchange coupling of nuclear magnetic moments by conduction electrons. *Physical Review*, 96:99, 1954.
- [76] T. Kasuya. A theory of metallic ferro- and antiferromagnetism on Zener's model. *Progress of Theoretical Physics*, 16:45, 1956.
- [77] K. Yosida. Magnetic properties of Cu-Mn alloys. *Physical Review*, 106:893, 1957.
- [78] W. Nolting and A. Ramakanth. *Quantum theory of magnetism*. Berlin–Heidelberg–New York: Springer–Verlag, 2008.
- [79] J. H. van Vleck. On the anisotropy of cubic ferromagnetic crystals. *Physical Review*, 52:1178, 1937.
- [80] P. Bruno. Tight-binding approach to the orbital magnetic moment and magnetocrystalline anisotropy of transition-metal monolayers. *Physical Review B*, 39:865, 1989.
- [81] P. Bruno. *Magnetismus von Festkörpern und Grenzflächen*. Jülich: Ferienkurse des Forschungszentrums Jülich, 1993.
- [82] C. A. F. Vaz, J. A. C. Bland, and G. Lauhoff. Magnetism in ultrathin film structures. *Reports on Progress in Physics*, 71:056501.
- [83] D. Jiles. *Magnetism and Magnetic Materials 2E*. Boca Raton: Taylor & Francis, 1998.
- [84] E. Engel and R. M. Dreizler. *Density Functional Theory – an Advanced Course*. Berlin–Heidelberg–New York: Springer–Verlag, 2011.

- [85] G. Grosso and G. Pastori Parravicini. *Solid State Physics*. London: Academic Press, 2000.
- [86] P. Hohenberg and W. Kohn. Inhomogeneous electron gas. *Physical Review*, 336:B864, 1964.
- [87] A. K. Rajagopal and J. Callaway. Inhomogeneous electron gas. *Physical Review B*, 7:1912, 1973.
- [88] A. K. Rajagopal. Inhomogeneous relativistic electron gas. *Journal of Physics C: Solid State Physics*, 11:L943, 1978.
- [89] A. H. MacDonald and S. H. Vosko. A relativistic density functional formalism. *Journal of Physics C: Solid State Physics*, 12:2977, 1979.
- [90] W. Kohn, A. Savin, and C. A. Ullrich. Hohenberg–Kohn theory including spin magnetism and magnetic fields. *International Journal of Quantum Chemistry*, 100:20, 2004.
- [91] W. Kohn and L. J. Sham. Self-consistent equations including exchange and correlation effects. *Physical Review*, 140:A1133, 1965.
- [92] M. D. Segall, P. J. D. Lindan, M. J. Probert, C. J. Pickard, P. J. Hasnip, S. J. Clark, and M. C. Payne. First-principles simulation: ideas, illustrations and the CASTEP code. *Journal of Physics: Condensed Matter*, 14:2717, 2002.
- [93] M. C. Payne, M. P. Teter, D. C. Allan, T. A. Arias, and J. D. Joannopoulos. Iterative minimization techniques for *ab initio* total-energy calculations: molecular dynamics and conjugate gradients. *Reviews of Modern Physics*, 64:1045, 1992.
- [94] S. J. Clark, M. D. Segall, C. J. Pickard, P. J. Hasnip, M. J. Probert, K. Refson, and M. C. Payne. First principles methods using CASTEP. *Zeitschrift für Kristallographie*, 220:567, 2005.
- [95] G. Kresse and J. Furthmüller. Efficient iterative schemes for *ab initio* total-energy calculations using a plane-wave basis set. *Physical Review B*, 54:11169, 1996.
- [96] G. Kresse and J. Hafner. *Ab initio* molecular dynamics for liquid metals. *Physical Review B*, 47:558, 1993.
- [97] G. Kresse and J. Furthmüller. Efficiency of *ab initio* total energy calculations for metals and semiconductors using a plane-wave basis set. *Computational Materials Science*, 6:15, 1996.

- [98] G. Kresse and J. Hafner. *Ab initio* molecular-dynamics simulation of the liquid-metal–amorphous-semiconductor transition in germanium. *Physical Review B*, 49:14251, 1994.
- [99] H. J. F. Jansen. Magnetic anisotropy in density-functional theory. *Physical Review B*, 59:4699, 1999.
- [100] U. von Barth and L. Hedin. A local exchange-correlation potential for the spin polarized case. i. *Journal of Physics C: Solid State Physics*, 5:1629, 1972.
- [101] D. M. Ceperley and B. J. Alder. Ground state of the electron gas by a stochastic method. *Physical Review Letters*, 45:566, 1980.
- [102] S. H. Vosko, L. Wilk, and M. Nusair. Accurate spin-dependent electron liquid correlation energies for local spin density calculations: a critical analysis. *Canadian Journal of Physics*, 58:1200, 1980.
- [103] J. Korringa. On the calculation of the energy of a Bloch wave in a metal. *Physica*, 13:392, 1947.
- [104] W. Kohn and N. Rostoker. Solution of the Schrödinger equation in periodic lattices with an application to metallic lithium. *Physical Review*, 94:1111, 1954.
- [105] J. Zabloudil, R. Hammerling, L. Szunyogh and P. Weinberger. *Electron Scattering in Solid Matter - A Theoretical and Computational Treatise*. Berlin–Heidelberg–New York: Springer–Verlag, 2005.
- [106] H. Ebert, D. Ködderitzsch, and J. Minár. Calculating condensed matter properties using the KKR-Green’s function method – recent developments and applications. *Reports on Progress in Physics*, 74:096501, 2011.
- [107] R. G. Newton. *Scattering Theory of Waves and Particles 2E*. New York: Dover Publications, 2002.
- [108] P. Weinberger. *Magnetic Anisotropies in Nanostructured Matter*. Boca Raton: Taylor & Francis, 2009.
- [109] S. Gasiorowicz. *Quantum Physics 3E*. Chichester: John Wiley & Sons Ltd., 2003.
- [110] O. K. Anderson. Simple approach to the band-structure problem. *Solid State Communications*, 13:133, 1973.

- [111] O. K. Anderson. Linear methods in band theory. *Physical Review B*, 12:3060, 1975.
- [112] L. Skriver. *The LMTO Method*. Berlin–Heidelberg–New York: Springer–Verlag, 1983.
- [113] O. Gunnarsson, O. Jepsen, and O. K. Andersen. Self-consistent impurity calculations in the atomic-spheres approximation. *Physical Review B*, 27:7144, 1983.
- [114] P. P. Singh and A. Gonis. Effective cluster interactions using the generalized perturbation method in the atomic-sphere approximation. *Physical Review B*, 47:6744, 1993.
- [115] J. Zabloudil. *The full-potential screened KKR method*. PhD thesis, University of Vienna, 2000.
- [116] W. H. Butler, A. Gonis, and X.-G. Zhang. Multiple-scattering theory for space-filling cell potentials. *Physical Review B*, 45:11527, 1992.
- [117] B. L. Györfy and G. M. Stocks. *Band Structure Spectroscopy of Metals and Alloys*, ed. D. J. Fabian and L. M. Watson. New York: Academic Press, 1972.
- [118] M. E. Rose. *Relativistic Electron Theory*. New York: John Wiley & Sons Ltd., 1961.
- [119] N. Y. Moghadam, G. M. Stocks, X.-G. Zhang, D. M. C. Nicholson, W. A. Shelton, Y. Wang, and J. S. Faulkner. Angular momentum convergence of Korringa-Kohn-Rostoker Green's function methods. *Journal of Physics: Condensed Matter*, 13:3073, 2001.
- [120] R. Zeller. Projection potentials and angular momentum convergence of total energies in the full-potential Korringa-Kohn-Rostoker method. *Journal of Physics: Condensed Matter*, 25:105505, 2013.
- [121] L. Szunyogh, B. Újfalussy, P. Weinberger and J. Kollár. Self-consistent localized KKR scheme for surfaces and interfaces. *Physical Review B*, 49:2721, 1994.
- [122] R. Zeller, P. H. Dederichs, B. Újfalussy, L. Szunyogh and P. Weinberger. Theory and convergence properties of the screened Korringa-Kohn-Rostoker method. *Physical Review B*, 52:8807, 1995.
- [123] J. Schwitalla and B. L. Györfy. On the 'screened' Korringa-Kohn-Rostoker (KKR) method for calculating the electronic structure of solids. *Journal of Physics: Condensed Matter*, 10:10955, 1998.

- [124] M. Weinert, R. E. Watson, and J. W. Davenport. Total-energy differences and eigenvalue sums. *Physical Review B*, 32:2115, 1985.
- [125] J. B. Staunton, S. Ostanin, S. S. A. Razee, B. L. Győrffy, L. Szunyogh, B. Ginatempo, and E. Bruno. Temperature dependent magnetic anisotropy in metallic magnets from an *ab Initio* electronic structure theory: $L1_0$ -ordered FePt. *Physical Review Letters*, 93:257204, 2004.
- [126] A. I. Liechtenstein, M. I. Katsnelson, V. P. Antropov and V. A. Gubanov. Local spin density functional approach to the theory of exchange interactions in ferromagnetic metals and alloys. *Journal of Magnetism and Magnetic Materials*, 67:65, 1987.
- [127] P. Bruno. Exchange interaction parameters and adiabatic spin-wave spectra of ferromagnets: A *renormalized* magnetic force theorem. *Physical Review Letters*, 90:087205, 2003.
- [128] A. Chitchekanova, S. A. Wolf, and Y. Idzerda. *Magnetic interactions and spin transport*. Berlin–Heidelberg–New York: Springer–Verlag, 2003.
- [129] G. H. O. Daalderop, P. J. Kelly, and M. F. H. Schuurmans. Magnetocrystalline anisotropy and orbital moments in transition-metal compounds. *Physical Review B*, 44:12054, 1991.
- [130] P. Strange, H. Ebert, J. B. Staunton, and B. L. Győrffy. A first principles theory of magnetocrystalline anisotropy in metals. *Journal of Physics: Condensed Matter*, 1:3947, 1989.
- [131] X. Wang, R. Wu, D. Wang, and A. J. Freeman. Torque method for the theoretical determination of magnetocrystalline anisotropy. *Physical Review B*, 54:61, 1996.
- [132] J. B. Staunton, L. Szunyogh, A. Buruzs, B. L. Győrffy, S. Ostanin, and L. Udvardi. Temperature dependence of magnetic anisotropy: An *ab initio* approach. *Physical Review B*, 74:144411, 2006.
- [133] L. Udvardi, L. Szunyogh, K. Palotás, and P. Weinberger. First-principles relativistic study of spin waves in thin magnetic films. *Physical Review B*, 68:104436, 2003.
- [134] L. Nordheim. The electron theory of metals. *Annalen der Physik (Leipzig)*, 9:607, 1931.
- [135] R. H. Parmenter. Energy levels of a disordered alloy. *Physical Review*, 97:587, 1955.

- [136] L. Bellaiche and D. Vanderbilt. Virtual crystal approximation revisited: Application to dielectric and piezoelectric properties of perovskites. *Physical Review B*, 61:7877, 2000.
- [137] P. Soven. Coherent-potential model of substitutional disordered alloys. *Physical Review*, 156:809, 1967.
- [138] P. Soven. Contribution to the theory of disordered alloys. *Physical Review*, 178:1136, 1969.
- [139] B. Velicky, S. Kirkpatrick, and H. Ehrenreich. Single-site approximations in the electronic theory of simple binary alloys. *Physical Review*, 175:747, 1968.
- [140] G. M. Stocks, W. M. Temmerman, and B. L. Gyórfy. Complete solution of the Korringa-Kohn-Rostoker coherent-potential-approximation equations: Cu-Ni alloys. *Physical Review Letters*, 41:339, 1978.
- [141] R. M. Martin. *Electronic Structure: Basic Theory and Practical Methods*. Cambridge: Cambridge University Press, 2004.
- [142] K. Ohno. *Computational Materials Science: From Ab Initio to Monte Carlo Methods*. Berlin–Heidelberg–New York: Springer–Verlag, 1999.
- [143] G. Choe, M. Zheng, B. R. Acharya, E. N. Abarra, and J. N. Zhou. Perpendicular recording CoPtCrO composite media with performance enhancement capping layer. *IEEE Transactions on Magnetics*, 41:3172, 2005.
- [144] B. Lu, T. Klemmer, K. Wierman, G. Ju, D. Weller, A. G. Roy, D. E. Laughlin, C. Chang, and R. Ranjan. Study of stacking faults in Co-alloy perpendicular media. *Journal of Applied Physics*, 91:8025, 2002.
- [145] B. Bian, W. Yang, D. E. Laughlin, and D. N. Lambeth. Stacking faults and their effect on magnetocrystalline anisotropy in Co and Co-alloy thin films. *IEEE Transactions on Magnetics*, 37:1456, 2001.
- [146] J. Aboaf, S. Herd, and E. Klokhholm. Magnetic properties and structure of cobalt-platinum thin films. *IEEE Transactions on Magnetics*, 19:1514, 1983.
- [147] M. S. Miller, A. E. Schultz, Y. M. Chow, and L. A. Heuer. Optimization of Co-Pt and Co-Cr-Pt-Ta thin films for use in magnetic data storage devices. *Surface and Coatings Technology*, 68–69:696, 1994.
- [148] J.-J. Delaunay, T. Hayashi, M. Tomita, and S. Hirono. Effects of Pt addition on the magnetic and microstructural properties of CoC granular films. *IEEE Transactions on Magnetics*, 34:1627, 1998.

- [149] S. S. A. Razee, J. B. Staunton, and F. J. Pinski. First-principles theory of magnetocrystalline anisotropy of disordered alloys: Application to cobalt platinum. *Physical Review B*, 56:8082, 1997.
- [150] C. Vieu, J. Gierak, H. Launois, T. Aign, P. Meyer, J.-P. Jamet, J. Ferre, C. Chappert, T. Devolder, V. Mathet, and H. Bernas. Modifications of magnetic properties of Pt/Co/Pt thin layers by focused gallium ion beam irradiation. *Journal of Applied Physics*, 91:3103, 2002.
- [151] J. Jaworowicz, A. Maziewski, P. Mazalski, M. Kisielowski, I. Sveklo, M. Tekielak, V. Zablotkii, J. Ferré, N. Vernier, A. Mougín, A. Henschke, and J. Fassbender. Spin reorientation transitions in Pt/Co/Pt films under low dose Ga⁺ ion irradiation. *Applied Physics Letters*, 95:022502, 2009.
- [152] A. Maziewski, P. Mazalski, Z. Kurant, M. O. Liedke, J. McCord, J. Fassbender, J. Ferré, A. Mougín, A. Wawro, L. T. Baczewski, A. Rogalev, F. Wilhelm, and T. Gemming. Tailoring of magnetism in Pt/Co/Pt ultrathin films by ion irradiation. *Physical Review B*, 85:054427, 2012.
- [153] M. Sakamaki, K. Amemiya, M. O. Liedke, J. Fassbender, P. Mazalski, I. Sveklo, and A. Maziewski. Perpendicular magnetic anisotropy in a Pt/Co/Pt ultrathin film arising from a lattice distortion induced by ion irradiation. *Physical Review B*, 86:024418, 2012.
- [154] M. Abes, M. V. Rastei, J. Venuat, A. Carvalho, S. Boukari, E. Beaurepaire, P. Panissod, A. Dinia, J. P. Bucher, and V. Pierron-Bohnes. Magnetic switching field distribution of patterned CoPt dots. *Journal of Applied Physics*, 105:113916, 2009.
- [155] M. Abes, J. Venuat, A. Carvalho, J. Arabski, D. Muller, G. Schmerber, E. Beaurepaire, P. Panissod, A. Dinia, and V. Pierron-Bohnes. Magnetic nanopatterning of CoPt thin layers. *Journal of Magnetism and Magnetic Materials*, 286:297, 2005.
- [156] M. F. Toney, E. E. Marinero, M. F. Doerner, and P. M. Rice. High anisotropy CoPtCrB magnetic recording media. *Journal of Applied Physics*, 94:4018, 2003.
- [157] A. Ishikawa and R. Sinclair. Analyses of stacking fault density in Co-alloy thin films by high-resolution transmission electron microscopy. *IEEE Transactions on Magnetics*, 32:3605, 1996.
- [158] A. Ishikawa and R. Sinclair. Effects of Pt addition on the magnetic and crystallographic properties of CoCrPt thin-film media. *Journal of Magnetism and Magnetic Materials*, 152:265, 1996.

- [159] N. Chetty and M. Weinert. Stacking faults in magnesium. *Physical Review B*, 56:10844, 1997.
- [160] G. B. Mitra and N. C. Hadler. Stacking fault probabilities in hexagonal cobalt. *Acta Crystallographica*, 17:817, 1964.
- [161] L. Holloway and H. Laidler. Measurement of stacking fault densities in CoCrPt thin film media using grazing incidence x-ray scattering. *Journal of Applied Physics*, 87:5690, 2000.
- [162] S. Saito, A. Hashimoto, D. Hasegawa, and M. Takahashi. Semi-quantitative evaluation of stacking faults in pseudo-hcp thin films by laboratory-scale in-plane x-ray diffraction. *Journal of Physics D: Applied Physics*, 42:145007, 2009.
- [163] Y. Takahashi, K. Tanahashi, and Y. Hosoe. Stacking faults in Co–Cr–Pt perpendicular magnetic recording media. *Journal of Applied Physics*, 91:8022, 2002.
- [164] H. Yuan and D. E. Laughlin. Stacking faults in smaller grain size perpendicular media. *IEEE Transactions on Magnetics*, 45:3569, 2009.
- [165] T. Kubo, Y. Kuboki, R. Tanuma, A. Saito, S. Watanabe, and T. Shimatsu. Study of stacking fault effect on magnetic anisotropy of CoPtCr–SiO₂ perpendicular media by synchrotron radiation x-ray diffraction. *Journal of Applied Physics*, 99:08G911, 2006.
- [166] R. Berliner and S. A. Werner. Effect of stacking faults on diffraction: The structure of lithium metal. *Physical Review B*, 34:3586, 1986.
- [167] S. Crampin, K. Hampel, D. D. Vvedensky, and J. M. MacLaren. The calculation of stacking fault energies in close-packed metals. *Philosophical Magazine A*, 5:2107, 1990.
- [168] N. M. Rosengaard and H. L. Skriver. Calculated stacking-fault energies of elemental metals. *Physical Review B*, 47:12865, 1993.
- [169] L. Wen, P. Chen, Z.-F. Tong, B.-Y. Tang, L.-M. Peng, and W.-J. Ding. A systematic investigation of stacking faults in magnesium via first-principles calculation. *The European Physical Journal B*, 72:397, 2009.
- [170] B. L. Györfy. Coherent-potential approximation for a nonoverlapping-muffin-tin-potential model of random substitutional alloys. *Physical Review B*, 5:2382, 1972.

- [171] J. B. Staunton, S. Ostanin, S. S. A. Razee, B. L. Győrffy, L. Szunyogh, B. Ginatempo, and E. Bruno. Long-range chemical order effects upon the magnetic anisotropy of FePt alloys from an *ab initio* electronic structure theory. *Journal of Physics: Condensed Matter*, 16:S5623, 2004.
- [172] F. J. Pinski, B. Ginatempo, D. D. Johnson, J. B. Staunton, G. M. Stocks, and B. L. Győrffy. Origins of compositional order in NiPt alloys. *Physical Review Letters*, 66:766, 1991.
- [173] D. D. Johnson, D. M. Nicholson, F. J. Pinski, B. L. Győrffy, and G. M. Stocks. Density-functional theory for random alloys: Total energy within the coherent-potential approximation. *Physical Review Letters*, 56:2088, 1986.
- [174] A. Bansil, S. Kaprzyk, P. E. Mijnarends, and J. Tobała. Electronic structure and magnetism of $\text{Fe}_{3-x}\text{V}_x\text{X}$ (X=Si, Ga and Al) alloys by the KKR-CPA method. *Physical Review B*, 60:13396, 1999.
- [175] C. J. Aas, L. Szunyogh, R. F. L. Evans, and R. W. Chantrell. Effect of stacking faults on the magnetocrystalline anisotropy of hcp Co: a first-principles study. *Journal of Physics: Condensed Matter*, 25:296006, 2013.
- [176] C. J. Aas, K. Palotás, L. Szunyogh, and R. W. Chantrell. The effect of a Pt impurity layer on the magnetocrystalline anisotropy of hexagonal close-packed Co: a first-principles study. *Journal of Physics: Condensed Matter*, 24:406001, 2012.
- [177] F. Vincent and M. Figlarz. Quelques précisions sur les paramètres cristallins et l'intensité des raies Debye–Scherrer du cobalt cubique et du cobalt hexagonal. *Comptes Rendus Hebdomadaires des Seances de l'Academie des Sciences*, 264:1270, 1967.
- [178] I. V. Solovyev, A. I. Liechtenstein, and K. Terakura. Is Hund's second rule responsible for the orbital magnetism in solids? *Physical Review Letters*, 80:5758, 1998.
- [179] I. V. Solovyev. Orbital polarization in itinerant magnets. *Physical Review Letters*, 95:267205, 2005.
- [180] M. S. S. Brooks. Calculated ground state properties of light actinide metals and their compounds. *Physica B*, 130:6, 1985.
- [181] O. Eriksson, B. Johansson, and M. S. S. Brooks. Meta-magnetism in UCoAl. *Journal of Physics: Condensed Matter*, 1:4005, 1989.

- [182] O. Eriksson, M. S. S. Brooks, and B. Johansson. Orbital polarization in narrow-band systems: Application to volume collapses in light lanthanides. *Physical Review B*, 41:7311, 1990.
- [183] H. Eschrig. *The Fundamentals of Density Functional Theory*. Leipzig: Teubner, 1996.
- [184] H. Eschrig, M. Sargolzaei, K. Koepernik, and M. Richter. Orbital polarization in the Kohn-Sham-Dirac theory. *Europhysics Letters*, 72:611, 2005.
- [185] H. Ebert and M. Battocletti. Spin and orbital polarized relativistic multiple scattering theory – with applications to Fe, Co, Ni and $\text{Fe}_x\text{Co}_{1-x}$. *Solid State Communications*, 98:785, 1996.
- [186] J. Trygg, B. Johansson, O. Eriksson, and J. M. Wills. Total energy calculation of the magnetocrystalline anisotropy energy in the ferromagnetic 3d metals. *Physical Review Letters*, 75:2871, 1995.
- [187] B. Lazarovits. *Diploma Thesis*. University of Vienna, 2000.
- [188] M. B. Stearns. *3d, 4d, and 5d Elements, Alloys and Compounds*. Berlin–Heidelberg–New York: Springer–Verlag, 1986.
- [189] J. Friedel. The distribution of electrons round impurities in monovalent metals. *Philosophical Magazine*, 43:153, 1952.
- [190] J. Patterson and B. Bailey. *Solid-State Physics: Introduction to the Theory 2E*. Berlin–Heidelberg–New York: Springer–Verlag, 2010.
- [191] L. Szunyogh and B. L. Györfly. Magnetic anisotropy of an impurity in a semi-infinite host. *Physical Review Letters*, 78:3765, 1997.
- [192] A. Szilva, S. Gallego, M. C. Muñoz, B. L. Györfly, G. Zaránd, and L. Szunyogh. Friedel-oscillations-induced surface magnetic anisotropy. *Physical Review B*, 78:195418, 2008.
- [193] I. V. Solovyev, P. H. Dederichs, and I. Mertig. Origin of orbital magnetization and magnetocrystalline anisotropy in TX ordered alloys (where $T = \text{Fe, Co}$ and $X = \text{Pd, Pt}$). *Physical Review B*, 52:13419, 1995.
- [194] H. Zhang, M. Richter, K. Koepernik, I. Opahle, F. Tasnádi, and H. Eschrig. Electric-field control of surface magnetic anisotropy: a density functional approach. *New Journal of Physics*, 11:043007, 2009.
- [195] B. Lazarovits, L. Szunyogh, and P. Weinberger. Fully relativistic calculation of magnetic properties of Fe, Co, and Ni adclusters on Ag(100). *Physical Review B*, 65:104441, 2002.

- [196] R. Abbaschian, L. Abbaschian, and R. E. Reed-Hill. *Physical Metallurgy Principles 2E*. Stamford: Cengage Learning, 2009.
- [197] R. R. Zope and Y. Mishin. Interatomic potentials for atomistic simulations of the Ti-Al system. *Physical Review B*, 68:024102, 2003.
- [198] J. P. Hirth and J. Lothe. *Theory of Dislocations*. Malabar: Krieger Publications, 1982.
- [199] F. C. Frank. LXXXIII. Crystal dislocations. Elementary concepts and definitions. *Philosophical Magazine Series 7*, 42:809, 1951.
- [200] B. Hammer, K. W. Jacobsen, V. Milman, and M. C. Payne. Stacking fault energies in aluminium. *Journal of Physics: Condensed Matter*, 4:10453, 1992.
- [201] P. J. H. Denteneer and J. M. Soler. Defect energetics in aluminium. *Journal of Physics: Condensed Matter*, 3:8777, 1991.
- [202] J. Xu, W. Lin, and A. J. Freeman. Twin-boundary and stacking-fault energies in Al and Pd. *Physical Review B*, 43:2018, 1991.
- [203] S. Schweizer, C. Elsässer, K. Hummler, and M. Fähnle. *Ab initio* calculation of stacking-fault energies in noble metals. *Physical Review B*, 46:14270, 1992.
- [204] A. F. Wright, M. S. Daw, and C. Y. Fong. Theoretical investigation of (111) stacking faults in aluminium. *Philosophical Magazine A*, 66:387, 1992.
- [205] M. H. Kryder, E. C. Gage, T. W. McDaniel, W. A. Challener, R. E. Rottmayer, G. Ju, Y.-T. Hsia, and M. F. Erden. Heat assisted magnetic recording. *Proceedings of the IEEE*, 96:1810, 2008.
- [206] G. Brown, B. Kraczek, A. Janotti, T. C. Schulthess, G. M. Stocks, and D. D. Johnson. Competition between ferromagnetism and antiferromagnetism in FePt. *Physical Review B*, 68:052405, 2003.
- [207] Z. Lu, R. V. Chepulskaa, and W. H. Butler. First-principles study of magnetic properties of L1₀-ordered MnPt and FePt alloys. *Physical Review B*, 81:094437, 2010.
- [208] S. H. Whang, Q. Feng, and Y.-Q. Gao. Ordering, deformation and microstructure in L1₀ type FePt. *Acta Materialia*, 46:6485, 1998.
- [209] T. B. Massalski, J. L. Murray, L. H. Bennet, and H. Baker. (ed.) *Binary Phase Diagrams*. Materials Park: ASM International, 1986.

- [210] S. Okamoto, N. Kikuchi, O. Kitakami, T. Miyazaki, Y. Shimada, and K. Fukamichi. Chemical-order-dependent magnetic anisotropy and exchange stiffness constant of FePt (001) epitaxial films. *Physical Review B*, 66:024413, 2002.
- [211] J. Lyubina, I. Opahle, K.-H. Müller, O. Gutfleisch, M. Richter, M. Wolf, and L. Schultz. Magnetocrystalline anisotropy in L₁₀ FePt and exchange coupling in FePt/Fe₃Pt nanocomposites. *Journal of Physics: Condensed Matter*, 17:4157, 2005.
- [212] P. V. Lukashev, N. Horrell, and R. F. Sabirianov. Tailoring magnetocrystalline anisotropy of FePt by external strain. *Journal of Applied Physics*, 111:07A318, 2012.
- [213] C. J. Aas, L. Szunyogh, and R. W. Chantrell. Effects of composition and chemical disorder on the magnetocrystalline anisotropy of Fe_xPt_{1-x} alloys. *Europhysics Letters*, 102:57004, 2013.
- [214] J. A. Christodoulides, P. Farber, M. Dannl, H. Okumura, G. C. Hadjipanaysi, V. Skumryev, A. Simopoulos, and D. Weller. Magnetic, structural and microstructural properties of FePt/M (M=C,BN) granular films. *IEEE Transactions on Magnetics*, 37:1292, 2001.
- [215] T. Burkert, O. Eriksson, S. I. Simak, A. V. Ruban, B. Sanyal, L. Nordström, and J. M. Wills. Magnetic anisotropy of L₁₀ FePt and Fe_{1-x}Mn_xPt. *Physical Review B*, 71:134411, 2005.
- [216] H. Ebert, H. Freyer, and M. Deng. Manipulation of the spin-orbit coupling using the Dirac equation for spin-dependent potentials. *Physical Review B*, 56:9454, 1997.
- [217] F. C. Nix and W. Shockley. Order-disorder transformations in alloys. *Reviews of Modern Physics*, 10:1, 1938.
- [218] B. E. Warren. *X-Ray Diffraction*. Dover Publications, 1990.
- [219] JCPDS – International Centre of Diffraction Data. 1999.
- [220] M. L. Yan, Y. F. Xu, and D. J. Sellmyer. Nanostructure and magnetic properties of highly (001) oriented L₁₀ (Fe₄₉Pt₅₁)_{1-x}Cu_x films. *Journal of Applied Physics*, 99:08G903, 2006.
- [221] R. V. Chepulskii and W. H. Butler. *Ab initio* magnetocrystalline anisotropy at nanoscale: The case of FePt. *Applied Physics Letters*, 100:142405, 2012.

- [222] A. B. Shick and O. N. Mryasov. Coulomb correlations and magnetic anisotropy in ordered L1₀ CoPt and FePt alloys. *Physical Review B*, 67:172407, 2003.
- [223] A. Sakuma. First principle calculation of the magnetocrystalline anisotropy energy of FePt and CoPt ordered alloys. *Journal of the Physical Society of Japan*, 63:3053, 1994.
- [224] J. S. Chen. Private communication. November 2011.
- [225] K. Barmak. L1₀ FePt: ordering, anisotropy constant and their relation to film composition. *Presented at the 12th Joint MMM Intermag Conference, Chicago, IL, January 2013.*
- [226] K. Barmak. Private communication. January 2013.
- [227] E. Yang, D. E. Laughlin, and J.-G. Zhu. Correction of order parameter calculations for FePt perpendicular thin films. *IEEE Transactions on Magnetics*, 48:7, 2012.
- [228] M. Birkholz. *Thin Film Analysis by X-Ray Scattering*. Weinheim: John Wiley & Sons Ltd. (Wiley-VCH), 2006.
- [229] P. J. Hasnip. Private communication. February 2013.
- [230] J. P. Perdew. Density-functional approximation for the correlation energy of the inhomogeneous electron gas. *Physical Review B*, 33:8822, 1986.
- [231] A. Dannenberg, M. E. Gruner, A. Hucht, and P. Entel. Surface energies of stoichiometric FePt and CoPt alloys and their implications for nanoparticle morphologies. *Physical Review B*, 80:245438, 2009.
- [232] W. Pfeiler. *Alloy Physics*. Chichester: John Wiley & Sons Ltd., 2007.
- [233] E. F. Kneller and R. Hawig. The exchange-spring magnet: a new material principle for permanent magnets. *IEEE Transactions on Magnetics*, 27:3588, 1991.
- [234] R. Skomski and J. M. D. Coey. Giant energy product in nanostructured two-phase magnets. *Physical Review B*, 48:15812, 1993.
- [235] F. Casoli, F. Albertini, L. Nasi, S. Fabbrici, R. Cabassi, F. Bolzoni, C. Bocchi, and P. Luches. Role of interface morphology in the exchange-spring behavior of FePt/Fe perpendicular bilayers. *Acta Materialia*, 58:3594, 2010.

- [236] D. Makarov, J. Lee, C. Brombacher, C. Schubert, M. Fuger, D. Suess, J. Fidler, and M. Albrecht. Perpendicular FePt-based exchange-coupled composite media. *Applied Physics Letters*, 96:062501, 2010.
- [237] A.-C. Sun, F.-T. Yuan, J.-H. Hsu, Y.H. Lin, and P.C. Kuo. Magnetic reversal behaviors of perpendicular exchange-coupled Fe/FePt bilayer films. *IEEE Transactions on Magnetics*, 45:2709, 2009.
- [238] D. C. Crew, J. Kim, L. H. Lewis, and K. Barmak. Interdiffusion in bilayer CoPt/Co films: potential for tailoring the magnetic exchange spring. *Journal of Magnetism and Magnetic Materials*, 233:257, 2001.
- [239] J. S. Jiang, J. E. Pearson, Z. Y. Liu, B. Kabius, S. Trasobares, D. J. Miller, S. D. Bader, D. R. Lee, D. Haskel, G. Srajer, and J. P. Liu. Improving exchange-spring nanocomposite permanent magnets. *Applied Physics Letters*, 85:5293, 2004.
- [240] F. Casoli, F. Albertini, S. Fabbri, C. Bocchi, L. Nasi, R. Ciprian, and L. Pareti. Exchange-coupled FePt/Fe bilayers with perpendicular magnetization. *IEEE Transactions on Magnetics*, 41:3877, 2005.
- [241] F. Casoli, F. Albertini, L. Nasi, S. Fabbri, R. Cabassi, F. Bolzoni, and C. Bocchi. Strong coercivity reduction in perpendicular FePt/Fe bilayers due to hard/soft coupling. *Applied Physics Letters*, 92:142506, 2008.
- [242] G. Varvaro, F. Albertini, E. Agostinelli, F. Casoli, D. Fiorani, S. Laureti, P. Lupo, P. Ranzieri, B. Astinchip, and A.M. Testa. Magnetization reversal mechanism in perpendicular exchange-coupled Fe/L1₀-FePt bilayers. *New Journal of Physics*, 14:073008, 2012.
- [243] B. Ma, H. Wang, H. Zhao, C. Sun, R. Acharya, and J.-P. Wang. FePt/Fe exchange coupled composite structure on MgO substrates. *IEEE Transactions on Magnetics*, 46:2345, 2010.
- [244] C. J. Aas, P. J. Hasnip, R. Cuadrado, E. M. Plotnikova, L. Szunyogh, L. Udvardi, and R. W. Chantrell. Exchange coupling and magnetic anisotropy at Fe/FePt interfaces. *Physical Review B*, Submitted., 2013.
- [245] K. Kambe. Theory of electron diffraction by crystals. Green's function and integral equation. *Zeitschrift für Naturforschung*, 22a:422, 1967.
- [246] E. G. McRae. Multiple-scattering treatment of low-energy electron-diffraction intensities. *The Journal of Chemical Physics*, 45:3258, 1966.

- [247] H. Ibach and H. Lèuth. *Solid-State Physics: An Introduction to Principles of Materials Science*. Berlin–Heidelberg–New York: Springer–Verlag, 2009.
- [248] K. Barmak, J. Kim, D. C. Berry, K. W. Wierman, E. B. Svedberg, and J. K. Howard. Calorimetric studies of the A1 to L1₀ transformation in FePt and related ternary alloy thin films. *Journal of Applied Physics*, 95:7486, 2004.
- [249] H. E. Hall and J. R. Hook. *Solid State Physics 2E*. Chichester: John Wiley & Sons Ltd., 1991.
- [250] B. Újfalussy, L. Szunyogh, P. Bruno, and P. Weinberger. First-principles calculation of the anomalous perpendicular anisotropy in a Co monolayer on Au(111). *Physical Review Letters*, 77:1805, 1996.
- [251] F. Gimbert and L. Calmels. First-principles investigation of the magnetic anisotropy and magnetic properties of Co/Ni(111) superlattices. *Physical Review B*, 86:184407, 2012.
- [252] K. Kyuno, J.-G. Ha, R. Yamamoto, and S. Asano. Perpendicular magnetic anisotropy of metallic multilayers composed of magnetic layers only: Ni/Co and Ni/Fe multilayers. *Japanese Journal of Applied Physics*, 35:2774, 1996.
- [253] G. H. O. Daalderop, P. J. Kelly, and M. F. H. Schuurmans. Magnetic anisotropy of a free-standing Co monolayer and of multilayers which contain Co monolayers. *Physical Review B*, 50:9989, 1994.
- [254] L. Szunyogh, B. Újfalussy, C. Blaas, U. Pustogowa, C. Sommers, and P. Weinberger. Oscillatory behavior of the magnetic anisotropy energy in Cu(100)/Co_n multilayer systems. *Physical Review B*, 56:14036, 1997.
- [255] U. Bauer, M. Dabrowski, M. Przybylski, and J. Kirschner. Experimental confirmation of quantum oscillations of magnetic anisotropy in Co/Cu(001). *Physical Review B*, 84:144433, 2011.
- [256] M. Przybylski, M. Dabrowski, U. Bauer, M. Cinal, and J. Kirschner. Oscillatory magnetic anisotropy due to quantum well states in thin ferromagnetic films (invited). *Journal of Applied Physics*, 111:07C102, 2012.
- [257] N. Zettili. *Quantum Mechanics – Concepts and Applications 2E*. Chichester: John Wiley & Sons Ltd., 2009.
- [258] L. S. Rodberg and R. M. Theler. *The Quantum Theory of Scattering*. New York: Academic Press, 1967.

- [259] P. Weinberger. *Electron Scattering Theory for Ordered and Disordered Matter*. Oxford: Clarendon Press, 1990.
- [260] B. A. Lippmann and J. Schwinger. Variational principles for scattering processes I. *Physical Review*, 79:469, 1950.
- [261] P. Lloyd. Wave propagation through an assembly of spheres II: the density of single-particle eigenstates. *Proceedings of the Physical Society, London*, 90:207, 1967.
- [262] P. Lloyd and P. V. Smith. Multiple scattering theory in condensed materials. *Advances in Physics*, 21:69, 1972.
- [263] R. Zeller. An elementary derivation of Lloyd's formula valid for full-potential multiple-scattering theory. *Journal of Physics: Condensed Matter*, 16:6453, 2004.